The Characterisation and Development of Silicon Microneedles

Megan Jessica M^{c}Namee, MPharmacology

Submitted to Swansea University in fulfilment of the requirements for the
degree of Engineering Doctorate

Swansea University

2025

Abstract

Oral drug delivery is widely regarded as the ideal administration route due to its ease of manufacture, storage stability, and high patient compliance. In many clinical instances, however, it proves unsuitable due to the hepatic first pass metabolism, which significantly reduces drug bioavailability and therapeutic efficacy. In response, microneedles (MNs) have garnered increasing attention from public and research sectors, offering painless administration and dose-sparing potential.

Silicon MNs were the first devices developed for minimally invasive drug delivery, and recent advances in semi-conductor processing have made their scalable production increasingly feasible. This research aimed to establish evidence for their effective and safe use by characterising their mechanical, biological, and functional performance.

Devices were fabricated at 100 mm wafer scale, with process optimisation focused on improving yield and structural fidelity. Devices were produced at heights up to 600 μm with good feature fidelity and yields reaching 82 %. Insertion mechanics were evaluated using digital image correlation (DIC), enabling comparison of strain profiles between MN and hypodermic insertion - the latter served as the clinical gold standard. Over the imaged period, hypodermic needles exerted approximately fourfold greater strain than MNs, indicating the potential for reduced tissue trauma.

Biocompatibility of both the silicon substrate and fabricated devices was confirmed using ISO 10993-5 compliant cytotoxicity assays, with no statistically significant impact on the viability of human immortalised keratinocytes. To assess repeatability, dye-based injections into dermal mimics were performed, demonstrating consistent bolus formation and reproducible diffusion. MN injection plumes were uniform in size and morphology, in contrast to the variability observed with hypodermic delivery.

To improve compatibility with continuous industrial manufacturing, etch steps were optimised at 150 mm wafer scale, which, when combined with the redesigned layout, resulted in a 140 % increase in usable device die. This research addressed key gaps in silicon MN literature, including fabrication throughput, potential cytotoxicity, and performance benchmarking. Furthermore, this work developed a standardised methodology for device performance assessment and demonstrated feasibility for the scaled manufacture of both hollow and solid silicon MNs.

Acknowledgement of Funding

I would like to acknowledge the COATED M2A funding from KLA, the European Social Fund *via* the Welsh Government (c80816), and the Engineering and Physical Sciences Research Council (Grant Ref: EP/S02252X/1) that has made this research possible.

Declaration

This work has not previously been accepted in substance for any degree and is not being concurrently submitted in candidature for any degree.

Signed: M.M^{c}Namee

Date: 14 Nov 2025

This thesis is the result of my own investigations, except where otherwise stated. Other sources are acknowledged by footnotes giving explicit references. A bibliography is appended.

Signed: M.M^{c}Namee

Date: 14 Nov 2025

I hereby give consent for my thesis, if accepted, to be available for electronic sharing.
Signed: M.M^{c}Namee

Date: 14 Nov 2025

The University’s ethical procedures have been followed and, where appropriate, that ethical approval has been granted.

Signed: M.M^{c}Namee

Date: 14 Nov 2025

Contents

For my grandad, Da — the first engineer of the family.

Acknowledgements

This research would not have been possible if not for the help, guidance, and support of a number of people. Support came from these people in a wide variety of forms, all as valuable as each other.

My first thanks go to my supervisor, Dr Hari Arora, for taking me on as a student. Your confidence in my abilities has ensured that I have pushed myself technically and made this body of work my own. I am very grateful. My thanks also go to Professor Owen Guy, for providing me with the opportunity to take on this research project.

My thanks to Dr David Warren and Mrs Rebecca White, for their continuous guidance, faith, and support. These four years would not have been possible without you.

To my once colleagues, now friends, Ffyon Moody, Sahar Sattar, and Tom Pritchard, for being a bottomless source of support through the good and trying times. Your guidance and willingness to listen have been constant, and I genuinely could not have reached this point without you.

To the academic and process team staff, who supported me in working within a field I could never have imagined myself capable of pursuing. Specifically, Dr Ryan Bigham, Dr Jon Evans, Dr Kirsty Meldrum, and Ian Hemming for fielding my constant questions and being so quick to laugh.

To my industrial sponsors, KLA. Dr Huma Ashraf, Kerry Roberts, Dr Chris Bolton, and Dr Jacob Mitchell — your support has exceeded technical guidance and has gone above and beyond what I could have expected. Special thanks to Jacob for his unwavering moral support, and Chris, who taught me lessons in fabrication and sarcasm in equal measure.

To my friends, who have put up with four years of the side effects from my studies — namely, Evie Williams, Sarah Bunton, and Keira Davies. I am so grateful for each of you and feel very lucky to have three strong women who have not only always had faith in me, but who have led me by example in their respective fields.

To my family — Cheryl, Mike, and Ffi M^{c}Namee. Words cannot describe how grateful I am for the support you've afforded me, and how much you've allowed me to lean on you, across the last four years. Mam and Dad, for both your confidence in my abilities and your patience. Ffi, for bragging about what your sister does for work to anyone who'll listen, despite not really knowing what's going on. I am truly grateful. You are all my biggest cheerleaders.

My final, and most sincere thanks, go to my partner, James Moriarty-Simmonds. It is impossible to articulate how grateful I am for everything you've enabled me to do over the last four years. You have been steadfast through the turbulence, and quick to celebrate every small win — truly my biggest fan. Without your unconditional support, understanding, and love, this thesis would genuinely not have been possible.

in omnia paratus

Acronyms

3D	3-Dimensional
AI	Artificial intelligence
ANOVA	Analysis of variance
APC	Antigen presenting cell
API	Active pharmaceutical ingredient
BOE	Buffered oxide etch
CD	Critical dimension
COVID-19	SARS-CoV-2
DI	Deionised
DIC	Digital image correlation
DMN(s)	Dissolving microneedle(s)
DMSO	Dimethyl sulfoxide
DNA	Deoxyribonucleic acid
DNQ	Diazonaphthoquinone
DOF	Depth of field
DRIE	Deep reactive ion etching
ECM	Extracellular matrix
EDTA	Ethylenediamine-tetra acetic acid
EMA	European Medical Agency
ESC	Electrostatic chuck
FDA	Food and Drug Administration
FOV	Field of view
GDP	Gross domestic product
GI	Gastrointestinal
GMP	Good manufacturing practices
HA	Hyaluronic acid
HaCaT	Human immortalised keratinocyte cells

HB	Hollow block
HF	Hydrofluoric acid
HMN(s)	Hollow microneedle(s)
Hypo	Hypodermic needle
ICP	Inductively coupled plasma
ID	Intradermal
IF	Interstitial fluid
IM	Intramuscular
IPA	Isopropyl alcohol
ISO	International Standards Organisation
IV	Intravenous
LED	Light emitting diode
MEMS	Micro-electro-mechanical systems
MHRA	Medicines and Healthcare products Regulatory Agency
MN(s)	Microneedle(s)
NU	Non-uniformity
OCT	Optical coherence tomography
OSD	Oral solid dose
OTC	Over-the-counter
PAC	Photoactive compound
PBS	Phosphate buffered saline
PDMS	Polydimethylsiloxane
PE-CVD	Plasma-enhanced chemical vapour deposition
PK	Pharmacokinetic
PMMA	Poly-methyl methacrylate
PR	Photoresist
PVA	Polyvinyl alcohol
RF	Radio frequency
RNA	Ribonucleic acid

SA	Sodium alginate
SB	Solid block
SC	Subcutaneous
SD	Standard deviation
SEM	Scanning electron microscopy
SLA	Stereolithography
SMN(s)	Solid microneedle(s)
SOD	Stand-off distance
TMAH	Tetramethylammonium hydroxide
TRL	Technology readiness level
UV	Ultraviolet

Units

%	Percentage
Bar	Pressure
cells/cm^2	Cells *per* square centimetre
cells/ml	Cells *per* millilitre
cm^2	Centimetre squared
Da	Dalton
fps	Frames *per* second
G	Gauge
mg	Milligram
mg/mL	Milligram *per* millilitre
mJ/cm^2	Millijoules *per* square centimetre
mL	Millilitre
mm	Millimetre
mM	Millimolar
mm/s	Millimetre *per* second
ng	Nanogram
ng/mL	Nanogram *per* millilitre
nm	Nanometre
^{o}	Degrees
^{o}C	Degrees centigrade
µg/mL	Micrograms *per* millilitre
µL	Microlitre
µm	Micrometre
µM	Micromolar
W	Watt

Equations

List of Figures

List of Tables

Publications

M^{c}Namee, M., Pritchard, T., Mitchell, J., Bolton, C., Roberts, K., Guy, O., Ashraf, H., & Arora, H. (2025). Novel stereo-DIC characterisation of microneedle and hypodermic needle insertion. *Frontiers in Bioengineering and Biotechnology, 13*, Article 1580464. https://doi.org/10.3389/fbioe.2025.1580464

M^{c}Namee, M., Wong, S., Guy, O., & Sharma, S. (2023). Microneedle technology for potential SARS-CoV-2 vaccine delivery. *Expert opinion on drug delivery*, *20*(6), 799-814. https://doi.org/10.1080/17425247.2023.2209718

Pritchard, T., van Loon, R., **McNamee, M**., & Arora, H. (under review, submitted 15 Aug 25). Novel volumetric strain measurement technique based on particle tracking. *Measurement.*

Conferences

Stereo-DIC Characterisation of Microneedle and Hypodermic Needle Insertion. *KLA WISE 2025* Presentation.

Stereo-DIC Characterisation of Microneedle and Hypodermic Needle Insertion. *Microneedles 2025* Flash presentation and poster.

Stereo-DIC Characterisation of Microneedle and Hypodermic Needle Insertion. *Materials and Manufacturing Annual Conference 2025* Presentation.

A Novel stereo-DIC Method for Comparing Microneedle and Hypodermic Insertions. *Materials and Manufacturing Annual Conference 2024* Poster presentation.

Sustainability and Development Goals. *Discover Engineering Festival 2024* Session lead.

Silicon Microneedles for Drug Delivery. *Materials and Manufacturing Annual Conference 2023* Poster presentation.

Silicon Microneedles for Drug Delivery. *BioMedEng 2023* Poster presentation.

The Development of Silicon Microneedles for Drug Delivery. *Materials and Manufacturing Annual Conference 2022* Poster presentation.

Discover Materials Conference 2022 Attendance.

Silicon Microneedles for Drug Delivery. *Engineering a Future in Wales 2022* Presentation.

Medical Wearables for Biosensors 2021 Attendance.

Awards

Nomination and Shortlist: **“***Outstanding Contribution to Public Engagement”* Swansea University, 2025.

Winner: *“Best Presentation Award”* Engineering Research Network Wales, 2022.

Winner: *“Best Presentation Award”* M2RI, Materials and Manufacturing Conference, Swansea University, 2025.

Public Engagement Activities and its Importance

Public engagement and science communication play a critical role in promoting awareness of science, technology, engineering, and mathematics (STEM), highlighting to younger generations the variety careers and pathways available to them within these fields. By actively fostering connections between research and higher education communities and non-specialist audiences, public engagement aids in the clear dissemination of complex scientific concepts, building transparency and trust between these parties. This pertains specifically to the present project, whereby research involving medical devices for the purpose of drug, and specifically vaccine, administration is prone to harmful misinformation. Researchers, including PhD students, have a responsibility to engage with non-specialist audiences and facilitate the translation of scientific progress in an accessible and clear manner, supporting education and fostering public trust. Below is a summary of public engagement activities which I have designed, led, or contributed to, organised by activity type.

Outreach Training

i. RAEng Reaching Wider Training Workshop (2022)
   This workshop provided strategies and techniques required for effective science communication to primary and secondary school children, to ensure both good engagement and effective comprehension of scientific advances.

School Outreach Workshops

ii. Pennard Primary School, Gower (2021)
   I introduced students to the microneedles research project, inspiring interest in medical device development.
iii. Monkton Primary School, Pembrokeshire (2022)
   We explored sustainable development within engineering, encouraging students to deliberate on societal challenges and responsible design to benefit all.
iv. Cowbridge Comprehensive School, Vale of Glamorgan (2024, 2025)

I organised and led multiple STEM careers session, sharing my microneedle research to illustrate real-world research and opportunities in STEM.

v. St Joseph's Cathedral Primary School, Swansea (2025)
I delivered activities on sustainability and development, promoting awareness of STEM's role in addressing societal challenges.

Outreach Conferences and Festivals

vi. Discover Materials Conference (2022)
We shared best practices for connecting children with materials engineering, sharing various mediums and techniques which are effective for engagement.

vii. Discover Engineering Festival (2024)
I delivered interactive demonstrations of biomedical devices, enhancing public understanding of STEM concepts and encouraging engagement with engineering research.

1. Chapter 1: Introduction

This introduction chapter begins to provide the context and rationale behind the present research. It reviews the scientific and clinical relevance of microneedle technologies, highlighting the requirement for them, their current shortcomings, and key hurdles to their translation into the clinic. This chapter defines the aim and objectives for the presented research, establishing a strong basis for the subsequent experimental chapters.

1.1. Research sphere background

Transdermal drug delivery has been investigated in various formats, ranging from non-invasive methodologies, such as patches, gels, and creams, to minimally invasive platforms, such as electroporation and microneedles (MNs). This transdermal administration route has long been favoured for providing over-the-counter alternatives and improved patient compliance. It is also useful for circumventing the physiological barriers that can compromise therapeutic efficacy such as the first-pass metabolism and variable pharmacokinetics (PKs).

MNs, of which the various different forms are detailed in Chapter 2, offer an attractive compromise between traditional transdermal platforms and injection-based delivery, merging minimal invasiveness and superior bioavailability. These micron-scale projections were designed to breach the physical *stratum corneum* barrier and efficaciously deliver drug formulations, without the activation of pain receptors deeper in the skin architecture.

Early MN prototypes culminated in the first patent filed in 1971 by Alza Corporation for silicon MNs. Despite providing excellent proof of concept, significant advances were not made until the 1990s, when the development of microfabrication matured.

Following this early conceptualisation, MN classifications and materials have diversified, to include solid, hollow, and dissolving device types manufactured from silicon, polymers, and ceramics. These developments expanded their potential further than pain reduction and precise dosing, offering the possibilities of self-administration, biosensing, and controlled release medications.

As MN research has progressed through successive stages of translational development, attention has pivoted to understanding the influence of design features on patient safety, therapeutic efficacy, and manufacturing feasibility. Devices produced from polymer and hydrogel materials are manufactured *via* additive or mould-based techniques such as 3-dimensional (3D) printing and micro-moulding, offering huge advantages with respect to production speed and process malleability. Alternatively, devices such as silicon MNs leverage an already well established manufacturing route, capitalising upon the micro-electro-mechanical systems (MEMS) industry for their understanding and scalability of semi-conductor based products. Specific to silicon MNs is the well-established precision infrastructure in place to repeatably and reliably produce high quality devices.

In a post SARS-CoV-2 (COVID-19) world, the clinical value of platforms that enable dose-sparing vaccination and self-administration enabled MNs to become increasingly recognised for their potential within healthcare. Although the diverse and versatile applications of the devices hold genuine promise, the translation of MN technologies through to clinical usage remains constrained by both regulatory and practical considerations. Chief among these considerations is the lack of standardisation and device/drug classifications. In particular, there is an urgent need for a more systematic approach to the study of mechanical, biological, and functional properties in order to streamline translation.

Despite substantial development within the sphere of MN research and diversification of device types and materials, significant gaps remain in our understanding of silicon MN's mechanical performance, biological compatibility, functional repeatability, and manufacturing limitations. As a result, this ambiguity has limited the translation of silicon devices in favour of more flexible alternatives, such as polymer devices. Despite this, there is solid rationale for furthering the understand of silicon MNs, with advantages offered in the form of rapid scalability, precision, and high quality manufacture, and the potential for integration with smart drug delivery platforms, including biosensing and controlled release. Before this potential can be realised and devices can be progressed to clinic, however, it is necessary to address these widely reported knowledge gaps pertaining to their mechanical performance, biological compatibility, functional repeatability, and manufacturing limitations .

In consequence, this research aimed to investigate the manufacture, biological compatibility, functionality and reliability of silicon MNs, before making ground on the scalability of the device production to a more industrially relevant scale. By systematically examining these key areas, this thesis contributes to the establishment of a robust foundation for translating silicon MNs from laboratory scale prototypes to a viable platform for industry-scale production and clinical use.

1.2. Silicon microneedles

Silicon was the first material utilised for MN fabrication, with early reports of their production in the Georgia Institute of Technology in the 1990s (1). Its adoption during this period reflected the maturity of the semi-conductor and MEMS processing industry, which was already being employed in both academic and industrial environments. The access to cleanroom infrastructure, together with established methodologies for patterning and etching, rendered silicon an excellent material for initial device development. The well-established manufacturing technologies enabled precise control over geometries and the production of repeatable, high resolution structures – critical considerations for consistent and pain-free skin penetration.

A major advantage of silicon MNs is found in the ability to exploit its crystal planes to produce sharp-tipped devices without the requirement for post-fabrication polishing (2). With traditional stainless steel devices, the hypodermic tips are sharpened using a grinding technique, which requires a trade-off to be made between sharpness and bevel length, making it more difficult to produce a sharper steel needle with a short bevel (2, 3). Silicon devices, however, can be etched to produce sharp tips with short bevels, offering a processing improvement from the gold standard hypodermics (3).

Complementing their sharpness, silicon MNs also offer exceptionally smooth surfaces. The lack of abrasive finishing methodologies such as grinding and polishing enable MNs to be inserted with minimal friction, reducing the tissue damage ensured during insertion (3). The smoother surface and lack of requirement for finishing techniques also results in a lower likelihood of contamination of insertion site from residual manufacturing debris, supporting the device safety profile (3).

A distinctive advantage to the utilisation of silicon as a MN substrate comes from its inherent compatibility with MEMS systems (4). Silicon is the foundation of the semiconductor industry and provides a platform which would facilitate the straightforward integration of additional functionalities into the device. This makes silicon MNs the ideal candidate for the integration of components to produce smart devices, such as sensors and drug reservoirs, opening the device potential up to areas including diagnostics, biosensing, and controlled release platforms.

1.3. Challenges facing silicon microneedle development

As with any emerging technology, the journey from laboratory innovation to clinical reality is a long and complex one. Numerous hurdles must be overcome in order to enable MN devices to progress from research and development to clinical application. Whilst certain obstacles are common to all MN platforms, others are material specific, for example pertaining to the unique intrinsic properties of silicon. Recognising and critically examining these challenges is key. Therefore, this section considers both categories, with specific focus on the material limitations of silicon MNs, highlighting where future work is necessary to support the advancement towards clinical translation. The challenges facing the development of silicon MN development will be expanded and evidenced in the literature review of this thesis (Chapter 2: Literature Review).

1.3.1. Mechanical limitations

Silicon MNs are widely acknowledged to face significant mechanical challenges, stemming predominantly from the intrinsic properties of silicon as a base material. Whilst silicon's structure offers a multitude of advantages, such as its amenability for precision microfabrication, and the potential for its integration into electronic, smart drug delivery systems, its crystalline nature results in brittleness and low fracture toughness, rendering it prone to cracking under mechanical stress (5). Consequently, this brittleness introduces a fundamental design constraint: a delicate balance must be struck between structural integrity and tip sharpness. This engineering trade-off must ensure that the devices are sufficiently sharp to penetrate the *stratum corneum*, whilst retaining a robust shaft capable of withstanding fracture during insertion. An additional consideration arises with the brittle nature of silicon, with a sharp tip geometry potentially leading to a high-stress concentration, localised most likely at the tip or the base, again exacerbating fracture risk (6). This brittleness also adds an additional layer of complication post-fabrication with respect to handling, packaging, and applicator integration, whereby unintended mechanical stress can compromise device integrity (7).

To best understand the clinical viability of silicon MNs as a medical device platform, it is critical to foster a deeper understanding of how this brittleness may manifest under biologically relevant conditions. Addressing these gaps through simulations and *in situ* mechanical testing will be crucial in informing future design iterations and evaluating the suitability for silicon MN platforms within clinically relevant settings.

1.3.2. Biocompatibility concerns

The fabrication of silicon MNs *via* MEMS-based manufacturing processes necessitates the use of harsh agents, including corrosive and, in some instances toxic, chemicals in both liquid and gaseous states. Therefore, it is essential that device cleaning and sterilisation procedures are rigorously established and validated, to prevent residual contamination from posing a cytotoxicity risk. Unfortunately, however, well established sterilisation methodologies including aggressive gamma irradiation and electron beam sterilisation may alter the surface chemistry and morphology of the devices, potentially compromising their performance as drug-release, sensing, and smart delivery platforms (8-10). In contrast to this, steam autoclaving and ethylene oxide sterilisation are alternative methodologies available to be utilised on silicon-based platforms which may be more compatible and appropriate, mitigating this specific concern.

Additional biocompatibility concerns require further addressing within the silicon MN research sphere. In particular, there is a lack of cytotoxicity testing with regarding interactions with location specific skin cells, such as keratinocytes, which reside in their majority in the *epidermis*. In the absence of comprehensive evaluation of how silicon MNs interact with these cells, it remains difficult to assess their cytotoxic potential and, by extension, their cellular biocompatibility. With the majority of studies focusing on very short-term exposure during the injection usage period, followed by limited injection site monitoring, further studies are required to investigate cellular effects following medium-to-longer-term exposure. This would enable more robust conclusions to be drawn regarding the cytotoxicity and biocompatibility of these silicon devices.

1.3.3. Manufacturing limitations

Despite the multitude of advantages afforded by the MEMS-driven fabrication, the production of silicon MNs remains constrained by several obstacles. Chief among these is the reliance on high grade cleanroom facilities and precision equipment, both of which require substantial financial investment and resultantly place them beyond the economic reach of many laboratories and research institutes. Financial demands stem not only from the silicon wafer starting materials, but also from the upkeep of these heavily regulated environments, with the outsourcing of fabrication steps rarely offering a more economical alternative. Despite this, the broader semiconductor industry is currently experiencing extraordinary expansion, with the global market projected grow at more than twice the rate of global gross domestic product (GDP), exceeding $1 trillion by 2030 (11). This expansion is attributable largely to the climbing demand for the Internet of Things, advanced automotive applications, and artificial intelligence (AI). In consequence, access to fabrication suites is broadening, and with it costs are likely to fall, offering a persuasive offset for current financial barriers.

In MEMS fabrication, whereby multi-step, subtractive manufacturing dominate, the modification of device geometry (either for improvement or functionalities purposes) requires the redesign and reproduction of photomasks and re-optimisation of fabrication recipes. This compounds layers of complexity to design iterations, manifesting as a slower product development cycle for silicon MNs. Contrastingly, the 'fail fast' product development philosophy applied to polymer MNs production offers a faster, more flexible development route *via* additive manufacturing.

When taking a wider view and looking beyond the intricacies of design, the production scale also poses difficulties. Currently, 100 mm silicon wafers are used as starting materials for the fabrication process, which offers reduced real estate for the device die than the 150 mm minimum industry standard, with a die defined as small section of wafer correlating to one device. This discrepancy renders the current process incompatible with industry standard manufacturing, necessitating different sized handling tools in all equipment used to enable integration into semi-automatic processing at these facilities. Furthermore, the restrictions surrounding wafer real estate prevent the inclusion of test die regions, which would enable the trialling of geometry changes on small wafer regions in an attempt to speed device development. Together, these factors limit both cost-effectiveness and scalability, supporting the need to transition silicon MN production to more industrially relevant scales.

1.3.4. Regulatory barriers

MN technologies, irrespective of their material or mechanism of drug delivery, face substantial regulatory barriers. Translating MNs from research to a clinical environment continues to navigate largely uncharted regulatory territory, where requirements are unclear and varied. Regulatory bodies such as the American Food and

Drug Administration (FDA), the European Medical Agency (EMA), and the Medicines and Healthcare products Regulatory Agency (MHRA) are yet to establish universally accepted and standardised testing protocols for evaluating MN safety, efficacy, and performance. Within the research sphere, the absence of harmonised protocols has created uncertainty for developers, leading to a divergence in the methodologies used preventing a real benchmark from being established. This ultimately renders progression through the regulatory pathway slow, and, to date, no MN device intended for medical applications has secured regulatory approval, highlighting the extensive progress required before this technology becomes accessible at the patient level.

Providing an additional layer of uncertainty to the regulatory pathway is the ambiguity surrounding device classification, with differences in device types and drug delivery method influencing their regulatory route. As regulatory bodies do not operate within a shared framework, approval pathways are inconsistent across jurisdictions. This heterogeneity is further compounded by the current scarcity of clinical trial evidence for MNs, particularly silicon devices, with very few late-stage studies available. This makes it difficult to demonstrate not only safety and efficacy, but also performance, to regulatory authorities. This lacuna adds difficulty to the navigation of an already complex regulatory system and consequently has resulted in researchers worldwide pursuing divergent strategies in what remains to be an uncertain regulatory landscape.

Additional challenges, as with any medical based technologies, stem from scepticism among patients, clinicians, and the wider public due to unfamiliarity of novel technology, particularly in the context of vaccine delivery, and the absence of long-term safety data. Overcoming these concerns is a considerable task, and requires a multi-prong, strategic approach, combining targeted outreach, education, and demonstration, with transparent communication of long-term safety and clinical efficacy data.

1.4. Research aim and objectives

1.4.1. Aim

The overarching aim of this research was to provide a foundation of evidence to support the progression of silicon MNs down the regulatory pathway. The strategy employed to achieve this was to manufacture and characterise these devices, fostering a deeper and more comprehensive understanding of their mechanical, biological, and functional performance.

1.4.2. Objectives

To achieve this aim, five objectives were defined, which formed the basis of the main research chapters of this thesis. These were as follows:

(i) To perform the batch manufacture of hollow and solid silicon MN devices *via* a small-scale, 100 mm silicon wafer fabrication process.

(ii) To investigate the mechanics of silicon MN insertion and their interaction with skin and tissue barriers.

(iii) To assess the cytotoxicity of silicon MN devices and their constituent materials using biologically relevant cell types.

(iv) To evaluate the repeatability of intradermal style delivery facilitated by hollow silicon MNs.

(v) To initiate the development of a scaled up manufacturing process from 100 mm to 150 mm silicon wafers, thereby aligning more closely with industry processes and infrastructure.

Collectively, these objectives were designed to provide a structured research pathway and project narrative: initiated with device manufacture, advancing through mechanical, biological, and functional assessment, and culminating in the optimisation of processes at a more industrially relevant scale.

1.5. Thesis structure

This thesis aimed to produce a comprehensive and well-rounded body of research, which focused on the development and characterisation of novel MN devices. The motivation behind the research direction was twofold: (i) to deepen the understanding of the function of the devices from a mechanical perspective and (ii) to provide the necessary foundation to support their progression and translation into industrial scale and clinical contexts.

The research was initiated through the initial small-scale manufacture of the devices, using a previously established and reported methodology as a starting point for process optimisation to improve yield and quality (Chapter 3: Small-scale Manufacture). From here, the research progressed towards gaining better understanding of the mechanical interaction between the devices and the surface which they penetrate during insertion. This saw a study performed focused on the quantification of strain during insertion facilitated by the previously produced MN devices and a gold standard comparator (Chapter 4: Insertion Mechanics). This novel phase of work was essential, providing a solid quantifiable basis for the comparison of device mechanical performance.

Building on this physical understanding of device capabilities and performance, the following phase of research turned to the investigation of device compatibility with relevant biological tissue, with specific focus placed on cytotoxicity evaluation (Chapter 5: *In Vitro* Cytotoxicity Assessment). This facilitated the progression of the research beyond the mechanics of insertion, addressing instead the vital regulatory question of biological compatibility and safety. Following the establishment of both mechanical performance and biological compatibility, this thesis progressed to exploring the functional repeatability through investigation of intradermal delivery simulations (Chapter 6: Intradermal Delivery Patterns). This demonstrated that the control and reproducibility of MN delivery patterns were comparable to, and exceeded, those produced *via* a gold standard delivery modality.

The final phase of work required the initiation of scaled-up manufacture, following Chapter 3's demonstration of small-scale batch fabrication. Here, the establishment of feasibility at 150 mm silicon wafer scale was assessed, through the optimisation of the constituent etch steps (Chapter 7: Scaled Up Manufacture). Following this, the narrative arc of this research was brought to a close, spanning the manufacture, testing, characterisation, and translational potential of silicon MN devices, laying solid groundwork for their progression down the regulatory pathway and industrial scale production.

2. Chapter 2: Literature Review

The literature review found here provides a critical review of the existing research MN technologies. It will examine various types of MN-style deliveries, the various materials available and their advantages, in addition to highlighting limitations and shortcomings which must be addressed to enable the field to progress devices towards regulatory approval. This literature analysis has informed the experimental strategies employed in subsequent chapters.

2.1. Introduction to parenteral drug delivery

One of the first forms of injection for medicinal purposes was vaccination. This long-standing medical practice has evolved since its early origins in the 7th century, when Buddhist monks reportedly ingested small volumes of snake venom to raise immunity to future bites (12). The modern hypodermic needle was conceptualised two centuries later, when Alexander Wood combined a hollow needle with a plunger in 1853 to inject morphine (13). Following this early use, the hypodermic needle has become a cornerstone of modern clinical medicine and is used for the delivery of an array of drug formulations far beyond vaccination and pain relief.

The intramuscular (IM) delivery route dominates among the common injection routes on account of both its ease of administration and relatively consistent absorption, however, subcutaneous (SC) injections into the hypodermis may be used in place where more localised effects are required (14). The topical route is one with widely acknowledged limitations which perturb its mass usage in clinical-based settings and restrict its usage to more over-the-counter (OTC) alternatives, owing to the robust barrier properties of the skin rendering onset delayed and limited bioavailability (15-17). Consequently, there is a clear demand for a platform which offers the advantages of topical delivery’s minimally invasive nature, with the bioavailability and absorption offered by IM and SC routes.

Parenteral drug delivery encompasses all delivery modes which bypass the gastrointestinal (GI) tract and is diverse in its subtypes, including IM, SC, intradermal (ID), and intravenous (IV) (18). From a PK perspective, parenteral routes are favoured heavily over oral solid dose (OSD), offering direct access to systemic circulation and target tissues, and circumvention of the hepatic first pass to ensure bioavailability preservation (19). This hepatic first pass avoidance enables precise dosing of therapeutics, which is critical in some cases, including the delivery of large biologics such as deoxyribonucleic acid (DNA)/ribonucleic acid (RNA) vaccines (20).

Despite the clinical and PK-based advantages of parenteral delivery, current approaches remain far from ideal from a patient perspective. The pain and discomfort associated with hypodermic needles is extensive, reinforcing needle-related phobia and anxiety, and often leading to poor patient compliance (13). Additionally, sharps disposal poses significant occupational hazards for healthcare workers, carers, patients who self-administer, and emergency workers, with incidences of needle-related injuries between 2012-2022 reaching 2,600, of which 75 % were successful claims, costing the NHS £10.8 million (21). Furthermore, operator technique may lead to inconsistencies in insertion depths and angles, which introduces significant variability and may further increase the likelihood of such device-based injuries (22). Taken collectively, these concerns emphasise the challenges of successfully achieving high patient compliance with clinical injections as well as safe, reproducible self-administration using conventional parenteral methodologies.

Given this context, the advancement of research into a more reliable and less invasive modality for achieving ID delivery is of significant interest among not just the medicine and research community, but also the general public. MNs represent such an innovation, with the potential to revolutionise parenteral delivery by minimising the pain and anxiety surrounding injections and resultantly improving patient compliance with dosing regimens. In addition to their user-experience benefits, emerging research is reporting MN-based delivery to enable dose-sparing, with efficacies measured to be up to 10-fold greater than that elicited *via* hypodermic-mediated delivery for trials in healthy adults for Japanese Encephalitis (23). This dose sparing potential is seen in greater effect in murine models, whereby a dissolving MN patch array yielded a 1,300-fold elevation in serum IgG tiers compared to the traditional injection (24). This efficacy augmentation is attributed to the more specific targeting of resident immune cells within dermis, amplifying immune-based responses.

This literature review therefore aimed to identify current gaps within the field and establish the scientific rationale justifying the research. To do this, it will firstly examine the skin as a physiological barrier to be overcome and an immune organ to be harnessed, before moving on to explore the shortfalls of other delivery modes. Lastly, recent developments within the sphere of MN technology will be discussed to aid in the identification of the limitations of current understanding and to support the conceptualisation of this work's scope.

2.1.1. The skin

The skin is the largest organ in the human body, providing not only the primary line of defence *via* a physical barrier, but also the secondary line of defence through its plethora of resident immune cells (25-27). In addition to its protective functions, the skin also provides sensory and homeostatic functions, enabling a more holistic interaction between the body's internal environment and the external environment. Nevertheless, in addition to its critical protective role, the skin also provides a barrier that prevents efficacious transdermal drug delivery. Hence, while protective, the skin is acknowledged to impede the delivery of drugs, posing a barrier to administration which must be overcome *via* the delivery platform (17). Furthermore, the skin architecture is now better understood, opening up the possibility of harnessing the cellular infrastructure to enhance therapeutic efficacy, particularly of immunotherapies (28-31). The skin's structure and architecture will be covered firstly, before detailing how this infrastructure supports both the barrier and immunological functions of the skin as an organ.

Structure and architecture

The skin is an extremely complex and intricate organ, with cellular architecture tailored to support both its barrier and immunological functions (Figure 1). This subsection outlines its composition, laying the foundations for subsequent discussion on how the skin serves as both a passive (barrier) and active (immunological) defence to the external environment. It must firstly be acknowledged that skin architecture varies across anatomical sites and is influenced compositionally by factors such as age, gender, and ethnicity, although this is currently not well characterised (32-36). This subsection focuses on the generalised composition of the skin and will make comment whereby there are significant differences relative to these variables. The following subsection is organised into a logical sequence through the epidermis, dermis, and hypodermis.

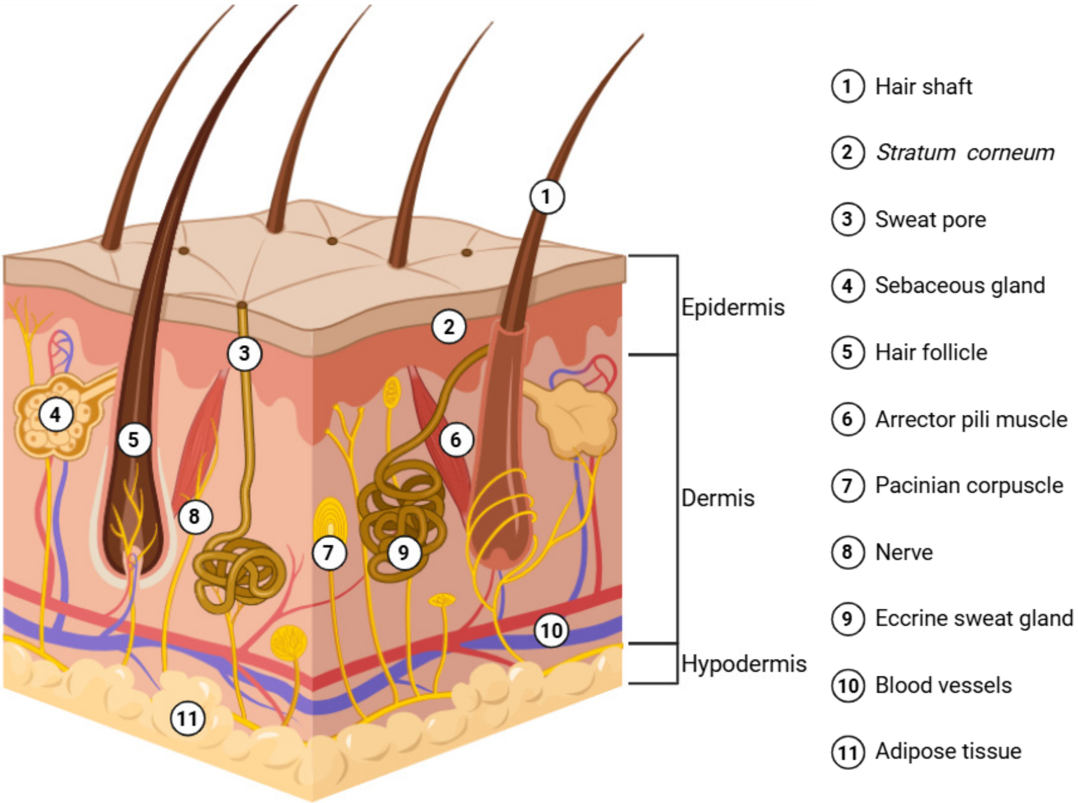

Figure 1. A cross-sectional diagram of the skin's layers, the epidermis, dermis, and hypodermis with skin architecture labelled

Epidermis

The epidermis is the outermost layer of the skin and is composed of stratified squamous epithelium (37). All parenteral routes must first penetrate the epidermis, bypassing this barrier to reach deeper tissue layers. It is this barrier, specifically the outermost layer (*stratum corneum*) which limits the efficacy and bioavailability of topical and transdermal drug delivery (38, 39). With a thickness and composition that vary based on site, the epidermis ranges from 0.05 mm (eyelid) to 1.5 mm (palms) in thickness, with this variation enabling better adaptation to its role as the primary physical barrier (40).

The epidermis consists of several *strata*, each with differing cellular architecture. The outermost layer, the *stratum corneum*, is composed of layers of flattened, dead cells, filled with keratin, providing a robust interface between the subsequent layers and the external environment (41). In thick skin such as fingertips and the palms, the *stratum* *corneum* is reinforced against friction and abrasion by the *stratum lucidum*, a secondary layer of dead, keratin-filled cells (42). The following layer, the *stratum granulosum*, marks the transition from dead, keratinised cells to living cells. Comprised of predominantly flattened keratinocytes and lamellar granules, these bodies are critical for establishing the waterproof barrier of the skin through their release of lipids such as ceramides into the intercellular space to maintain barrier integrity (43).

Deeper still is the *stratum spinosum*. Composed of several layers of keratinocytes which decrease in maturity as they descend, these cells have tightly bound junctions and produce keratin to provide support for the skin's integrity (44). In addition to keratinocytes, Langerhans cells are present and comprise 5 % of the nucleated cells in the whole epidermis, acting to support the innate immune response (45). The deepest layer of the epidermis is the *stratum basale*. Resting directly on the basement membrane separating the epidermis from the dermis, the *stratum basale* is composed of a single layer of column-like keratinocytes which are solely responsible for providing regenerated cells for the upper epidermal layers (46). Interspersed amongst the basal keratinocytes are melanocytes and Merkel cells which act to produce melanin and provide mechanosensory input respectively (47, 48).

Dermis

Located immediately beneath the epidermis is the dermis, a connective tissue rich in collagen and elastin, providing structural integrity and mechanical support. This layer is critical for nutrient exchange *via* blood vessels and lymphatics, immune defence through resident immune cells including dendritic cells, macrophages, and mast cells, and sensory perception *via* embedded nerve endings (48). It also houses key adnexal structures such as sebaceous and sweat glands, as well as hair follicles (49). The dermal layer is anatomically divided into two structurally and functionally distinct layers: the papillary dermis and the reticular dermis (49).

The uppermost region, the papillary dermis, is comprised of a loosely arranged network of collagen and elastin fibres. This layer is rich in features such as capillaries, lymphatics, and sensory nerve endings, in addition to cells critical to immune surveillance, such as mast cells and dendritic cells (49). Together, these features enable the papillary dermis to support epidermal nutrition, transmit sensory input, and mediate immune surveillance. The layer and its interface with the reticular dermis is typically the target of MN-based drug delivery, leveraging its lymphatic network and sparse neural innervation, as opposed to the hypodermis which is accessed typically by deeper parenteral injection routes (49).

Progressing to the deeper dermal layer, the reticular dermis exhibits a denser, more irregular structure, with thicker collagen bundles, unlike the looser structure of the papillary dermis (49). It houses larger blood vessels and glands, and providing enhanced mechanical strength, elasticity, and support. Importantly, this deeper dermal layer holds specialised sensory receptors, such as Pacinian corpuscles and Ruffini endings, that detect deep pressure and sustained stretch, respectively (49). While together the papillary and reticular dermis support structural integrity and immune surveillance, the underlying hypodermis, more commonly targeted by parenteral delivery routes, contributes primarily to insulation, energy storage, and more complex, deeper vasculature (50).

Hypodermis

The hypodermis, also referred to in clinical settings as the SC layer, is the lowest layer of the skin and is primarily composed of adipose tissue interspersed with connecting fibres. This layer provides a soft matrix for the vascular and lymphatic networks to embed into (51). As an adipose-based soft matrix, it provides thermal insulation and serves as a reservoir for metabolic energy, whilst functioning as an anchor for the dermis to muscle and bone (52). Although not considered a primary immunological site for skin-based defence, the hypodermis contains macrophages which contribute to local immune responses (53). Whilst acknowledged to be structurally simpler than the more superficial epidermal and dermal regions, the hypodermis plays a greater role in metabolic regulation and mechanical protection.

Functions

The skin's diverse and purposive structure enables it to function as a multifaceted organ, providing a dynamic interface between the internal and external environments. Although certain physiological roles are confined to distinct regions of the skin, many functions rely on the co-ordinated interplay between the epidermis, dermis, and hypodermis. These functions span protection, regulation, sensation, and cellular communication, among others.

The following subsections focuses on the protective capacity of the skin, which is expressed in two principal lines of defence: primary protection *via* its barrier properties, and secondary protection *via* immunological infrastructure. These functions are especially relevant for drug delivery strategies, as they present key factors for both the impedance and enhancement of parenteral administration.

Barrier functions

As discussed in previously, the skins main barrier is provided by the outermost layer of the epidermis: the *stratum corneum*. This brick-like arrangement of terminally differentiated keratinocytes provides the first line of defence, physically preventing penetration and infection from outside the body. Further support is found in the lipid matrix composition of the *stratum corneum*, which plays a critical role in this protection by preventing (i) excessive transdermal water loss and (ii) the penetration of unwanted pathogens (54).

This brick-and-mortar-like system provides toxin exclusion and selective chemical absorption, and therefore, requires some form of penetration to efficiently deliver medication through, traditionally performed by a hypodermic needle (55). Despite only requiring penetration through the *stratum corneum* (0.01 - 0.03 mm) for certain medications such as vaccinations, hypodermic needles can range from 16 mm for SC injections to 38 mm for IM injections; an unnecessarily invasive length, often resulting in pain and bleeding (Figure 2) (55, 56).

This challenge has prompted the development of devices that can accurately target the dermal space, limit the invasion of the procedure and consequently prevent pain and improving patient compliance. MN devices are designed to breach this epidermal barrier, bypassing the *strata* and enabling delivery directly into the dermis.

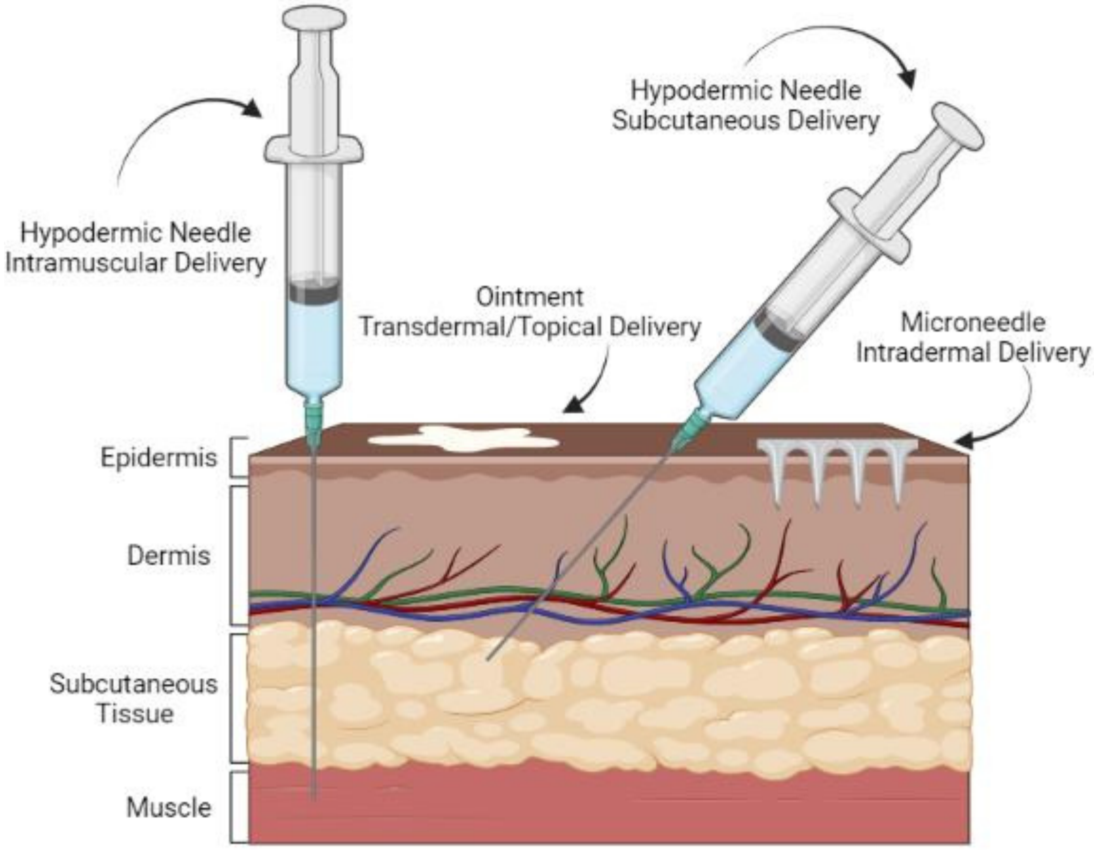

Figure 2. Common parenteral drug delivery routes and their relative penetration depths (57)

Immunological functions

The skin is not merely a physical barrier to the environment; it is an active immune organ which contributes to both innate (immediate, non-specific response) and adaptive immunity (slower, targeted response) (25, 58, 59). An armamentarium of immune-competent cells and signalling proteins, the dermal space is a sink of immune potential (Figure 3). Epidermal keratinocytes, in concert with dendritic cells such as Langerhans cells (the resident antigen presenting cells (APCs) of the epidermis) aid in raising a local immune response to neutralise the threat (25, 45). In addition to the keratinocytes and Langerhans cells, the dermis contains a wide variety of immunocompetent cells, including macrophages and T lymphocytes, each contributing to the immunological surveillance and response (60). Furthermore, signalling proteins, termed cytokines, in connection with local lymph nodes, play a key role in flagging the invasion of unwanted pathogens into the skin to the immune system, mobilising a systemic immune response, and directing it to the cutaneous injury site (61). By targeting and delivering into the dermis, MNs are uniquely and well positioned to engage directly with these local immune cell populations, offering a minimally invasive route that avoids commonly experienced systemic side effects (62).

Studies have demonstrated the increased efficacy of drugs such as vaccinations through merely altering the depth of penetration, which could maximise dosage and elicit dose/antigen sparing effects (23, 63, 64). Dose sparing refers to the ability to achieve comparable or enhanced immunogenicity with reduced dosing antigens, a feature greatly prized in the drug development sector, offering cost savings and faster, more widespread, medication rollout (65, 66). Dose sparing through dermal targeting is suggested to be due to the increased number and variety of immune cells within the dermis and expediting their interactions and resultantly immunogenicity raised against the vaccine antigens (67). Leveraging the dermis for immune stimulation has proved effective in vaccination, and this principle is beginning to be applied to cancer immunotherapies, where precise delivery may enhance tumour-specific targeting (68).

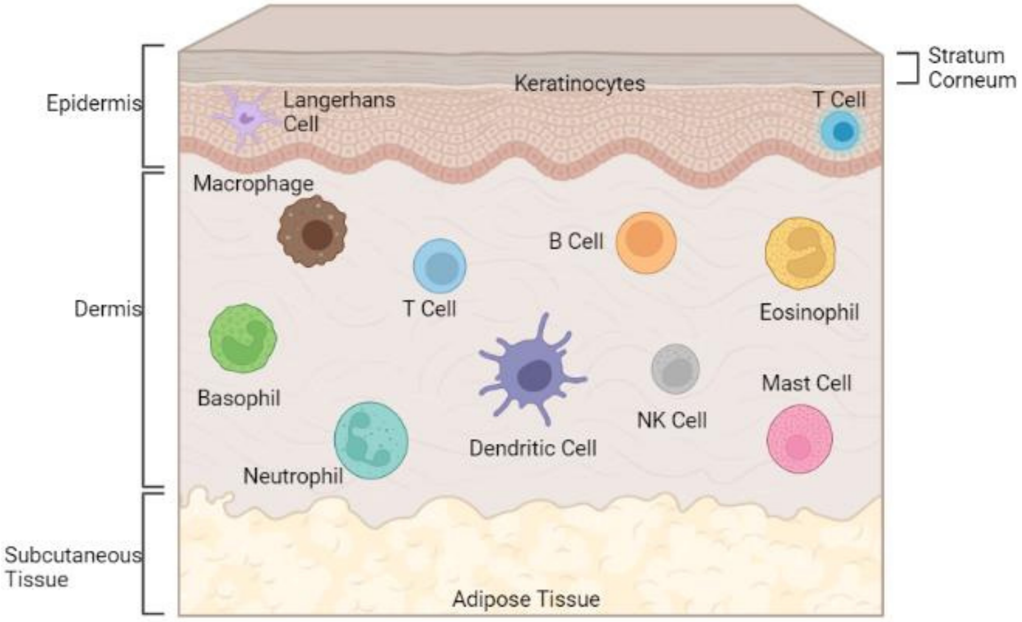

Figure 3. The layers of the skin with their resident immune cells (57)

To support the multidisciplinary use of the MN platform for drug delivery, dose sparing potential and increased efficacy is being demonstrated in a variety of disease states. Breast and abdominal cancer studies have identified tumourigenic cells to evade immune detection partly by metastasising to, and residing in, the layers of the skin, such as adipose tissue (69-71). With a key role in the development and growth of breast and ovarian cancers, adipose cells-cancerous cell co-cultures have demonstrated promotion of tumour growth in *in vitro* and *in vivo* environments (72, 73). Specifically, due to the direct transfer of lipids to aid cancer cell metabolism, it is widely acknowledged that this fatty acid transfer provided by adipocytes promotes cancer progression through a plethora of mechanisms (74, 75).

With an increasing number of immunotherapies available and in development, local activation of the epidermal and dermal immunocompetent cells with this classification of anti-cancer drugs offers a promising modality to utilise the skin immune cell architecture to target "hidden" tumorigenic cells (76, 77). This demonstrates the elevated efficacy of an immunotherapy, whether for cancer or vaccination, when directly targeting the skin. Research is now progressing towards fabricating a reliable and safe device to accurately deliver these medications.

2.1.2. Drug delivery routes

Drug delivery route selection is key in capitalising on therapeutic efficacy, ensuring optimal duration of onset, and enhancing patient compliance. Each layer of tissue in the skin architecture offers different physiological environments which influence these factors. The following subsections will introduce four key delivery routes in order of anatomical descent: transdermal, ID, SC, and IM.

Transdermal application

Transdermal drug delivery involves the passage of therapeutic formulations across the skin barrier and into the underlying systemic circulation *via* passive diffusion. It typically offers OTC formulations that are applied in a non-invasive manner, facilitating sustained release and ultimately improved patient compliance. Despite these benefits, the use of transdermal application is restricted by the physio-chemical properties of the active pharmaceutical ingredients (API) and any critical excipients (78, 79). Typically, transdermal therapeutics are designed to be a topical in administration, in gel or cream-like form, and are semi-solid formulations aided by chemical enhancers or excipients to support and promote API permeability through the skin barrier and into the systemic circulation (80). In some cases, sustained release is sought after, and the dosage is integrated into an adhesive patch style delivery platform, which enables improved control over dosage. The following subsections introduce both gel-like and patch transdermal application styles.

Gels and creams

Semi-solid formulations, such as gels and creams, are applied directly to the skins surface and rely on drug absorption *via* passive diffusion (81). Even when formulated with chemicals that support and enhance permeation, these formulations are only suitable for lipophilic drugs with low molecular weights (< 500 Da) (82). With advantages including flexible dosing, self-administration, and rapid onset, this route is favoured by patients and is commonly used for pain relief and hormone therapies (83, 84). However, topical application is not feasible in most cases, as drug permeation is not limited by molecular size and solubility alone, but additionally by variations in skin conditions thickness, and hydration levels (82, 85, 86).

Patches

Transdermal patches are adhesive-based platforms that are applied to the skin's surface, that contain a drug-containing reservoir or matrix that facilitates and sustained release. This passive diffusion can deliver consistent dosing over extended periods of time, from hours to days (87). Commonly used for dosing nicotine and fentanyl, patches do not provide any improvement on the scope of drugs which can be delivered transdermally (87). The limitations in molecular size and skin permeability and condition still apply, with additional variables such as skin irritation, allergic reaction, and adhesive failure remaining challenges to be overcome (87).

Intradermal administration

ID delivery refers to the administration of therapeutics into the outer layers of the skin, specifically targeting the dermis (Figure 3). Residing within the dermis is a rich population of immune cells, which, upon direct targeting, become activated, initiating a cascade of immune stimulation (28). Additionally, due to a reduction of blood vessel networks in the dermis in comparison to the SC layer, the therapeutic resides within this dermal layer for a more prolonged period, enabling a greater degree of immune cell activation than SC and IM injections (88).

This enhanced immune engagement allows for lower doses to result in greater immunogenicity. This is a significant advantage, with smaller doses reducing cold chain storage and transportation costs; all crucial when considering mass roll out of schemes such as the COVID-19 vaccination campaign. Furthermore, ID delivery enables direct targeting of skin-based conditions such as psoriasis and vitiligo, resulting in improved efficacy and bioavailability, and in some cases, reduced side effects due to limited systemic circulation (89-91). Research interest in ID delivery is increasing, with multiple devices being developed for this administration mode. The following subsection will introduce multiple deliver platforms which support ID delivery, discussing their relevant advantages and limitations.

Mechanical-based devices

The field of needleless injection systems is progressing, effectively developing both liquid jet and ballistic powder injectors. The principle of the devices requires a liquid to be passed through a micro-aperture, generating a high-speed, thin jet stream that penetrates the surface of the skin (92, 93). Although not a novel concept, with jet injections used in smallpox and tetanus vaccinations in 1966 and 1999 respectively, it has required development since its fall from favour (94). Initial concerns surrounding splash-back, infection risk, and retrograde flow required addressing (95). With jet injectors approved for the delivery of the Afluria Quadrivalent flu vaccine, these issues have been addressed, making the device single use (96). The single use nature of this device is unideal from a sustainability perspective, with concerns over consistency in dosage often arising. Reports from patients indicate that application of these devices is associated with irritation and discomfort (97). Furthermore, the manufacture of these devices, in combination with the gases required to generate the high power jet, highlights the need for further developments in the field that require minimal apparatus and training for administration (93). As a result, attention has shifted towards MN-based systems, which offer more precise dosing and a better patient-experience of ID delivery.

Microneedles

MNs themselves are not a novel technology. First conceptualised by Gestel and Place in 1976, their initial device comprised of multiple 100 μm needle-like projections was used for the penetration of the stratum corneum for the purpose of drug delivery (98).

The mid-1990s saw the first production of MNs *via* microfabrication, as first reported by Henry *et al*., in 1998, where calcein was delivered through MN-penetrated stratum corneum (1). Various geometries, dimensions, and materials are now used to fabricate both in and out of plane MNs, with out of plane becoming increasingly favoured. MN type and material depend upon their application and are widely researched in three different fields: cosmetics; therapeutics; and diagnostics. MNs offer the ability to capitalise on the plethora of immune cells and interstitial fluid (IF) present following epidermal penetration, but avoids cellular structures such as nociceptors, nerve and capillary networks. In addition to their minimally invasive nature, MNs boast benefits such as minimal irritation and dose sparing, as well as improved skin recovery and reduced infection risk (99). Despite both patient-centred and PK advantages, there are widely acknowledged hurdles to the widespread adoption of MN technologies. As discussed later in section 2.4, the challenges facing their implementation vary depending on their material, with dosing accuracy, loading capacity, and needle strength commonly assessed.

Energy-assisted devices

While the primary focus of this thesis is on needle-based drug delivery platforms, energy-assisted devices will be discussed here for more comprehensive contextualisation, while acknowledging their peripheral relevance. Energy-assisted devices for parenteral drug delivery include, but is not limited to, electroporation, sonophoresis, and laser ablation. These methodologies function through the creation of transient pores and microchannels in the skin's lipid barrier to enable therapeutic agents to be delivered effectively (100). Each of these approaches utilises a different energy source to achieve this disruption, with electroporation, sonophoresis, and laser ablation using electrical pulses, ultrasound, and light/thermal energy respectively (101-103).

These energy-assisted devices are primarily used for the administration of larger drug molecules exceeding a molecular weight of 500 Da (100). Unfortunately, due to the complexity of the equipment, specialist training is required, and there remains a significant risk of variable skin responses, including irritation and damage (101). This has resulted in slow progress though the regulatory approval pathway and therefore has impeded its adoption into the clinic, with lower-risk device platforms such as MNs being increasingly preferred.

Subcutaneous administration

The modality which delivers directly into the hypodermis is clinically referred to as the SC administration route. This involves the injection of loading doses into the fatty hypodermis, which lies beneath the dermis. Injecting directly into this area results in slower drug absorption and, due to the limited presence of resident immune cells, a more dampened immune response due to a delayed absorption (104). This route is widely used for the delivery of therapeutics such as insulin and heparin, and is often preferred for ease of use by healthcare workers and compatibility with infusion pumps and patch injectors (105). However, more extensive training is required for the utilisation of this administration, and the variable absorption being vulnerable to factors such as fat distribution and thickness, local blood flow, and injection site temperature, make consistent PKs more difficult to achieve (106, 107).

Intramuscular administration

IM delivery is perhaps the most utilised delivery mode, using a 1-1.5” hypodermic needle to administer medication into muscular tissue at a 90° angle to the injection site, typically at the deltoid, vastus lateralis, or dorsogluteal muscles (108). This classic delivery technique is superior to other delivery modes such as the OSD route, enabling the bypass of harsh chemical and physical barriers posed by the GI system, namely the 1-2 pH stomach acid (109). This allows better bioavailability and more rapid absorption into the bloodstream *via* IM. IM delivery offers a moderate onset time, with responses typically expected up to 30 mins post-administration depending on the formulation type, which can range from aqueous solutions to sustained release suspensions (108).

Penetrating through each layer of skin, layers of adipose tissue, and into the muscle renders it near impossible to avoid contact with nerve nets and blood vessels, making immediate or medium-term muscular pain, and slight bleeding at the injection site inevitable (110). Due to the associated pain, this often leads to patient anxiety and resultantly poor patient compliance. This is supported by a recent Oxford University large-scale study, which showed that a quarter of the adult population of the United Kingdom suffer from potential injection phobia, and that tackling this would reduce COVID-19 vaccine hesitancy by 10 % (111). Taking this learning and applying it to the other common medications delivered by the IM route, including other vaccinations and antibiotics, the replacement of the IM dosing methodology with one more favoured by patients could lead to a dramatic improvement in public health, reducing the ever-increasing burden on healthcare services.

Nevertheless, further to poor patient experience, IM delivery also fails to capitalise on the wealth of immune potential housed in the bypassed layers of the skin, specifically within the dermis. The skin is being revealed as a sink of immune cells, allowing notable enhancement of the dosage-response ratio of multiple drugs, such as vaccines (112). Simply put, despite retaining markedly more bioavailability than the OSD alternative, IM injections have been demonstrated to require a greater quantity of drug to elicit the same response as ID delivery modes such as MNs (113). Therefore, despite their ability to deliver higher dosage volumes, this is not ideal in most cases. This is not due to excessive clearance, as is it with OSD, but instead due to poor targeting and failure to capitalise on the body's innate defence mechanisms. As such, despite its widespread use, the IM delivery route presents several intrinsic limitations, which have promoted the investigation of alternative platforms such as MN devices.

2.2. Microneedle technologies

As an alternative to conventional parenteral drug delivery routes, MN technologies offer a novel route for ID drug administration. The wide variety of geometries, materials, and mechanisms of action allows for tailored delivery based on clinical and therapeutic requirements. This structural diversity offered enables a range of release profiles also, with both rapid diffusion and sustained infusion capabilities. This section outlines key classifications, solid and hollow, and their constituent mechanisms of action, outlining their key design features, therapeutic delivery, materials, advantages, and current limitations.

2.2.1. Solid microneedles

Solid microneedles (SMNs) were among the earliest MN platforms to be conceived, and as a result, represent the most saturated area of research within the field. The first reports of their fabrication were published by Hashmi *et al.*, in 1995, originally conceptualised for gene transfixion (114). A subsequent study published by Henry *et al.,* (1998) is now credited with pioneering the application of SMNs for transdermal drug delivery (1). The most frequently used materials for SMN fabrication include metal, silicon, and non-degradable polymers, with the latter favoured from a financial and manufacturing perspective, and the former two offering advantages including lower injection pressures and reduced administration-associated pain (115, 116) Although easier to manufacture *en masse*, the translational aspect of SMNs is relatively close to its ancestor, the traditional “poke and patch” approach, with developments mainly emerging through coating technologies and the “coat and poke” approach. With obvious disadvantages in comparison with the poke and patch approach related to scalability, reliability, and consistency of dosing, SMNs research is currently focusing on coating formulations that facilitate ease of use.

Geometry and classifications

This subsection introduces different categories of SMN based on their drug administration and release mechanisms. These mechanisms plays a central role in not only the pharmacological performance of the API but also in the experience of the patient and the clinical feasibility of the platform. Here, three classifications are presented: (i) poke and patch, (ii) coat and poke, and (iii) poke and release. Despite all being forms of SMNs, these differ significantly in materials selection, fabrication methodologies, application technique, and drug release mechanisms.

Poke and patch

SMNs are closely associated with the “poke and patch” approach, whereby projection devices are used to mechanically pre-treat the skin creating micropores, that are exposed topically to an external drug reservoir (Figure 4) (117). This method relies heavily on the integrity and size of the micropores, as well as the ability of the skin infrastructure, such as capillary networks and IF, to enable the passive diffusion of the topical formulation. Although benefiting from its simplicity, the dosage delivered is notoriously difficult to control or measure (118). Despite reports that the barrier properties of the targeted area recover within 2 hours, this may restrict the time available for drug diffusion into the skin compartment, with patch/tape formulations occasionally applied to extend this period (117, 119). In these cases, it is crucial to consider the potential increase in infection risk associated with prolonging the open state of the micropores (120).

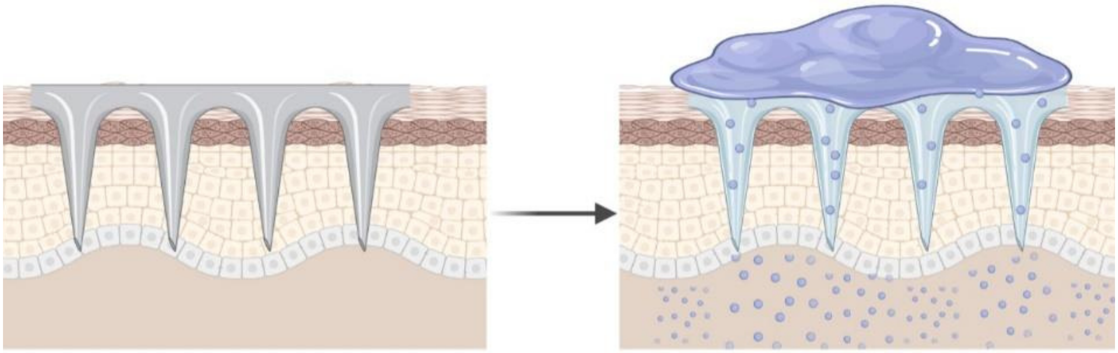

Figure 4. Schematic of poke and patch style solid microneedle insertion

Coat and poke

The coat and poke approach represents an evolution of the poke and patch technique, whereby the surface of the SMNs is coated with a drug-loaded formulation (Figure 5). Superior to poke and patch, this approach guarantees drug diffusion to a deeper degree, allowing delivery of higher molecular weight molecules and enabling rapid delivery (121, 122). SMN coating techniques can be roughly categorised into two subsets; those which coat the MN shaft only, and those which coat the MN shaft and the array base substrate. The ideal coating would produce a selectively uniform coating of the MN shaft, without contaminating the array base. Dip coating and inkjet printing fall into the former category (123). Dip coating is the simplest method, whereby the device is dipped into a solvent-based coating formulation, which upon evaporation leaves a drug-containing thin liquid film on the MN surface (123). The degree of shaft coverage can be controlled by the depth of the coating well, however, increasingly, masking plates are utilised to protect the base of the array during dip coating, producing selectively coated SMN shafts (123).

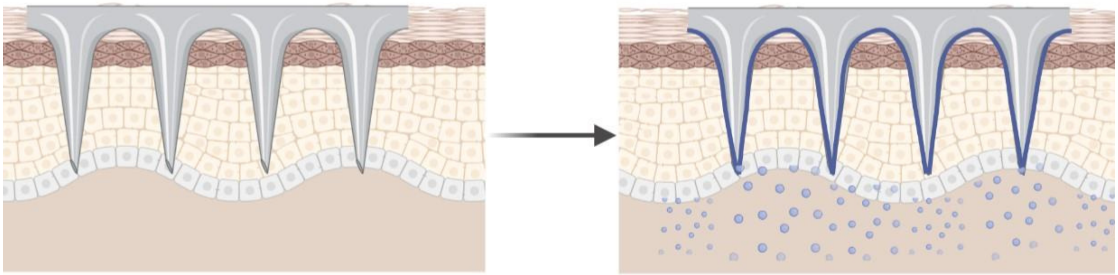

Figure 5. Schematic of coat and poke style solid microneedle insertion

The less selective techniques, such as immersion and drop coating, offer little to no control over the area coated. During immersion coating, the entire device, inclusive of the backside of the array is coated, while drop coating enables the protection of the base (124). Not only are these techniques non-selective, but they also contribute to coating wastage, with delivery efficiency to the skin reported in the broad range of 60-90 % (125-127). This is financially unattractive, as, in some cases, the expensive antigen/drug formulations, are either wasted during the coating process, or lost during application, since the base coating cannot diffuse into the micropores and is disposed of with the used device.

Although coat and poke is rapidly becoming one of the most popular MN approaches, benefiting from scalable processing and simple administration, is has its own subset of disadvantages. For example, the available surface area of SMNs greatly limits the amount of coating, and therefore the quantity of drug delivered *via* this method (128). Furthermore, there are limits to coating thickness, as increased thickness significantly impacts the sharpness of the device, and therefore their penetration efficiency and pain experienced by the patient (118).

Poke and release

Dissolving MNs (DMNs) have been conceptualised in response to the demand for a reduction in medical device and sharps waste and enable large scale manufacture. Termed “poke and release”, the devices are fabricated from a variety of biodegradable and water-soluble scaffold materials, which encapsulate the drug within the device, allowing an attractive one-step delivery process (Figure 6). This can result in some constraints, as it requires compatibility of the drug properties and device chemical composition (129). Boasting precise dosage, DMNs are currently fabricated using scalable technologies such as micro-moulding, droplet-born air drying, and drawing lithography methodologies (129, 130).

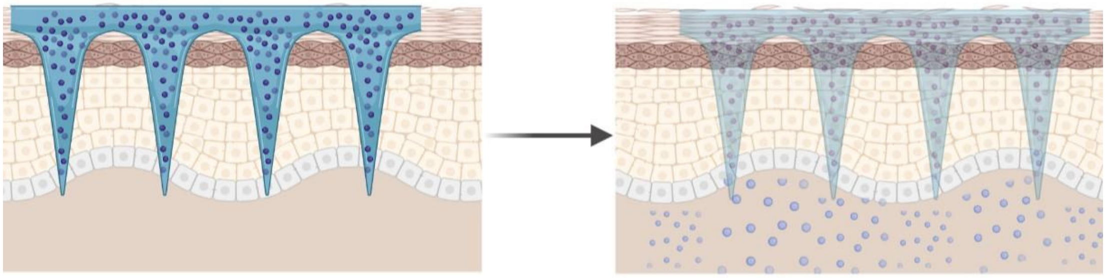

Figure 6. Schematic of poke and release style dissolving microneedle insertion

A slight modification has been made to the original design, producing a porous version, whereby a large volume of drug-loaded pores litter the surface of the MNs, allowing absorption of the drug solution by the skin IF following penetration. The pores, however, compromise the mechanical integrity of the MN shaft when exceeding a cargo:device ratio of 1:1, leading to increased fragility, and therefore negatively impacting their clinical adoption to date (129).

The delivery kinetics of DMNs are unique to the device’s matrix composition and the drug formulation being delivered. This provides a significant advantage, enabling the addition of excipients to influence delivery kinetics, such as the inclusion of amylopectin, which has been reported to not only improve the mechanical properties of the DMN structure, but also permit tuning of the dissolution properties, facilitating controlled release (131). Water soluble patches are seemingly favoured due to their superior dissolution and resultant delivery efficiency (132).

On account of their material and fabrication processes, the DMN tip diameter and angle are often suboptimal, requiring an applicator to generate sufficient force to achieve a complete penetration, often due to variability in skin elasticity and hair density (115, 133, 134). Without this, penetration may be incomplete, leading to insufficient dosing. Importantly, although the patch boasts no sharps waste potential, the applicator must be disposed of.

Following insertion, the devices dissolve into the IF, with the needle length and insertion depth limiting the dosage; a widely acknowledged disadvantage of DMNs. Only a fraction of the matrix can be API to ensure sufficient structural integrity for injection, with a bolus from a DMN patch suggested to provide less than 1 mg of drug (135). Furthermore, for full dosage to be achieved, the patch cannot be detached and removed until complete dissolution occurs, leaving a large margin for human error in premature removal.

Although ideal for the delivery of standardised dosages, such as vaccinations, DMNs are less suitable for applications which require patient-tailored dosing based on height and weight-adjusted regimes, as these must be considered during manufacture. Despite these limitations, the concept of DMNs, to produce minimally invasive devices to deliver a standardised dose with no waste, remains promising, with further advancement in its drug loading and delivery still required.

Materials and fabrication approaches

Microneedle fabrication is fundamentally dependent upon the material composing the device, with material selection having direct influence on their mechanical strength, biocompatibility, and drug delivery efficiencies. Whilst the field of SMNs continuous to diversity, this subsection focuses on providing an overview of the most commonly fabrication techniques for the most commonly studied materials: silicon, metal, and polymer.

Various fabrication and production approaches have been developed, with material selection frequently influenced by priorities such as unit cost, ease of administration, and sustainability. Rarely does one device simultaneously satisfy all criteria. Table 1 summarises each SMN sub-classification, material, and fabrication methodology, which will be developed upon in the following subsections.

Table 1. A summary of microneedle types, material, and common fabrication techniques

SMN Classification	*Material*	*Fabrication Technique*	*Ref*
Solid	Silicon	Deep reactive ion etching	(136, 137)
		Wet etching	(136, 138, 139)
	Polymer	Mould casting using centrifugation or vacuum	(140)
		Stereolithography	(141, 142)
		Thermal compression moulding	(143)
		Photolithography	(144, 145)
	Ceramic	Soft-lithography and ceramic micro-moulding	(146)
	Metal	Micromachining	(121)
		Metal electroplating	(147)
		Laser cutting	(148)
	Glass	Thermoplastic drawing	(149)
Dissolving	Polymer	Mould casting using centrifugation or vacuum	(150, 151)
		Stereolithography	(142)
		Photolithography	(152, 153)

Solid microneedles

Silicon-based SMNs are being produced by relatively established fabrication methodologies, such as isotropic dry, and anisotropic wet etching techniques, with the industry looking to progress toward all-dry processing methodologies to lower fabrication cost and reduce processing complications. Deep reactive ion etching (DRIE) methodologies also facilitate a deeper etch, enabling a taller final needle structure, which allows for deeper penetration and a greater surface area for coatings, thereby improving delivered dosage. This method holds great advantage, offering a reduced processing cost by eliminating wet-etch techniques, whilst providing superior final device geometries. Despite the benefits of advanced peak angles that facilitate insertion with minimal application pressure and minimal pain for the patient, initial material costs and the brittle crystal structure of silicon have been questioned by researchers within this field (154).

The fabrication of metal SMNs uses an array of well-established techniques, such as metal electroplating, wet etching, laser cutting, and 3D laser ablation. While metal electroplating and laser cutting are among the leading industrial techniques currently adopted, their respective drawbacks, lengthy processing times and limited throughput, hinder scalability for mass production (155). Despite this, these processes are successful and widely used at the research level, with techniques such as 3D laser ablation offering benefits such as non-cleanroom manufacture. Furthermore, material sourcing, most commonly titanium and stainless steel, as well as nickel and palladium-cobalt alloys is guided by their beneficial mechanical properties (38).

Polymeric SMNs are very popular within MN research groups currently, offering fast and scalable manufacturing processes. Injection moulding is fast becoming the favoured technique for polymeric SMNs, facilitating high-throughput production by injecting heated polymers/thermoplastics such as polycarbonate and poly-methyl methacrylate (PMMA) into master moulds (156). However, limitations in mechanical strength and tip sharpness are often reported, with polymer devices often leading to tip deformation during insertion, preventing skin rupture (157). Regardless of these challenges, polymeric SMNs research is expanding rapidly and continue to garner serious interest, due to its transferable, scalable fabrication infrastructure, and cost-effectiveness.

Dissolving microneedles

The fabrication of DMNs is continually evolving, with numerous matrix compositions being trialled alongside varying processing methodologies, as summarised in Table 2. Microcasting, also referred to as micro-moulding, and spray moulding are generally acknowledged to be the most feasible DMN fabrication methodologies for low-cost scalable production (158). The former requires a suspension containing a biocompatible matrix and drug formulation to be loaded *via* vacuum or centrifugation into an appropriate MN mould, before being allowed to dry and demoulded (159). Advancements have been made to improve the scalability of DMNs, mitigating the requirement for centrifugation or vacuum, by utilising atomised spray to fill the moulds (160). Furthermore, drying techniques such as symmetrical air-blowing methodologies are now being utilised to expedite the drying phase (161).

Although manufactured through scalable processes, there are shortcomings associated with DMNs and their fabrication. Due to the constraints of the moulding techniques, the tip angle achievable is often limited, resulting in MNs that are blunter than their metal or silicon alternatives (135). Furthermore, with needle size ideally kept minimal to capitalise on the minimally invasive, pain free nature of MNs, this restricts the dosage capabilities of the devices. It is increasingly being suggested that, to ensure accurate and maximal delivery efficiency, the dosage should be concentrated at the tip. This, however, further constrains the dosage capabilities (162). Furthermore, recent reports have revealed as little as 10% of drug released from DMNs, citing the null or void volume of the array base as the cause (163). In some instances, such as vaccination, this is not problematic, as immune responses can be triggered by nanogram-scale doses (163).

In addition, the heating process used during solidification or encapsulation during manufacture must be carefully controlled and tailored to the drug formulation. This is critical, as excessive heat during fabrication may alter the integrity of sensitive chemical components, particularly proteins, present within the formulation (164).

Table 2. A summary of common matrix materials and their general advantageous properties

Common Matrix Material	*Properties*	*Ref*
Polylactic-co-glycolic acid	Slow degrading, biodegradable	(165)
Sodium hyaluronate	Naturally present in skin	(166)
Sodium caroxymethylcellulose	Good water solubility at any temperature, physiologically inert	(167)
Poly(vinylalcohol)	Good water solubility and biocompatibility	(126, 168)
Poly(vinylpyrrolidone)	Self-assembly into hollow fibres, enables delivery of intact proteins to the skin, low manufacturing cost and good biocompatibility	(169)
Sodium chondroitin sulphate	Dissolvable	(170)
Carboxymethyl cellulose	Biocompatible, easy processing at low temperatures, low cost	(131)
Dextran	Good biological safety profile, widely used in biomedicine, easily modified	(171, 172)
Hydroxypropyl methylcellulose	Good mechanical strength	(173)
Hyaluronic acid	Rapid dissolution within 60 mins of application	(174, 175)
Sodium alginate	Low cost, biocompatible, non-toxic	(176)
Polylactic acid	Biodegradable, low cost	(177)
Chitosan	Biodegradable, non-toxic	(178)
Methylcrylated hyaluronic acid (MeHA)	Bioresponsive, increased rigidity	(179)

2.2.2. Hollow Microneedles

Hollow microneedles (HMNs) represent a distinct class of MN platforms, characterised by a central lumen through which liquid drug formulations are actively delivered through once the device is inserted into the dermal compartment. To address the limitations of dosage volume and coating reliability of SMNS, HMNs were conceptualised in the early 2000s. HMNs enable active fluid delivery through injection, as opposed to the passive diffusion of drug formulation required by SMNs that utilise the coat and poke or poke and patch methodologies. HMNs therefore have the potential of greater control and tunability over dosage and delivery kinetics (180). Fabricated from an array of base materials, including - but not limited to - silicon, stainless steel, and glass, HMNs are most appropriate for applications which require precise or loading doses, including insulin and vaccinations (137, 181, 182). The clinical appeal of HMNs stems from their compatibility and ease of integration with conventional delivery systems, including luer lock syringes. Yet, despite this, challenges remain, with their broader adoption constrained by hurdles in fabrication complexity, mechanical integrity, and sterility-assurance.

Geometry and classifications

HMNs boast a broad range of applications and are often considered superior to SMNs due to their ability to deliver liquid formulations through their lumen with controlled infusion directly into the skin, enabling effective lymphatic targeting (Figure 7). The major advantage of HMNs is that they can deliver a higher dosage, if required, into vascularised dermal tissue, rich in immune cells and capillary networks (183). This infrastructure, paired with the capability for increased dosages, has led to a reported increase in absorption rates, with infusion rates for HMNs being reported within the range of 50 nL/min - 300 nL/min (182, 184).

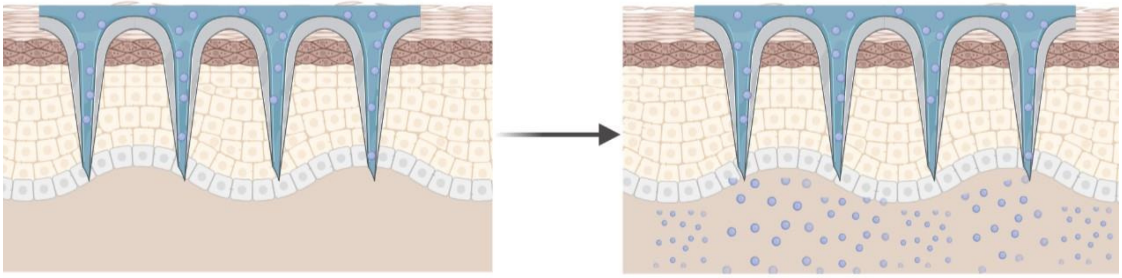

Figure 7. Schematic of poke and flow style hollow microneedle insertion

Additionally, HMN devices benefit from compatibility with continuous manufacture. Unlike DMNs or coated SMNs, HMNs do not require the drug formulation to be incorporated during fabrication and can be provided in a separate vial as currently produced. This decoupling allows for variations in formulations based on drugs required, height, weight, gender, *etc*., and facilitates the smooth progression through the regulatory pathway as an individual, not combination, medical product.

Material choice plays a substantial role in device performance. Polymeric HMNs specifically, due to their material composition and tip diameter, require strictly perpendicular insertion and adequate pressure, typically achieved *via* an applicator (185). Without this, particularly in conical designs, the needles have been demonstrated to bend on insertion and fail to penetrate *stratum corneum* effectively (186). In contrast, silicon HMNs, with their smaller tip angle, require less insertion pressure, resulting in reduced pain. However, their brittle crystalline structure necessitates further investigation to determine a reliable safety margin (137, 154, 187).

All types of HMN, regardless of material, require some degree of training/awareness for the user as to the pressure required. Studes demonstrate the variation in understanding of the instruction of "apply thumb pressure" (188). Both polymeric and silicon HMNs hold great potential for not just drug administration but for IF extraction.

HMNs are gaining traction in the research sphere due to their potential for minimally invasive delivery of a wide range of drugs at a higher dosage and increased molecular weight drugs, than is possible *via* SMNs and DMNs (189). They provide a channel for liquid formulations to flow through, hence their more colloquial name “poke and flow”. Typically mounted onto a classic luer lock syringe, HMNs are similar in assembly and application to traditional hypodermic injections.

In some instances, HMN arrays are coupled with external reservoir of drug, enabling the potential for controlled, sustained release, and therefore extended therapeutic effect (190, 191). Their ability to deliver dosages with greater precision and control supports wider range of clinical applications, offering improved bioavailability, higher dosing capabilities, and enhanced penetration efficacy (192). HMNs are fabricated from various materials, each with their own advantages and disadvantages.

Materials and fabrication approaches

MNs are fabricated from a wide array of materials and therefore require vastly different fabrication techniques. This subsection introduces these materials and methodologies, firstly by presenting a list of the types of materials HMNs are currently fabricated from (Table 3) and secondly focusing on two key types: polymeric and silicon.

Table 3. A summary of hollow microneedle materials and their common fabrication techniques

Microneedle Classification	*Material*	*Fabrication Technique*	*Ref*
Hollow	Silicon	3D laser ablation	(193)
		Deep reactive ion etching	(137, 194)
	Metal	Electromoulding	(195)
		Metal electroplating	(196)
		Laser cutting	(197)
	Polymer	Mould casting using centrifugation or vacuum	(198)
		Stereolithography	(142)
		Photolithography	(145)
	Glass	Thermoplastic drawing	(149)

Polymer

Polymeric HMNs have historically been fabricated *via* photo- and stereolithography (SLA) however, more recently have been manufactured using injection moulding techniques. Using a femtosecond laser to engrave the mould insert, PMMA HMNs are fabricated under tightly regulated temperature and injection rate controlled (199). Other common fabrication processes include ultraviolet (UV) lithography, whereby a lithography mask is used in conjunction with a micro-mould to generate the bevelled tip and lumen (186). Unlike other polymeric MNs, it has been demonstrated that the bevelled tip reduces insertion pressure, resulting in less tip damage and an improved insertion efficiency, enhancing insertion efficiency and improved safety profile of the device (186). However, this technique has also been associated with reports of fewer than 90 % of lumens being open following insertion, again reducing drug delivery efficiency (186). Polymer HMN shape has been demonstrated to significantly impact insertion efficiency, with shapes such as conical, chiselled under investigation. Thus far, bevelled tips have been evidenced to have the best safety and penetration profile (186).

Silicon

Alternatively, silicon HMNs are fabricated most commonly *via* MEMS, such as DRIE. Although other techniques are used, such as microfabrication, to facilitate transition to scalable manufacturing, DRIE in combination with photolithography is favoured as it enables all steps to be performed in one set of conditions, supporting continuous automated processing. This form of processing also enables the production of HMNs with uniform critical dimensions (CDs), such as the bevel and near vertical side walls (137). Although currently facing criticism regarding the potential safety profile of the devices due to the brittle nature of silicon, the devices demonstrate superiority in tip size and shaft length, both contributing towards better insertion efficiency and bioavailability by improving immune cell targeting (154, 187).

2.3. Silicon microneedles

Silicon MN are a form of parenteral drug delivery that leverage precision and scalable MEMS fabrication from the established semi-conductor industry. Available in a hollow and solid form, they have long been a focal point within the field of MN research due to their high-resolution geometries and compatibility with ‘smart’ drug delivery platforms. This section explores the rationale underpinning their research, the fabrication methodologies, emerging applications, and what challenges remain for the translation of this platform.

2.3.1. Rationale

Silicon MNs have garnered significant clinical interest on account of their precision fabrication, high-resolution structural control, and compatibility with micro-electro-mechanical systems. Their early adoption was driven by silicon’s widespread availability and the maturity of microfabrication techniques (200). This movement began in the 1990s, when the accessibility of silicon and rapid advancements in MEMS processing technologies were substantially accelerated by the broader technological boom of the past two decades (1, 201).

Progressions in photolithography, etching, and continuous wafer-level processing, largely propelled by the demand in the semiconductor and chip industry, have now enabled the manufacture of higher aspect ratio MN devices. These devices boast sub-micron tip radii, near vertical sidewalls, and increasingly larger shaft lengths. These impressive geometric characteristics are now attainable through the utilisation of these advanced fabrication techniques.

A further advantage of silicon lies in the post-processing flexibility. In polymeric MN fabrication, array configuration must be predetermined and embedded into the master mould design, whereas for silicon MNs arrays, post fabrication wafers can be diced in multiple orientations, including as individual needles, larger, dense arrays, or as a patch-based design. This flexibility in fabrication, paired with precision and scalable manufacture, reflects the efficiencies already demonstrated in the chip production sector.

2.3.2. Fabrication techniques

The fabrication of silicon MNs begins with a silicon wafer, typically produced on a small-scale at research institutes with 100 mm silicon wafers, onto which patterns are applied *via* photolithographic processes. This requires the deposition of photo-sensitive chemicals, termed photoresists (PRs), which are then exposed to ultra-violet (UV) light through a specifically designed mask. Depending on the resist polarity, this results in the exposed regions either hardening (negative PR) or softening (positive PR).

Post-exposure, the pattern on the wafer is developed, with the softened resist dissolving away and hardened regions of the pattern remaining on the wafer, providing a chemical-based stencil on the wafer for subsequent etching. This chemical mask during etching facilitates the production of precise device structures. This process is repeated, allowing the accumulation of different individual aspects of device structure, such as the bevelled tip surface and the straight edged shaft.

For hollow devices, an additional step is added to create the lumen feature. Finally, the device wafer is diced into the desired format (individual, array, or patch) using either saw-dicing or plasma dicing. This flexibility supports their integration into a wide array of drug delivery platforms.

2.3.3. Applications

Silicon MNs represented one of the pioneering MN technologies for biomedical use, attracting attention due to their precise microstructure and compatibility with MEMS. Consequently, silicon MNs have been trialled across a range of biomedical applications, including vaccine delivery, insulin administration, biosensing, and gene therapy delivery. The following subsections outline some of their recent applications within these domains.

Diagnostics and sampling

A particularly valuable application of silicon HMNs is the minimally invasive extraction of biological fluids, specifically dermal ISF. This use case illustrates how the geometric precision of silicon MNs facilitates controlled insertion with sharp tips, minimising tissue trauma and reducing contamination or artificially elevated inflammatory markers in collected ISF. Most recently, a silicon MN-based chip was reported to extract ISF for biomarker analysis in patients with heart failure, employing submicron tips (202). The silicon devices fabricated were measured to present a maximum height of 300 μm, and were manufactured using a hybrid approach, utilising DRIE and wet etching, which should be noted elevated manufacturing costs.

Despite demonstrating utility, the half-shaft structure of these devices and arrangement of 130 MNs *per* chip limit these devices to sampling applications. They rely on a vacuum-assisted system to draw the skin onto the MNs to facilitate penetration without such negative pressure, insertion of all 130 MNs in a patch-style assembly, would require significantly higher force and could produce a 'bed-of-nails' effect. Whilst the devices achieved consistent sampling rates of 1 ml/min over a 15 min period, concerns surrounding their elevated fabrication costs, lack of flexibility in application, and relatively shallow penetration depths should be noted.

Drug delivery

The drug delivery capabilities of silicon MNs has been demonstrated in multiple preclinical and clinical studies. Early work reported by Ma *et al.,* (2006) utilised hollow silicon MNs (~ 200 μm height) fabricated *via* wet etching and integrated with a piezoelectric transducer (PZT) insulin pump to enable minimally invasive, precise insulin administration (203). However, despite providing a compelling proof-of-concept for a miniature SC delivery device, the short needle height and cost-intensive fabrication process represent significant barriers to scalable application.

Subsequently, clinical investigations explored ID delivery of the influenza vaccination in healthy adults using a four-needle silicon MN array administered up to 6 mg of vaccine and elicited immune responses comparable to 15 mg delivered *via* IM (204). This three-fold dose-sparing potential is highly desirable within the pharmaceutical and vaccination fields. Additionally, the study further highlighted the reproducibility of responses measured, which is vital to support regulatory filings for medical devices (204). This study, however, failed to include any individual over the age of 40 which, with respect to the influenza vaccination administered, would be the population most heavily requiring this medical intervention. To further support their progression through latter clinical trial stages, studies with a greater cohort size are required, in addition to short-term follow up investigation with vaccination trial participants.

More recently, silicon MN arrays have been applied for ID delivery of live attenuated malaria vaccination in female BALB/c murine models (205). The devices, termed the ImmuPatch, were shown to influence the induction of central memory CD8^{+}T cells, with design parameters such as needle height and total pore volume significantly impacting immunogenicity. It is important to acknowledge, however, that the ImmuPatch was fabricated *via* wet etching, which, although precise, is both financially and environmentally costly, and significantly limits the achievable needle length.

Biologic delivery

Silicon MNs have been explored in the realm of biologics delivery, including that of nucleic acid-based treatments in pre-clinical murine models (206). Chiappini *et al.,* (2015) utilised solid silicon nanoneedles manufactured from porous silicon, which, as opposed to bulk crystalline silicon, is degradable under physiological conditions. The study highlighted that the high aspect-ratio devices efficiently penetrated the skin and delivered the nucleic acid payload without inducing significant tissue damage.

Similarly, Deng *et al.,* (2016) deployed a solid silicon MN array (~ 200 μm height) to deliver a cholesterol-modified GAPDH small interfering RNA (siRNA) sequence into mouse ear skin with the aim of knocking down the GAPDH housekeeping gene as a proof-of-concept (207). This was successful, with a reported 66 % knock-down measured without significant off-target accumulation, promoting the benefit of local ID delivery. Despite presenting successful results from a drug delivery usage, the utility of the device was poorly characterised, with usage described as “press[ing] six times” with no measured insertion force or mechanical reproducibility (207). Notwithstanding these limitations, there is further scope for the utilisation of silicon MNs within the sphere of biologics delivery, with the expense surrounding their quality fabrication offset by the expense of the therapeutics delivered.

Integrated platforms

Silicon MNs lend themselves to integration with sensors and electronic based medical devices due to their semi-conductor properties and MEMS-compatibility. High density silicon MN arrays (~ 9800 MN/cm^2) have been integrated with electrochemical electrodes by Dervisevic *et al.,* (2022) and used to monitor glucose levels in murine models *in vivo* (208). This study has been repeated within the field by Huang *et al.,* (2024), who utilised silicon HMNs to simultaneously monitor glucose levels and deliver insulin in rats (209). This offers promise within the field, highlighting the potential of silicon MNs to produce fully integrated, wearable, minimally invasive systems.

While these studies showcase the potential and versatility of silicon MNs within integrated platforms, current evidence is limited to preclinical testing and devices shorter than 600 μm. Nonetheless, they collectively highlight the utility of silicon MNs as core components for complex diagnostic and therapeutic systems.

2.3.4. Limitations

As with any emerging technology, silicon MNs face a range of hurdles that must be overcome to improve its translational potential. A principal obstruction to their clinical translation lies in the brittleness of silicon, which may increase the risk of fracture during insertion (210, 211). This presents safety concerns surrounding the risk of fractured fragments remaining in embedded in tissue, necessitating biocompatibility and cytotoxicity assessment to comply with regulatory standards for medical devices (212). Although silicon's compatibility with integration into smart devices makes it attractive as a material choice, its rigidity may limit skin comfort for prolonged usage (213). Furthermore, the insertion mechanics of the devices are currently insufficiently understood, rendering it difficult to definitively quantify fracture risk under clinical conditions. Even so, their geometric precision, specifically their sub-micron tip, have been evidenced to reduce insertion force, which may in turn mitigate potential fracturing (154, 187).

Beyond the realm of mechanical concerns, cost-related limitations are often raised when comparing silicon MNs to their polymer alternatives (214). However, this is largely attributable to the small-batch fabrication and academic cleanroom settings currently used. In reality, the fabrication processes (specifically the photolithography, etching, and dicing) are very well established at scale within the semi-conductor industry and were developed on decades of advancement in the technology. As demonstrated within the chip industry, this fabrication process works on the economy of scale, and therefore costings of fabrication, are expected to decrease as fabrication scale increases. In this context, scalability remains both a realistic and achievable goal.

Despite being widely regarded as an inert material, the biocompatibility of silicon in MN applications is lacking in evidentiary support. To date, there is insufficient evidence of compliance with the regulatory framework set out by the International Standards Organisation (ISO) Section 10993, which is the internationally agreed-upon series of standards for the biological evaluation of medical devices (215). This guidance sets out the scope of testing required to assess biocompatibility, including assessment of sensitisation, irritation, and importantly, cytotoxicity (215). Given the documented concern surrounding the fracture risk of silicon MNs, it is critical that cytotoxicity assessment is performed, particularly if the long-term wear in smart biosensing and drug delivery devices is to be capitalised on (215). Without clear evidence of compliance, the safety profile of silicon MNs cannot be fully established which, in turn, provides a barrier to regulatory approval and therefore clinical translation.

Taken as a whole, these limitations highlight the key areas of silicon MN research that require further investigation to enable the platform to progress through higher Technology Readiness Levels (TRLs). Each constraint, from mechanical performance and delivery repeatability to biocompatibility and manufacturing scalability, present a distinct challenge which must be addressed before commercialisation can be realised. Research targeting these areas will be fundamental to position silicon MNs as viable candidates for next-generation medical devices.

2.4. Challenges and considerations

As MN-based platforms progress towards clinical and commercial translation, several key hurdles must be overcome to ensure successful rollout and long-term viability. Although widely discussed in modern product development, sustainability is often overlooked with respect to medical devices, where regulatory compliance with respect to biocompatibility and excellent safety profiles is prioritised. Nonetheless, concerns relative to material waste and environmentally intensive fabrication processes must be considered, both of which influence the cost-effectiveness and feasibility of scaled-up production. This section explores these factors, highlighting the challenges which must be addressed to enable these MN technologies to realise their full translational potential.

2.4.1. Sustainability

Sustainability with respect to environmentally friendly material choices and recyclability is increasingly recognised as a critical requirement in the development and introduction of new products. However, for medical devices, this issue may be eclipsed by performance demands. Medical implements are inherently performance-prioritised, with serious, and in some cases grave, consequences when cost is prioritised over safety and functionality. This poses a substantial challenge to the development of MNs, especially silicon and metal devices. As recycling is not feasible, and nor is reuse, needles in general exhibit poor sustainability profiles.

Since sustainability cannot be prioritised post-fabrication, considerations must be crafted during the fabrication process. This could cover the reduction of plastics and polymers usage in device fabrication, in addition to the reduction of chemical usage in semi-conductor based MN fabrication, both of which carry extensive environmental costs. The environmental implications associated with silicon based MNs is reflective of the broader silicon and semi-conductor manufacturing industry, which is known for its high energy demands. A single Intel fabrication facility (Ocotillo, Arizona) generated approximately 15,000 tonnes of waste in just three months (Jan – Mar 2021), with around 60 % of this classified as hazardous (216). Figures such as these highlight that *en masse*, wet chemical production of silicon MNs represents a significant contributor to global emissions. This calls for a dry-only fabrication process, which is achievable, but not yet commercially scaled in the medical field, such as dry etching in the production of silicon MNs.

2.4.2. Scalability and manufacturability

Manufacturability is a crucial criterion when considering the development of a new product. A forward-thinking approach is required to understand how best to scale up the research-level fabrication processes in order to streamline and simplify it, thereby significantly reduce production costs and render it suitable for cheaper, mass scale production. Furthermore, future research must broach methodologies for sterile good manufacturing practice (GMP); a topic whose importance has been stressed by regulatory bodies such as the FDA and the EMA (217, 218).

Current fabrication processes, such as those utilised by NanoPass, require a mix of wet and dry etching, which may lead to inflated costs (219). Therefore, a key consideration for future developments is the creation of process uniformity to streamline fabrication and improve cost-*per*-device efficiency (136, 220).

2.4.3. Biocompatibility

Biocompatibility, in the context of MNs, is defined as the ability of a device material to perform its intended function without eliciting an unacceptable adverse event in the host (221). This consideration is especially critical for MNs, which breach the skin barrier, reside within the dermal compartment, and deliver therapeutic agents. Therefore, given their direct contact with the skin and the potential for systemic exposure, long-term safety risks must be thoroughly evaluated.

Biocompatibility profiles must be established for each material and classification, with literature reports often forming the basis for justification in investment in one material over the other. Metals, while generally well-tolerated, may pose allergy risks; polymers, though tuneable in degradation and integrity, can trigger inflammatory responses; and silicon, despite its inert nature, is brittle and may fracture under stress (222).

For SMNs specifically, biocompatibility considerations extend beyond the base material to include the formulation coating, which must be assessed individually and in combination with the device (223). Sterility and stability studies are vital to ensure safety and efficacy throughout the product's shelf life and clinical usage.

The industry standard for the biocompatibility and cytotoxicity testing of medical devices, ISO 10993, lays out the regulatory expectations for MNs as standalone and combination products (215). This standard must be articulated clearly within the regulatory pathway to aid the successful translation of MN-based products from research to the clinic.

2.4.4. Regulation and safety

Despite an already rigorous regulatory assessment pathway, scrutiny surrounding medical devices is at a peak, with widespread misinformation available to the general public and heightened public scepticism, particularly following the rise of the anti-vax movement during the COVID-19 pandemic (224). Further challenges include the requirement for a co-approval process, which requires the submission of both the constituent drug and the product as a whole (225). For example, NanoPass silicon MN has received FDA regulatory approval, however this is limited, with it registered as a non-combination device, and only licenced for use delivering substances which have existing intradermal delivery approval (226). Despite the constraints around this approval, this may potentially pave the way for a smoother process of regulatory pathway for future MN platforms (219).

As a novel medical device aiming to surpass a well-established current technology, safety concerns, spanning from breakages to increased local irritation, must be negligible. Polymeric MNs currently demonstrate favourable safety profiles, due to the wider range of biocompatible polymers available (38, 227). Despite the more favourable polymeric material, these needles require a significantly greater penetration force requiring an applicator to ensure proper puncture and to prevent the needle bending upon contact (228). This presents a gap in current literature for a product which is sharp enough to limit insertion force and therefore minimise damage to the surrounding tissue; an area where silicon MNs may offer a distinct advantage in.

For vaccination applications, chronic usage studies will not be necessary. However, for applications with chronic dosage such as the treatment of pain, cancer, and diabetes, continuous safety monitoring will be required. Safety considerations go beyond material selection to include the quantity of dosage actually delivered in the case of dissolvable polymeric and coated MNs, which can be difficult to confirm. This highlights a key benefit of HMNs, as the quantity of drug delivered can be measured in the conventional manner with tools such as luer lock syringes.

2.5. Conclusion

MNs are a rapidly evolving area of research, with substantial translational and clinical potential. An increasing array of MN materials and geometries are available, each requiring thoughtful selection based on their intended application. Among these, SMNs are the most evolved devices thus far, typically fabricated from polymers. These, however, are typically associated with high penetration forces, reduced penetration efficiency, and limited dose loading capabilities.

Current research stresses a need for a taller, mechanically robust MNs, with a reduced tip angles to improve patient comfort and insertion repeatability. There is a particular growing demand for taller HMNs that enhance the dosing capacities and enable better immune cell targeting. Silicon-based SMNs and HMNs offer a promising solution, providing longer, sharper tipped needles with larger bores for increased dosage. Nonetheless, they require further development to fulfil their clinical potential, with a focus on their mechanical strength and safety profile.

This research was designed to address crucial technical barriers to silicon MN development – tackling fabrication scale, insertion mechanics, cytotoxicity, and delivery performance. This thesis serves to provide foundational evidence to support the advancement of silicon MN characterisation and industrial-scale manufacture.

3. Chapter 3: Small-Scale Manufacture

The focus of this chapter is to outline the fabrication processes utilised for the small-scale manufacture of solid and hollow silicon MNs. Manufacturing reported here focuses on 100 mm silicon wafers and reports the fabrication workflow and characterisation techniques used for device assessment. Challenges associated with small-scale MEMS production are also discussed.

3.1. Introduction

MNs are devices designed to facilitate minimally invasive drug delivery with improved dermal targeting, offering a promising alternative to conventional hypodermic needles. As MN research continues to expand, a wide range of device formats and corresponding fabrication methodologies have emerged, including injection- and micro-moulding-based polymer devices, wire-bonded metal structures, and hydrogel MNs produced *via* 3D printing (229). The first MN devices developed for drug delivery were manufactured from silicon, utilising scalable processes adapted from the MEMS industry. These silicon-based fabrication techniques enable a stepwise, photolithography-driven approach capable of producing both solid and hollow geometries with minimal variation between process runs.

Although recent years have seen a shift towards polymer-based MNs due to their manufacturing simplicity, limitations in achievable tip sharpness and confinement to solid geometries have prevented them from matching the structural precision and functional versatility offered by silicon-based designs (145, 214, 230). Despite the high resolution and tunability of MEMS-based processes, the reproducible fabrication of high-aspect-ratio silicon MNs, particularly hollow architectures with well-defined bores, remains a non-trivial challenge. In addition to process intricacies, further fabrication difficulties associated with deep etches can lead to common defects in high-aspect ratio MEMS devices including tapering at the base, and the formation of silicon ‘grass’ on the substrates base (231). This ‘grass’, also referred to as black silicon, is areas which have been unevenly masked and etched, producing residual spike like material on device trenches. These issues must be addressed to ensure high-quality manufacture.

In this chapter, DRIE was utilised as previously reported by Bolton *et al.,* to fabricate the MN devices pictured in Figure 8 (137). This past work established the base methodology for device production, with the work reported here focused on adapting this approach to produce both better quality and yield of solid (SMN) and hollow (HMN) silicon MNs. Detailed in this chapter are the additions made for incremental improvement of the methodology, including a smoothing etch (US Patent Number: US12417910B2), SiO_2 hard masks, and a wet etch which were used to improve fabrication fidelity and reduce common defects, such as the presence grass and residual walls (232, 233). Yield was evaluated at both the individual needle and array level, allowing correlation between design choices and process success. Visual characterisation was conducted using profilometry and scanning electron microscopy (SEM) as the field standard, with mechanical characterisation performed on the final array structures to assess structural integrity under compressive loading.

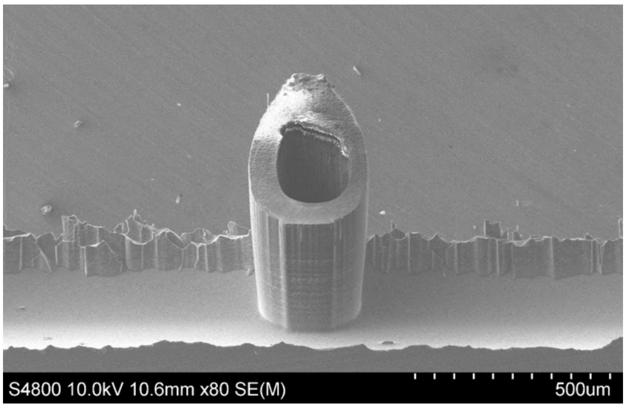

Figure 8. Scanning electron microscope image of silicon microneedle previously produced based on the methodology used in this project

3.2. Materials and methodology

This section outlines the materials, chemicals, methodologies, and process flows used for the small-scale manufacture of both hollow and solid silicon MNs at 100 mm wafer scale. The core approach reported builds on previously reported fabrication processes, with modifications and inclusions aimed to improving feature fidelity, quality, and yield.

3.2.1. Materials

The materials used in the initial fabrication process are reported here. It details the substrates, equipment, and chemicals utilised, providing a foundation for the following subsection on experimental implementation.

Silicon wafers

Device wafers were custom ordered to meet the criteria detailed in Table 4. The batch process was initiated with 10 device wafers. Oxide coated standard 150 mm diameter silicon wafers (675 μm thickness) were utilised as carriers for the 100 mm devices wafers due to the tools 150 mm handling size infrastructure.

Table 4. Properties of silicon wafer starting material

Property	*Value*
Material	Silicon
Diameter	100 mm
Thickness	1400 μm
Polish	Double sided
Doping	p-type
Resistivity	< 10 Ω·cm
Orientation	<100>

Chemicals

The solvents and chemicals required for the fabrication of silicon MN devices, including solvents, PRs, and chemical etchants, are outlined below.

Solvents

Acetone (CAS: 67-64-1) and isopropyl alcohol (IPA) (CAS: 67-63-0) were used for solvent cleans throughout the fabrication process.

Adhesion promoters

Ti Prime was used as a wafer adhesion promoter in device fabrication. Due to its hexamethyldisilane (HMDS) base, Ti Prime modified the blank device wafer surfaces to form a hydrophobic silane monolayer to promote resist bonding and reduce resist lifting and edge bead formation.

Crystalbond 555-HMP (CAS: 9016-45-9) adhesive was used to bond device wafers to carrier wafers. Upon heating (66 ^{o}C thermal flow point) the Crystalbond enabled wafer mounting, which solidified upon cooling. Post etch, the wafers unmounted by heating again to melt the Crystalbond.

Photoresists

Three PRs were utilised in the fabrication process: two positive (AZ MIR 701 and AZ 4999) and one negative (AZ 125nXT-10A). AZ MIR 701, a spin coating resist, contains the photoactive compound (PAC) diazonaphthoquinone (DNQ). Upon exposure to UV light, DNQ underwent a Wolff rearrangement, producing a carboxylic acid derivative which has increased solubility to developer. Resultantly, exposed resist regions dissolved upon developing, leaving the desired pattern. AZ 4999, also a positive resist, was utilised primarily for spray coating. AZ 4999 underwent thermal degradation of its resin matrix under high dose UV, resulting in the dissolution of exposed areas under development.

AZ 125nXT-10A, a negative PR, was applied *via* spin coating to the wafer surface. AZ 125nXT-10A crosslinked under exposure to UV, resulting in polymerisation of the exposed regions. Resultantly, upon development, the unexposed areas dissolved, producing the required pattern.

Developing agents

Developing agents were used to selectively dissolve portions of PR after UV exposure, revealing the desired patterning on the wafer. AZ 726, a mild, tetramethylammonium hydroxide (TMAH)-based, metal ion free developer, was used to dissolve uncrosslinked resist. AZ 400K, a strong TMAH-based developer, was used for more aggressive development of exposed areas of positive resist.

Chemical etchants

Hydrofluoric acid (HF) in the form of buffered oxide etch (BOE) 7:1 was utilised to perform a wet etch for SiO_2 removal. BOE 7:1 consisted of a mixture of seven parts ammonium fluoride (NH_4F) solution and one part 40 % HF, with the ammonium fluoride acting as a buffering agent to stabilise the etch rate and improve process control. The BOE etching process was based on a dissolution-precipitation mechanism, which was underpinned by the following chemical reaction:

$$SiO_2 + 6HF \rightarrow H_2SiF_6 + 2H_2O$$

Stripping agents

P1316 was used as a PR stripping agent post etch, functioning by swelling and dissolving the resist polymer and releasing resist adhesion to wafer surfaces.

Photolithography masks

Photolithography masks were designed using KLayout (version 0.27.11) and manufactured by Photronics with the appropriate polarity specified for each layer. Each mask included alignment marks to ensure accurate registration between successive etch steps, ensuring the bore patterning was placed correctly on the bevel structure, and subsequently the shaft patterning was placed correctly on the bevel structure with respect to bore location. CD check structures were also incorporated into each mask to enable verification of feature sizes following development and etching.

Marker

Alignment mark bases required for each subsequent etch step were patterned onto the wafer using the marker photolithography mask. Each CD check region on the marker mask was labelled according to its corresponding etch step (marker, bevel, bore, shaft, and dicing), and each alignment mark on the respective etch masks was likewise labelled to maintain consistency and enable accurate registration throughout the fabrication process (Figure 9).

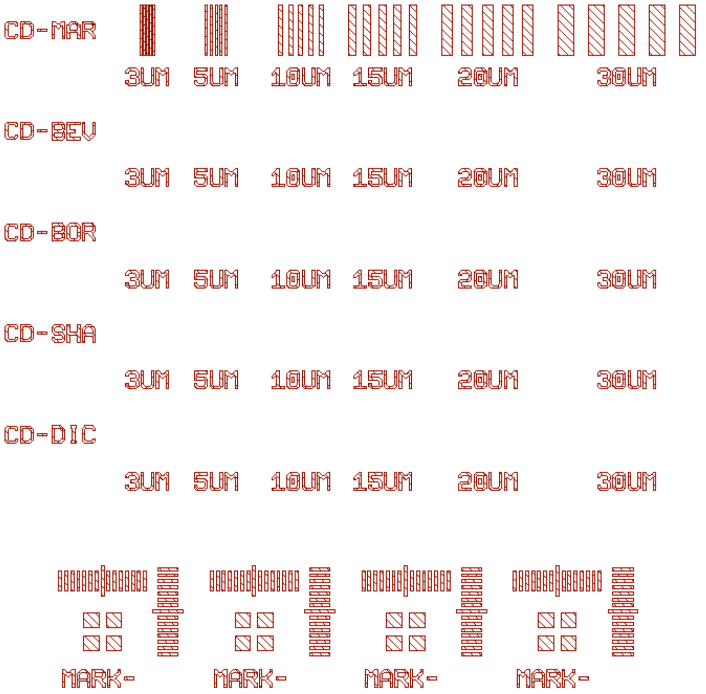

Figure 9. Alignment marks and critical dimension checks etch steps and dicing

Bevel

The bevel patterning can be seen below, with the bevel alignment marks (Figure 10).

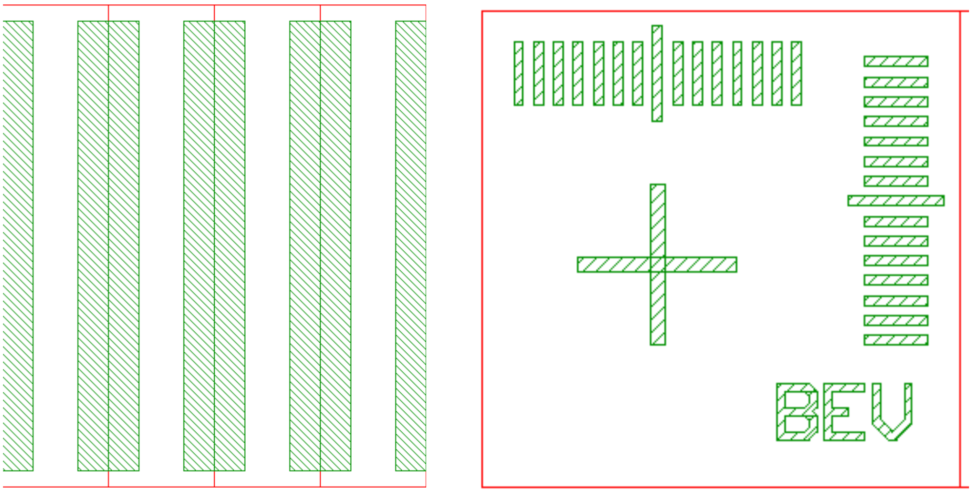

Figure 10. Photolithography patterning for bevel etch (left) and bevel alignment marks (right)

Bore

The bore patterning can be seen below, with the corresponding alignment marks (Figure 11). The pitch on these device wafers are 1300 µm.

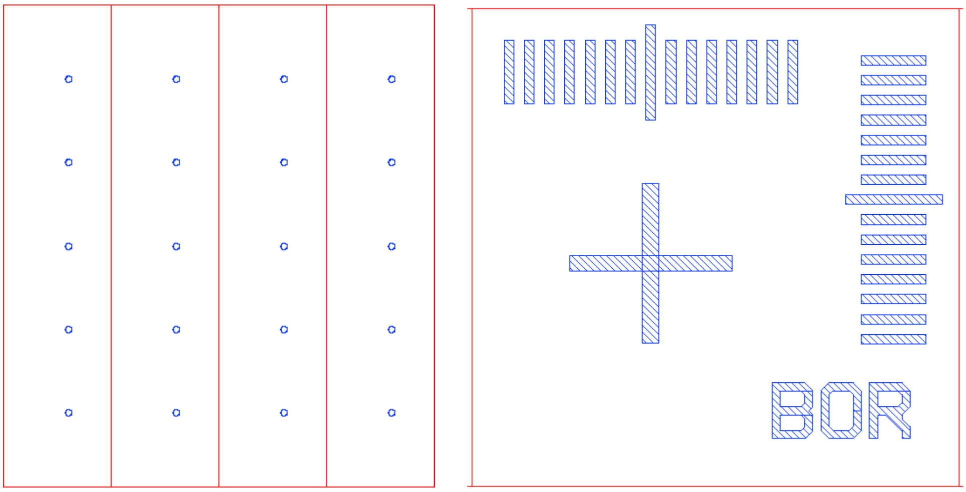

Figure 11. Photolithography patterning for bore etch (left) and bore alignment marks (right)

Shaft version 1

Two versions of the shaft pattern were employed across different wafers within the processed batch. Version 1 featured a box-style architecture surrounding each array, which reduced the open silicon area exposed for etching (Figure 12). Both versions utilised identical alignment marks and CD check structures; the only variation was the inclusion of the coffin-style design in Version 1.

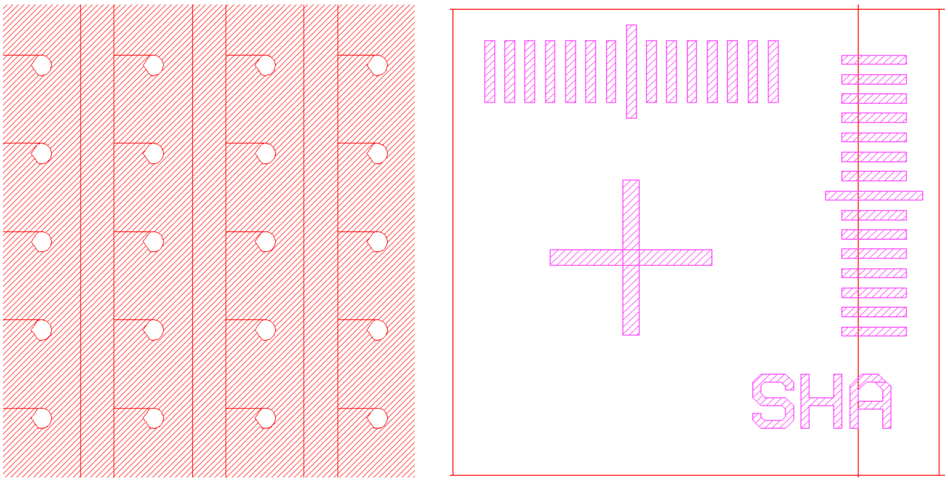

Figure 12. Photolithography patterning for shaft etch (left) and shaft alignment marks (right)

Shaft version 2

The Version 2 of the shaft mask can be seen below Figure 13, with the coffin style walls absent. Alignment marks for the shaft design can be seen in Figure 12.

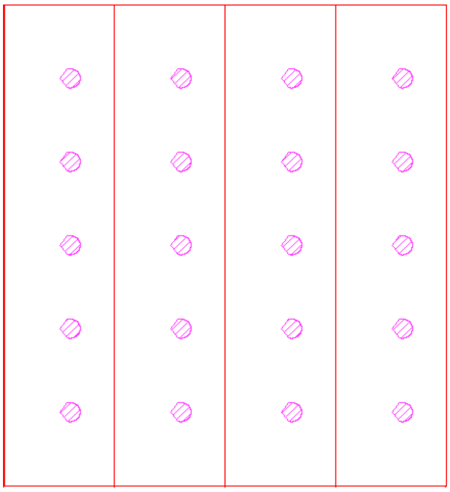

Figure 13. Photolithography patterning for shaft etch

3.2.2. Experimental instrumentation and manufacture methodology

This subsection details the equipment and chemicals used in the manufacturing process, before the detailed process flow is presented in subsection 3.2.3. A schematic of the manufacturing process can be seen in Figure 14.

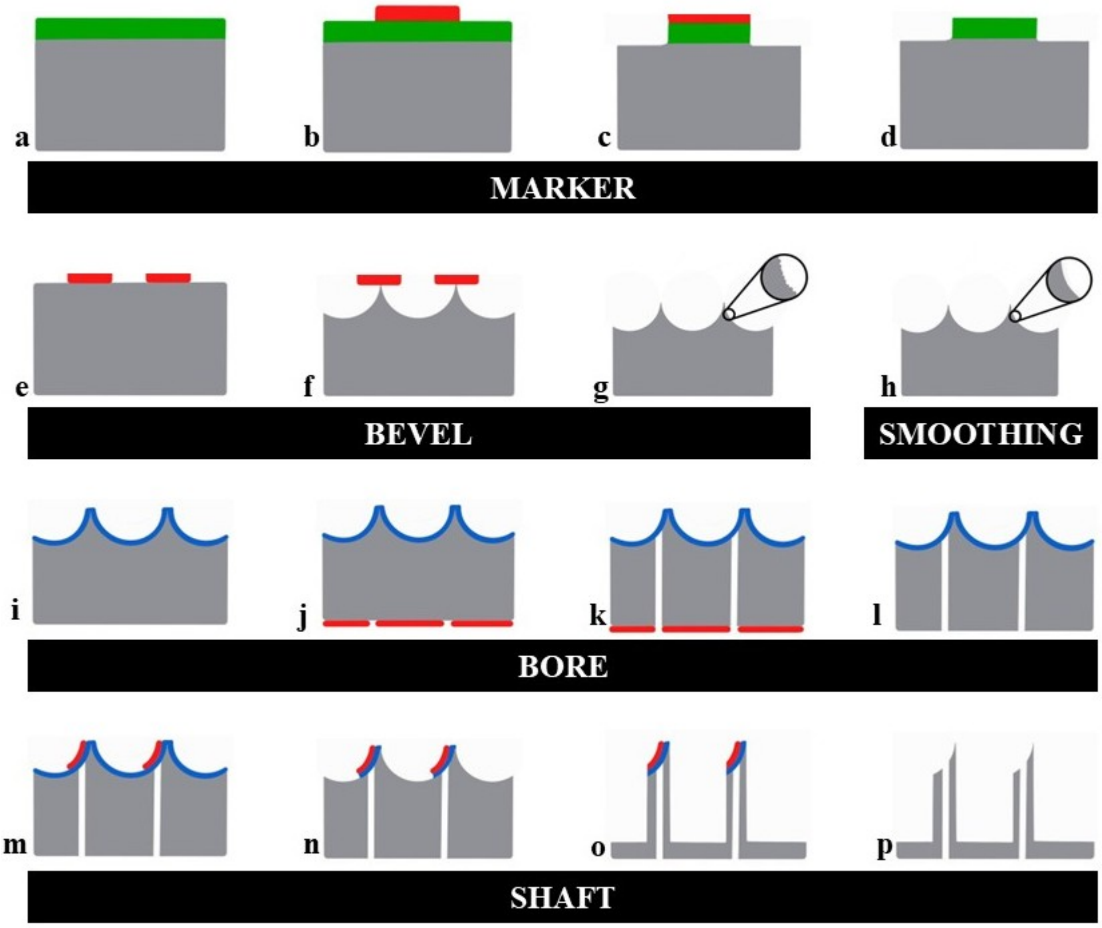

Figure 14. A schematic representation of the fabrication process flow to manufacture hollow silicon microneedles. Four distinct etch steps are labelled as marker (a-d), bevel (e-g) smoothing (h), bore (i-l), and shaft (m-p). Colours represent silicon (grey), silicon nitride (Si_3N_4, green), photoresist (red), and silicon dioxide (SiO_2, blue). Fabrication of solid microneedles omits bore processing (i-l). Fabrication steps are provided in detail in subsection 3.2.4: Out of plane silicon microneedles 100 mm fabrication

Wafer cleaning

Sonicator

A sonicator was used for solvent-based wafer cleaning steps at various stages throughout fabrication. This process, referred to as a solvent clean, involved immersing the wafers in 100 ml of acetone for 10 mins, followed by 100 ml of IPA for 5 mins.

Ultrasonic agitation was utilised to enhance the removal of organic contaminants and surface residues. The cleaning mechanism relies on the generation of high-frequency acoustic waves in the solvent bath, which produce cavitation bubbles that collapse near the wafer surface and dislodge adhered material without mechanical abrasion.

Plasma asher

A plasma asher was used as a surface cleaning tool for device wafers to ensure that no organic residue remained prior to processing. The system operates by applying a radio-frequency electromagnetic field to oxygen gas under vacuum conditions, ionising the gas to form a reactive plasma composed of atomic, ionic, and radical oxygen species. These species chemically react with organic materials on the wafer surface, generating volatile by-products such as carbon dioxide (CO_2), water (H_2O), and carbon monoxide (CO). Exposure time was limited (< 5 mins) to avoid unwanted degradation of PR layers, where applicable, while ensuring sufficient removal of surface contaminants.

Compressed N_2 gun

A compressed air gun was used during post-cleaning and drying steps to remove residual solvent, moisture, or particulate from the wafer surface. The device delivers a controlled stream of pressurised air, enabling non-contact removal of contaminants prior to subsequent processing, without introducing mechanical stress or surface damage.

Photolithography and coating

The photolithographic processes used in the fabrication of hollow and solid silicon MNs, including spin and spray coating techniques, are detailed in this subsection. Each process of applying a PR is referred to as a recipe, those reported here are optimised to ensure uniform coverage across a 100 mm wafer.

Spin coater

A Laurell WS-650 spin coater was used for the uniform application of adhesion promoters and PRs onto the wafer surface. A 100 mm vacuum chuck was used to securely hold each device wafer in place during spinning. The materials were manually dispensed onto the centre of the wafer prior to spin initiation. The system operates by spreading the material *via* centrifugal force, forming a thin, uniform film. Multi-stage spin protocols were employed in some cases to accommodate the increased mass of the wafers and the viscosity or thickness of certain resists. Acceleration and spin speed parameters were adjusted to ensure consistent coverage and minimise defects such as edge beading or streaking. The recipes used are detailed in Table 5 and are based on industry standard advice taken from the manufacturers datasheet.

Table 5. Spin coating recipes for Ti Prime, AZ MIR 701, and AZ 125nXT-10A

<table>
<tr><th rowspan="3"><i>Spin Coater Recipe #</i></th><th colspan="2" rowspan="2"><i>Chemical</i></th><th colspan="6"><i>Recipe</i></th></tr>
<tr><th colspan="3"><i>Step 1</i></th><th colspan="3"><i>Step 2</i></th></tr>
<tr><th>name</th><th>class</th><th>rpm</th><th>accr</th><th>time (s)</th><th>rpm</th><th>accr</th><th>time (s)</th></tr>
<tr><td>1</td><td>Ti prime</td><td>adhesion promoter</td><td>4000</td><td>1000</td><td>20</td><td></td><td></td><td></td></tr>
<tr><td>2</td><td>AZ MIR701</td><td>positive photoresist</td><td>3000</td><td>1000</td><td>45</td><td></td><td></td><td></td></tr>
<tr><td>3</td><td>AZ 125nXT-10A</td><td>negative photoresist</td><td>300</td><td>300</td><td>5</td><td>1500</td><td>1000</td><td>30</td></tr>
</table>

Spray coater

A SUSS MicroTec AS8 spray coater was employed for PR deposition on substrates where spin coating was unsuitable, such as mid-process wafers with significant topography *e.g.,* bevels. This system utilises a fine atomised spray to deposit a uniform resist layer by directing aerosolised PR down onto the substrate, allowing uniform coverage over three-dimensional features. Process parameters utilised are detailed in Table 6 and are based on industry standard advice taken from the manufacturers datasheet. PR AZ 4999 was dedicated to this spray coater therefore the typically required dilution with acetone was not necessary.

Table 6. Spray coating recipe used for AZ 4999

Chemical		*Recipe*						
name	resist type	pump flow (ml/min)	chuck temperature (°C)	N_2 flow (bar)	sled speed (mm/s)	pitch	scan number	nozzle height (mm)
AZ 4999	positive	2.5	70	1.3	120	4	12	20

Hot plates

An EMS 1000-3 precision electronic hot plate was used for thermal processing steps including PR baking. This model features lift pins positioned within a 20 mm radius. The hot plate provided stable and accurate temperature control, ensuring consistent soft-bake and hard-bake conditions critical for optimal resist adhesion and profile development.

Mask aligner

A SUSS MicroTec MA8 UV mask aligner was used for photolithographic patterning of the wafers. This contact aligner utilises UV light exposure to transfer patterns from photomasks onto PR-coated substrates *via* polymerisation. The MA8 allowed the soft contact of a glass mask, held *via* vacuum, to the wafer during exposure to minimise damage to the resist layer and maximise accuracy. It provided precise alignment capabilities (accuracy < 0.5 μm) on both the top and bottom sides of the wafer, ensuring accurate patterning, critical for MN fabrication such as bore and shaft alignment. Exposure was facilitated by a 1000 W mercury lamp positioned perpendicular to the mask. Details of the exposure energy (mJ/cm^2) are provided in the relevant manufacturing step in subsection 3.2.3.

Thin film processing

Thin film processing in the form of plasma-enhanced chemical vapour deposition (PE-CVD) was utilised and is reported here. This was used to form a hard mask and etch stop layer to facilitate processing and ensure device quality.

Plasma-enhanced chemical vapour deposition

A PE-CVD system (KLA UK) was used to deposit dielectric thin films at two stages of the process. In the first instance, a layer of silicon nitride (Si_3N_4) was deposited to act as a hard mask on the wafer surface for subsequent etch patterning steps. Later in the fabrication process, a silicon dioxide (SiO_2) layer was deposited to serve as an etch-stop layer and hard mask.

PE-CVD operated by introducing precursor gases into a low-pressure vacuum chamber, where a radio-frequency (RF) plasma was generated to dissociate and activate the gas species. For the Si_3N_4 deposition, the precursor gases were silane (SiH_4), ammonia (NH_3), and nitrogen (N_2). For the SiO_2 deposition, silane (SiH_4) and nitrous oxide (N_2O) were used. The plasma provided sufficient energy to initiate surface reactions at relatively low substrate temperatures, leading to the formation of thin, conformal dielectric layers. This process allowed for the controlled deposition of Si_3N_4 and SiO_2 with good step coverage and uniformity.

Etching

Inductively coupled plasma reactive ion etching

An inductively coupled plasma (ICP) etcher (KLA UK) was used to etch through the silicon nitride (Si_2N_4) hard mask and expose the underlying silicon according to the mask design. Inductive coupling between the radio-frequency (RF) antenna and the plasma generates a region of high-density plasma, whereby an alternating radio frequency (RF) magnetic field induces an electric field that energises free electrons and sustains process gas ionisation. A primary RF generator (2 MHz) powers the ICP coil to control both plasma density and ion flux, while a secondary RF generator (13.56 MHz) was applied to the lower electrode (platen) to establish a substrate bias which accelerates ions toward the wafer surface, enhancing directional etching.

Deep reactive ion etching

DRIE was performed using the DSi-v™ system (KLA UK) to define high-aspect-ratio features on the MN wafers, including the deep bore and shaft structures. The system utilised an ICP source to generate a high-density plasma, and a RF bias was applied beneath the platen to accelerate ions toward the substrate surface. To accommodate the 150 mm wafer handling configuration of the tool, all 100 mm device wafers were mounted onto standard 150 mm silicon carrier wafers to ensure compatibility with the electrostatic chuck (ESC) and robotic wafer handling.

The bore and shaft etching was performed using a three-step switched Bosch process consisting of: (i) deposition (passivation), (ii) a physical etch (E1), and (iii) a chemical etch (E2) (Figure 15). A mix of SF_6 and O_2 gases were utilised switched etching to physically and chemically remove material respectively. The bevel etch (E2) was performed using non-switched etching.

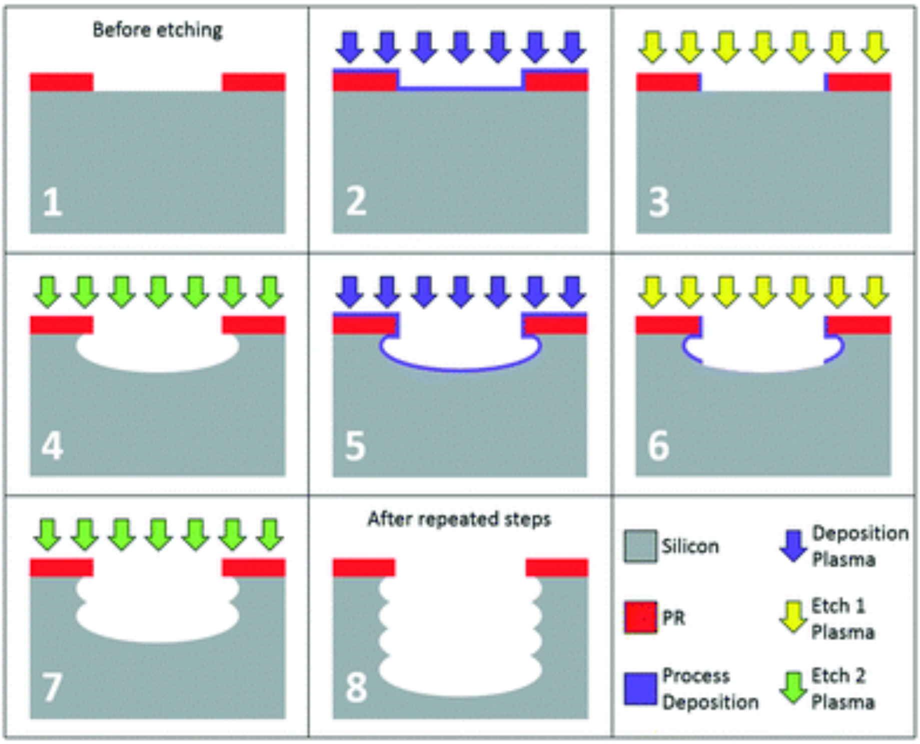

Figure 15. Etch cycle diagram depicting the deposition, physical, E1 and chemical E2 etches (137)

In the deposition step, octafluorocyclobutane (C_4F_8) was introduced into the chamber where it was ionised, producing fluorocarbon polymer precursors, which deposited conformally (Equation 1).

$$C_nF_k^- + C_4F_8 \rightarrow C_{n+4}F_{k+8} + e^-$$

Equation 1. The ionisation of octafluorocyclobutane during the deposition step

E1-mediated physical removal of the passivation from the base of the etched features was achieved through ion bombardment. O_2 gas dissociates reacted with carbon in the polymer to enable chemical based removal. Sulphur hexafluoride (SF_6) gas was introduced into the plasma and underwent dissociation and ionisation, producing charged species (SF_5^+ and SF_6^-) which were accelerated by the RF bias towards the wafer (Equation 2). These ions remove passivation layer from horizontal surfaces, exposing the silicon beneath, while preserving sidewall protection due to their anisotropic trajectory.

$$SF_6 + e^- \rightarrow {SF_5}^+ + F\bullet + 2e^-$$

$$SF_6 + e^- \rightarrow {SF_6}^-$$

Equation 2. The ionisation of sulphur hexafluoride during the physical etch (E1)

In the chemical etch (E2), the exposed silicon reacted chemically with neutral fluorine radicals (F•), which were also produced from SF_6 dissociation in the plasma (Equation 3). These fluorine radicals etched the silicon to form volatile silicon tetrafluoride (SiF_4), which was continuously removed by the exhaust pump (Equation 3).

$$SF_x + e^- \rightarrow SF_{x-1} + F\bullet + e^-$$

$$4F\bullet + Si \rightarrow SiF_4$$

Equation 3. The reaction underpinning the chemical etch (E2)

The cyclic repetition of these three steps enabled vertical, high-aspect-ratio structures to be etched. The DSi-v™ tool included additional hardware features such as an automatic pressure control (APC) valve to finely regulate chamber pressure, an internally cooled platen to manage wafer temperature, and a backside helium gas flow to enhance thermal conduction. The ESC ensured uniform wafer clamping and positional stability throughout the extended etch cycles. These features collectively contributed to the process uniformity and precision required for MN fabrication.

3.2.3. Analytical methodology and characterisation

Outlined in this subsection are the analytical techniques and characterisation methodologies used for the evaluation of the fabrication process and final devices. This includes procedures for within-production quantitative assessment, in addition to qualitative imaging of fabricated devices.

Structural and optical characterisation

Characterisation of devices has been performed both structurally and optically throughout the fabrication process. The subsection below outlines the methodologies and techniques used for performing this characterisation.

Ellipsometer

An ellipsometer (J. A. Woollam M-2000) was used to measure the thickness of the dielectric layers deposited *via* PECVD. Ellipsometry is a non-destructive optical technique that determines thin film thickness by measuring the change in the polarisation state of light upon reflection from the wafer surface. The incident polarised light undergoes a change in amplitude and phase, which was measured and modelled to extract film thickness.

Profilometer

A stylus profilometer (Bruker Dektak XT, Bruker Corporation) was used to measure the thickness of PR layers following spin coating and soft baking. The stylus was scanned across a resist-free step under a defined contact force, and the resulting height profile was used to determine the resist thickness.

Optical microscopy

A digital optical microscope (VHX-6000 Series, Keyence Corporation) was used to perform CD checks on patterned wafers following photolithography development and post-etch processes. Measurements included feature sizes specific to each photomask design, such as bore and shaft diameters of the MN structures. The system enabled high-magnification imaging and dimensional analysis to verify patterning, resist integrity, and etch accuracy.

Scanning electron microscopy

SEM was used to image MN structures at key stages of fabrication. Two systems were employed: a Hitachi S-4800 ultra-high-resolution field emission SEM and a Zeiss EVO LS25 variable pressure SEM.

Samples were mounted onto aluminium stubs using conductive adhesive and sputter-coated with a thin layer of gold to minimise charging. The stubs were placed on the sample stage within the SEM chamber, which was pumped down to ensure a vacuum environment. A focused electron beam was generated at the top of the SEM column and accelerated toward the sample under high voltage (Figure 16). The beam was directed through a series of electromagnetic lenses, which narrowed and focused it onto the sample. On impact, the primary electrons interacted with surface atoms, resulting in the emission of secondary electrons. These were detected and mapped to construct a high-resolution greyscale image of surface morphology.

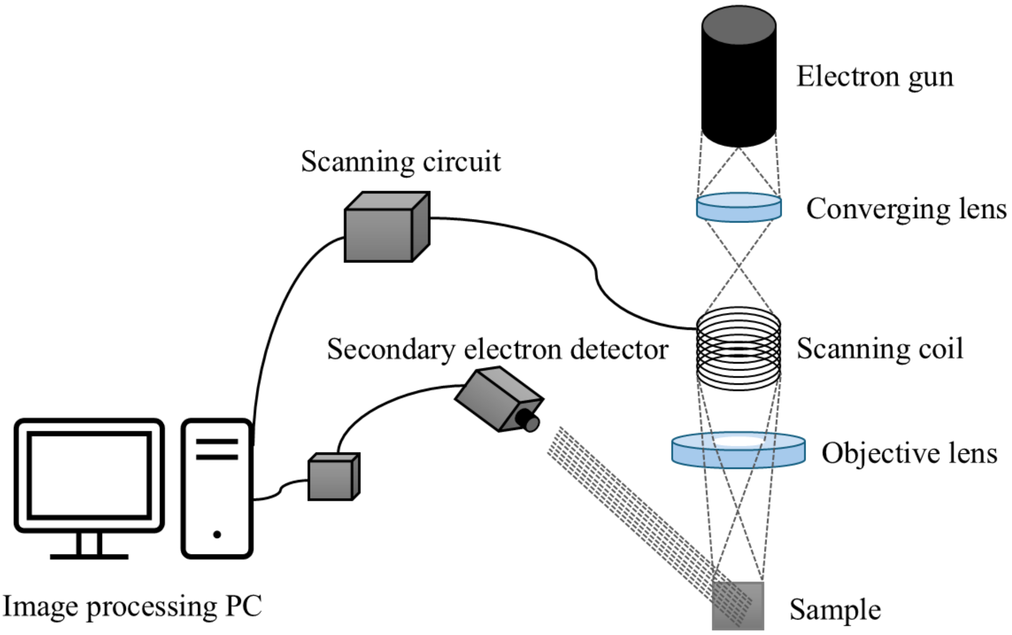

Figure 16. Schematic of scanning electron microscope apparatus

The Hitachi S-4800 system, equipped with a cold field emission electron source, provided magnification up to x1,000,000 and a resolution of approximately 1 nm. Imaging was conducted under high vacuum to assess sidewall structure, tip morphology, and surface quality. The Zeiss EVO LS25 system, equipped with a tungsten filament electron source, offered the same magnification range (x1,000,000) and a resolution of approximately 3.49 nm. Sputter-coated samples were used throughout to ensure consistency across both platforms.

Mechanical characterisation

Mechanical characterisation is critical to understanding of device safety and performance. The equipment and methodology used for this characterisation is reported below.

Force station

Mechanical compression testing was performed using a Tinius Olsen Universal Testing Machine 1ST. The silicon MN samples were arranged into a square comprised of five linear 1x5 arrays. The tested groups included silicon SMNs, silicon HMNs, and polymer MNs. Compression was applied using flat aluminium platens at a controlled displacement rate of 0.01 mm/s. The maximum applied force was set to 5 N with a load cell capacity of 25 N and a force limit of 5 N to prevent damage exceeding the intended testing range, in line with that reported as appropriate for human skin insertion by Singh *et al.*, and Satti *et al.*, (234, 235). This method enabled evaluation of force-displacement behaviour and mechanical robustness under quasi-static loading conditions. MN samples were visually inspected *via* SEM post compression.

3.2.4. Out of plane silicon microneedles 100 mm fabrication

This subsection outlines the fabrication process flow for the production of silicon microneedles in an out of plane manner. The manufacturing process described below was performed on 100 mm wafers, and produced solid and hollow devices, depending on the inclusion of the bore etch.

Marker

A solvent clean (sonication in 100 ml acetone and IPA for 10 and 5 mins respectively) was performed on all wafers, followed by a 10 mins O_2 plasma ash. PE-CVD was used to deposit 50 nm Si_3N_4 on each wafers surface. The thickness of this was measured and confirmed using the ellipsometer.

Wafers were then spin coated with Ti Prime (recipe 1, Table 5) and baked for 2 mins at 120 ^oC. Wafers were spin coated with 5 ml AZ MIR 701 (recipe 2, Table 5). Coated wafers were softbaked (90 ^oC, 180 s) and allowed to rehydrate (2 mins rest) prior to hard contact UV exposure (150 mJ/cm^2) *via* the MA8 mask aligner utilising the marker glass mask (alignment marks found in Figure 9). A post-exposure bake (110 ^oC, 90 s) was performed, prior to a 1 min development in 2:1 AZ 726: deionised (DI) H_2O. Wafers were rinsed in DI wafer, and dried with a N_2 gun, before having CD and development checks across (centre, north, east, south, west) *via* the Keyence microscope.

Patterned wafers were etched using the ICP (200 nm Si_3N_4), following which a strip of residual PR was performed using P1316 (75 ^oC, 10 mins). Wafers were then rinsed in DI water and dried.

Bevel

A solvent and plasma clean was performed on all wafers prior to being spin coated with 5 ml AZ 125nXT-10A (recipe 3, Table 5). Resit was allowed to homogenise (5 mins) prior to a softbake (130 °C, 13 mins), after which they were rested again (5 mins rehydration). Coated wafers were exposed with using the bevel glass mask (Figure 10) with soft contact (1500 mJ/cm^2) and then developed in AZ 726 (4 mins). DI water rinses were performed, wafers were dried, and CD, development, and alignment checks were performed on the patterned wafers.

Wafers were mounted onto 150 mm carrier wafers (Section 3.2.1.2.2) and then loaded into the DSi-v™ and etched using an E2 etch recipe. Upon etch completion, the wafer was un-mounted from carrier, which was disposed of. Etched wafers underwent a PR strip, submerged in P1316 (70 °C) in two 30 min baths, prior to DI water rinses, and a solvent clean.

Smoothing

To reduce surface roughness of the bevelled surface, improve etch uniformity, and ensure a smooth surface for the deposition of photolithography, a smoothing etch was performed. Wafers were mounted to carriers, and a smoothing etch was performed using the DSi-v™, following which they were debonded and a solvent clean was performed on the device wafers.

Bore

SiO_2 (4000 nm) was deposited *via* PE-CVD on the topside (bevel side) of the wafer to produce a backstop for the bore etch. Wafers were pre-baked at 150 °C (10 mins) prior to spin coating 5 ml AZ 125nXT-10A on the backside of the wafer. Resist was allowed to homogenise for 5 mins prior to undergoing a softbake at 130 °C for 13 mins. The wafers were then rested and allowed to rehydrate for a further 5 mins. Coated wafers were exposed using the bore glass mask (Figure 11) under soft contact mode, with a dose of 1500 mJ/cm^2, and subsequently developed in AZ 726 for 2 mins. DI water rinses were carried out, the wafers were dried, and CD, alignment, and development checks were performed on the wafers.

Wafers were then mounted onto 150 mm carrier wafers using Crystalbond, loaded into the DSi-v™, and etched using switched etching. Upon completion of the etch, the device wafers were unmounted from their carriers, which were discarded.

P1316 (2x 30 min baths at 70 °C) was then used to strip residual resist from the etched wafers. DI rinses and solvent cleans were performed, followed by CD checks using the Keyence microscope.

Shaft

Wafers underwent a 10 minute dehydration bake prior to being spraycoated (topside) with AZ 4999 (recipe found in Table 6). Coated wafers were allowed to homogenise (5 mins) before a short soft bake (100 °C, 2 mins) and longer rehydration (2 hours). Wafers were exposed to UV at 2800 mJ/cm^2 using soft contact on the MA8 mask aligner, utilising the shaft glass mask. Wafers 3-5, 7, 9-10 used shaft mask version 1, and wafer 6 and 8 used shaft mask version 2 (Table 7). Post-exposure, a 10 minute submergence in AZ 400K was used to develop the shaft patterning. Wafers were rinsed in DI water and dried with compressed N_2.

An HF etch (BOE 7:1, 21 mins) was used, followed by 2x DI H_2O rinses, to remove the 400 nm SiO_2 from the topside of the wafer in areas not protected by the shaft-patterned PR.

Shaft-patterned wafers were mounted onto carriers using Crystalbond (3.2.1.2.2) and were loaded into the DSi-v™ where they were etched. Etch recipe R07 was utilised for wafers 3-6 and 9-10, and R08 utilised for wafer 7, with differences being an increase in the number of loops of switch etching utilised. A hybrid between the two was also trialled (R07.2) for wafer 8. Post-etch, device and carrier wafers were debonded, and the device wafer was submerged in P1316 for a PR strip (2x 30 min baths, 80 °C) followed by 2x DI H_2O rinses.

Table 7. A matrix of the wafer number, the device type produced, and the shaft mask and recipe number utilised

Wafer #	*MN Type*	*Shaft Mask*	*Shaft Etch Recipe*
3	HMN	V1	R07
4			
5			
6		V2	
7		V1	R08
8		V2	R07.2
9	SMN	V1	R07
10			

A second HF etch (BOE 7:1, 23 mins) was used to remove any remaining SiO_2, followed again by 2x DI H_2O rinses. To complete device fabrication, wafers were then rinsed in DI water and dried with compressed air.

Dicing

Device wafers were saw diced by DISCO HI-TECH EUROPE to release the MN arrays with the below specifications on die size (Table 8).

Table 8. The parameters and dimensions specified for dicing lanes

Parameter	*Value*
Wafer size	100 mm
Wafer thickness	1400 µm
Die dimensions	1650 x 7500 µm
Street width	600 µm

3.3. Experimental results

The experimental results reported in this chapter will cover each wafer sample produced *via* each etch recipe optimised, as well as mechanical characterisation. This section reports on the post-fabrication results of hollow devices produced *via* recipe R07 (wafers 3, 4, 5, and 6), R08 (wafer 7), R07.2 (wafer 8), in addition to solid devices produced *via* recipe R07 (wafer 9 and 10).

3.3.1. Visual characterisation

Results reported here pertain to the SEM images obtained post-fabrication, enabling comment on the quality of the devices produced. Comment will be made highlighting the fidelity of the features and the presence of any defects.

Hollow: R07

The below reports on the visual characterisation of hollow devices on wafers number 3-7. These devices were produced using shaft recipe R06.

Wafer 3

The wafer had areas of unetched silicon with lots of areas of artifacts across the surface (Figure 17). Pitting was present on the wall area as well as in some areas at the wafer base. Crystalbond used for bonding device to carrier wafer appeared to weep up and flow through bores, masking a wider area than required for the shaft patterning, preventing etching.

On devices that were etched, good height was measured (approximately 600 μm). Tip area was damaged during the etch, preventing the formation of a sharp tip, as the design intended. Over etching was present around the bevelled face of the needle where the Crystalbond would have met the wafer surface. Minimal residual wall was observed immediately behind the devices; however, it cannot be determined if the wall was present in areas which were masked by the Crystalbond. Minimal grass on the open area of silicon was observed.

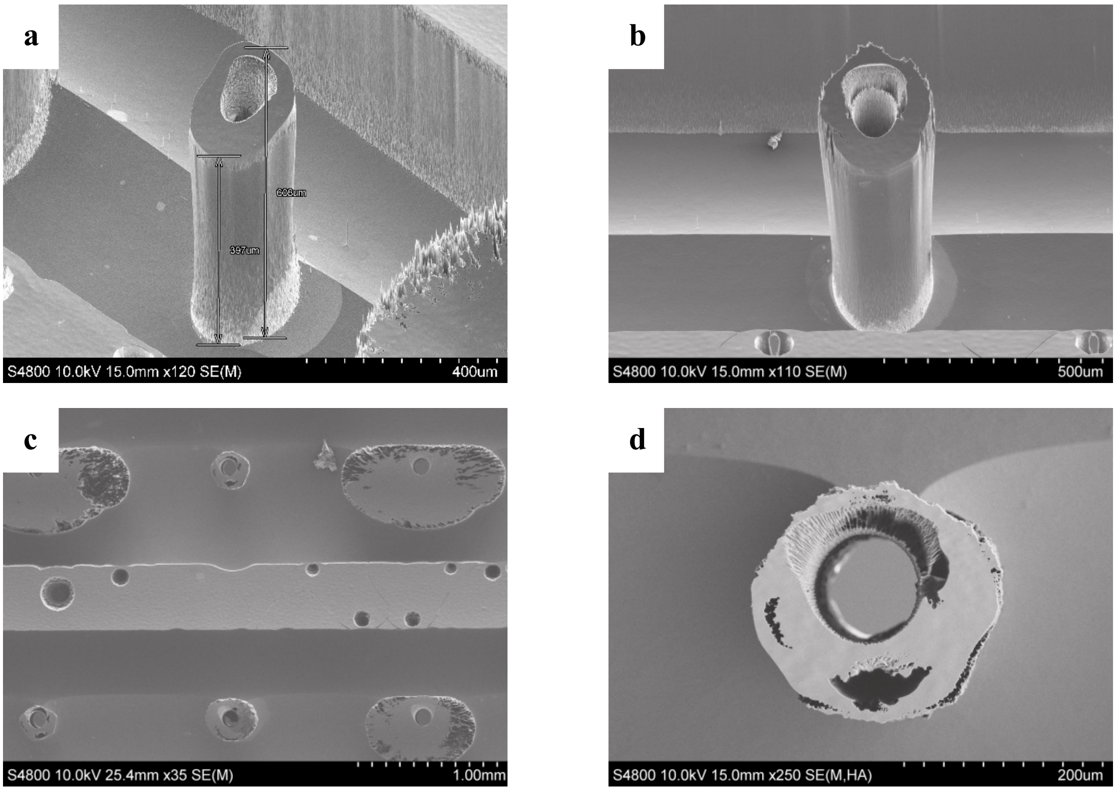

Figure 17. Scanning electron microscope images of wafer 3 post fabrication (a) full height device side on (b) full height device front on (c) six devices top down (d) one device top down. Scales can be seen on the bottom right of each image

Wafer 4

Device features and CDs were consistent across wafer 4, with consistent height (approximately 550 μm) (Figure 18). No pitting was observed. The bevelled face has minimal undercutting, and a sharp, defined tip was observed across all devices. A thin, short wall was present behind the devices in some areas, and absent in others, appearing sporadically across the wafer. No other grass was observed across the device wafer.

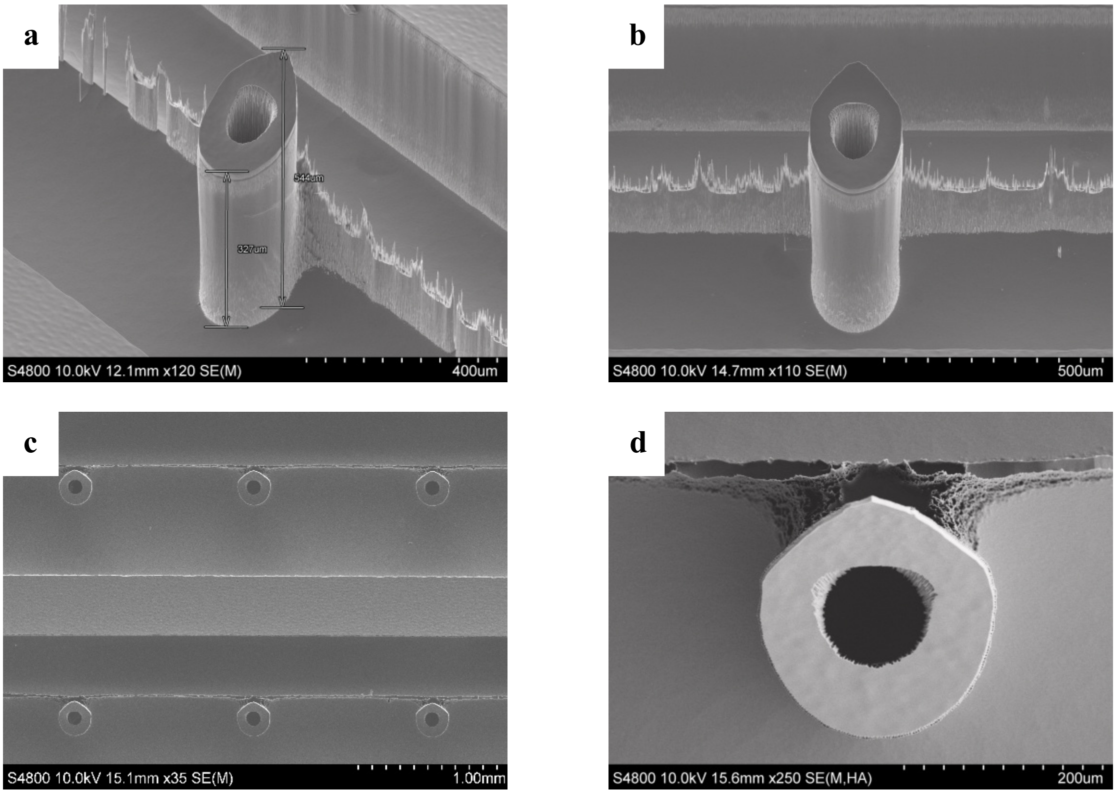

Figure 18. Scanning electron microscope images of wafer 4 post fabrication (a) full height device side on (b) full height device front on (c) six devices top down (d) one device top down. Scale for each image can be seen on the bottom right

Wafer 5

Wafer 5 showed a good quality etch across the entirety of the device wafer. A consistent height device was produced across the wafer, at approximately 600 μm (Figure 19). A consistent bevelled surface and tip sharpness was observed, with minimal bevel and shaft undercutting. A thin wall was present in some areas but was not consistently present. Very minimal grass was observed in the open area, with a clean etch observed across the majority of the wafer.

The use of the SiO_2 cap improved the protection of the bevel structure of the MN (Figure 20). These needles produced with the cap displayed a greater degree of control over the areas etched, reducing the over etching and undercutting of the PR, resultantly preserving the bore size and the encroachment of the silicon surface between the bore and the edge of the needle.

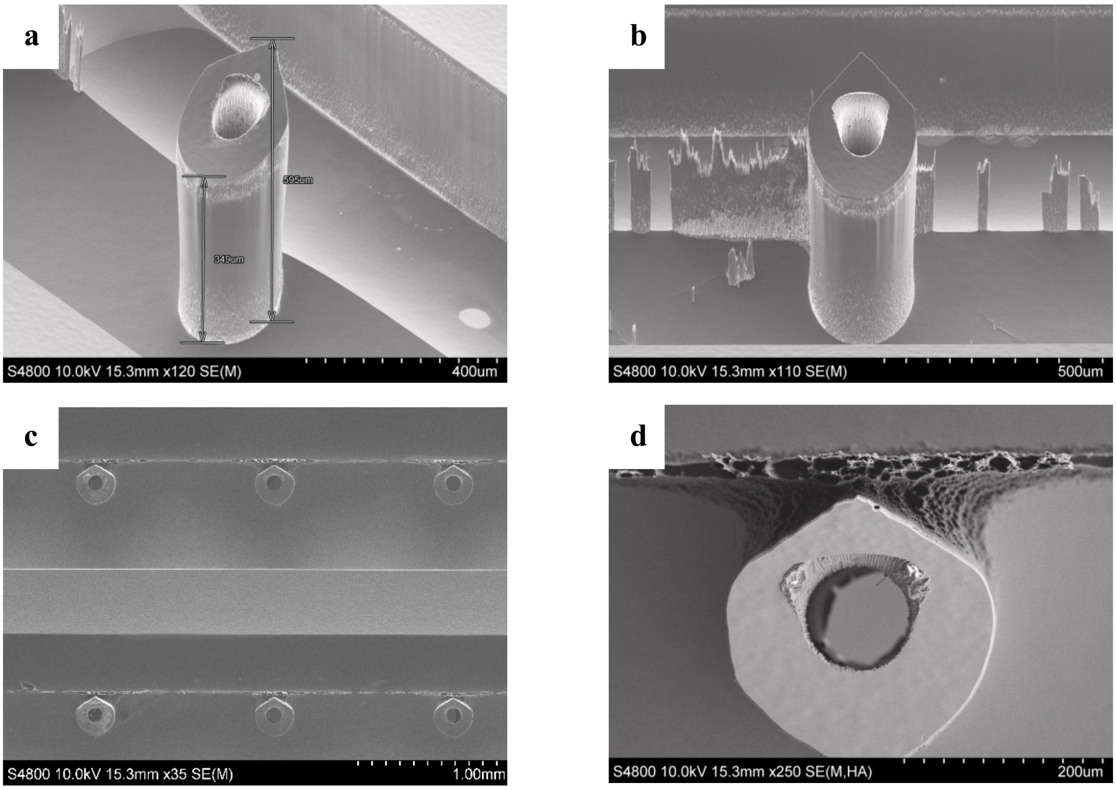

Figure 19. Scanning electron microscope images of wafer 5 post fabrication (a) full height device side on (b) full height device front on (c) six devices top down (d) one device top down. Scales can be seen on the bottom right of each image

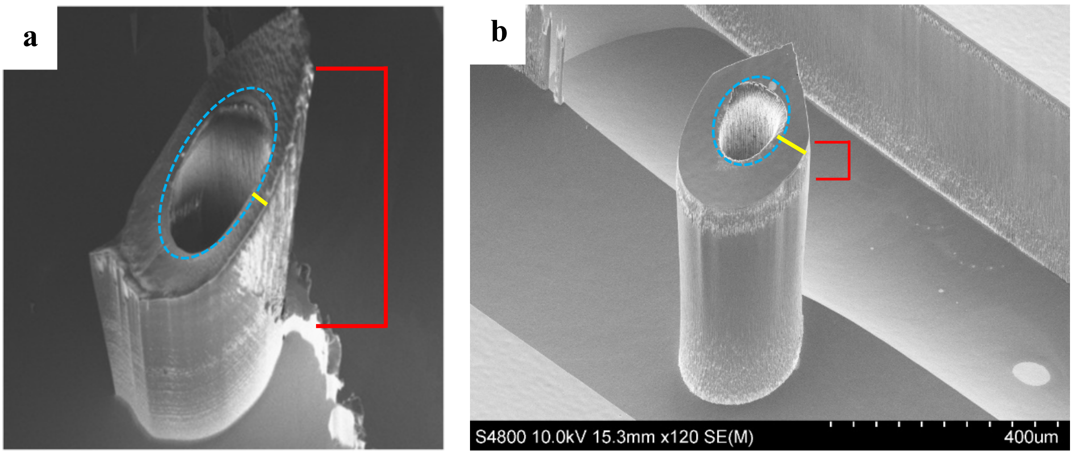

Figure 20. Scanning electron microscope images of a silicon microneedle produced (a) previously without an SiO_2 cap and (b) during this project with an SiO_2 cap. The blue oval represents the expansion of the bore, yellow bar representing the encroachment of the bore on the side walls, and red bracket highlighting the etch defects on the shaft

Wafer 6

Wafer 6 showed a consistent reduction in size with a shorter shaft height (< 400 μm) (Figure 21). Despite a consistent bevel profile and tip shape, the wall structure and grass was present almost continuously across the wafer, with it now reaching a greater proportion of the device height. The wall proved thin in some areas and was sporadically absent.

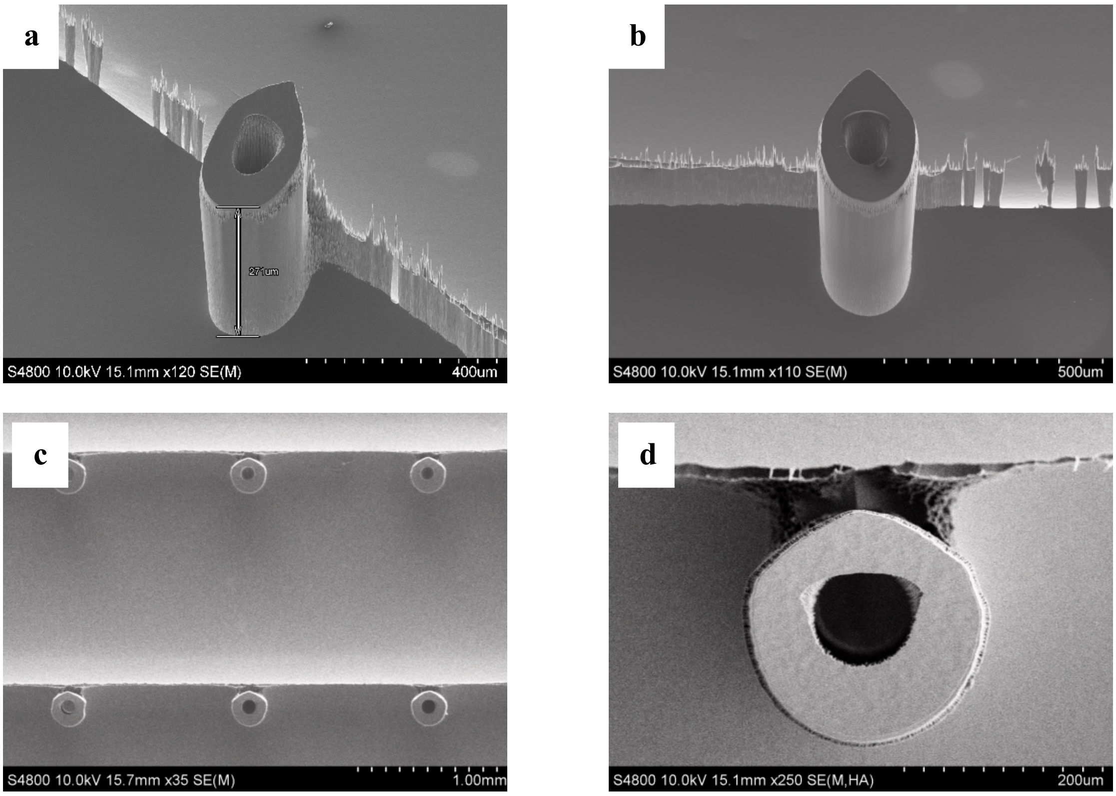

Figure 21. Scanning electron microscope images of wafer 6 post fabrication (a) full height device side on (b) full height device front on (c) six devices top down (d) one device top down. Scales can be seen on the bottom right of each image

<u>Hollow: R08</u>

The below reports on the visual characterisation of hollow devices on wafer number 7. These devices were produced using shaft recipe R08.

Wafer 7

A clean etch was observed across the entirety of wafer 7 surface. A greater height (approximately 680 μm) was observed across the devices, which presented with a slight taper on the shaft, narrowing at the base (Figure 22). A sharp tip was observed across all needles, however over etching resulted in a smaller area of the bevelled face with a thinner wall between the bore and bevel edge. No grass or wall was observed, and there were no other residual etch effects such as pitting observed.

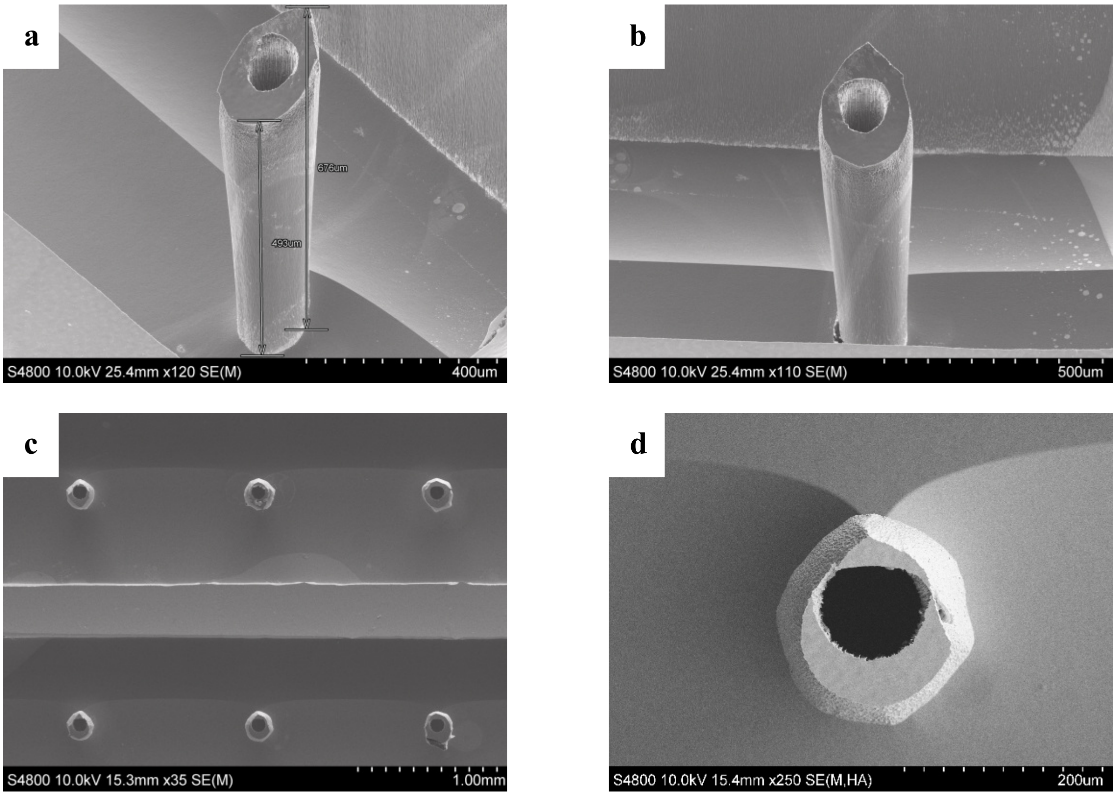

Figure 22. Scanning electron microscope images of wafer 7 post fabrication (a) full height device side on (b) full height device front on (c) six devices top down (d) one device top down. Scales can be seen on the bottom right of each image

<u>Hollow: R07.2</u>

The below reports on the visual characterisation of hollow devices on wafer number 8. These devices were produced using shaft recipe R07.2.

Wafer 8

Despite consistent height (approximately 600 µm), devices were enclosed by a tall wall with grass present along the ridge (Figure 23). The bevelled surface and sharp tip were well defined. The wall was present in half height in places, but its presence was consistent in some form. The backside of the device was attached to the wall. No tapering was present with minimal undercutting under the bevelled surface.

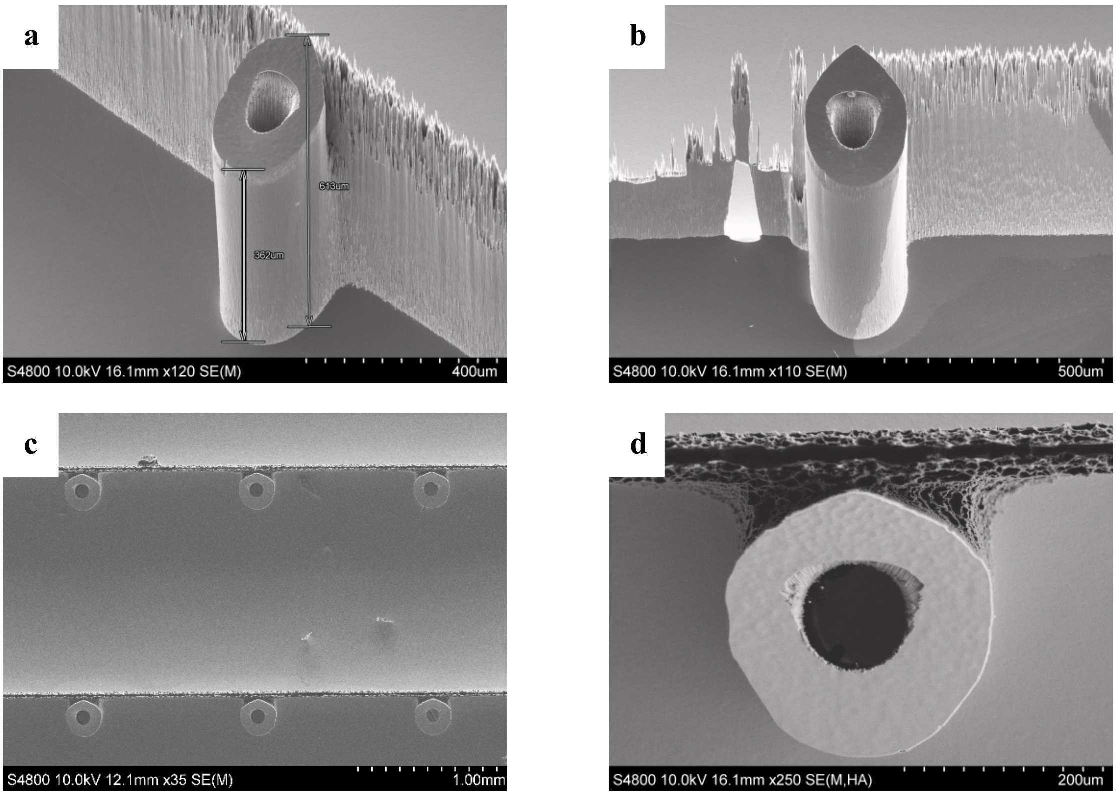

Figure 23. Scanning electron microscope images of wafer 8 post fabrication (a) full height device side on (b) full height device front on (c) six devices top down (d) one device top down. Scales can be seen on the bottom right of each image

Solid: R07

The below reports on the visual characterisation of solid devices on wafers number 9 and 10. These devices were produced using shaft recipe R07.

Wafer 9

Wafer 9 displayed a consistent and clean etch, with devices measured at approximately 560 µm in height (Figure 24). The bevel profile was consistent and clean, with very minimal undercutting and a clear tip. The shaft displayed slight tapering, with no wall present behind the devices and no grass across the open area.

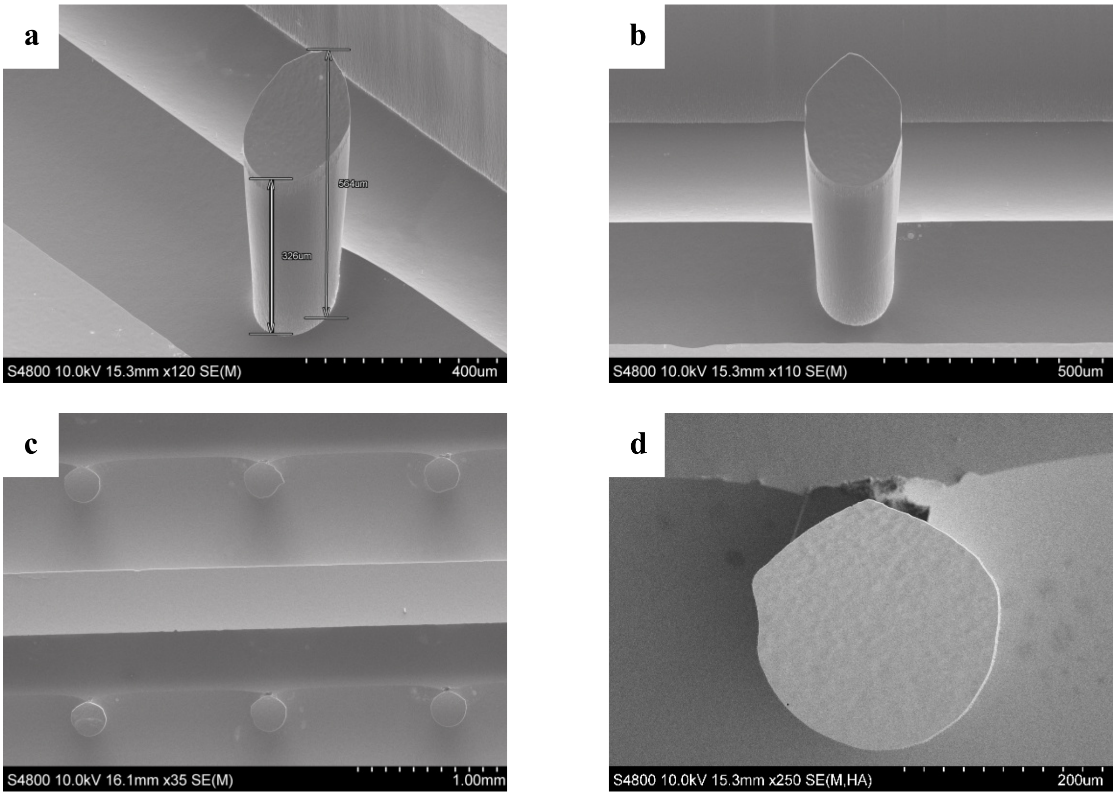

Figure 24. Scanning electron microscope images of wafer 9 post fabrication (a) full height device side on (b) full height device front on (c) six devices top down (d) one device top down. Scales can be seen on the bottom right of each image

Wafer 10

Wafer 10 produced no devices, despite a clear bevelled surface and shaft patterning (Figure 25). This shaft etch failed, resulting in grass across the wafers open area.

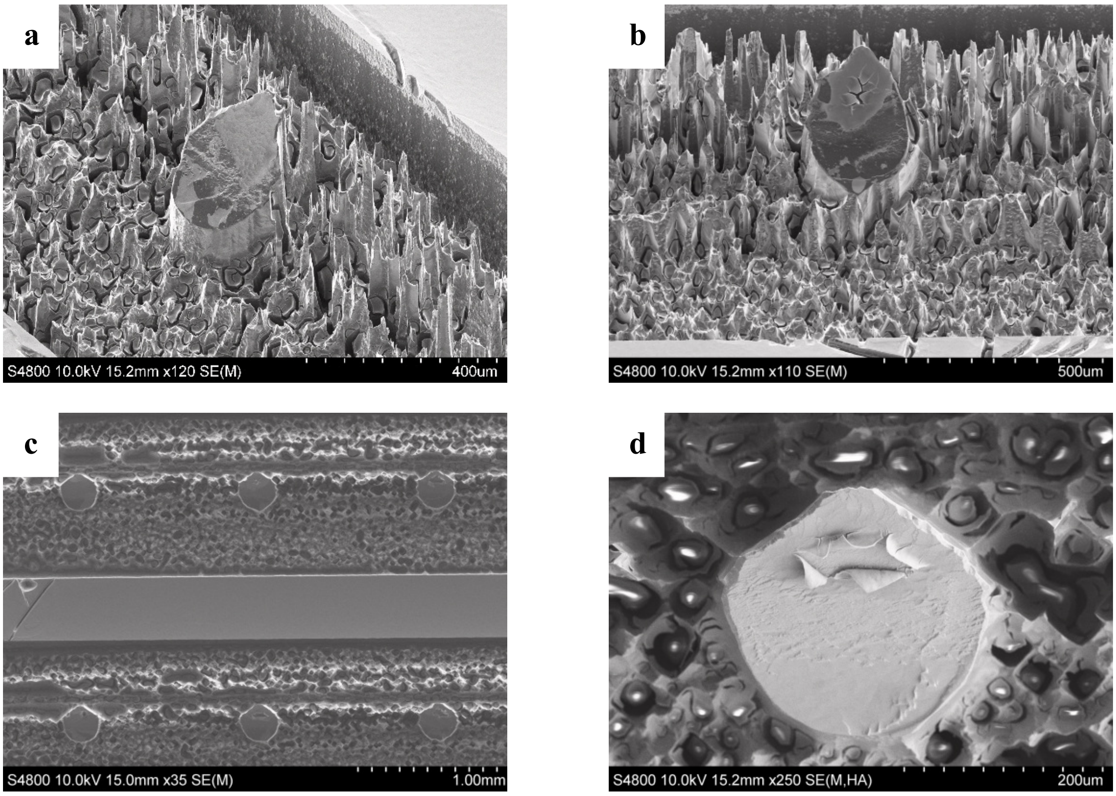

Figure 25. Scanning electron microscope images of wafer 10 post fabrication (a) full height device side on (b) full height device front on (c) six devices top down (d) one device top down. Scales can be seen on the bottom right of each image

3.3.2. Manufacturing yield

Manufacturing yield was assessed for both hollow and solid MN arrays across multiple wafers. Percentage yield was quantified at the individual needle level and at the array level, using two criteria: (i) arrays with ≥ 3 intact needles and (ii) arrays with all 5 intact needles (Table 9). The influence of shaft mask version and etch recipe was evaluated, and qualitative process observations were recorded during fabrication. The total number of individual needles and arrays possible was 1580 and 316 respectively.

Table 9. A matrix of the wafer number, device type, its fabrication route through the shaft etch, and the resultant yield. Yield is presented as a percentage, and has been calculated based on individual needle yield, and two types of array yield

Wafer #	*MN Type*	*Shaft Mask*	*Shaft Etch Recipe*	*Yield (%)*		
				Individual Needles	*Array (≥3 needles)*	*Array (=5 needles)*
3	HMN	V1	R07	13	11	3
4				86	88	82
5				38	36	28
6		V2		80	86	61
7		V1	R08	26	30	9
8		V2	R07.2	71	84	32
9	SMN	V1	R07	75	85	40
10				0	0	0

Hollow microneedles

HMN yield showed substantial variability depending on the shaft mask version and the etch recipe used. Wafers 3, 4, and 5 were processed using shaft mask version V1 with the R07 etch recipe. Wafer 3 demonstrated poor yield (13 %, 11 %, and 3 % for individual needles, ≥3 needle arrays, and 5 needle arrays respectively) due to Crystalbond adhesive weeping through the bores during mounting, which obstructed etching across much of the wafer. Although partially resolved in subsequent attempts, this represented a process limitation associated with the mounting of 100 mm sample wafers to 150 mm carrier wafers. Wafer 5 also yielded poorly (38 %, 36 %, and 28 % for individual needles, ≥3 needle arrays, and 5 needle arrays respectively), with uneven etching and incomplete bore formation observed in multiple regions. However, the quality of the complete arrays was high, with good consistent height, minimal wall present, and little to no grass. In contrast, wafer 4 achieved excellent yield (86 %, 88% and 82% for individual needles, ≥3 needle arrays, and 5 needle arrays respectively), with successful bore formation and good feature height. Importantly the wall observed surrounding the features was very thin or absent in some areas and was lesser than the height of the devices.

Improved consistency was achieved using shaft mask version V2. Wafer 6, processed with the same R07 etch, yielded 80 % of individual needles, 86 % arrays of ≥3 needles, and 61% of full arrays. However, needles were notably shorter due to the increased open silicon area in the V2 design, which slowed the etch rate. The wall feature was again very thin or absent, with minimal grass present. Wafer 8 was fabricated using mask V2 and the modified R07.2 recipe, which involved an increased number of etch loops (from 750 to 1000) to compensate for the higher open area. Although yield remained good at 71 % (needle level) and 84 % (arrays of ≥3 needles), the etch proved too aggressive, causing over-etching and feature distortion near wafer edges. This resulted in a reduction in yield for complete arrays (32 %).

Wafer 7, which used mask V1 with the more aggressive R08 recipe, yielded poorly (26 % needle, 30 % arrays of ≥3 needles, and 9 % full array). The etch produced significant structural damage tapered profiles of the needles, indicating that the R08 recipe was unsuitable for this geometry.

Solid Microneedles

SMN arrays were fabricated using shaft mask V1 and the R07 etch recipe. Wafer 9 achieved good yield (75 % needle, 85 % ≥ 3-needle arrays, 40 % full arrays), with successful formation of MNs across the wafer. The needles showed a good height of 554 μm but were slightly tapered, and no separation wall was present in the majority of cases.

Wafer 10, processed with identical mask and recipe conditions, yielded no usable structures. Yield was 0 % across all metrics. Post-etch inspection revealed the presence of silicon ‘grass’ and unremoved material between all needle sites, suggesting severe under-etching. This was attributed to possible contamination or residue left inside the DSi-v™ chamber, compromising plasma activity and etch uniformity.

3.3.3. Mechanical characterisation

Results reported in this subsection are those collected post compression testing. Device results are reported for silicon SMNs and HMNs, and polymer SMNs.

Compression testing

Results obtained from the compression testing for each device type are reported here in triplicate. All device types are presented individually, and collectively as the average of each material and MN classification and are depicted graphically.

Hollow microneedle array

Compression testing of HMNs demonstrated a good level of repeatability, especially between 0 - 2 N. The same trend was observed across each repeat, with distinctive jumps in force observed between 1 - 4 N (Figure 26).

Some debris was observed when SEM was performed on the compressed arrays, with a variation of degrees of damage identifiable (Figure 27). Some devices displayed no damage, however Figure 27d-e depicts notable damage to the tip specifically down a vertical cleave plane.

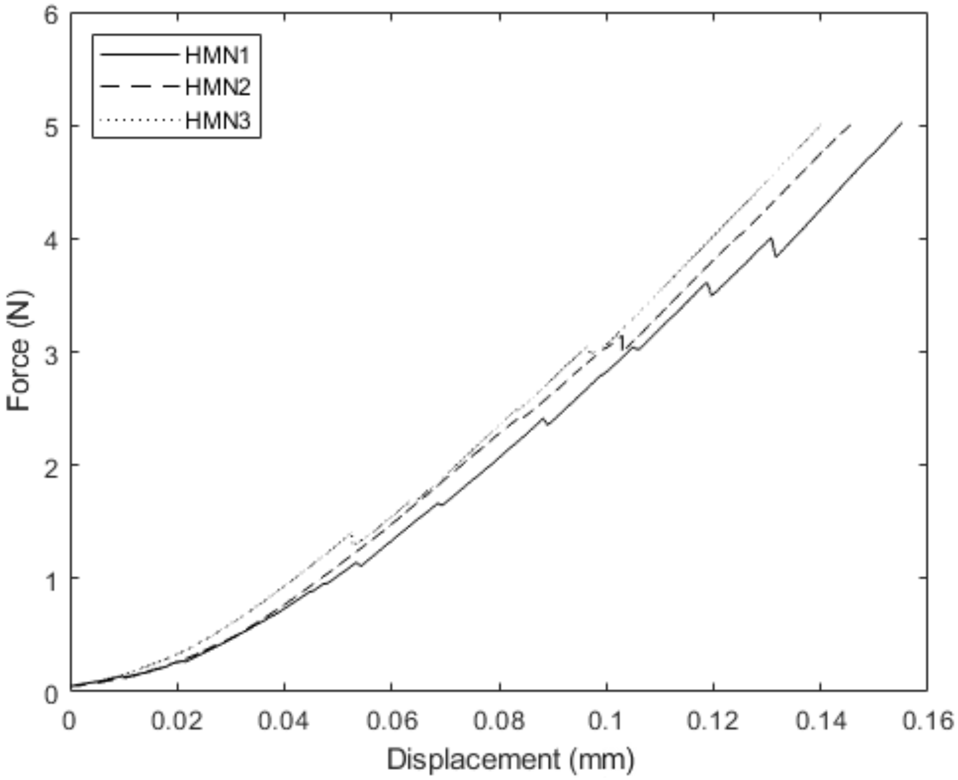

Figure 26. Force displacement curve for hollow microneedle (n = 3) array compression

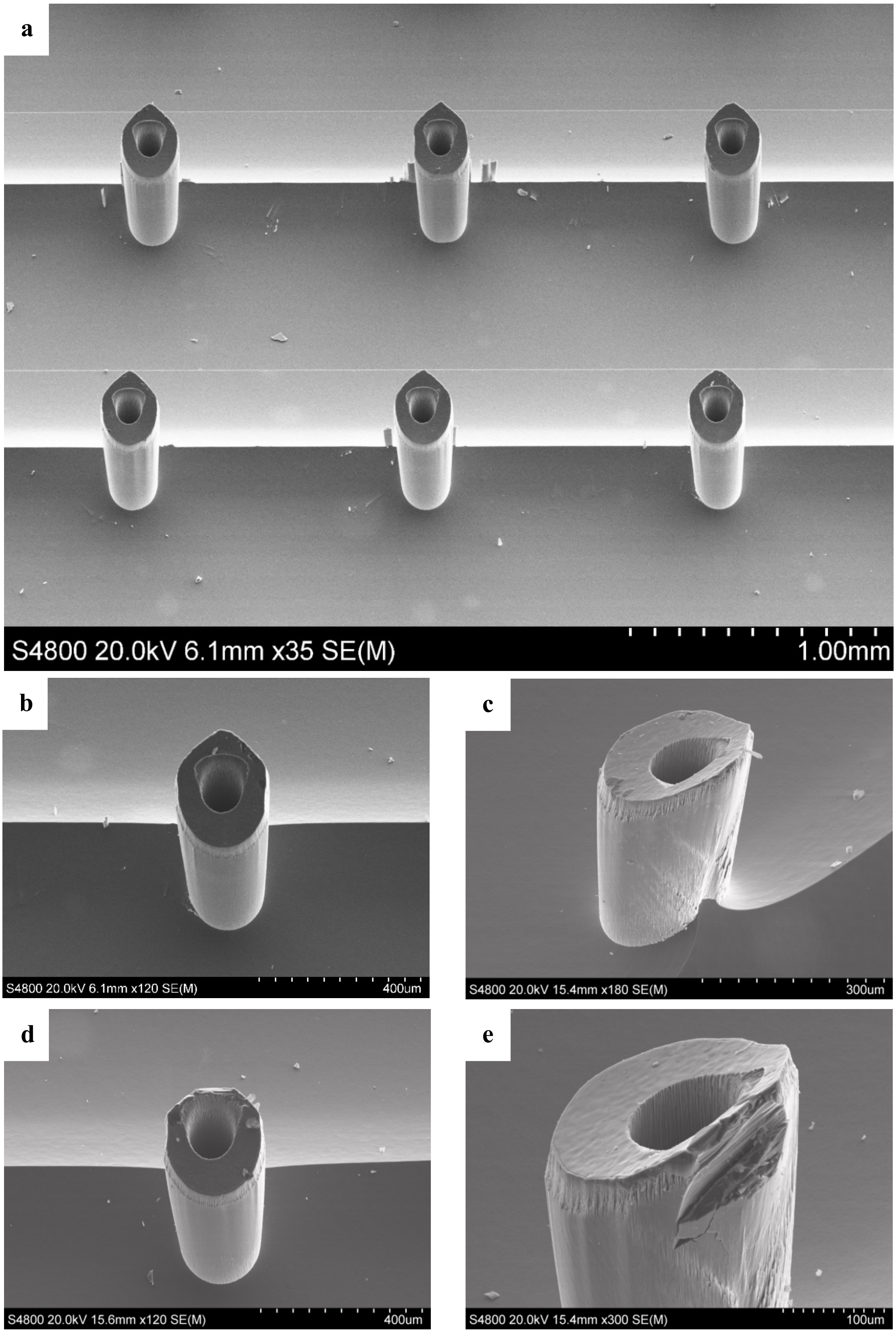

Figure 27. Scanning electron microscope images of hollow microneedle samples post compression (a) section of array (b-c) front and back of a needle with good integrity (d-e) front and back of needle with absent tip. Scales can be seen on the bottom right of each image

Solid microneedle array

The results of the SMNs compression testing demonstrated a greater degree level of repeatability from 1.5 - 5 N in comparison to the HMN devices, however there was greater degree of variation in earlier stages of the test (0 - 1.5 N) (Figure 28).The distinctive jumps in readings present in the HMN force-displacement trace are also visible in Figure 28. These notches and irregularities along the curve between 0.08 – 0.17 mm were consistent with micro-fracture events along the device shafts, consistent with brittle silicon under axial compression. Minimal debris was observed when the compressed samples were imaged using the SEM, with the thin wall observed sporadically (Figure 29). Very minimal damage was observed on the individual needle level, with a slight peeling of material on the tip side profile of the devices (Figure 29d-e).

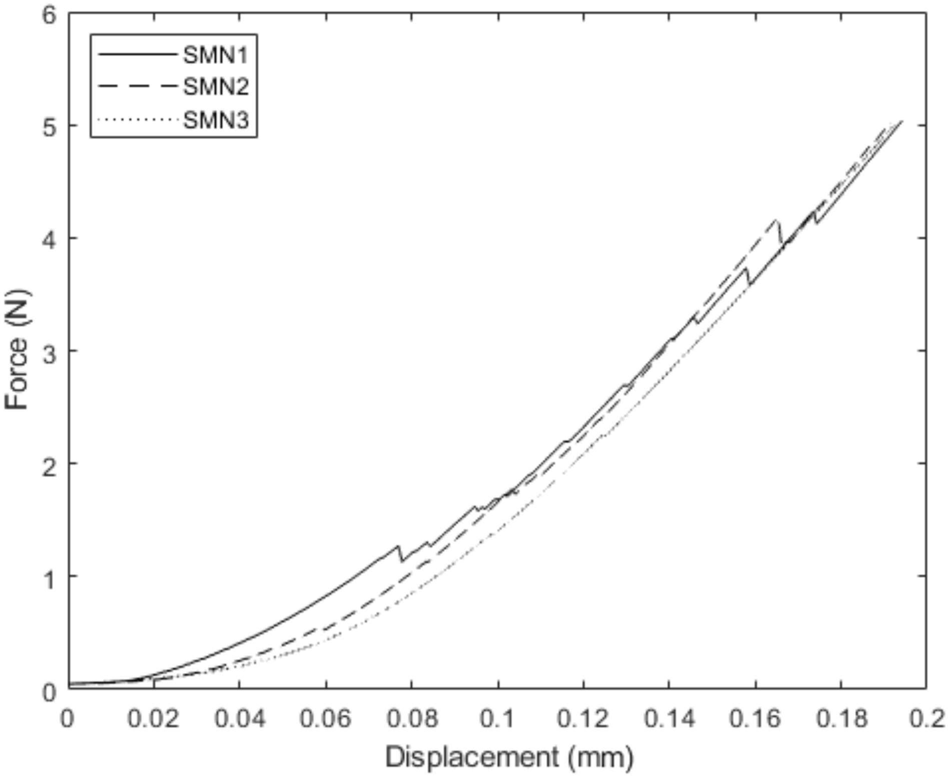

Figure 28. Force displacement curve for solid microneedle (n = 3) array compression

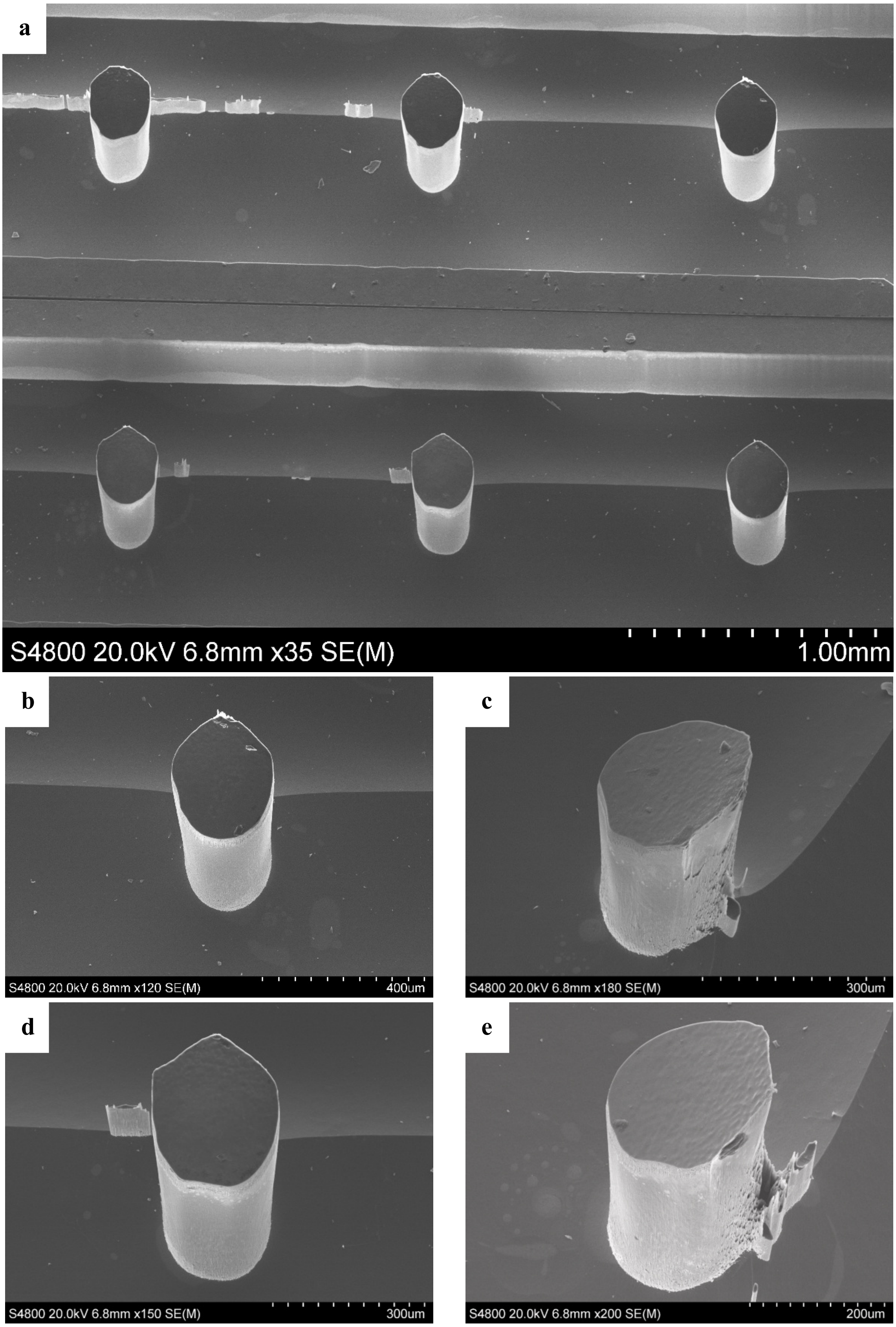

Figure 29. Scanning electron microscope images of solid microneedle samples post compression (a) section of array (b-c) front and back of a needle with good integrity (d-e) front and back of needle with cleave visible. Scales can be seen on the bottom right of each image

Polymer microneedle array

Polymer MN arrays demonstrated a repeatable response during the compression test (Figure 30). The traces for all three repeats present a largely linear trend, with minor differences in the slope of each repeat, likely due to minor variations in individual device stiffnesses. No catastrophic failure was identifiable in the traces, likely due to elastic bending deformation *i.e.,* ductile failure, rather than brittle.

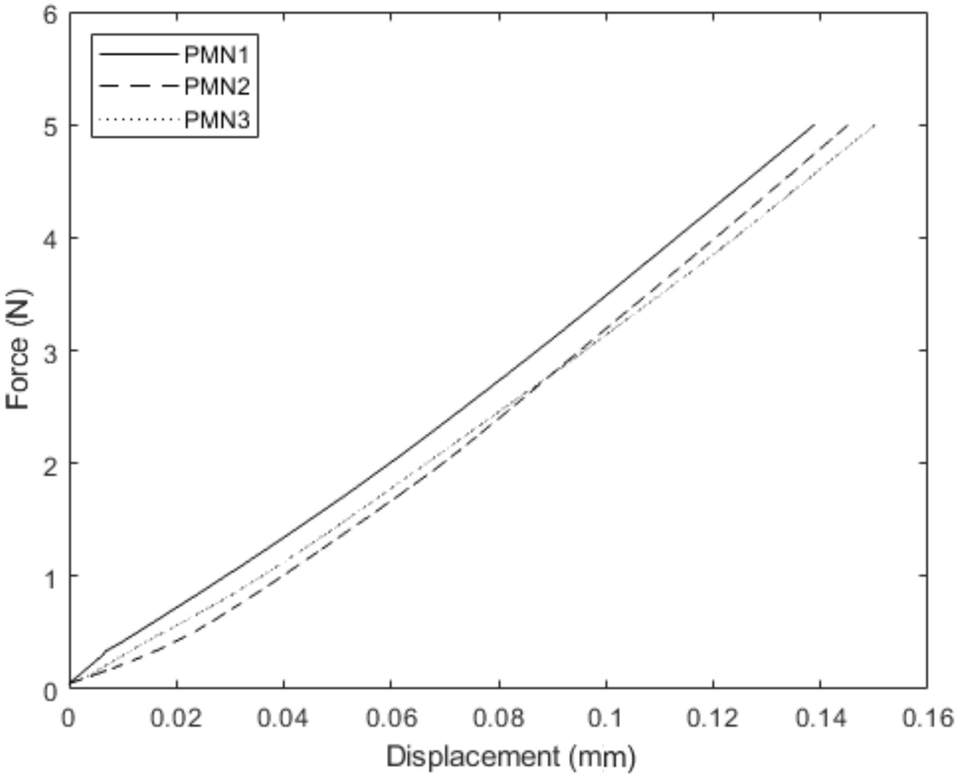

Figure 30. Force displacement curve for polymer solid microneedle (n = 3) array compression

Device comparison

When plotted collectively in Figure 31, the silicon HMN array perform similarly to the polymer MN array, however both silicon arrays present with characteristic staggered response across all repeats. The SMN devices responded most repeatably under 5 N force, but presented with a more exaggerated response under the continuous loading between 0 - 4.5 N.

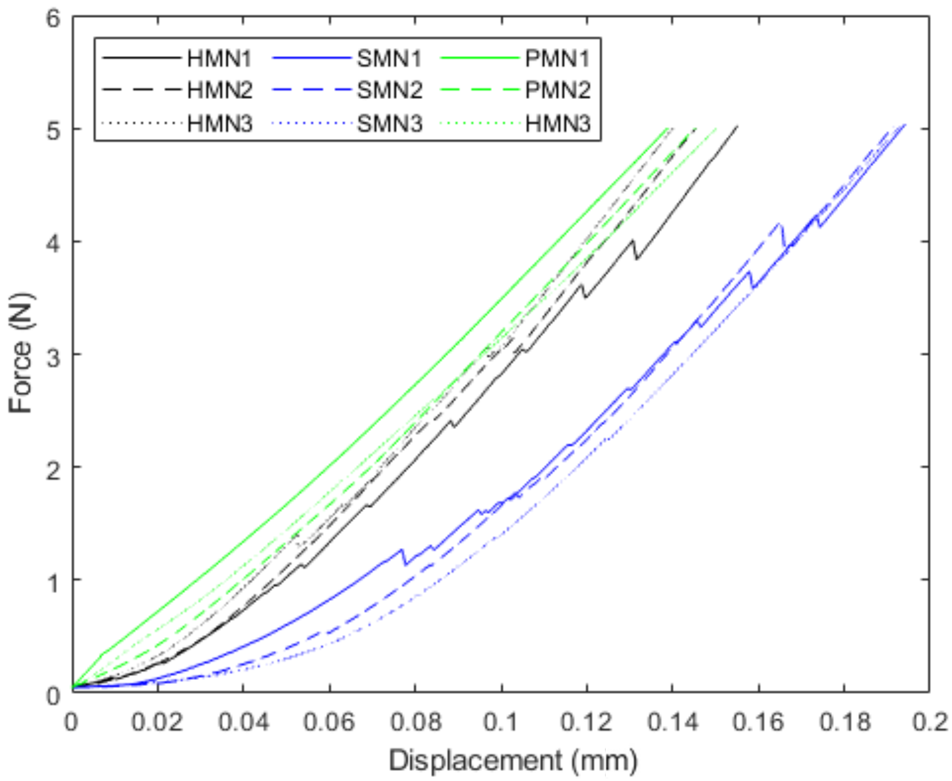

Figure 31. Force displacement curve of polymer (green), hollow silicon (black), and solid silicon (blue) microneedles

3.4. Discussion

The aim of this chapter was to produce a small batch of silicon MN (SMN and HMN) device wafers while systematically trialling variations in shaft mask architecture and etch recipes. Fabrication outcomes were evaluated through comprehensive visual and mechanical characterisation, enabling insight into etch quality, geometric consistency, and mechanical robustness. These data collectively informed process reproducibility and validated the suitability of the fabricated devices for subsequent experimental work in future chapters.

3.4.1. Influence of shaft mask iterations

In this batch process, two shaft mask variations were trialled in an attempt to improve on the original mask by removing the coffin style wall around each array in the second version, as visible in Figure 17d (Figure 12, Figure 13). As a result, Version 2, with no perimeter wall, had a greater open area of silicon, and therefore required alterations in the etch recipe to maintain final device structure. The larger open area of silicon has an impact on plasma loading, with a slower etch rate as a result of the dilution of the concentration of reactive ions *per* feature. Furthermore, etch uniformity, as well as etch depth, may be negatively impacted as a result. Therefore, modifications of the number of Bosch cycles in the etch recipe was required.

HMN device wafers fabricated using the original shaft mask version and etch recipe (wafers 4 and 5) produced needles with good height and consistent geometries, with minimal grass observed along the wall boundaries (Figure 18, Figure 19). Yield assessment revealed a good consistency and needle morphology when utilising the combination of the original version of the shaft mask and R07 recipe, with the reliable etch depth contributing to improved array integrity (Table 9). In contrast, HMNs manufactured on wafer 6 using shaft mask Version 2 and the original etch recipe (R07), produced significantly shorter needles, evidencing that the original recipes loop number to produce insufficient etch depth when the open area of silicon was increased (Figure 21).

A more aggressive etch (R08) was applied to wafer 7, masked with shaft Version 1 patterning, which produced a clean etch with very minimal grass, and notably taller devices (Figure 22). However, the increased etch loops resulted in a tapered profile of the devices. This was potentially due to mask erosion and excessive lateral etching, which is reported widely in the literature (236). In compensation for the reduced etch rate, an intermediate recipe (R07.2) was trialled (wafer 8), which, despite producing adequate height devices, produced extensive grass along the device line, potentially as a result of the accumulation of the deposited polymer (Figure 21, Figure 23). HMN device wafers fabricated using Version 2 of the shaft mask resulted in either under-etched needles with poor height (wafer 6) or significant grass artifacts (wafer 8) (Figure 23). Both of these effects substantially limit their suitability for further characterisation and testing. Solid devices were fabricated exclusively using the original mask and etch recipe (Version 1, R07), yielding devices of consistent height and minimal artifacts (Figure 24).

While shaft Version 2 was preferable from a design perspective due to its simplified geometry and absence of isolating walls, its increased open silicon area necessitated further and more precise etch tuning for future scalability. However, for the current batch, further optimisation was not essential, as the saw dicing lanes utilised during array dicing were aligned along the wall regions.

3.4.2. Yield outcomes

A wide range of percentage yields were calculated in this batch process, ranging from 0 % – 88 % and 0 % – 82 % for arrays with ≥3 and 5 needles respectively (Table 9). Although unideal from a manufacturability perspective, key learnings were made which should be taken forward when scaling up production. Root causes of poor yield such as Crystalbond adhesive weeping (wafer 3) will inherently be eradicated upon scale-up, as the requirement for wafer-to-carrier mounting will not be necessary (Figure 25). Notably, there were significant failures in yield, such as wafer 10 with 0 % success, which arose due to poor etch chamber cleaning leading to contamination due to dual processing usage: an easily rectifiable issue ahead of scale-up (Table 9). Despite these occasions of low yield, wafers 4, 6, 7, and 9 presenting with > 80 % yield at the ≥ 3 needle level, and wafer 4 presenting with > 80 % yield at the 5 needle level (Table 9). This represents successful proof of concepts for future scale-up activities as well as producing a rich sample base for characterisation and investigation in future chapters.

3.4.3. Mechanical characterisation

Mechanical testing of the MN arrays revealed clear differences in performance under compression between the three device types. Each device type, in a 5x5 array, was subjected to uniaxial compression, and force-displacement data were collected under a nominal 5 N force. This value was selected based on precedent in the literature and represents a conservative estimate of the force achievable *via* thumb pressure (234, 235). Prior to discussing the mechanical characterisation of these devices, it is important to acknowledge that the compression testing of MNs on a rigid surface is not identical to loading during skin insertion. Insertion of devices within a clinical setting involves deformable tissue, friction, and cutting forces, all of which cannot be mimicked in this study design (115, 237). This context is critical, as it may overestimate the mechanical load on the devices, resulting in failure which may not be seen during patient usage. Despite this, the methodology used for the mechanical testing of the MN devices was the appropriate approach to identify failure modes in isolation from biological compliance (115, 237). The influencing factor of tissue compliance will be addressed *via* the inclusion of phantoms in Chapter 4.

The polymer MN arrays exhibited the highest overall stiffness and load-bearing capacity, with all replicates displaying steep, linear force-displacement profiles and failure loads exceeding 5 N (Figure 30). This linear behaviour has been previously reported to arise from the elastic response of the polymer material, with bending observed as the predominant failure mode rather than brittle fracture (238). In contrast, HMNs showed intermediate stiffness and higher deformation capacity prior to failure (Figure 26). The SMNs demonstrated the lowest stiffness and more gradual force accumulation (Figure 28). Surprisingly, these trends suggested that both HMNs and polymer MNs had superior mechanical robustness under axial loading compared to SMNs (Figure 31).

However, a more critical assessment of the force–displacement behaviour suggests that the apparent superiority of HMNs may be somewhat artificial. As all compression testing was performed against flat aluminium platens rather than into skin or a compliant substrate, the loading conditions were not physiologically representative. The sharp hollow tips of HMNs likely fractured early in the compression cycle, which would have shifted the applied load onto the broader, blunt shaft. This redistribution of force may have resulted in a smoother or more repeatable rise in the force response, not because the device was more robust, but because the tip, being the most fragile feature, had already failed. In contrast, the SMNs retained their intact tips throughout loading, which led to greater variability in force traces due to sustained stress concentrations at the tip apex (Figure 29). Therefore, the perceived robustness of the HMNs under axial compression may in fact reflect early tip breakage and not a superior structural integrity. The observed jumps in the traces of both silicon device types reflect progressive fracture of the devices, as opposed to a single more catastrophic failure event (Figure 27, Figure 28). Minor fabrication imperfections and variations may have contributed to small geometric differences, and are therefore likely responsible for non-uniform loading, which in turn caused the fractures identifiable by the notches.

Visual examination of post-test devices under SEM confirmed distinct failure mechanisms. HMNs frequently exhibited localised fracture down the plane between the tip and the back of the device, consistent with brittle failure due to stress concentration (Figure 27). SMNs also showed brittle fracture features, with a higher incidence of partial shearing was noted (Figure 29). In contrast, the polymer MNs primarily failed *via* ductile deformation or blunting at the tip. These observations were consistent with the known and previously reported material properties of silicon (brittle) and polymer (more ductile) and suggested that design factors such as shaft thickness and tip sharpness also played a role in failure localisation (238-240).

Importantly, all device types fabricated in this study withstood initial compressive loading without immediate catastrophic failure, demonstrating that the small-batch fabrication methodologies produced MN arrays that were structurally sound and mechanically testable. Specifically, both SMNs tolerated compressive loading up to test completion (5 N) without significant mechanical compromise, a conservative load range compatible with skin insertion forces reported in previous literature (234, 235). This supported the suitability of these devices for further functional testing, including *ex vivo* insertion and penetration trials.

The polymer devices were fabricated as a monolithic 5x5 array, while the silicon devices, originally produced as 1x5 arrays. Therefore, to enable valid mechanical comparisons, the silicon devices were arranged to form equivalent 5x5 configurations. This approach controlled for differences in array layout and spacing, allowing axial stiffness and failure behaviour to be attributed to needle architecture and material properties rather than array footprint or any distribution effects. Although the monolithic polymer MN baseplate may have offered marginally greater interfacial stiffness than the assembled silicon array, the structural performance of the HMN and SMN arrays was sufficient to allow a comparative analysis.

Collectively, these results demonstrated that the DRIE-based fabrication process yielded HMN and SMN arrays that were not only structurally complete but also capable of withstanding the mechanical demands of skin insertion. Further, the data confirmed that the methodologies used in this study facilitated fair comparative evaluation between HMNs, SMNs, and polymer MNs, thereby establishing a strong foundation for the subsequent functional assessment of insertion performance and strain generation in Chapter 4.

3.4.4. Future recommendations for upscale

Several refinements could enhance the scalability and translational potential of the fabrication process described in this study. First, the elimination of the coffin-style wall structure around individual arrays is recommended for future mask iterations. Whilst it aided in dicing alignment for small-scale production, it occupies valuable and expensive wafer real estate. Removing this structure would simplify the layout and increase the available area for device placement, though it would require alternative strategies for dicing alignment in large-scale manufacturing.

Second, the reliance on Crystalbond mounting limited both process yield and reproducibility, rendering the process manual and engineer dependent. Scaling up to 150 mm wafers would not only allow elimination of manual mounting steps but also offer greater compatibility with industry-standard MEMS workflows. The use of larger wafers would not only increase potential yield, but also reduce handling variability, aligning with established semiconductor processing infrastructure.

Additionally, future device iterations could explore altered bore positioning and inter-needle pitch spacing to determine their effect on mechanical performance under compressive loading. Modifications such as these may allow more systematic optimisation of HMN designs for enhanced robustness and insertion performance and allow investigation of the ‘bed of nails’ theory.

Finally, although the DRIE process was inherently complex and equipment-intensive, this study has demonstrated its suitability for fabricating MN devices. The broader

MEMS industry provides a robust precedent for its scalability, indicating that with appropriate process refinement, DRIE can be effectively employed for higher-throughput production of both SMN and HMN arrays.

4. Chapter 4: Insertion Mechanics

This chapter reports the development of a novel methodology to examine the insertion mechanics of MNs in comparison to hypodermic needles. Measurements were obtained in the form of force-displacement data and visual strain mapping to characterise the strain induced during penetration at key stages of insertion.

4.1. Introduction

The introduction for this chapter serves to provide context surrounding the current methodologies utilised within the field of assessing MN performance as a device which punctures the skin, as opposed to focusing on their drug delivery function. This will highlight the need for quantitative methodologies and will provide literature based evidence for the appropriate selection of a digital image correlation (DIC)-based methodology.

4.1.1. Current pain assessment methodologies

The traditional and current gold standard for assessing the pain experienced following medical device usage is the Visual Analogue Scale (VAS) (241, 242). Widely used for its simplicity, its ease of implementation has facilitated its popularity within the medical field. The VAS, available in various forms, relies entirely on patient self-reporting and personal perception, and is therefore widely acknowledged to be subjective (243, 244). Variability introduced by psychological, contextual, and environmental factors makes it difficult to standardise across studies and populations (243). In an effort to address the limitations of the VAS, alternative methodologies have been developed, such as the Sensation/Pain Rating Index (SPRI), which aims to enhance descriptive detail by separating intensity from quality of pain and incorporating a range of pain descriptors (*e.g.,* sharp, throbbing, tingling) (245). Despite this, the SPRI still suffers from the inherent subjectivity of self-reported measures. It cannot account for individual variability, response bias, and non-linear perception between individuals, proving quantitative comparisons difficult (245, 246). These limitations represent significant obstacles during early-stage medical device development and evaluation, where objective measurement is preferable, either as a replacement for or complement to subjective feedback.

4.1.2. Justification for objective strain-based assessment

Within both research and regulatory contexts, there is growing interest in identifying objective physiological correlates of pain to complement or potentially replace traditional subjective assessment methodologies. Mechanical strain in skin tissue during device insertion is a promising candidate, due to its direct interaction with sensory structures known to mediate pain perception (247, 248). This physiological basis is supported by the presence and function of specialised mechanoreceptors within the skin that transduce mechanical strain into neural signals implicated in pain perception (249-251). Merkel cells, predominantly located in the basal layer of the epidermis between 150 - 900 µm beneath the skin surface, are closely associated with mechanoreceptors and other nerve endings (252, 253). These cells convert localized, sustained skin strain (micro-deformation) into electrical signals that are relayed to the brain, contributing to tactile and pain perception (252, 253). In contrast, other mechanosensitive nerve endings, such as Ruffini corpuscles found deeper in the dermis ranging from 200 - 1500 µm beneath the skin surface, respond primarily to larger-scale skin stretch and sustained strain (macro-deformation) (254). The activation of these sensory structures by mechanical strain contributes to the sensation of pain (255).

Emerging experimental evidence demonstrates that mechanical strain can directly trigger neural excitation in these receptors, supporting a link between strain and pain perception (256). The responsiveness of mechanoreceptors to subtle, small-scale tissue deformations underscores the need for accurate, localised strain assessment methodologies like DIC. Unlike subjective pain scales, strain-based assessments such as DIC provide objective, continuous, and reproducible data that are not affected by individual psychological or contextual factors. Consequently, measuring mechanical strain offers a valuable, quantifiable indicator that contributes to the perception of pain and is particularly suited to early-stage medical device evaluation. Furthermore, strain mapping enables localisation of areas experiencing the highest deformation, giving insight into potential pain-inducing sites and device-tissue interactions (248). Incorporating objective strain metrics can support the development of design criteria and regulatory standards for minimally invasive devices, ultimately expediting their development, improving their safety and efficacy, and accelerating their regulatory approval.

4.1.3. Relevance to microneedles and hypodermic needles

Both hypodermic needles and MNs interact with Merkel discs, mechanoreceptors located predominantly in the basal layer of the epidermis approximately 50 - 100 μm below the skin surface, which contribute to tactile and pain perception (48). Hypodermic needles, such as the commonly used 25-gauge (G) devices, penetrate well beyond the epidermis and dermis, reaching into the deeper dermal and hypodermis/SC layers. At these depths, they engage larger myelinated Aδ and unmyelinated C nociceptive fibres, as well as free nerve endings distributed throughout the dermis, which are principally responsible for the transmission of sharp and burning pain sensations (Figure 32) (257). Additionally, deeper insertion with hypodermic needles may sometimes stimulate Ruffini endings, located in the dermis at depths ranging from 200 to 1500 µm, which respond to skin stretch and sustained pressure (258).

With MNs designed to facilitate much shallower insertions, they typically penetrate only the stratum corneum and upper viable epidermis to depths of approximately 100 to 900 µm beneath the skin surface (259). This limited penetration allows MNs to largely avoid the nociceptor-rich dermal layer where most pain-mediating nerve fibres reside. Microneedles, typically less than 1 mm in length, are confined to interacting with the *epidermis* and *dermis*. Contrastingly, 25-G hypodermics can extend to 16 mm, penetrating through the dermis and into the SC tissue (hypodermis). These varying depths result in marked different modes of tissue interaction, providing a strong physiological basis for the consistently lower pain responses reported during MN applications.

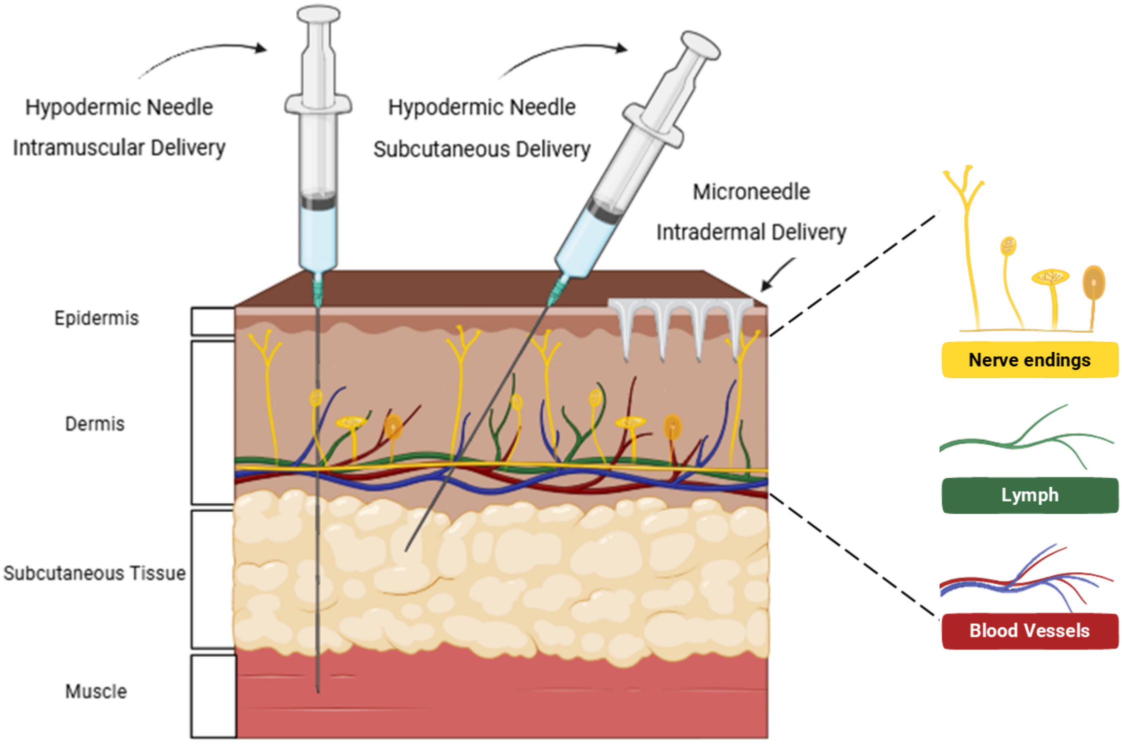

Figure 32. Schematic of layers of the skin, various parenteral delivery routes, and additional nerve, lymph and blood networks. Adapted from (57)

As previously established in subsection 4.1.1, subjective pain reporting is confounded by perceptual bias, particularly the common association of larger needles with greater pain, and thus direct comparisons between MNs and hypodermic needles are inherently limited. This context presents a strong use case for the application of objective, quantifiable proxies such as mechanical strain, measured *via* DIC, to evaluate device-tissue interaction. The use of strain-based metrics offers a validated and reproducible alternative to overcome the limitations of subjective sensation assessment in this comparison.

Strain mapping has grown in interest within the field of MNs in recent years, as attention turns to the MN-skin interactions, however, thus far remains largely within the modelling domain. Notably, Potts *et al.*, (2022) investigated the effect of needle pitch on strain accumulation during the indentation phase of needle insertion, reporting that pitches below 3 mm resulted in non-uniform forces across individual needles in both 2- and 9-needle arrays (260). Although the authors acknowledge that their analysis was limited to the indentation stage and did not encompass full penetration, this research highlighted the influence of array geometry and arrangement on local strain, as assessed using the finite element method. This research is one of a growing number which utilise finite-element to quantify the interactions between MNs and their various geometries, and skin. Studies reported by Shu *et al.*, (2021) have focused on using finite element to model the impact of pretension on reducing penetration force and local deformation, with a 10 % pretension reported to reduce penetration force and deformation by 13 % and 22 % respectively (261). However, only rigid materials were modelled here due to the replication of stainless steel arrays, and this falls short of including the variation which would come from the use of other needle types such as polymer. In more recent years, they further reported that skin deformation alone reduced transdermal insulin penetration by 25 %, while the incorporation of strain effects further decreased the overall permeation by over 45 % over 24-hours (262). These studies have collectively enhanced the field's comprehension of MN-skin interactions and mechanics; however, most findings remain model-driven. Experimental approaches, such as DIC, offer a means to complement existing computational models and provide validation for theoretically predicted strain.

4.1.4. Introduction to digital image correlation

DIC is a non-contact, optical measurement technique that utilises pattern recognition algorithms to track surface displacements during mechanical deformation, from which it calculates full-field strain maps (Figure 33) (263). Stereo-DIC specifically employs two synchronised cameras, which facilitate image capture from different angles and resultantly enable a three-dimensional reconstruction of the surface geometry and deformation (264). This stereo approach allows precise measurement of both in-plane and out-of-plane displacements, yielding highly accurate 3D displacement and strain fields with micrometre-scale spatial resolution and sub-pixel displacement sensitivity (265). Sub-pixel displacement refers to the detection of pixel movements which are smaller than the camera's resolution. This is possible as, unlike image registration, DIC uses a correlation within small, unique subsets of speckles to estimate the most probable displacement, enabling subtle, sub-pixel displacements to be captured (263, 265).

Stereo-DIC requires a high-contrast speckle on the specimen surface, which provides a unique pattern for the correlation algorithms to track during deformation (264). The technique then compares images captured before (reference images) and during mechanical loading (deformed images) to compute displacement vectors in three dimensions, from which detailed strain maps of the surface deformation can be derived.

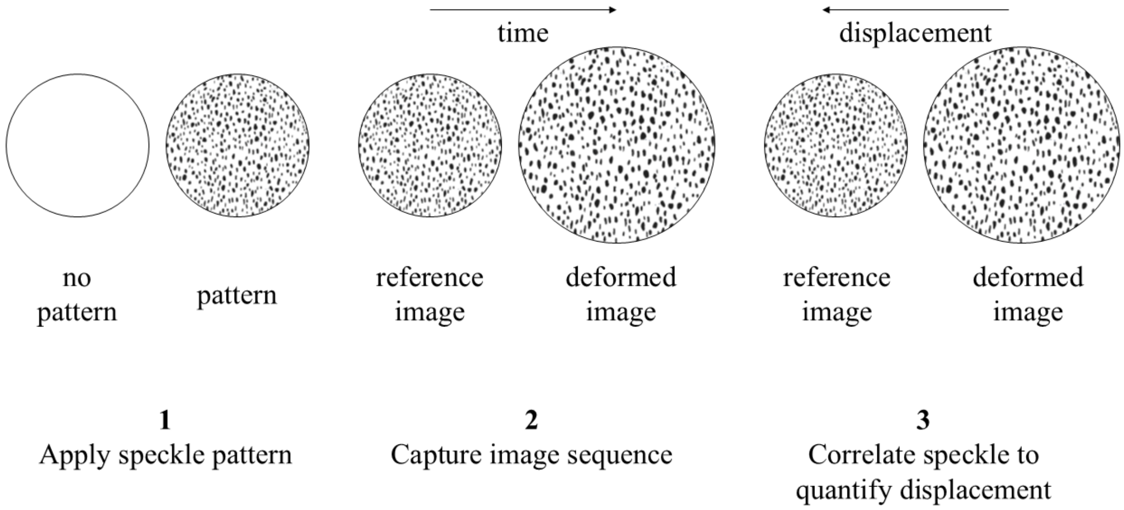

Figure 33. Schematic visually depicting the process of using speckle patterns to correlate strain as used by digital image correlation

The enhanced spatial accuracy offered by stereo-DIC, and its ability to measure out-of-plane motions, make it particularly well-suited to biomechanical investigations of soft tissues and skin-mimicking phantoms. In the context of MN and hypodermic needle insertion studies, stereo-DIC enables objective characterisation of small-scale localised deformation and strain progression during device insertion, providing insights into the mechanical interactions at the device/skin interface which underpinning both device insertion dynamics and associated sensory responses.

Although stereo-DIC has been widely applied in materials science and engineering for complex deformation analyses, its specific use in quantifying strain induced by medical device insertions remains relatively underexplored (266). Given its ability to capture full-field, time-resolved 3D strain distributions, stereo-DIC offers significant potential to advance understanding of the mechanobiology of device-induced strain and improve assessment methodologies beyond subjective scales.

4.1.5. Study aim and scope

This study employs stereo-DIC to measure the strain generated during the insertion of two distinct medical devices, a standard 25-G hypodermic needle and a 1x5 array of silicon HMNs, and allow their objective comparison (Figure 34). By capturing full-field, three-dimensional strain maps throughout the insertion process, the study characterises how the two devices differ in their mechanical interaction with a skin-mimicking substrate. Particular attention was given to differences in strain magnitude, spatial distribution, and temporal progression during insertion. The experimental design, methodology, and results reported in this chapter have been peer reviewed and published in Frontiers in Bioengineering and Biotechnology (247).

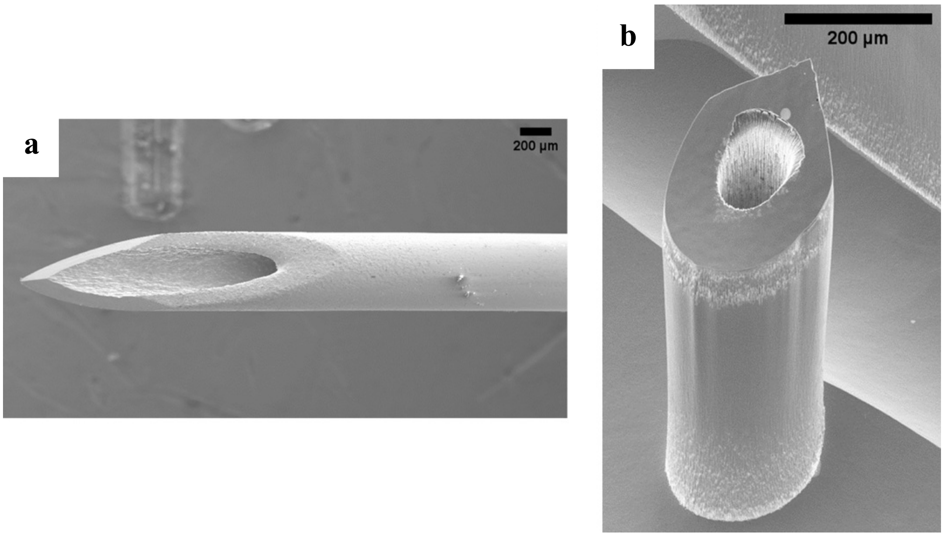

Figure 34. Needle samples being compared in this study (a) 25-gauge hypodermic and (b) an individual needle from a 1x5 hollow silicon microneedle array. Scales can be seen on the top right of each image (247)

The overarching aim was to develop a novel method which provides quantitative supplement to subjective assessment methodologies for needle-based device performance. The subsequent section describes the experimental methodology in detail, including the device insertion protocol, imaging setup, and image processing pipeline. Quantitative outputs including insertion force profiles and strain field evolution are presented, forming the basis for the comparative analysis of device-membrane interaction between the two sample types.

4.2. Materials and methodology

This section provides detail on the materials used and methodology developed during this study. It will cover experimental instrumentation and setup, in addition to analytical methodology and data handling and processing.

4.2.1. Experimental instrumentation

This subsection will cover all equipment used, from the physical apparatus and mounts holding the samples, to the production of phantoms, to the camera settings and setup. The camera hardware in addition to the DIC software parameters are also detailed in this subsection.

Insertion test rig design and manufacture

The setup of this experiment required the design and production of apparatus to hold the skin phantom and mirror directly below the force station insertion head which the sample devices were affixed to. This chapter outlines the design and fabrication of both the apparatus, and both MN and hypodermic sample mounts.

Apparatus

An insertion test rig was designed and manufactured to accommodate force-displacement controlled device insertion in conjunction with stereo-DIC. The rig was designed using SolidWorks (2022) and fabricated using clear photopolymer resin (FormLabs Clear Resin V4) on a FormLabs 3B SLA printer. The design incorporated a ring mounting platform for the epidermal phantom with a recessed circular cavity at its centre. This central cavity provided a viewing window to allow unobstructed optical access to the insertion site and surrounding area from below, ensuring optimal light penetration and uniform illumination for stereo-DIC imaging. A 42° angled slot was integrated into the rig to accommodate a mirror, enabling imaging of the underside surface during insertion procedures (Figure 35).

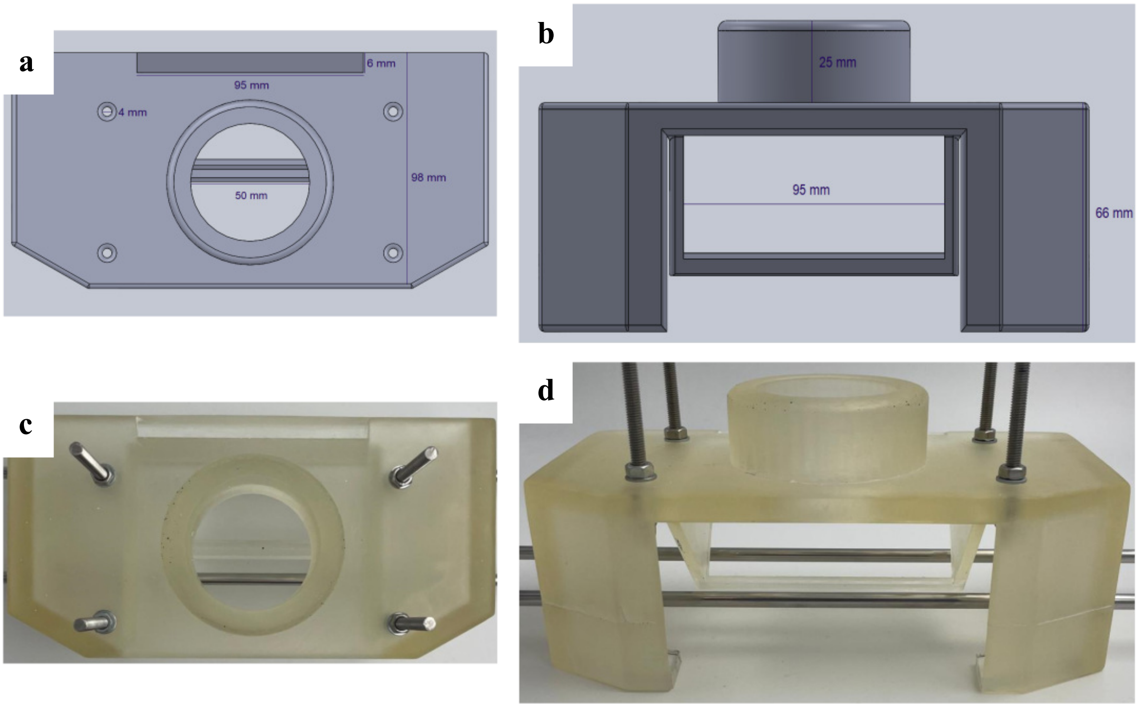

Figure 35. Membrane and mirror support apparatus (a-b) structure design (c-d) structure post 3D printing and processing. Adapted from (247)

Needle sample mounts

Custom-designed needle mounts were fabricated to secure each device to the Tinius Olsen mechanical testing machine (Model 1ST, Tinius Olsen Ltd., UK). A mount was designed for the 1x5 array of silicon HMNs and printed in Tough resin using a FormLabs 3B SLA 3D printer (FormLabs) (Figure 36a-b). The hypodermic needle mount was adapted from a drill chuck and secured within the load cell grip (Figure 36c-d). Both mounts were designed to eliminate any physical interference of the mount and the membrane during testing, and to maintain alignment along the insertion pathway throughout.

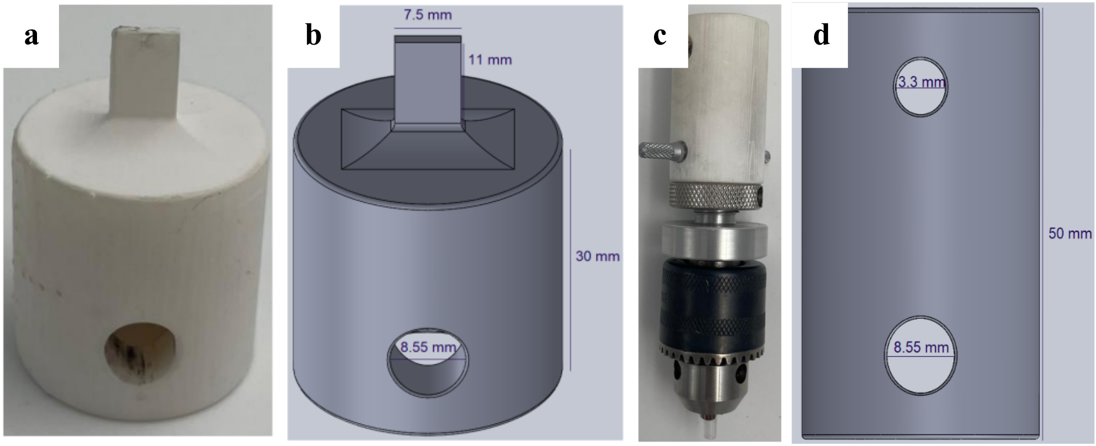

Figure 36. Sample mounts (a-b) microneedle adaptor (c-d) 25-gauge hypodermic adaptor. Adapted from (247)

Phantom preparation

Two phantoms required production in this chapter: the epidermal phantom used to mimic the skin during insertion, and the PDMS support plug used to prevent the unwanted excessive stretching of the epidermal phantom. The production of both of these is reported in this subsection.

Epidermal phantom

An epidermal-mimicking membrane was fabricated using Ecoflex™ 00-35 Fast (Smooth-On Inc.), a soft, platinum-catalysed addition-cure silicone, selected for its low elastic modulus (~0.125 MPa), closely approximating that of human epidermis (~0.1 MPa) (267, 268). Parts A and B were mixed in a 1:1 ratio by volume with a 5-minute cure time. Black silicone pigment was added to produce an opaque background suitable for a high contrast speckle pattern. The mixture was applied using a bar coater (RK control coater, RK Printcoat Instruments, UK) to a target thickness of 50 µm and left to cure overnight to ensure complete polymerisation and dimensional stability.

A high-contrast speckle pattern was applied to the cured black silicone membrane by airbrushing a white silicone pigment mixed with acrylic paint thinner, generating a random distribution suitable for stereo-DIC. Speckle density and contrast were optimised for full-field strain capture (Figure 37). A new epidermal phantom was used for every sample repeat performed.

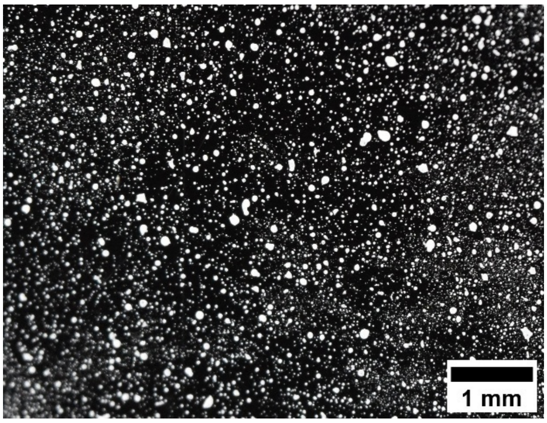

Figure 37. Example of white speckle pattern, density, and contrast on black silicone membrane. Scale can be seen on the bottom right

Support structure phantom

Polydimethylsiloxane (PDMS) was used to simulate the mechanical behaviour of the hypodermis/SC layer, including muscle, fat, and connective tissue, providing necessary mechanical support to prevent unrealistic stretching of the epidermal-mimicking membrane during insertion (269). PDMS is widely reported in the literature for replicating *in vivo* soft tissue environments and for its optical transparency, which was essential in this experimental design to enable accurate imaging from below during needle insertion (269-271).

Each PDMS plug was prepared by mixing 50 mL PDMS (CAS: 63148-62-9) with 8 % crosslinker by volume, as advised by the manufacturer. The mixture was degassed and poured into a silicone mould designed as a negative of the rig's central viewing void, with an acrylic disc placed at the base to create a flat surface with minimal artifacts which may impact imaging quality (Figure 38). A new PDMS plug was prepared for every sample repeat performed. This support structure ensured physiologically relevant mechanical conditions during testing and maintained optical clarity for image capture.

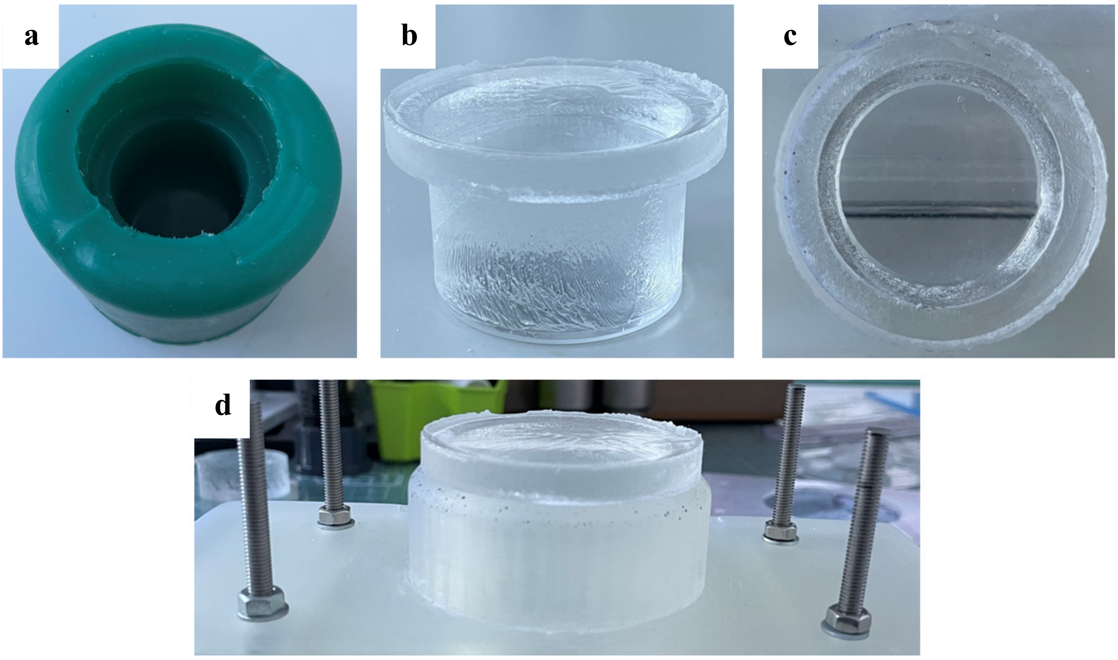

Figure 38. PDMS plug creation (a) silicone mould used for casting (b) plug post casting (c-d) plug in situ within apparatus

<u>Sample devices and repeat structure</u>

Two device types were evaluated: a 1x5 array of silicon HMNs (pitch 1300 μm) and a conventional hypodermic needle (Figure 34). The silicon MNs were fabricated as described in Chapter 3 and mounted to a custom holder designed to ensure stable vertical alignment during insertion (Figure 36). The hypodermic device was a 25-G stainless steel needle (Medisave), mounted using a custom assembly (Figure 36).

All mechanical insertion tests were repeated five times *per* device type (*n* = 5). Each trial used a new membrane and PDMS plug to eliminate cross-sample mechanical degradation and preserve test independence. All insertions were performed using new, unused device samples to ensure comparability and accuracy in both force and image-based analysis. Zero-displacement control tests were conducted prior to each insertion to identify baseline system noise and confirm camera stability.

Environmental conditions were standardised across all trials. Test temperatures were recorded for each insertion, and lighting conditions were maintained consistently using a fixed dual-source setup.

Imaging and sensor setup

High-speed cameras were utilised in this experimental setup, of which the setup was critical to successful imaging. This subsection reports the camera setup measurements, including imaging parameters and physical positioning, in addition to the lighting setup requirements.

Camera setup and calibration

Critical parameters for DIC are depicted schematically in Figure 39. All camera hardware and DIC measurement values can be found in Table 10. Two Photron FASTCAM Nova S6 high-speed cameras were utilised, each fitted with Laowa 100 mm f/2.8 2x Ultra Macro APO lenses and linear polarising filters to reduce glare. The stereo imaging system was configured with a 100 mm focal length, a stereo angle of 33°, and an incline angle of 6°, providing appropriate convergence and depth resolution for stereo-DIC (Figure 40, Figure 41). The cameras were mounted with a stand-off distance (SOD) of 310 mm, resulting in a field of view (FOV) of 30 mm and a depth of field (DOF) of approximately 3 mm (Figure 40, Figure 41). To facilitate optimal image acquisition geometry, mirrors were positioned at an angle of 42° to the base of the mechanical testing machine. Stereo calibration was conducted using LaVision’s 3D Calibration Plate (model 025-3.3), which provides defined separations of calibration planes and precise mark spacing. This empirical calibration method ensures high spatial accuracy without requiring direct measurement of physical angles or distances. The working distance and baseline between the cameras were carefully optimised for the experimental setup, enabling robust three-dimensional strain measurements. A photo of the camera and apparatus setup can be found in Figure 42.

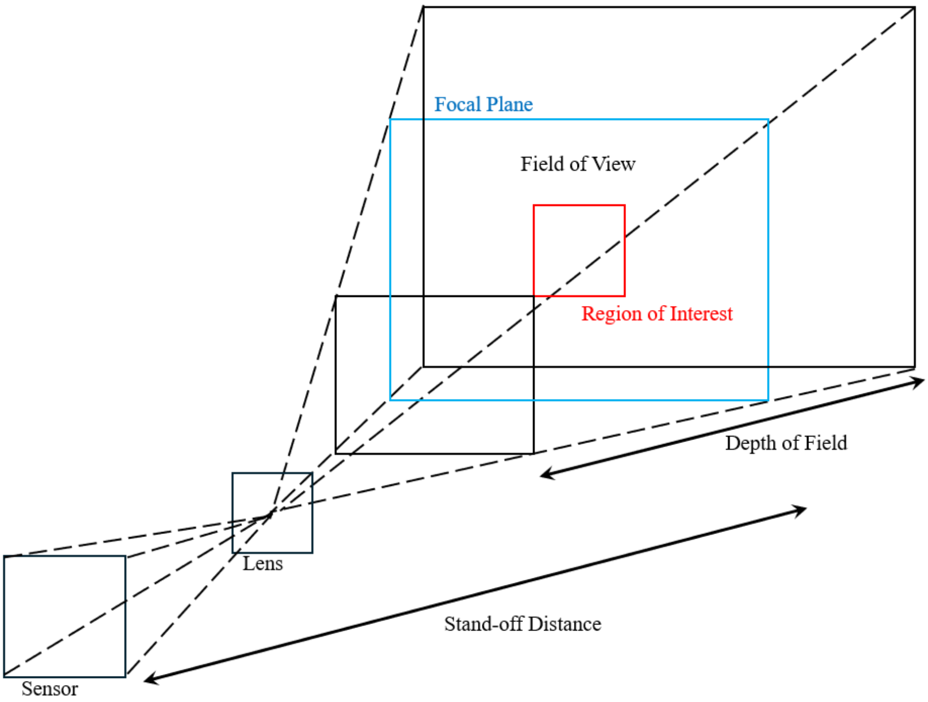

Figure 39. Schematic of the setup and key parameters important to camera and sample setup for digital image correlation

Table 10. Camera settings and positioning values for this experimental setup (247)

	Parameter	*Value*
Camera	Manufacturer and model	Photron FASTCAM Nova S6
	Lens make and model	Laowa 100 mm f/2.8 Ultra Macro APO
	Frame rate	1000 fps
	Shutter speed	1/3000
	Resolution	1024 x 1024
	Aperture	8
DIC Measurement	Focal length	100 mm
	Incline angle	6°
	Stereo angle	33°
	Standoff distance	310 mm
	Depth of field	3 mm
	Field of view	30 mm
	Mirror angle	42°

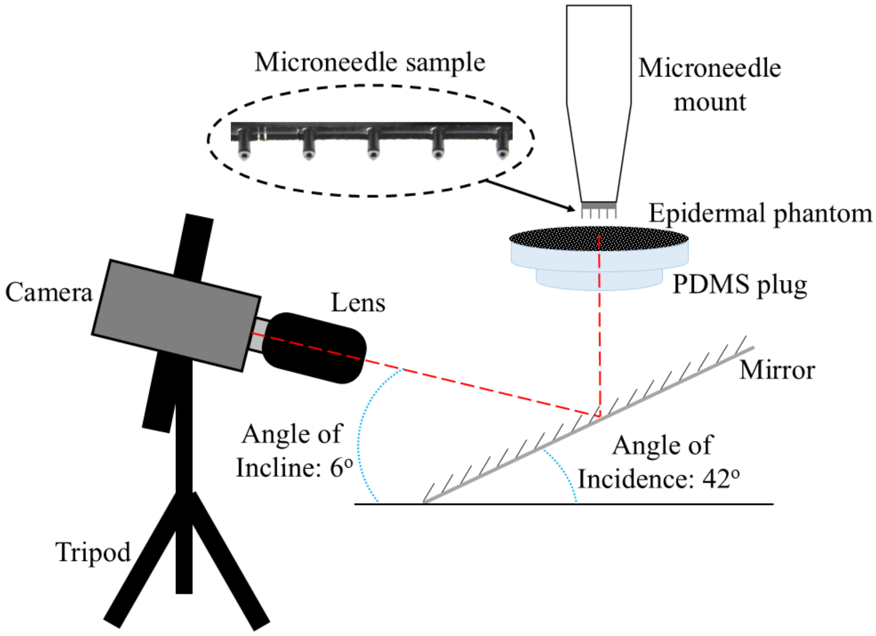

Figure 40. Schematic of experimental setup including camera, mirror, PDMS plug, membrane, sample mount, and sample (247)

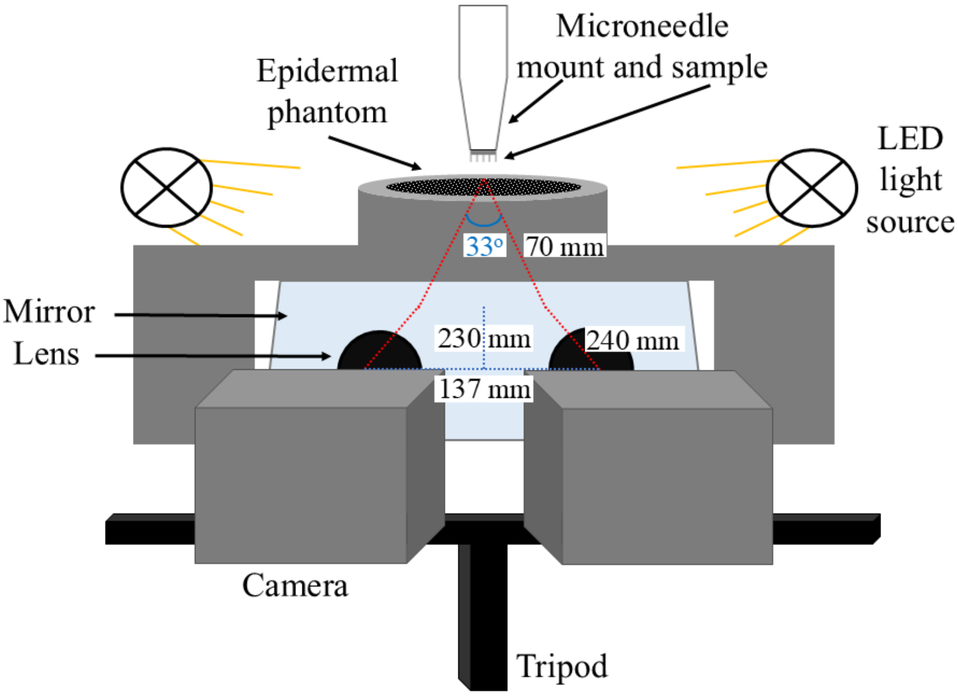

Figure 41. Schematic of experimental setup with apparatus, cameras, sample and mount, mirror, lights, and imaging angles

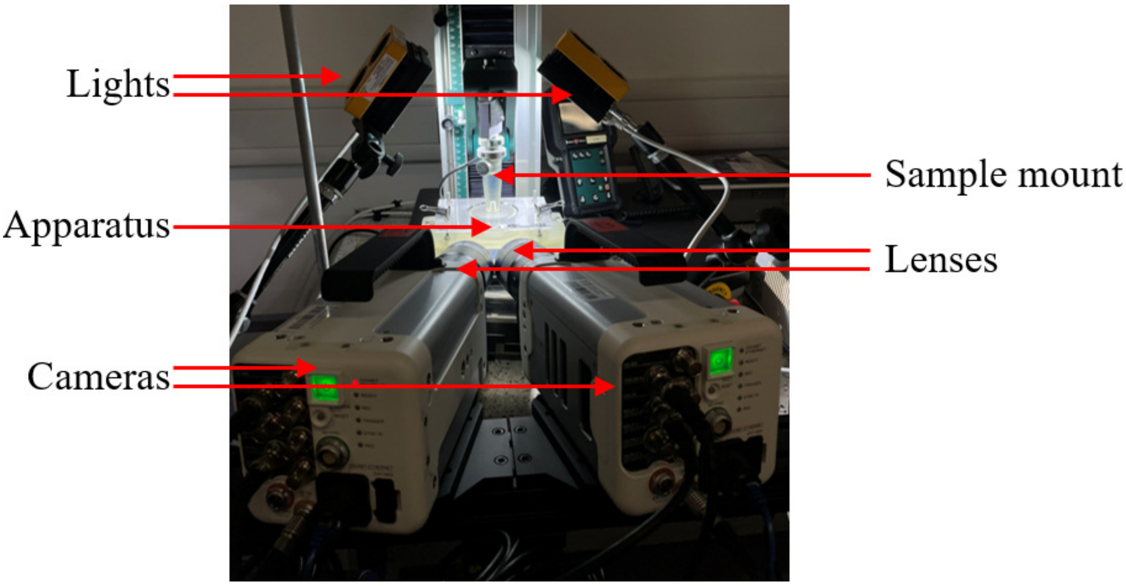

Figure 42. Photo of experimental setup. Adapted from (247)

Imaging parameters and synchronisation

Image acquisition was conducted at 1000 fps (5437 total) with a shutter speed of 1/3000 s, producing a resolution of 1024 x 1024 pixels. A manual trigger was used with a 10 % pre-trigger applied to capture any initial deformation states prior to needle insertion.

Lighting and environmental conditions

Illumination was provided by two GS Vitec MultiLED QT light sources, positioned above the sample and angled downward to ensure uniform, shadow-free lighting critical for high quality imaging and accurate particle tracking *via* DIC. Natural ambient light was present but controlled by the addition of synthetic illumination in order to maintain imaging conditions. The experimental rig was situated on a concrete table to minimise vibrations. Ambient temperature was recorded throughout to monitor environmental consistency.

4.2.2. Analytical methodology

The analytical methodology covered in this subsection will be the collection of force-displacement data, imaging collection, handling and processing, in addition to the parameters used for digital image correlation analysis. Reported here also is the technique for strain discretisation when each needle point in the MN array was investigated.

Force-displacement data collection

Mechanical insertions were performed using a Tinius Olsen Model 1ST mechanical testing machine operating in displacement-controlled mode. Insertions were conducted at a constant speed of 1 mm/s. A 25 N load cell was employed to measure insertion force, with test initiation triggered at a force threshold of 0.01 N to ensure detection above the noise floor, which was confirmed to be lower than this value. A load protection limit of 20 N, 80 % of the load cell capacity was applied to safeguard the experimental setup. Quantitative force-displacement data were recorded continuously throughout each insertion.

Image handling and processing

Raw camera images were extracted from cameras and imported into LaVision, as shown in the figures below (Figure 43, Figure 44). Rupture was defined as the first frame in which speckle pattern distortion indicated membrane breakthrough. The frame number of the following insertion depths (50 and 100 % for MNs, 15 and 30 % for hypodermics) were determined, utilising known frame rate (1000 fps) and insertion speed (1 mm/s). The frame corresponding to 100 % insertion was identified as the rupture point plus the number of frames required for device length, and 50 % identified as half of this interval. The same approach was taken for hypodermic samples, for equivalent frames at 15 and 30 % insertion depth. The identification of the mid and full insertion point frames for this study is detailed further, with accompanying raw merged images, in frame identification.

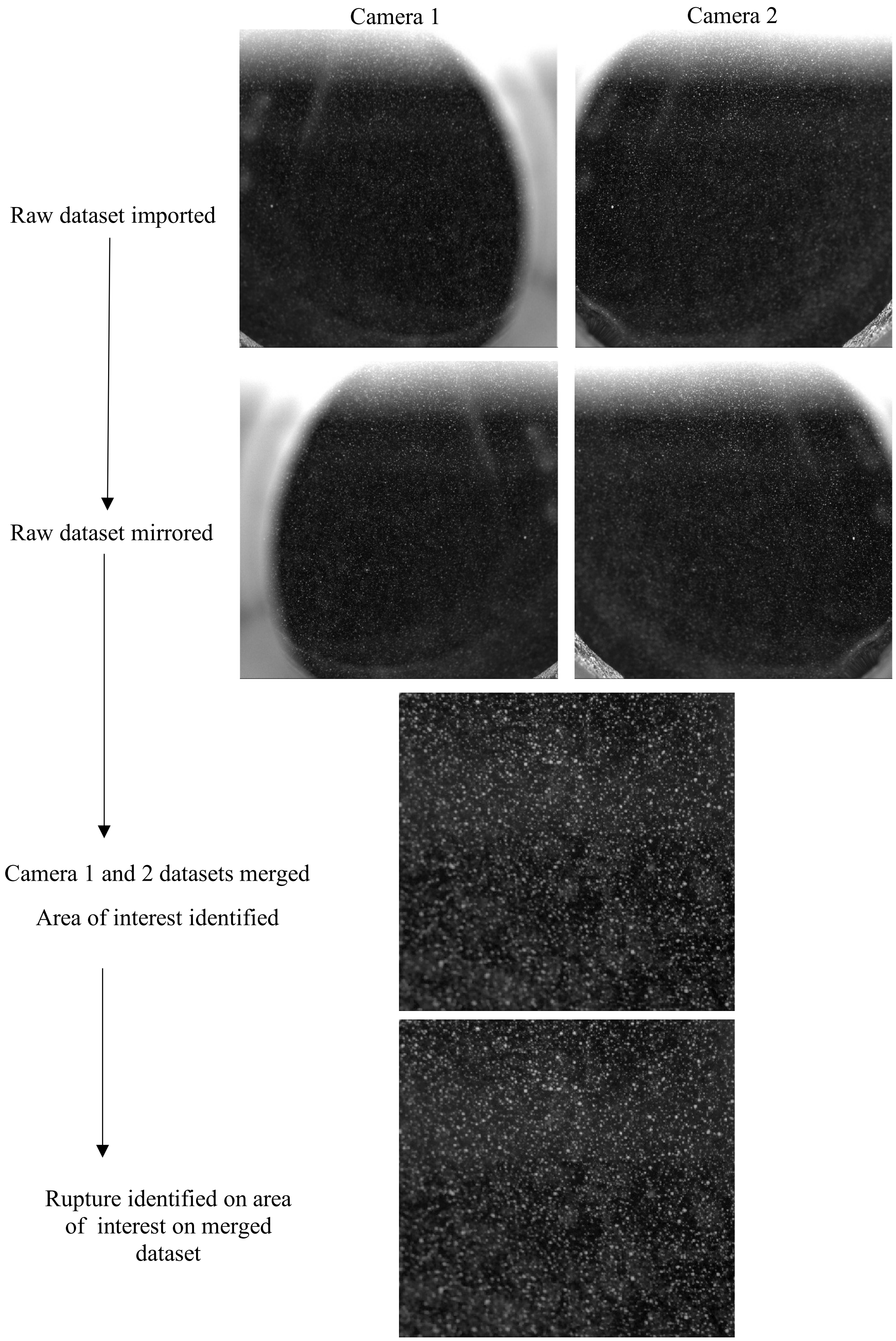

Figure 43. Example of image handling route for microneedle samples

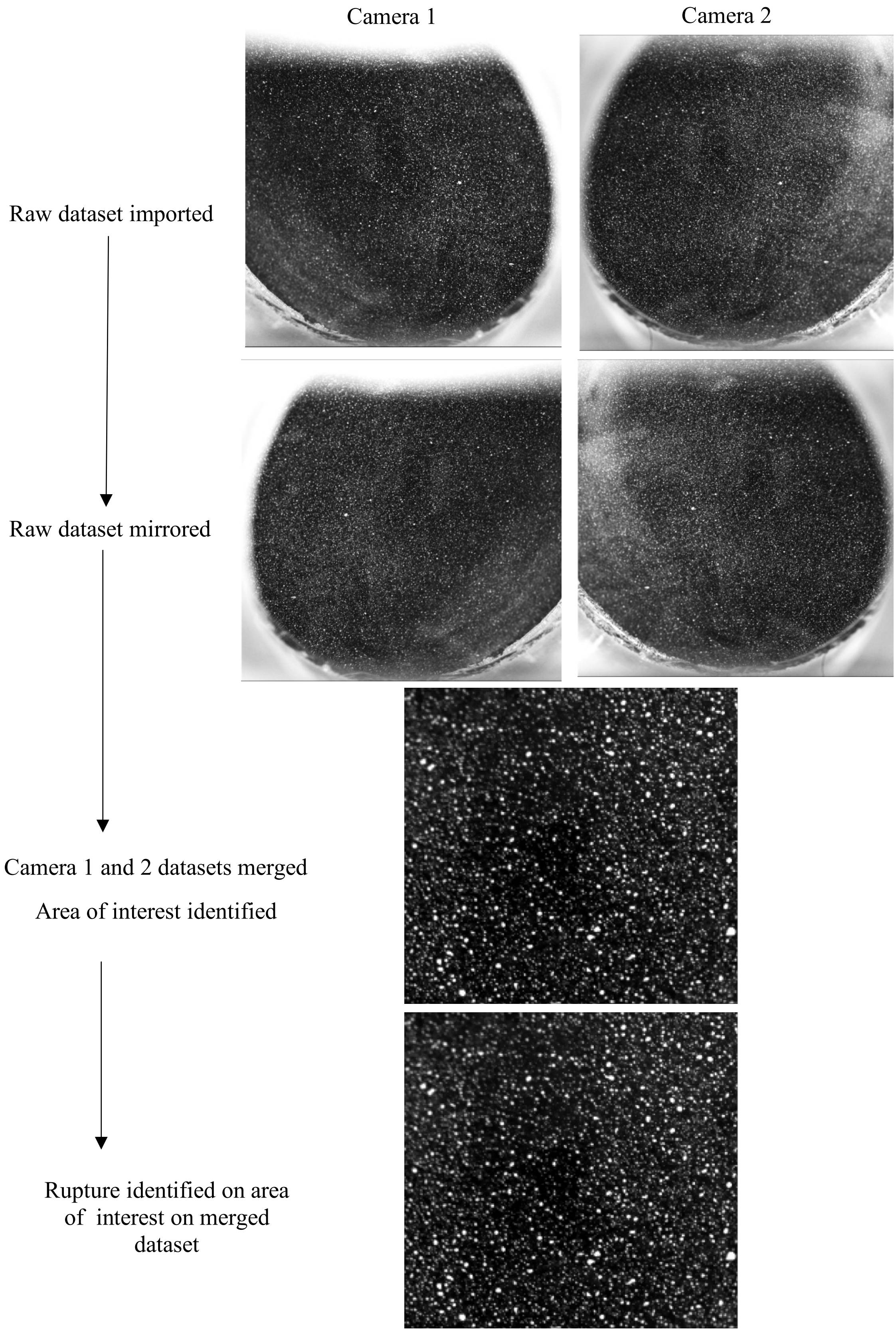

Figure 44. Example of image handling route for hypodermic samples

Digital image correlation analysis

DIC (LaVision DaVis 10 StrainMaster) was employed to quantify surface strain of the epidermal phantom immediately prior to, during, and post needle insertion. The white speckle pattern applied on a black background provided high contrast for accurate tracking. Strain values were calculated using stereo-DIC with a dual high-speed camera system. Lighting, speckle pattern quality, and camera alignment were optimised to maximise measurement accuracy. A zero-displacement test was first conducted to identify and quantify any baseline noise or artefacts. The correlation mode utilised was the sum of differential, with the following optimised calculation settings found in Table 11. This approach enabled quantification of the maximum normal strain experienced by the epidermal phantom, thereby providing an objective measure of mechanical deformation induced by needle insertion.

Table 11. Parameters used for digital image correlation for strain calculation (247)

Parameter	*Value*
Correlation mode	Sum of differential
Minimum number of valid pixels	100 %
Pyramid levels	1
Maximum iterations	30
Epsilon	30
Threshold for correlation value	0.5
Threshold for confidence margin	0.25 pixel
Threshold for triangulation error	3.00 pixels
Interpolation mode	Bi-linear
Subset size	19 pixels
Step size	12 pixels
Noise floor (peak)	2.98 x 10^{-13} %

Strain discretisation approach

Local strain data was extracted using LaVision DaVis 10 StrainMaster software by manually defining a net of facets to surround and only cover the tip of each MN. All other facets beyond this immediate region were excluded from the calculation to isolate strain local to the puncture event. This allowed strain to be quantified in the area directly affected by each MN tip as deformation progressed. The procedure was repeated for each individual tip on every 1x5 array, across all repeats. The same region geometry and net discretisation were consistently applied to each sample to ensure comparability between insertions and across devices. The DIC processing parameters used for this analysis were identical to those reported in Table 11, maintaining consistency in subset size, step size, and all correlation thresholds.

4.3. Experimental results

This experimental results section is comprised of the force-displacement data of device insertion in addition to the visual strain field data calculated from the captured membrane distortion. Data is also provided whereby the calculated strain was discretised to each MN tip to provide a greater level of detail over the performance of each individual device in the array of 5.

4.3.1. Force-displacement

Representative force-displacement curves for the hypodermic needle insertion into the epidermal phantom-PDMS support system are shown in Figure 45 (*n* = 5) exhibited greater variability in force response within the initial 0-0.15 mm displacement window. A distinct rise in force up to 0.033 N was observed between 0 and 0.14 mm, followed by a small but repeatable decrease to 0.025 N at 0.15 mm (Figure 45). This localised force decline was observed consistently across all repeats and was interpreted as the point of phantom rupture - defined here as the moment at which the needle tip penetrates and breaches the silicone surface.

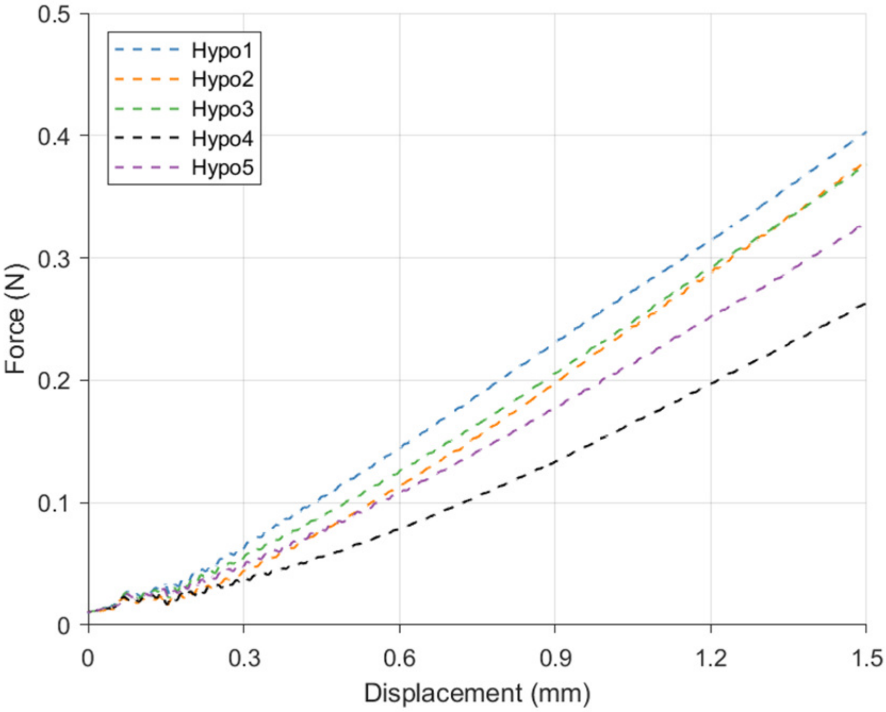

Figure 45. Force displacement curve during hypodermic needle (n = 5) insertion into the silicone membrane (247)

Figure 46 depicts the representative force-displacement curves for HMN insertion into the epidermal phantom-PDMS support system (*n* = 5). In all samples, the force initially increased gradually between 0 and 0.15 mm displacement, reaching a peak of 0.049 N. Beyond this point, a steeper rise in force was observed, reaching a maximum of approximately 1.1 N at 0.8 mm displacement (Figure 46). This trend was consistent across all five repeats, with MN2 and MN4 recording the highest (1.12 N) and lowest (0.85 N) peak insertion forces, respectively.

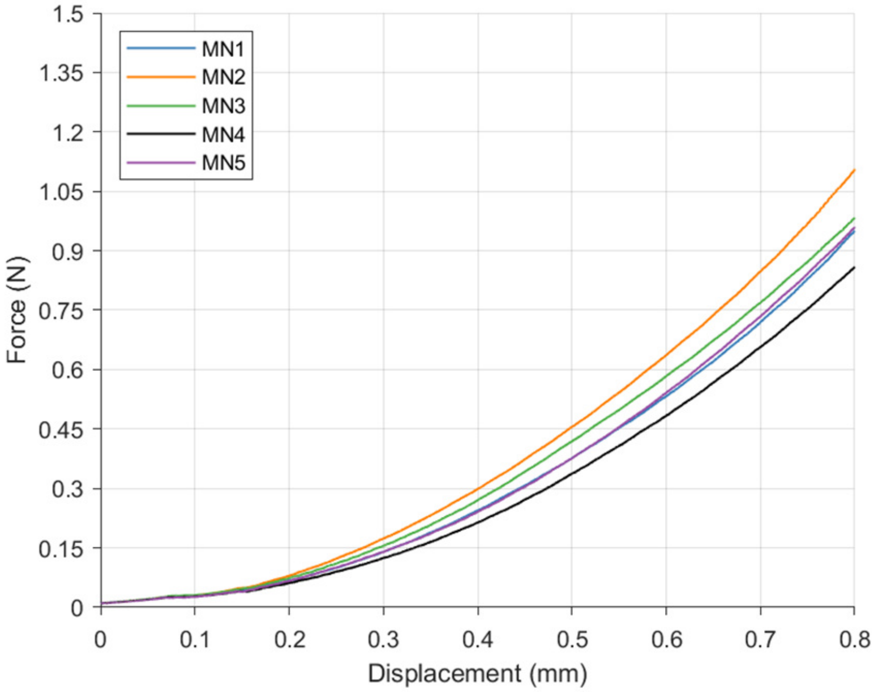

Figure 46. Force displacement curve during hollow silicon microneedle (n = 5) insertion into the silicone membrane (247)

A comparison of MN and hypodermic needle insertion forces is presented in Figure 47 with solid and dashed lines denoting MN and hypodermic insertion, respectively. The data has been truncated to cover the MN insertion displacement depth. This comparative plot illustrates that, whilst both device types showed comparable force magnitudes in the early displacement range (0 - 0.15 mm), MN insertion forces increased more rapidly following this (Figure 47). In contrast, the hypodermic needle exhibited a more gradual increase in force, indicating reduced resistance during deeper penetration.

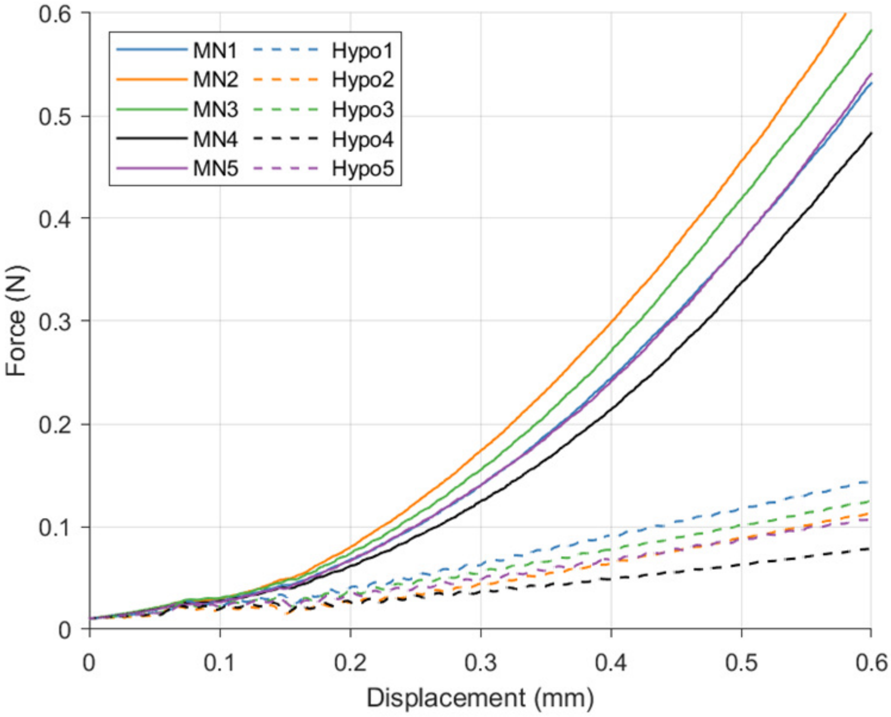

Figure 47. A comparison of the force displacement curves during microneedle (n = 5, -) and hypodermic needle (n = 5, - -) insertion into the silicone membrane (247)

4.3.2. Digital image correlation

This subsection will present the results which DIC was performed on, and the subsequent frame with calculated strain maps. The data presented here serve as the basis for subsequent discussion and assessment of how insertion mechanics and strain localisation impact device functionality and performance.

Frame identification

Here the frames of interest are presented, post mirror and merge steps as described in image handling and processing. The images in Figure 48 present examples of the frames, from zero through to the deepest insertion point recorded, which were used for DIC and strain measurement in subsequent subsections of this chapter.

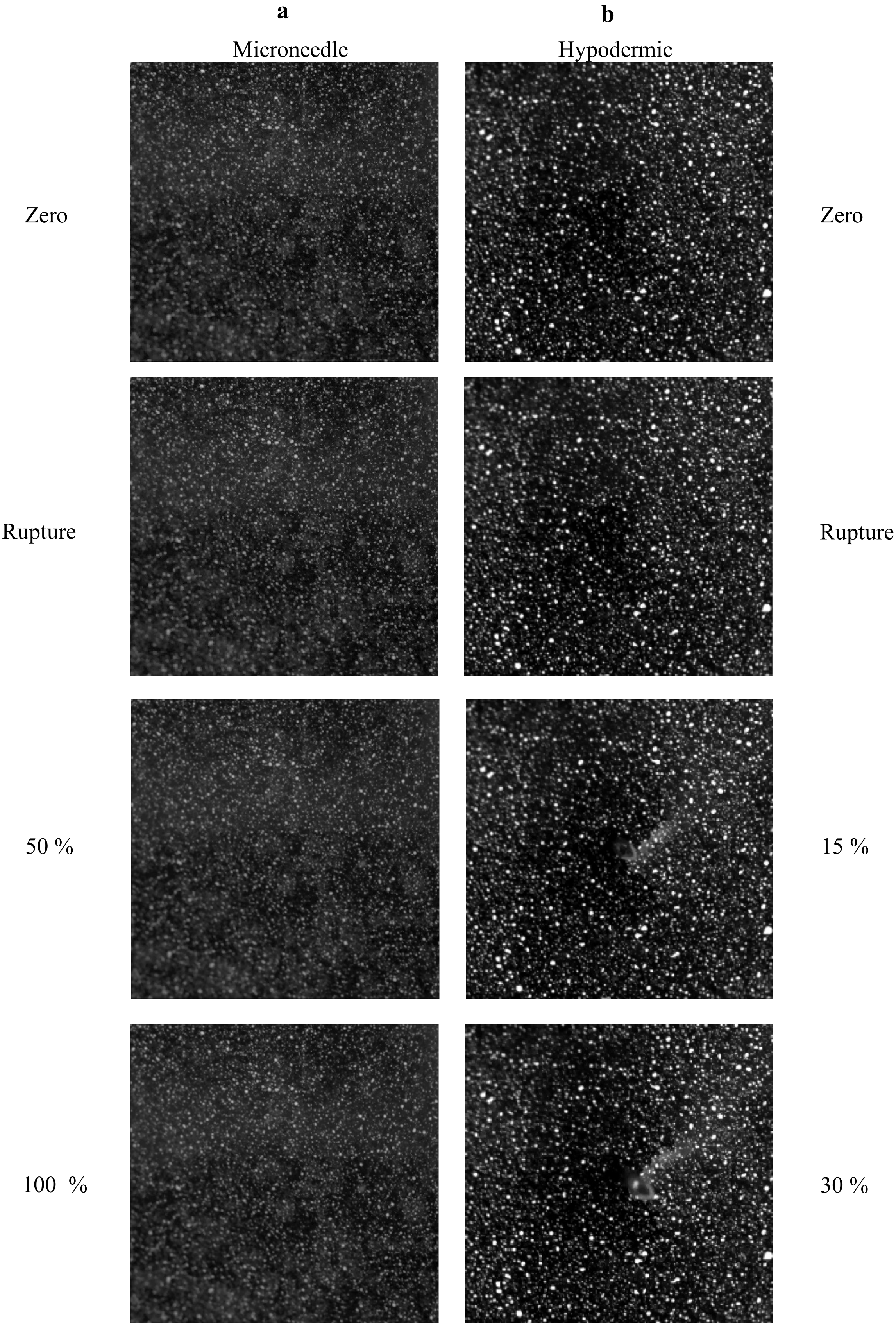

Figure 48. Example frames used for (a) microneedle strain analysis and (b) hypodermic strain analysis. Both present frames for no contact (zero) and rupture, and microneedle and hypodermic samples present with 50 % and 100 %, and 15 % and 30 % of the needle depth inserted respectively

25-G hypodermic induced strain fields

Strain fields induced by 25-G hypodermic needle insertion was calculated according to the parameters specified in Table 11. Strain field images were extracted at four critical timepoints during the insertion tests: initial contact (zero displacement), phantom rupture, 15 % insertion depth, and 30 % insertion depth (Figure 49). The insertion depth percentages refer to the fraction of the total needle length.

A colour scale ranging from -10 % to 65 % maximum normal strain was employed for ease of visualisation, with deliberate saturation at the maximum strain values (notably sample repeat 5 peaked at 72.7 %) to allow optimal comparison across the dataset. The average maximum normal strain values and corresponding standard deviations at these timepoints were 1.61×10^{-13} % (7.44×10^{-14} %), 1.59 % (0.64 %), 23.22 % (5.95 %), and 51.43 % (13.97 %), respectively (Figure 49).

Notably, the strain magnitude at rupture was comparatively low, averaging 1.59 %, representing only 3.09 % of the strain measured at 30 % insertion depth. This finding demonstrates that the hypodermic needle progress to generate significantly higher strains during deeper penetration stages than at the moment of phantom rupture.

The strain distribution was highly localised to the immediate vicinity of the needle tip, with areas of higher strain concentrated at the tip and bevelled regions, with minimal propagation into the surrounding areas. This localised effect contrasts with the strain patterns observed for MNs.

It should be noted that for sample 3, the final image was taken at 29 % rather than 30 % insertion depth due to facet loss in the DIC analysis. This loss was likely caused by interference factors such as shadows, objects obstructing the optical path, or excessive membrane deformation, which compromised facet tracking by the DIC algorithm.

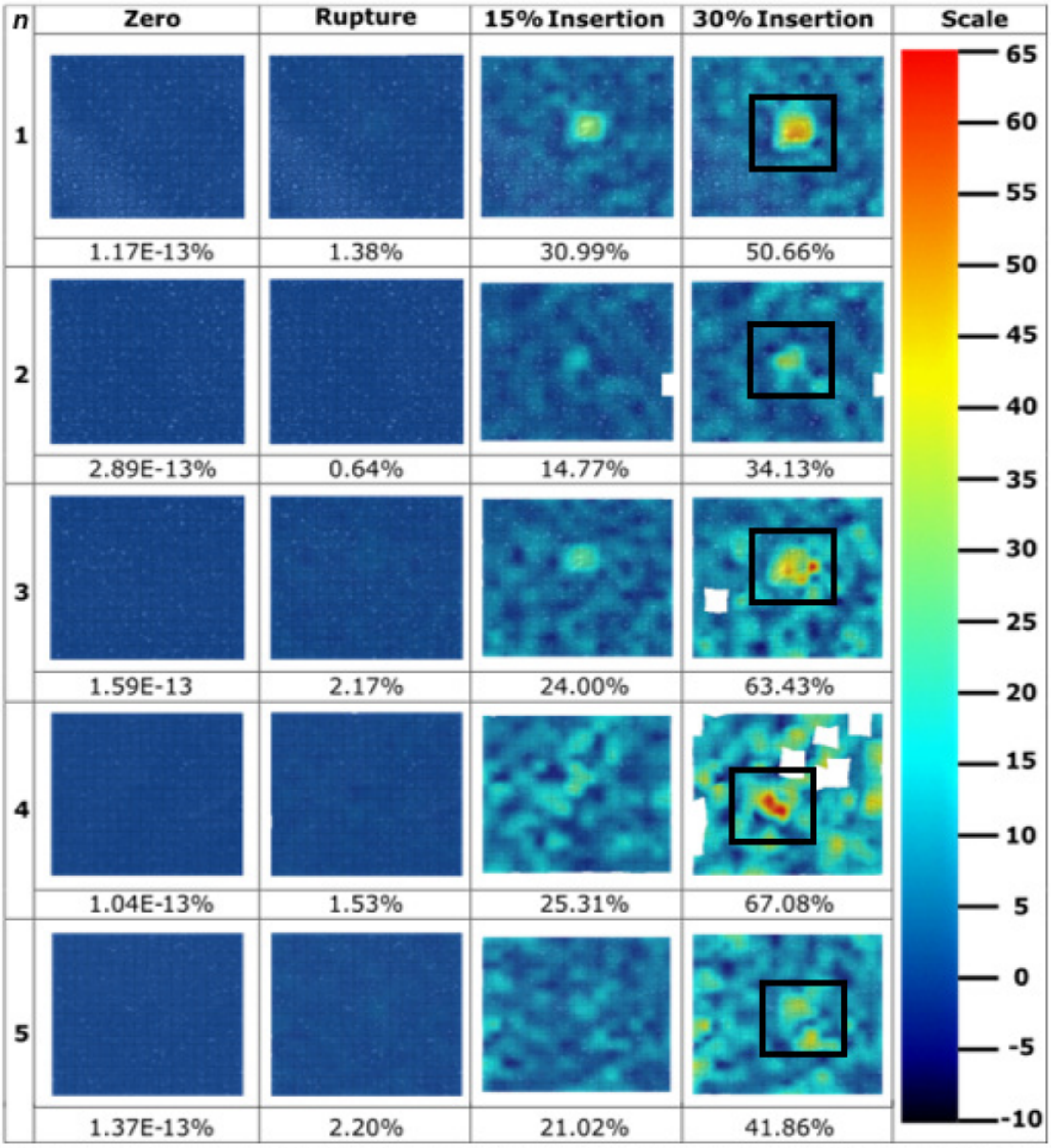

Figure 49. Strain field images showing maximum normal strain (%) throughout hypodermic needle insertion (n = 5) extracted at four points (zero contact, rupture, 15 %, and 30% insertion). The area of interest has been denoted by a black box (247)

Hollow microneedle induced strain fields

Strain fields induced by HMN insertion were evaluated using the same parameters as specified in Table 11. Representative strain images were extracted at four key insertion points: zero displacement, phantom rupture, 50 % insertion depth, and 100 % insertion depth (Figure 50). The insertion depth percentages correspond to the proportion of total needle length.

A colour scale of -4 % to 14 % maximum normal strain was applied. Slight saturation occurred in some samples (MN1: 14.89 %, MN2: 14.88 %) to permit clear visualisation of the entire strain distribution dataset (Figure 50). The average maximum normal strain and associated standard deviation at the four timepoints were 1.41×10^{-13} % (3.86×10^{-14} %), 3.5 % (2.6 %), 8.2 % (2.7 %), and 12.7 % (2.2 %), respectively.

Maximum normal strain at rupture ranged from 1.00 % to 6.69 %, with an average of 3.52 % (Figure 50). At 100 % insertion depth, the strain range increased to a range of 9.88 % - 14.89 %, averaging 12.74 % (Table 12). The average strain induced at epidermal phantom rupture by the HMN was found to be 27.6 % of the strain at full insertion depth, indicating substantial strain accumulation as insertion progresses. Visually, linear strain hotspots were consistently identifiable across the region corresponding to the 1x5 array of MNs (Figure 50), highlighted for ease with black rectangles. These hotspots suggest that strain localisation aligns closely with each MN in the array, reflecting the spatial distribution of mechanical loading.

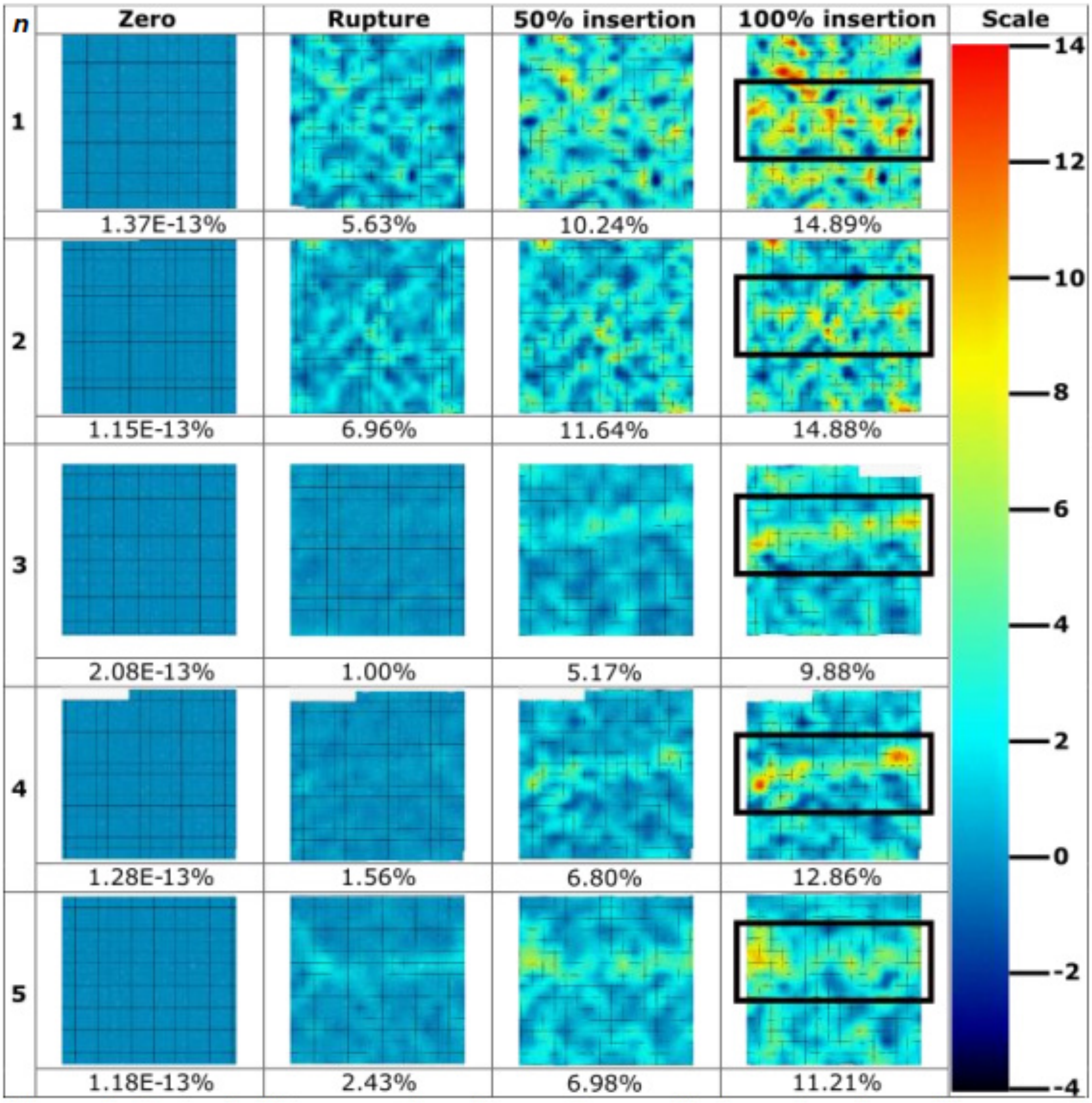

Figure 50. Strain field images showing maximum normal strain (%) throughout microneedle insertion (n = 5) extracted at four points (zero contact, rupture, 50 %, and 100% insertion). The area of interest has been denoted by a black box (247)

Comparative strain distribution: 25-G *versus* microneedles

A direct comparison of maximum normal strain distributions for 25-G hypodermic needles and HMN is presented in Figure 51. The median sample has been used for both device types to provide a fair comparison (Hypo1, MN4). Strain images were analysed at membrane rupture and at key insertion depths - full insertion (100 %, 600 µm) for MNs and 30 % insertion depth for hypodermic needles - using a consistent colour scale to facilitate comparison.

At the point of rupture, the HMN median sample induced slightly greater (1.56 %) maximum normal strain over a larger phantom area compared to hypodermic needles (1.38 %) (Table 12). In contrast, the hypodermic needle generated highly localised strain patterns with multiple hotspots exceeding 50 %, whereas the HMN strain at full insertion peaked considerably lower, at approximately 12.86 %.

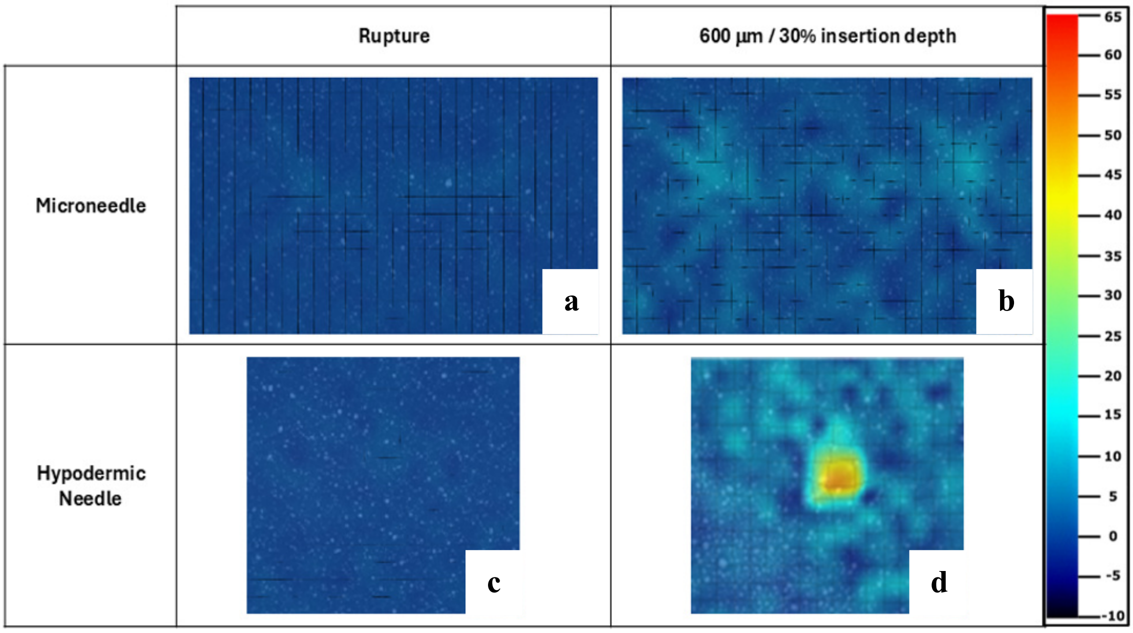

Figure 51. Strain fields of the median strain sample for rupture and the full/30 % insertion frames for (a-b) microneedle and (c-d) hypodermic needle insertions (247)

These observations indicate fundamental differences in strain distribution between the two device types. Microneedles produce more diffuse strain across the insertion area, while hypodermic needles generate intensely localised strain focused near the needle tip. The strain concentration factor of each device type in Figure 51b and Figure 51d were calculated to be 7.5 and 33.5 for the MN and hypodermic device types respectively.

Table 12. The average extracted values for maximum normal strain (%) for each sample type at 4 stages per sample type (247)

	Maximum normal strain (%)							
	Microneedles				*Hypodermic Needle*			
	Zero	Rupture	50 %	100 %	Zero	Rupture	15 %	30 %
Min	$1.15\text{x}10^{-13}$	1.00	5.17	9.88	$1.04\text{x}10^{-13}$	0.64	14.77	34.13
Max	$2.08\text{x}10^{-13}$	6.96	11.64	14.89	$2.89\text{x}10^{-13}$	2.00	30.99	67.08
Mean	$1.41\text{x}10^{-13}$	3.52	8.17	12.74	$1.59\text{x}10^{-13}$	1.59	23.22	51.43

Strain discretisation, localisation, and progression

Figure 52 presents the individual MN profiles of average maximum normal strain during HMN insertion, grouped by needle position within the 1x5 array, while Figure 54a shows analogous data for the 25-G hypodermic needle insertions. All plots for both device types demonstrate a continuous increase in average maximum normal strain over the insertion period of 0-0.6 s. Notably, each curve exhibits a distinct, sharp, and repeatable initial peak occurring within the first 0.01 s. The maximum and minimum strain values within this peak range from 0.38 % to 0.57 % for the MN samples, and approximately 0.42 % for the hypodermic needle samples.

Examining the MN array positions in greater detail (Figure 52; Table 12), position 1 needles (Figure 52a) show a continuous increase in average maximum normal strain from 0 % at contact to 7.91 % at 0.6 s, with some degree of noise between 0.2-0.6 s. Similarly, position 5 needles (Figure 52b) demonstrate a comparable continuous increase, reaching 8.24 % average maximum normal strain at 0.6 s and exhibiting a similar noise pattern in the same time interval as position 1. The difference in peak strain between positions 1 and 5 was minimal, at only 0.33 %.

Position 2 needles (Figure 52c) display a more gradual incline in strain over time, achieving a peak average maximum normal strain of 5.42 % at 0.6 s. Moreover, these position 2 data exhibit noticeably less noise compared with positions 1 and 5. Position 4 needles (Figure 52d) follow a similar pattern to that of position 2, showing the initial sharp strain peak between 0 and 0.01 s and reaching a maximum strain of 5.34 % at 0.6 s, only 0.08 % less than position 2’s peak. The noise profiles for positions 2 and 4 are analogous.

Position 3 needles (Figure 52e) also demonstrate a continuous increase in strain similar to the other positions, peaking at 6.04 % at 0.6 s with minimal noise, consistent with positions 2 and 4.

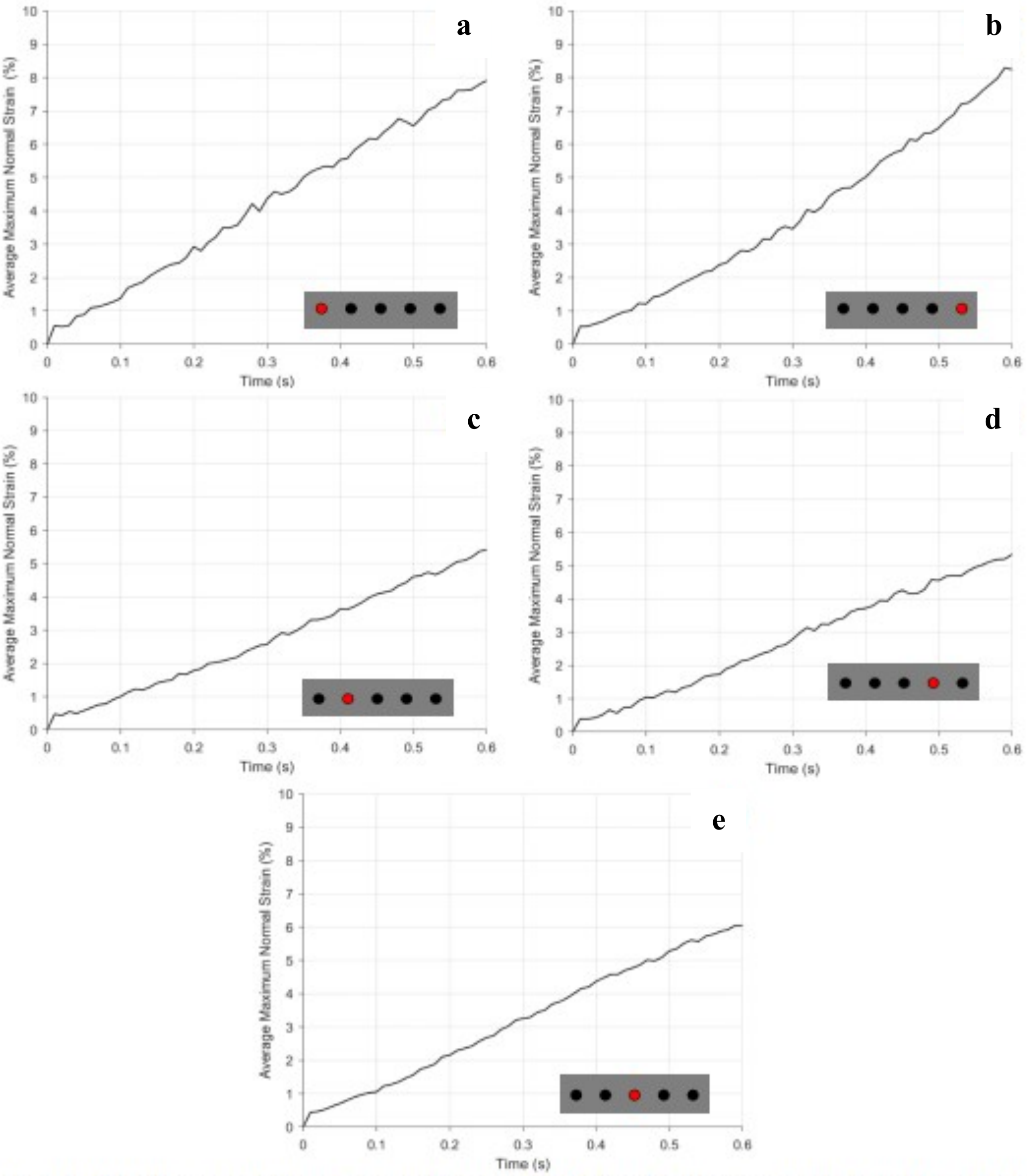

Figure 52. Average maximum normal strain (%) for each microneedle position. The microneedle position can be seen as identified on the schematic insert on graphs (a-e) (247)

The peak % maximum normal strain for each needle position, on average, reported in Table 13 is presented graphically in Figure 53. For the hypodermic needle insertion (Figure 54a), although the strain increases continuously throughout the entire insertion duration, the curve reveals multiple distinct phases: from 0 to 2 s, strain rises from 0 % to 20.34 %; between 2 and 3.5 s, it increases further to 34.14 %; and from 3.5 to 4.43 s, it reaches a final peak of 50.89 % (Table 13).

Table 13. Maximum average maximum normal strain values relative to microneedle position compared to the hypodermic needle average (247)

	Microneedle Position					*Hypodermic Needle*
Maximum Average Maximum Normal Strain (%)	1	2	3	4	5	50.89
	7.91	5.42	6.04	5.34	8.24	

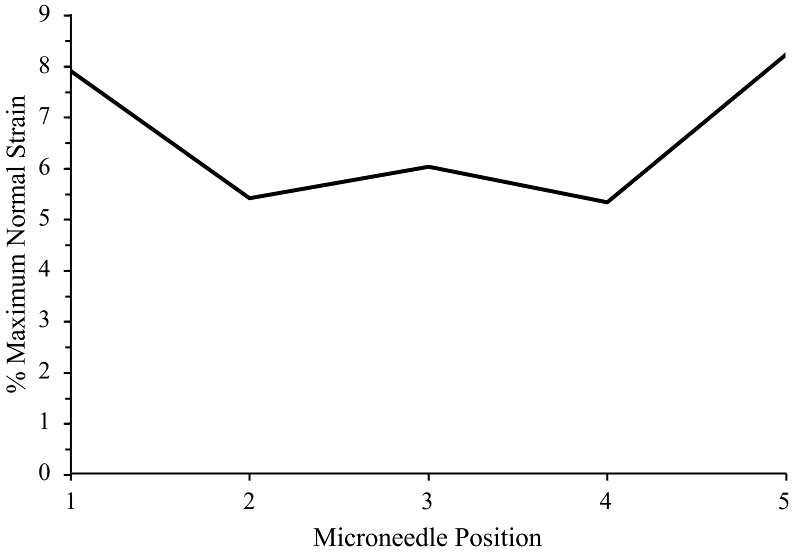

Figure 53. The peak % maximum normal strain experienced by the membrane at each microneedle position

A comparative plot of average maximum normal strain induced by MN and hypodermic needle insertions during the MN insertion timeframe is shown in Figure 54b. Initially, both devices exhibit a similar rate of strain increase from 0 to 0.1 s, following which, the profiles begin to diverge, with the hypodermic needle strain increasing at a higher rate until 0.5 s. The curves then separate more distinctly as the MN full insertion completes at 0.6 s. The hypodermic needle strain continues to increase substantially beyond 0.6 s, reaching a peak value of 50.89 %, well above the maximum strain experienced during MN insertion.

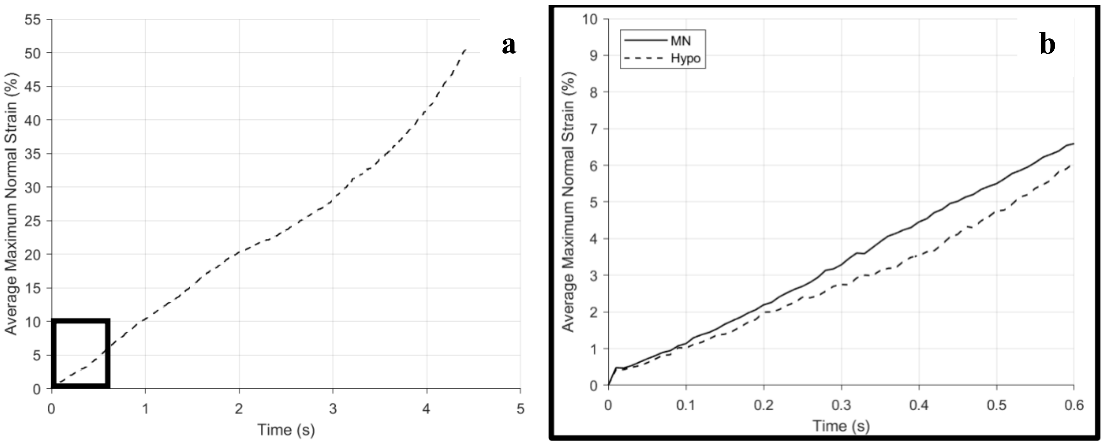

Figure 54. Average maximum normal strain (%) for (a) hypodermic needle insertion and (b) a comparison of the hypodermic needle (- -) and microneedle (-) insertion over the entirety of the microneedle insertion time (247). The box visible on graph (a) is expanded and presented as graph (b)

4.4. Discussion

Discussed in this section is the insertion mechanics and strain behaviour calculated during MN and hypodermic needle insertion. A global assessment of the response to insertion is discussed, in addition to a comparison of the maximum normal strain following both device insertions. In parallel, there is also an examination of rate of strain increase and progression to aid in establishing a more detailed understanding of device/surface interactions.

4.4.1. Global mechanical response comparison

Force-displacement behaviour is a key parameter in the evaluation of needle-based devices, with lower insertion forces correlating with reduced pain perception and improved patient compliance being generally accepted in the field (272). In this study, the HMN array exhibited a smooth and consistent force-displacement profile from the point of initial contact up to 0.22 mm insertion depth, representing 36 % of the full insertion depth (Figure 46). This initial phase observed a gradual increase in insertion force and a notable absence of signal noise, suggesting a controlled and stable rupture of the membrane. Such mechanical consistency is highly desirable in clinical contexts, where repeatable skin penetration contributes to both therapeutic reliability and user acceptability.

The stability observed in MN insertion contrasts markedly with the behaviour of the hypodermic needle, which displayed distinctive oscillations in the force-displacement profile during the early phase of insertion, specifically within the 0-0.2 mm range (Figure 54). These oscillations were consistently observed across all repeats, eliminating the possibility of instrumentation artefact and instead suggesting unwanted variation within the device-phantom interface, potentially of a more mechanical nature. The likely cause of these oscillations was the single-point contact at the lancet tip of the hypodermic needle, which, when interacting with the layered phantom-PDMS structure, may generate local frictional loading and sporadic device slippage (273, 274). This behaviour reflects a fundamental difference in the mechanical interaction mode between conventional hypodermic needles and multi-point MN arrays (273, 274).

Despite the presence of early force oscillations, the hypodermic needle showed predictable rupture behaviour, consistent with its clinical design, whereby its small bevel angle and sharp lancet geometry achieve reproducible penetration (275). This was expected on account of its repeatable, controlled, and regulatory-compliant manufacture. Beyond initial rupture, a distinct mechanical divergence between the two device types becomes evident. In the MN array, a further increase in force was observed after 0.4 mm of displacement (Figure 46). This additional force was attributed to the compression of the phantom by the rigid silicon wafer baseplate that connects the five 600 μm MNs. This compression was a structural artefact stemming from the array's design. In contrast, once rupture was achieved in hypodermic needle insertions, the force-displacement curve began to smoothen beyond 0.5 mm displacement (Figure 45). However, the latter stages of insertion were characterised by a marked increase in variability between repeats. This variability was likely due to differences in the extent of slippage between the hypodermic needle shaft and the PDMS plug, which becomes more prominent as greater needle length was inserted. Importantly, such sliding behaviour introduces clinically relevant variability, modelling how factors such as individual differences in skin hydration, elasticity, and structure may impact insertion force and user experience (115, 274).

This phenomenon aligns with the broader clinical literature, which suggests that pain and discomfort during needle-based procedures are influenced not only by the initial puncture force but also by sustained drag force and displacement during insertions which disrupt deeper layers of tissue architecture (272). Hypodermic needles, by virtue of their greater length and higher penetration depth requirements, inherently generate more extensive tissue interaction and strain, further exacerbating patient discomfort relative to minimally invasive MN systems.

4.4.2. Digital image correlation

Here, DIC has offered a high-resolution and non-invasive method to study the dynamic strain fields associated with needle insertion. By capturing full-field deformation over time, DIC enabled the visualisation and quantification of strain localisation and progression, allowing for deeper insight into the underlying insertion mechanics and their relation to tissue trauma.

Strain progression and localisation during insertion

The DIC-derived strain maps for MN insertion proved to be highly repeatable across trials, with maximum normal strain at 100 % insertion depth ranging from 9.88 % to

14.89 % (SD = 2.22 %) (Figure 50). Furthermore, the standard deviation values at rupture, 50 %, and full insertion, were comparably low (2.63 %, 2.67 %, and 2.22 % respectively), indicating consistency of insertion across the arrays from a mechanical perspective.

The high resolution enabled by the stereo-DIC method developed here was sufficient to resolve strain distribution at the level of individual needles within the 1x5 MN array (Figure 53). This capability enables the assessment of the commonly referenced "bed of nails" hypothesis, which assumes uniform deformation across the array (276). Instead, the DIC strain maps generated in this experiment clearly demonstrated inter-needle variation in strain, highlighting the role of local mechanical interactions and baseplate-induced effects. Throughout all MN insertions, no facet loss was observed, suggesting robust experimental conditions were maintained, including optimal speckle quality, uniform lighting, and minimal out-of-plane deformation. This ensured reliable particle tracking and repeatable strain quantification.

One consistent finding was the presence of increased background strain in the MN datasets, most notably in repeat 1, where compression and potentially silicone phantom sliding contributed towards the introduction of noise around the baseplate region (Figure 50). This elevated background strain likely arose due to a compressive interaction between the MN array and the phantom, with the potential for effects such as local friction at the PDMS interface to have contributed also. As the maximum strain values generated by MN insertions were relatively low, sometimes approaching the threshold of background noise, this likely contributed to the increased prominence of background strain observed in the MN datasets.

As expected, the strain fields derived from the hypodermic needle insertions differed significantly in their spatial profile (Figure 49, Figure 51). Notably, the maximum normal strain was observed to extend beyond the immediate lancet tip of the device, which suggests a broader deformation zone. Facet loss was minimal, with only a single occurrence detected at 29 % insertion depth in repeat 3, which deviated only marginally (by 1 %) from the targeted 30 % depth, indicating reliable DIC tracking, well maintained conditions, and high quality patterning. Unlike with the MN samples, hypodermic insertions demonstrated less compression-induced background strain but were more affected by sliding and drag effects. These could not be fully decoupled from true strain contributions in the strain maps, presenting an inherent limitation of the current methodology.

The stress concentration factors of the median samples illustrate a key difference in their performance: MN produced a factor of 7.5 at full insertion, whereas the hypodermic device generates 33.5 at 30 % insertion (Figure 51). This highlights the hypodermic device to generate substantially greater local stress past the point of rupture than the MN device. It must be acknowledged that a high stress concentration is desirable to ensure cutting and reliable penetration at insertion point (277). However, a high stress concentration factor beyond rupture is largely superfluous and may exacerbate tissue trauma (278). Beyond membrane rupture, the stress concentration factor indicates that MNs generate moderate stress to achieve full penetration, whereas the hypodermic device produced approximately a four times greater stress concentration factor at only 30 % insertion, reflecting aggressive mechanical behaviour.

Despite their regulated manufacture, and a consistent experimental setup, the hypodermic device insertions induced a considerably greater degree of strain variability. At 30 % insertion depth, the standard deviation reached 13.97 %, indicative of significant inter-sample mechanical divergence (Figure 49). This variability likely reflects the increased complexity of the needle-tissue interaction over longer insertion paths and again highlights the potential for clinically meaningful differences in patient response and experience. From a translational perspective, such variation may underpin inconsistencies in user pain experience, potentially affecting patient anxiety and compliance in currently available needle-based procedures.

Rate of strain increase

Understanding the rate at which strain progresses during insertion is essential for identifying how quickly tissue is deformed or ruptured, which is directly relevant to user experience and pain perception (115, 247). Strain rate is not only a mechanical parameter but has also been suggested as a factor influencing physiological discomfort, with sharper increase in strain generally associated with greater nociceptor activation and thus greater reported pain (115, 247).

The stereo-DIC method developed here enabled time-resolved tracking of strain evolution around individual needle points, allowing spatially and temporally resolved strain rate measurements. In the MN array, strain rate varied by needle position. Edge-positioned needles (positions 1 and 5) exhibited higher peak strain values, reaching 7.91 % and 8.24 % respectively (Figure 52, Table 13). Needles adjacent to the edges (positions 2 and 4) displayed slightly lower peak strains (5.42 % and 5.34 %), and the central needle (position 3) peaked at 6.04 % (Figure 52, Table 13). This spatial trend suggests a pinning effect of the phantom material, particularly between adjacent needles, which may restrict lateral membrane displacement and resultantly have a dampening effect on local strain magnitude. The result was reduced penetration efficiency in needles not located at flanking edges of the array. This finding has important implications for MN array design. Alterations to the pitch or arrangement of needles could be explored to mitigate pinning effects, potentially improving uniformity of insertion and reducing strain asymmetry. This would contribute to both the mechanical effectiveness and patient comfort of MN-based systems.

A comparative analysis of hypodermic *versus* MN induced strain at 0.6 s into the insertion further demonstrates differences in mechanical behaviour. At this point, MN insertions produced a slightly higher average maximum strain (6.59 %) than the hypodermic needle (6.07 %) (Figure 54). However, this corresponds to full MN insertion *versus* only 30 % penetration of the hypodermic needle, which equates to approximately 3.75 % of its total length. This context was crucial in interpreting the data, as although the strain values appear comparable, it in fact underscores the mechanical efficiency of MNs in generating similar strain levels to hypodermic needles, despite operating at significantly shallower penetration depths.

Initial force-displacement data support these findings, confirming that the sharp lancet geometry of the 25-G hypodermic needles allows for an effective initial penetration with relatively low applied force. However, over full insertion, hypodermic needles produce substantially higher strain values due to their larger shaft diameter and extended penetration depth. These geometric and mechanical differences contribute to the more invasive nature of hypodermic injections compared to MN arrays.

4.4.3. Methodological limitations and future work recommendations

Several limitations should be acknowledged when interpreting the findings of this study. The silicone/PDMS phantom provides a useful approximation of human skin mechanics but cannot fully replicate *in vivo* human tissue and physiological responses, including perfusion, immune activation, and pain perception. Therefore, while the method developed here has proved repeatable and provided informative trends, definitive clinical extrapolation should be approached with caution.

The PDMS backing, selected to mimic the mechanical support provided by underlying dermal architecture, played a critical role in enabling realistic epidermal deformation and rupture behaviour. Its inclusion prevented excessive or unrealistic stretching of the epidermal phantom during insertion, thereby contributing to physiologically relevant failure patterns. However, the presence of this backing introduced potentially artefactual or exaggerated compressive behaviour and membrane/device slippage, complicating the interpretation of the DIC strain data. These effects were particularly evident in the MN samples, where background strain originating from baseplate compression could not be fully isolated from insertion-induced strain. In the hypodermic needle samples, membrane drag and lateral displacement introduced additional confounding strain patterns, particularly across the lateral deformation fields, and may have contributed to the premature loss of a facet in hypodermic repeat 3, which occurred 1 % earlier than the targeted depth (Figure 49).

The stereo-DIC system and experimental design developed in this study enabled measurement of both in-plane and out-of-plane surface deformations, including sub-surface strain distributions beneath the epidermal phantom. However, limitations related to the spatial resolution and frame rate of the cameras must be acknowledged. In particular, as this study focused primarily on MN insertion, a high frame rate was selected to capture rapid deformation events with sufficient temporal resolution. Consequently, the recording duration was limited, resulting in a shorter observation period that did not encompass the full insertion of the hypodermic devices. Although a sufficient number of frames were captured to enable a fair and valid comparison, these factors represent limitations of the experimental design and may contribute to underestimation of peak strain magnitudes and temporal strain gradients within the hypodermic needle group, as well as restrict direct temporal comparisons of insertion dynamics between both device types.

Inter-sample variability in strain measurements may have been influenced by minor inconsistencies in the fabrication of the bar-coated silicone epidermal phantom. While the use of synthetic materials offered improved reproducibility compared to *ex vivo* biological tissue, small variations in membrane thickness, surface topography, and coating uniformity still introduced experimental variability (279). Standard deviations in the MN datasets were generally within acceptable limits, but the greater spread exhibited by the hypodermic needle samples likely reflects the increased mechanical disruption and deformation associated with larger, deeper insertions. This amplified the impact of even small differences in phantom properties on strain distribution outcomes.

Future work should consider the integration of volumetric imaging techniques capable of capturing subsurface and internal deformation, such as micro-computed tomography, optical coherence tomography (OCT), or high-resolution ultrasound. These approaches could complement surface-level data obtained *via* stereo-DIC, offering a more comprehensive understanding of device-tissue interaction. The inclusion of *in vivo* studies or the use of excised human skin would improve both clinical relevance and translational applicability. Of particular interest is further examination of the membrane pinning phenomenon observed in MN arrays, which may significantly affect insertion efficiency and localised tissue trauma and can inform device optimisation with variations in array pitches and device geometries. Finally, to bridge the gap between experimental mechanics and patient outcomes, future research should adopt a multidisciplinary approach integrating computational modelling, experimental validation, and clinical trials.

5. Chapter 5: *In Vitro* Cytotoxicity Assessment

This chapter presents a study investigating the cytotoxicity of silicon SMN and HMN, as well as silicon starting material. The study design utilised a human immortalised keratinocyte cell line to evaluate cell viability post exposure to devices. Cytotoxicity was assessed utilising an *in vitro* cell viability assay in compliance with the ISO 10993 standards (225).

5.1. Introduction

5.1.1. Biocompatibility in medical devices

Biocompatibility, as defined by ISO 10993-1, is the ability of a material to perform with an appropriate host response in a specific application (215, 221). This definition highlights that biocompatibility is not an intrinsic property of a material but heavily depends on its intended use, contact site, and the duration of exposure. The ISO 10993 series, developed by the International Organization for Standardisation, provides an internationally recognised framework to assess the biological safety of medical devices, helping to ensure the quality, safety, reliability, and regulatory compliance across global markets (215). In the context of medical devices, biocompatibility evaluation is essential to confirm that materials will not induce harmful effects including but not limited to cytotoxicity, sensitisation, irritation, or systemic toxicity when in contact with the human body (212). Effective biocompatibility assessment supports risk management strategies and standardises regulatory approval processes, ultimately safeguarding patient health and device performance, and expediting regulatory processes (212).

Poor biocompatibility has the potential to lead to inflammation, toxic reactions, and even failure in clinical trials (280). Consequently, this may result in costly redesigns, regulatory delays, or funding loss, with regulatory agencies such as the FDA and the MHRA mandating comprehensive biocompatibility testing for device approval. Factors influencing biocompatibility include material composition, surface properties, device design, and the nature and duration of contact with the body (281). Evaluation strategies utilise a tiered testing approach, as outlined in the ISO 10993 series, which tailors assessment to the type of device, materials used, anatomical location, and exposure time (215). Among these tests, *in vitro* cytotoxicity screening, particularly guided by ISO 10993-5, serves as one of the earliest and most vital steps in identifying potentially harmful materials (215).

5.1.2. Cytotoxicity and biocompatibility

Cytotoxicity and biocompatibility, despite being closely related, are distinct concepts through the lens of medical device evaluations. Biocompatibility refers to the overall ability of a material or device to perform its intended function without eliciting adverse local or systemic effects within the host (221). It encompasses the evaluation of broad range of biological responses, from inflammation to immunogenicity. In contrast, cytotoxicity specifically addresses the material's potential to cause cell damage or death (282). Cytotoxicity testing forms a critical subset of biocompatibility assessment, offering a fast, cost-effective means of identifying materials likely to produce harmful cellular responses before progressing to more complex and costly *in vivo* evaluations. As such, while cytotoxicity is not synonymous with biocompatibility, it represents a solid foundation in determining whether a material is likely to be biocompatible in its intended application.

5.1.3. ISO 10993-5: Guidance for *in vitro* cytotoxicity testing

The ISO 10993 series provides a comprehensive framework for evaluating the biological safety of medical devices (215). Within this series, ISO 10993-5 specifically addresses the *in vitro* assessment of cytotoxicity, offering standardised guidance for determining whether a material causes harmful effects on cultured cells (215). This is particularly relevant as cytotoxicity serves as an early and essential indicator of biocompatibility, as previously discussed.

ISO 10993-5 outlines three testing approaches:

- Direct contact, whereby the test material is placed in immediate contact with a cell layer;
- Indirect contact, involving a barrier (*e.g.,* agar or filter) between the material and cells;
- Extract testing, in which material leachables are incubated with cells to assess potential toxicity.

These methodologies are typically carried out over 24 - 48 hours, using cell lines relevant to the devices intended site of contact and application. Human immortalised keratinocyte cells (HaCaT), for example, are often used for evaluating skin-contacting technologies such as MNs (283, 284). Results are assessed based on cell viability, with a $\geq$ 70% viability threshold relative to controls commonly accepted as indicating non-cytotoxicity.

The use of positive and negative controls, as well as standardised test conditions, ensures reproducibility and comparability of results across laboratories and device types. However, it is acknowledged that this method offers only a preliminary indication of safety and must be used to gather a foundational understanding prior to *in vivo* assessments as advised under ISO 10993 (215).

This standard plays a critical role in the regulatory approval process, providing early evidence that a device material is unlikely to provoke acute cellular toxicity. In the context of novel transdermal systems such as MNs, compliance with ISO 10993-5 is foundational for risk mitigation in early-stage device development and progressing safely down the roadmap to clinical roll out, as will be discussed in the next subsection.

5.1.4. Relevance to microneedle-based technologies

Microneedle technologies often employ novel materials or coatings, including polymers, composites, or bioactive agents, which may not have extensive safety data. Furthermore, the unique geometry and fabrication methodologies (*e.g.,* moulding, lithography, or additive manufacturing) introduce potential residuals, leachables, or surface contaminants that warrant cytotoxic evaluation. In this context, extract testing under ISO 10993-5 serves as a valuable tool for identifying any acute cytotoxic effects arising from the device in its final, fabricated form.

For novel medical devices such as MN, early assessment of biocompatibility using *in vitro* cytotoxicity protocols are crucial in translational success, allowing for a smooth transition between research and clinical deployment. Beyond regulatory compliance, such testing facilitates risk mitigation in design and material selection, ensuring that devices are safe for their intended short- or long-term application (285).

In this study, HaCaT keratinocytes were selected for the cytotoxicity assay due to their strong biological relevance. As an immortalised human keratinocyte cell line, HaCaTs are widely used in dermatological research because they retain many of the structural and functional characteristics of normal epidermal keratinocytes (284). Given that MNs primarily interact with the epidermis during application, HaCaTs provide an appropriate and representative *in vitro* model to evaluate potential cellular toxicity and predict localised skin responses (286). Their robustness, reproducibility, and standardised culture conditions also make them well-suited for regulatory-aligned cytotoxicity testing (286). Demonstrating cytocompatibility with this cell type is therefore a key milestone in building both scientific credibility and regulatory acceptance for the MN platform developed in this research.

5.2. Materials and methodology

The experimental approach employed within this chapter to evaluate the biocompatibility and potential cytotoxicity of the silicon MN devices is detailed in this section. HaCaT keratinocytes were utilised as a representative epidermal cell line to model skin responses to exposure conditions and materials. The below will detail sample preparation, cell culture, viability assays, and the statistical analysis used. All methodology employed in this chapter was in line with the ISO 10993-5 guidelines.

5.2.1. Experimental methodology

All experimental work was conducted under aseptic conditions using a Class II biological safety cabinet, which was disinfected before and after each use. All instrumentation and consumables introduced into the cabinet were sterilised immediately prior to transfer to maintain sterility throughout all procedures.

Media preparation

Complete keratinocyte growth medium was prepared by supplementing Dermal Cell Basal Medium (ATCC PCS-200-030) with the Keratinocyte Growth Kit (ATCC PCS-200-040), as *per* the manufacturer’s instructions. This formulation creates a serum-free environment specifically optimised for keratinocyte culture, with a low calcium concentration (0.06 mM) to reduce spontaneous differentiation and inhibit fibroblast overgrowth. No feeder layers or additional extracellular matrix (ECM) proteins were required. The final concentrations of the individual components in the complete medium and their biological role can be found in Table 14.

Table 14. The composition of growth medium utilised for HaCaT cell culture, their concentrations, and the purpose of each component

Component	*Final Concentration in Growth Medium*	*Purpose in Keratinocyte Culture*
Extract P	0.4 %	Provides growth-promoting peptides and nutrients to support keratinocyte proliferation
rh TGF-α	0.5 ng/mL	Stimulates cell growth and survival *via* EGF receptor activation
L-glutamine	6 mM	An essential nutrient for energy and protein synthesis
Hydrocortisone	100 ng/mL	Reduces inflammation and supports cell differentiation and barrier function
Insulin	5 µg/mL	Promotes glucose uptake and cell metabolism to support growth
Epinephrine	1.0 µM	Modulates signalling pathways to enhance cell survival and reduce oxidative stress
Apo-transferrin	5 µg/mL	Supplies iron in a bioavailable form without promoting oxidative damage

HaCaT keratinocyte cell culture

HaCaT keratinocytes were used as the representative epidermal cell for biocompatibility testing in this chapter. Below details the culture of these cells, from storage to seeding and splitting.

HaCaT cell thawing

Cryovials containing HaCaT keratinocytes at passage 8 (P8, 8th culture split) and passage 26 (P26, 26th culture split) were retrieved from liquid nitrogen storage and immediately placed in a 37 °C water bath to minimise dimethyl sulfoxide (DMSO)-induced cell lysis. The cryovial caps remained above the water level at all times to avoid contamination.

Under aseptic conditions, the thawed HaCaT cells were transferred into sterile 15 ml Falcon tubes containing 5 ml of growth medium and centrifuged at 300 × g for 5 mins. The supernatant was discarded, and the cell pellets were resuspended in 1 ml of fresh growth medium.

Cell viability was assessed using an erythrosin B (16423-68-0) exclusion assay. This dye was selectively taken up by cells with compromised plasma membranes, thereby staining only non-viable cells. Live cells excluded the dye and remain unstained, allowing for differentiation between viable and non-viable cells. A cell count was performed on each passage by pipette mixing 10 µl of cell suspension with 10 µl of erythrosin B. A 10 µl sample of this was then transferred onto a glass slide, which was then inserted into the LUNA-II™ Automated Cell Counter (Logos Biosystems) in brightfield mode for analysis. Cell counts were obtained (Table 15) and used to calculate appropriate seeding densities (Section 5.2.1.2.3: Cell Seeding).

Table 15. Cell counts and viabilities for each passage cultured (P8 and P26)

	P8	*P26*
Total cell concentration (cells/ml)	$1.35\text{x}10^6$	$6.33\text{x}10^6$
Live cell concentration (cells/ml)	$1.25\text{x}10^6$	$5.99\text{x}10^6$
Dead cell concentration (cells/ml)	$1.0\text{x}10^5$	$3.4\text{x}10^5$
% Viability	92.2	94.6

Cell seeding

A seeding density of $1\text{x}10^4$ cells/cm² was targeted, as commonly recommended for culturing expanding HaCaT keratinocytes. For T75 flasks (75 cm²), this corresponds to approximately $7.5\text{x}10^5$ cells *per* flask in 15 ml medium.

Flasks were incubated at 37 °C, 5 % CO_2. After 24 hours, a media change was performed to support proliferation. Cells were grown to ~80 % confluency, typically by 72 hours.

Cell splitting

Prior to cell splitting, old growth media was aspirated and immediately replaced. Cells were washed with 5 ml sterile phosphate-buffered saline (PBS), which was then aspirated. Cells were detached by adding 3 ml of prewarmed 0.05% trypsin-ethylenediamine-tetra acetic acid (EDTA) solution and incubating for 5 mins at 37 °C with 5 % CO_2. The flasks were then tapped manually to promote detachment. Once detached, 3 ml of growth medium was added, and the cell suspension was mixed by pipetting.

The detached cell suspension was transferred to a sterile 15 ml falcon tube and centrifuged at 300 g for 5 mins. The supernatant was discarded, and the cell pellet resuspended in 1 ml of fresh growth medium. A cell count was performed as described under HaCaT cell thawing. The cell suspension was then diluted to achieve the desired final concentration for seeding into 6 well plates (Table 16), which have a working volume and total growth area *per* well of 2 ml and 9.5 cm^2 respectively. The seeding densities and incubation periods used for each exposure are summarised in Table 16.

For repeat 2, the initial seeding density was reduced compared to repeats 1 and 3 due to limited lab access preventing a 4-day incubation. The incubation period was extended to 7 days to ensure the cell density at exposure matched that of the other repeats (2.0×10^4 cells/cm^2). With the HaCaT cells typically double every 24 - 36 hours, the 1.5-fold increase in cell number over 7 days to reach the target density well within expected proliferation capacity, while maintaining consistent exposure conditions across all repeats.

Table 16. Cell culture schedule including seeding dates and cell seeding density, in addition to the incubation period, cell density at exposure, and exposure date

n	*Seed date*	*Cell seeding density*		*Incubation period (days)*	*Cell density at exposure (cells/cm^2)*	*Exposure date*
		cells/ml	cells/cm^2			
1	10 Apr	9.5x10^4	2.0x10^4	4	2.0x10^4	14 Apr
2	16 Apr	6.3x10^4	1.3x10^4	7	2.0x10^4	23 Apr
3	24 Apr	9.5x10^4	2.0x10^4	4	2.0x10^4	28 Apr

Device sterilisation and preparation

Device samples used *per* exposure consisted of one HMN array, one SMN array, one block from the HMN wafer edge (HB), and one block from the SMN wafer edge (SB). The HB and SB samples were included as controls for weight, being taken from unetched wafer areas to account for any potential effects of device weight on the cell monolayers.

Samples were extracted from the wafer carrier boxes and sterilised using a moist heat autoclave cycle at 121 °C and 2 bar pressure for 20 mins. These conditions were consistent with validated sterilisation cycles described in ISO 17665-1:2006 and widely accepted industry standards such as the United States Pharmacopeia <1211> and the European Pharmacopoeia. After sterilisation, the devices were retained under sterile conditions until use.

Plate layout and experimental controls

The experimental plate layout is illustrated in Figure 55, with each labelled according to its contents. One plate was used *per* repeat.

Two types of controls were included in the experiments:

- **Positive control:** 1% Triton X-100 (20 µl) was added to induce cell death. Triton X-100, a non-ionic surfactant, disrupted cell membranes by solubilising membrane lipids and proteins, causing rapid loss of membrane integrity and cell viability. This control served to verify the assay’s sensitivity to cytotoxic effects.

- **Negative control:** No treatment to serve as a baseline for normal cell viability.

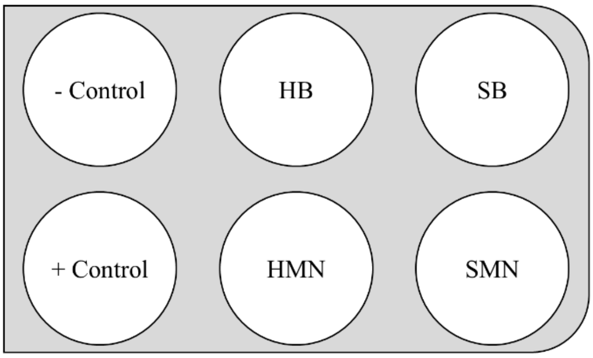

Figure 55. Plate plan for each exposure sample

Following exposure, cells were allowed zero recovery time before device removal and viability counting to ensure immediate effects were measured without interference from cellular repair or proliferation.

Cell viability assay

Cell viability assays were conducted at 24 hours post-exposure for all three experimental replicates. To investigate potential longer-term cytotoxic effects, a single additional replicate was performed at the 48-hour timepoint. This extended timepoint was included to assess sustained cell viability beyond the standard 24-hour exposure period stipulated by ISO 10993-5. Due to practical limitations, only one 48-hour replicate was conducted; therefore, statistical comparisons were not performed for this timepoint. A summary of seeding, exposure, and extraction timepoints for all repeats is provided in Table 17.

Table 17. The seeding, exposure, and extraction date for each repeat

n	*Seeding date*	*Incubation period (days)*	*Exposure date*	*Extraction date*	
1	10 Apr	4	14 Apr	15 Apr	
2	16 Apr	7	23 Apr	24 Apr	25 Apr
3	24 Apr	4	28 Apr	29 Apr	

Immediately prior to exposure, a growth medium change was performed in all wells to ensure standardised metabolic conditions. Subsequently, the positive control and devices were applied consecutively to the assigned wells, allowing them to incubate for 24 hours before assessment. Well assignments and control types are as previously stated under plate layout and experimental controls. Plates were then incubated for 24 hours (or 48 hours for the extended replicate) at 37 °C and 5 % CO_2.

At the appropriate timepoint, MN devices were carefully extracted using sterile tweezers and discarded to sharps waste. The culture supernatant was then collected from each well into sterile 15 ml falcon tubes to capture any detached cells and centrifuged at 300 × g for 5 mins. The resulting supernatant was aspirated into a new Falcon tube and stored at -20 °C. The cell pellet was retained in the original tube.

Each well was washed twice with 1 ml sterile PBS. To detach adherent cells, 500 µl of prewarmed 0.05 % trypsin-EDTA was added to each well and incubated at 37 °C, 5 % CO_2 for approximately 10 mins (not exceeding 15 mins). Manual tapping was used to promote full detachment. Following detachment, 500 µl of fresh growth medium was added to neutralise the trypsin.

To assess viability, 10 µl of the cell suspension was combined with 10 µl erythrosin B. This membrane-impermeable dye was excluded by viable cells but taken up by dead cells, allowing distinction by microscopy. Cell counts were then performed on each sample following the previously described process.

5.2.2. Analytical methodology

This subsection describes the analytical procedures used in this study to quantify cell viability post-exposure to MN devices and silicon material. Viability was determined *via* an erythrosin B exclusion assay, with percentage viability calculated and analysed statistically, in accordance with ISO 10993-5 guidelines.

Cell viability assay

Cell viability was quantified using erythrosin B exclusion staining combined with automated cell counting. Following staining, counts were performed to determine the total number of cells, live cells, and dead cells/ml of suspension. The percentage viability was calculated using Equation 4.

$$Viability\ (\%) = \left(\frac{number\ of\ live\ cells}{total\ number\ of\ cells}\right)\ x\ 100$$

Equation 4. The formula used to calculate the % cell viability post exposure

Cell suspensions were mixed in equal volumes (10 µl each) with erythrosin B dye, which selectively penetrates cells with compromised membranes, thereby staining only non-viable cells. Viable cells exclude the dye and remain unstained, allowing differentiation by brightfield microscopy.

Cell counts were performed using the LUNA-II™ Automated Cell Counter (Logos Biosystems) in brightfield mode, with manual verification to ensure accuracy. The counts obtained were used to calculate the cell concentration and viability for each sample, informing subsequent seeding densities and exposure assessments.

Statistical analysis

Statistical analyses were performed using Microsoft Excel. A summary of the statistical analysis parameters and rationale can be found in Table 18. Cell viability was calculated as the percentage of live cells relative to the total number of cells for each sample. For the 24-hour timepoint, three independent replicates were performed *per* group. For the 48-hour timepoint, one replicate was conducted.

Table 18. A summary of the statistical elements applied in this study

Element	*Summary and Justification*
Dependent variable	% of live cells relative to the total cell count
Independent variable	Treatment group (negative control, HMN, HB, SMN, SB)
Descriptive statistics	Mean, standard deviation, standard error of the mean
One-way ANOVA	Parametric test comparing mean % viability across groups, generating F and *p* values. F value quantifies the ratio of the variance between groups to within groups, with larger F indicating greater between group differences. Statistical significance is determined by the *p* value relative to a.
Dunnett's post-hoc	Compares each treatment group to the control group, whilst controlling Type I error. An adjusted *p* value is generated from this.
Bonferroni correction	Used to limit false positives by dividing the α value by the number of comparisons.
Significance threshold (a)	$p = 0.05$. After Bonferroni adjustment, $\alpha = 0.0125$.
Normalisation/ scaled viability	Viability is expressed relative to control to allow comparison and evaluation against the ISO 10993-5 threshold of < 70 % cytotoxic

Descriptive statistics, including means, standard deviations, and standard errors of the mean, were calculated for each group at the 24-hour timepoint. These data were visualised using bar graphs with error bars representing the standard error of the mean. To assess statistical differences in cell viability between groups at 24 hours, a one-way analysis of variance (ANOVA) was conducted. This test compared five groups: Negative Control, HMN, HB, SMN, and SB. Although formal tests for normality (*e.g.,* Shapiro-Wilk) and homogeneity of variances (*e.g.,* Levene's test) were not conducted due to small sample sizes ($n = 3$ *per* group), the use of ANOVA was deemed appropriate based on the relatively low variability observed across all replicates. Parametric tests are generally robust to modest deviations from these assumptions in small, balanced designs. Following ANOVA, Dunnett's post-hoc test was used to compare each treatment group directly against the negative control. This test controls for Type I error in multiple comparisons made to a single control group. Bonferroni-adjusted p-values were calculated, and a significance threshold of $\alpha \leq 0.0125$ was applied to account for the four comparisons.

Scaled viability values were also calculated by normalizing each sample's mean % viability to the mean viability of the negative control (set as 100 %). This allowed expression of relative viability across samples and enabled interpretation against the ISO 10993-5 threshold of 70 %, which defines cytotoxicity as < 70 % viability relative to the negative control. No formal statistical analysis was performed on the 48-hour data due to the limited sample size (*n* = 1); results are presented descriptively.

5.3. Experimental results

The following section summarises the results of the erythrosin B assay performed at both 24 and 48 hour time points post exposure to silicon base material and silicon MNs. Cell viability was calculated relative to negative controls and assessed statistically.

5.3.1. Cell viability assay: 24 hour timepoint

Cell viability at the 24-hour timepoint was assessed across all sample groups, with raw data presented in Table 19. Total, live, and dead cell counts, and percentage viability were measured in three independent replicates *per* group. The positive control samples consistently showed 0 % viability, which confirmed complete cytotoxicity. Negative control samples exhibited mean percentage viability of 89.19 % (± 2.2 % SD), indicating a healthy baseline of cell survival.

Treatment groups showed similarly high viability, with mean percentage viability values of 91.86 % (± 2.5 % SD) for HMN, 96.53 % (± 1.0 % SD) for HB, 95.55 % (± 2.9 % SD) for SMN, and 92.99 % (± 6.2 % SD) for SB. Standard error of the mean ranged from 0.6 - 3.6 % across treatments, reflecting low variability between replicates. A summary of the mean % viabilities for each group and their corresponding standard deviation and error can be found in Table 20. This data indicates that cell viability remained consistently high across all treatments and comparable to the negative control after 24 hours of exposure. Error bars in the bar graphs in Figure 56 represent the standard error of the mean, reflecting variability between biological replicates.

Table 19. Cell count (cells/ml) and viability (%) results for each well across three replicates. Samples reported include all controls (positive and negative) and all samples tested (hollow and solid, microneedles and blocks) post 24 hour exposure

n	*Well*	*Sample*	*Cell Count (cells/ml)*			*% Viability*
			Total	*Live*	*Dead*	
1	1	+ control	2.87x10^{4}	0.00	2.87x10^{4}	0.00
	2	- control	5.35x10^{5}	4.78x10^{5}	5.73x10^{4}	89.35
	3	HMN	2.82x10^{5}	2.63x10^{5}	1.91x10^{4}	93.26
	4	HB	5.54x10^{5}	5.35x10^{5}	1.91x10^{4}	96.57
	5	SMN	4.01x10^{5}	3.92x10^{5}	9.55x10^{3}	97.76
	6	SB	3.39x10^{5}	3.30x10^{5}	9.55x10^{3}	97.35
2	1	+ control	4.78x10^{3}	0.00	4.78x10^{3}	0.00
	2	- control	3.96x10^{5}	3.44x10^{5}	5.25x10^{4}	86.87
	3	HMN	3.63x10^{5}	3.39x10^{5}	2.39x10^{4}	93.39
	4	HB	3.10x10^{5}	2.96x10^{5}	1.43x10^{4}	95.48
	5	SMN	1.19x10^{5}	1.15x10^{5}	4.78x10^{3}	96.64
	6	SB	3.25x10^{5}	3.11x10^{5}	1.43x10^{4}	95.69
3	1	+ control	9.55x10^{3}	0.00	9.55x10^{3}	0.00
	2	- control	1.62x10^{5}	1.48x10^{5}	1.43x10^{4}	91.36
	3	HMN	2.53x10^{5}	2.25x10^{5}	2.87x10^{4}	88.93
	4	HB	1.62x10^{5}	1.58x10^{5}	4.78x10^{3}	97.53
	5	SMN	6.21x10^{4}	5.73x10^{4}	4.78x10^{3}	92.27
	6	SB	3.34x10^{4}	2.87x10^{4}	4.78x10^{3}	85.93

Table 20. Summary of mean viability (%), standard deviation, and standard error of the mean for each sample group post 24 hour exposure

Sample	*Mean % Viability*	*Standard Deviation*	*Standard Error of the Mean*
+ control	0.00	0.0	0.0
- control	89.19	2.2	1.3
HMN	91.86	2.5	1.5
HB	96.53	1.0	0.6
SMN	95.55	2.9	1.7
SB	92.99	6.2	3.6

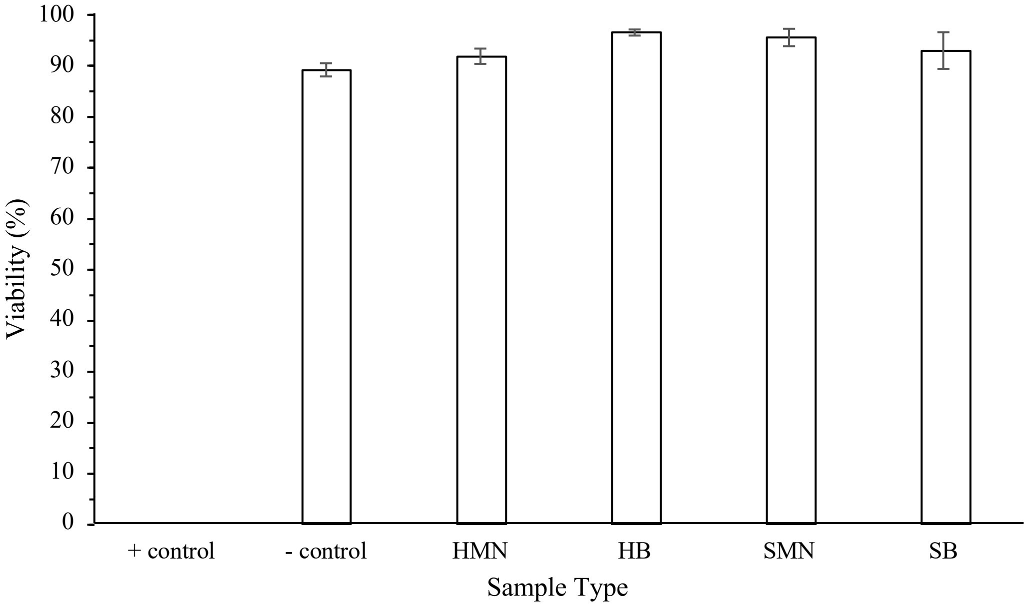

Figure 56. The viability (%) of HaCaT cells from each group (n = 3) following 24 hour exposure

A one-way ANOVA was performed to assess differences in cell viability (% viability) among five groups: negative Control, HMN, HB, SMN, and SB. The analysis indicated no statistically significant differences between the groups (F(4, 10) = 2.19, $p = 0.143$), suggesting that none of the treatments had a significant overall effect on cytotoxicity (Table 21).

Table 21. One way ANOVA results comparing sample group viability indicate no statistical difference between groups

Statistic	*Value*
F-value	2.19
p-value	0.143

Despite the lack of overall significance, Dunnett's post-hoc test was conducted to compare each treatment group directly against the negative control, as this method specifically controls for type I error when making multiple comparisons to a single control group. The post-hoc analysis revealed that none of the treatments significantly differed from the negative control after adjustment for multiple comparisons (Bonferroni-adjusted *p*-values > 0.0125). Although the HB treatment approached significance in the raw p-value (*p* = 0.017), this difference was not statistically significant following correction for multiple testing (adjusted *p* = 0.068) (Table 22). Therefore, none of the treatments demonstrated a significant cytotoxic effect compared to the negative control.

Table 22. Dunnett's post hoc analysis results comparing each sample group to the negative control. No sample group showed statistically significant differences in viability relative to the negative control at the adjusted significance threshold

Negative control versus	*t-statistic*	*raw p-value*	*Bonferroni-adjusted p-value*	*Significant (Threshold a ≤ 0.0125)*
HMN	-1.36	0.246	0.984	No
HB	-5.14	0.017	0.068	No
SMN	-3.00	0.043	0.172	No
SB	-1.00	0.403	1.612	No

Cell viability was assessed at the 24-hour timepoint to evaluate any potential cytotoxic effects of the device test samples. The negative control was used as the baseline, with its mean viability normalized to 100%. The viability of each test sample was expressed as a percentage relative to this baseline. As shown in Table 23, the negative control exhibited a mean viability of 89.19 %. All test samples demonstrated viability values equal to or exceeding the negative control, with scaled viability percentages ranging from approximately 103.0 % - 108.3%.

Scaled viability values above 100 % occur due to the raw viability measurements experienced by some samples being slightly higher than the negative control. This was attributable to biological variability, experimental noise, or minor differences in cell proliferation or assay conditions. Such variations are typical in cell viability assays.

According to ISO 10993-5 standards, a viability of 70 % or higher compared to the negative control indicates no cytotoxicity. Therefore, all tested samples are considered non-cytotoxic under the conditions of this assay.

Table 23. Raw mean percentage viability and scaled viability of each sample group relative to the negative control

Sample	*Mean % Viability (Raw)*	*Scaled Viability (% of Negative Control)*
+ control	-	-
- control	89.19	100.0
HMN	91.86	103.0
HB	96.53	108.3
SMN	95.55	107.1
SB	92.99	104.2

5.3.1. Cell viability assay: 48 hour timepoint

A single replicate of the cell viability assay was conducted at the 48-hour timepoint to provide additional insight into longer-term cytotoxicity. As shown in Table 24, cell viability remained high across all treatment groups, ranging from 90.00 % - 96.50 %, with the negative control at 87.94 %. The positive control showed 0 % viability, which confirmed assay validity. Results are displayed graphically in Figure 57. Although only one replicate was performed at 48 hours, these results were consistent with the 24-hour data and indicate sustained cell viability beyond the standard ISO 10993-5 24-hour exposure period. Importantly, the 48-hour timepoint extends well beyond both the ISO 10993-5 requirement and the intended use period of the devices, and given the absence of adverse effects, further replicates at this timepoint were not pursued. Due to the single replicate performed at the 48-hour timepoint, statistical analysis was not possible, limiting the ability to draw definitive conclusions about long-term cytotoxicity. Nonetheless, the observed viability levels align with the 24-hour data, providing preliminary evidence of sustained cell compatibility.

Table 24. Summary of mean viability (%), standard deviation, and standard error of the mean for each sample group post 48 hour exposure

n	*Well*	*Sample*	*Cell Count (cells/ml)*			*% Viability*
			Total	*Live*	*Dead*	
1	1	+ control	0	0	0	0.00
	2	- control	2.82×10^5	2.48×10^5	3.34×10^4	87.94
	3	HMN	4.35×10^5	3.96×10^5	3.82×10^4	91.03
	4	HB	4.30×10^5	3.87×10^5	4.30×10^4	90.00
	5	SMN	3.44×10^5	3.20×10^5	2.39×10^4	93.02
	6	SB	1.43×10^5	1.38×10^5	4.78×10^3	96.50

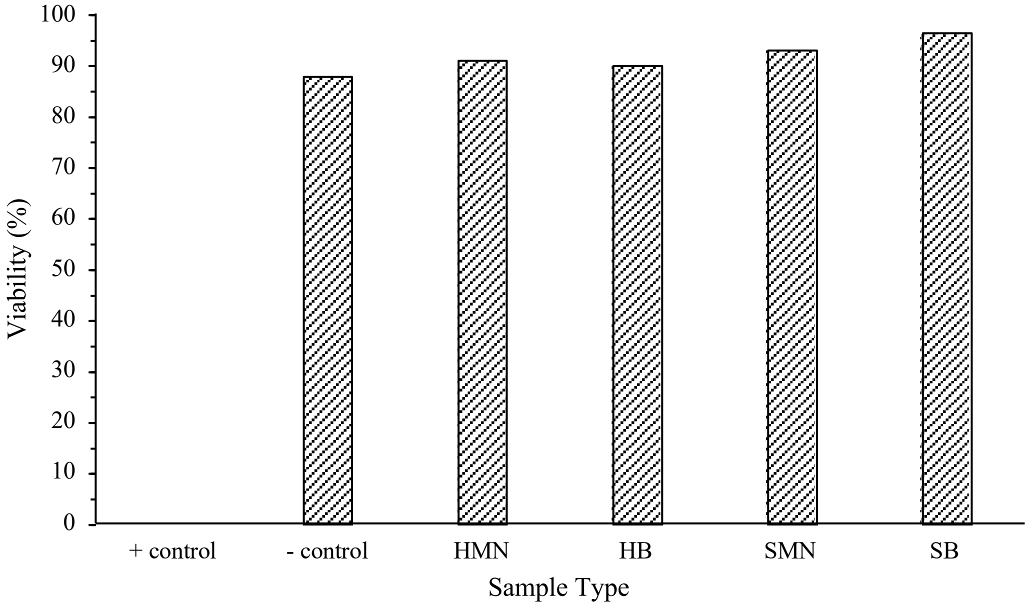

Figure 57. The viability (%) of HaCaT cells from each group (n = 1) following 48 hour exposure

The bar graph (Figure 58) illustrates the mean percentage cell viability for each sample group at both 24 (blank) and 48-hours (crosshatch) post-exposure. Viability remained consistently high across all samples and timepoints, with values generally above 85%, indicating minimal cytotoxic effects. The 48-hour single replicate data align closely with the 24-hour mean values, suggesting sustained cell viability over the extended exposure period. Due to the limited number of replicates at 48 hours, no formal statistical comparison was performed; however, the similar viability levels support the conclusion that the MN devices and wafer blocks do not induce significant cytotoxicity up to 48 hours.

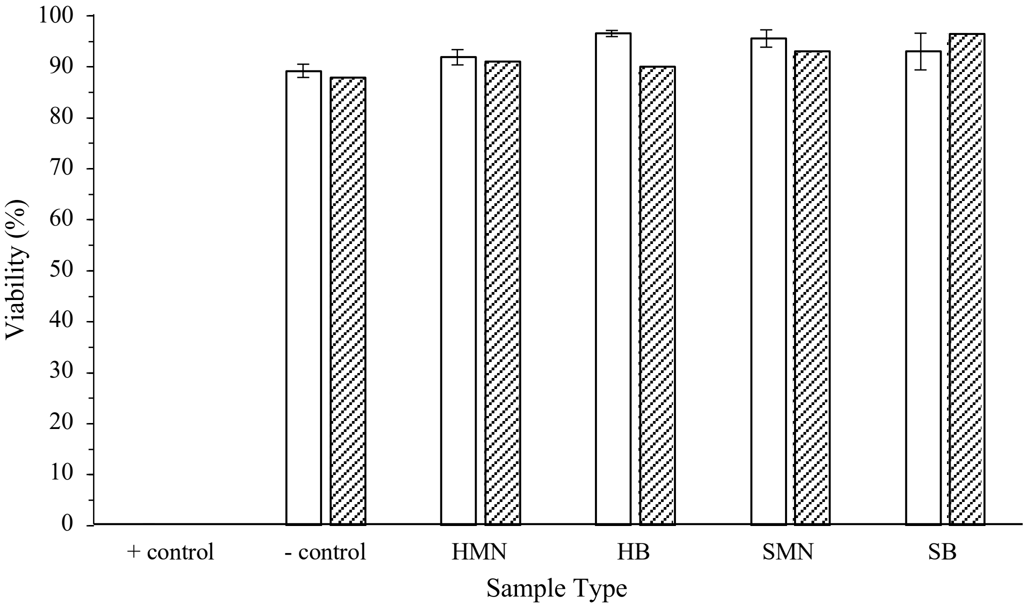

Figure 58. A comparison of cell viability (%) from each group post 24 and 48 hour exposure

At 48 hours, the negative control (87.94 % viability) was set as the reference for scaling. All test samples surpassed this baseline, with scaled viabilities between 102.3 % - 109.7 %, while the positive control confirmed assay function with 0 % viability (Table 25).

Values exceeding 100 % reflect slight increases in raw viability relative to the negative control, likely due to typical biological variation or minor experimental differences. Despite only one replicate, all test samples remained well above the ISO 10993-5 cytotoxicity threshold of 70 %. As 48 hours exceeds both the ISO-defined exposure period and the expected device use duration, these results further indicate acceptable long-term cytocompatibility.

Table 25. Raw mean percentage viability and scaled viability of each sample group relative to the negative control post 48 hour exposure

Sample	*Mean % Viability (Raw)*	*Scaled Viability (% of Negative Control)*
+ control	-	-
- control	87.94	100.0
HMN	91.03	103.5
HB	90.00	102.3
SMN	93.02	105.8
SB	96.50	109.7

5.4. Discussion

The following discussion investigates the reported results of the cell viability assay at both the 24 and 48 hour timepoint. The interpretation of these results focused on whether the devices or silicon material induced any adverse effects on cellular viability and therefore whether the tested materials had any cytotoxic effects over the investigated time periods.

5.4.1. Cell viability at 24 hours timepoint

The high cell viability observed across all test samples at the 24 hours timepoint consistently exceeded the ISO 10993-5 threshold of 70 % of the negative control, which confirmed that the MN devices and wafer blocks tested do not elicit cytotoxic effects in HaCaT keratinocytes under the assay conditions (Figure 56) (215). The complete loss of viability in the positive control validates the sensitivity and robustness of the cytotoxicity assay employed in this study.

Notably, the viability outcomes between the MNs and blocks taken from the same wafer showed no statistically significant differences despite minor variations in mean values (HMN: 91.86 % ± 2.5 % SD *versus*. HB: 96.53 % ± 1.0 % SD; SMN: 95.55 % ± 2.9 % SD *versus*. SB: 92.99 % ± 6.2 % SD) (Figure 20). This indicates that the physical form and weight of the samples do not substantially influence keratinocyte viability at the 24-hour point. The slightly elevated viability observed in HB samples could reflect minor effects related to sample geometry or surface characteristics; however, these remain within normal biological variability and do not raise concerns regarding cytotoxicity.

Furthermore, the low standard deviations and standard errors across replicates highlight the reproducibility and reliability of the experimental procedure, strengthening confidence in these findings. Collectively, these results substantiate the biocompatibility of the materials and designs tested, supporting their potential for safe progression into *in vivo* studies and further in their application in clinical scenarios involving short-term skin contact.

Statistical analysis and interpretation of 24-hour timepoint

The one-way ANOVA conducted on raw % viability data (F(4,10) = 2.19, $p = 0.143$) indicated no statistically significant differences in cytotoxicity between the test groups and the negative control at 24 hours (Table 21). This lack of significance suggests that the MN devices and wafer blocks did not adversely affect HaCaT cell viability under the tested conditions. The subsequent Dunnett's post-hoc comparisons, which control for Type I error when evaluating multiple treatments against a single control, further corroborated this finding; none of the adjusted *p*-values fell below the corrected α threshold of 0.0125 (Table 22). Although the HB group exhibited the lowest raw p-value ($p = 0.017$), this did not reach statistical significance after Bonferroni adjustment (adjusted $p = 0.068$), indicating that any observed differences are likely attributable to random variation rather than a true cytotoxic effect.

The choice of parametric methodologies, despite the small sample size ($n = 3$), was supported by the absence of outliers, consistent with the known robustness of ANOVA and Dunnett's tests under these conditions. However, it is acknowledged that formal normality and homogeneity of variance tests were not feasible given the sample size, representing a limitation that should be considered when interpreting the results. Nevertheless, the consistent high viability percentages and low variability strengthen confidence in the results and conclusion of no cytotoxic effects observed.

Overall, the statistical analyses provide robust evidence that the tested MN and wafer formulations do not induce significant cytotoxicity in HaCaT cells at 24 hours. This aligned with the qualitative viability observations and support their cytocompatibility for potential biomedical application.

Adjusted viability interpretation of 24-hour timepoint

Cell viability data was normalised by defining the mean viability of the negative control group (89.19 %) as the reference baseline set at 100 % (Table 23). The viability of each test sample was then expressed as a percentage relative to this baseline. Under this scaling, all treatment groups demonstrated adjusted viability values exceeding 100 %, indicating that raw viability measurements in the treatment groups slightly surpassed those of the negative control. These variations were consistent with expected biological variability, minor fluctuations in cell proliferation, and typical technical or assay noise as reported in previous studies (287). Crucially, adjusted values greater than 100 % do not imply increased cytotoxicity or enhanced cell health beyond normal conditions. Instead, they confirmed that cell survival under test conditions was comparable to, or marginally higher than, the negative control.

Importantly, all results exceeded the ISO 10993-5 viability threshold of 70 % relative to the negative control, confirming compliance with the relevant cytotoxicity standard (215). This finding demonstrates that none of the MN devices or wafer blocks induced cytotoxic effects on HaCaT cells under the test conditions applied. While the slightly elevated adjusted viability values might suggest a minor proliferative effect or assay variation, the lack of statistical significance and biological plausibility indicates these differences are not meaningful. The data therefore supports the conclusion that all tested devices exhibit good cytocompatibility at 24 hours, with no evidence of cytotoxicity.

5.4.2. Cell viability at 48 hour timepoint

A single replicate at the 48-hour timepoint was included to explore the possibility of delayed or progressive cytotoxic effects beyond the standard 24-hour exposure recommended by ISO 10993-5 (215). The negative control viability remained high at 87.94 %, with test samples showing similarly elevated viability levels: 91.03 % for HMN, 90.00 % for HB, 93.02 % for SMN, and 96.50 % for SB (Table 24). The positive control again confirmed assay validity by demonstrating complete cytotoxicity (0 % viability).

All samples remained well above the ISO 10993-5 threshold of 70 % viability, affirming the absence of cytotoxicity at this extended timepoint. These findings suggest that the materials tested do not induce delayed toxicity in HaCaT cells, which was an important consideration given the potential for progressive cellular responses to biomaterials. However, the reliance on a single replicate at 48 hours constitutes a significant limitation. Statistical analysis was not possible, and biological variability cannot be fully accounted for. Nevertheless, the consistency of the 48-hour viability results with the more robust 24-hour dataset lends preliminary support to the sustained biocompatibility of the MN devices and wafer blocks over the likely clinical exposure duration.

It is also important to acknowledge the rationale for limiting 48-hour assessments. The ISO standard primarily specifies 24 hours as the standard exposure period for cytotoxicity testing, reflecting typical short-term clinical use of these devices. Extended exposure assessments may not be as clinically relevant, though they can offer supplementary reassurance regarding safety. In conclusion, while further replication would strengthen confidence, the available 48-hour data reinforce the conclusion that the tested materials do not elicit delayed or progressive cytotoxic effects, supporting their safety profile within the intended timeframe of use.

5.4.3. Methodological limitations and future work recommendations

The study detailed in this chapter presents a modest sample size (*n* = 3 *per* group), which is acknowledged to reduce the statistical power of results analysis. Notwithstanding this, within preliminary *in vitro* cytotoxicity evaluations, triplicate investigation is widely accepted and compliant with ISO 10993-5. Despite this, future work could increase the replicate number beyond triplicate to reinforce the statistical power of the analysis performed. A single assay endpoint, cell viability, was utilised. Complementary assays, such as lactate dehydrogenase (LDH)-release and caspase activity assays, commonly applied to assess HaCaT membrane damage and apoptosis respectively, were not performed. While these additional assays would support a more detailed understanding of cellular responses and mechanistic insights, the assay performed was sufficient to meet the criteria for the ISO 10993-5 cytotoxicity assessment.

The major timepoint for analysis within this investigation was at 24 hours, which for the device type, reflects relevant clinical exposure and aligns with ISO recommendations. Additionally, a single 48-hour replicate was performed for exploratory purposes, and not used for formal statistical analysis, which may be seen as a limitation of this methodology; however, this was considered acceptable as extended exposure past the 24-hour point is unlikely to be utilised within clinical settings.

This study was built on the architecture of utilising a single type of cell line, HaCaT keratinocytes. Despite being the most appropriate choice due to MNs' primary interaction with the epidermis, where keratinocytes are abundant, this study design decision limits the broader generalisation of results and the translatability to *in vivo* dermal cell viability. To address this, and to promote a more well-rounded assessment of the impact of the devices and material on cell viability, future work should diversify the cell type to include dermal fibroblasts and microvascular endothelial cells. Finally, using *in vitro* studies such as the one performed here establishes a good foundation of preliminary screening. Further work should incorporate the use of *ex vivo* human skin to improve the physiological relevance and therefore the translation of findings for incorporation into regulatory submissions.

6. Chapter 6: Intradermal Delivery Patterns

Chapter 6 presents the intradermal delivery patterns of a dye injected into a dermal simulant through both a silicon HMN array and through a 25-G hypodermic device. The distribution of injected dye across the injection period and the 60 minutes following was captured and evaluated with respect to repeatability and consistency of deposition. This repeatability and delivery performance was compared between device types to provide an insight into the differences between hypodermic-mediated and silicon HMN-mediated injections.

6.1. Introduction

The following introduction will outline the context and gap in the currently available literature surrounding the assessment of device drug delivery performance with respect to the drug load itself, as opposed to the therapeutic efficacy of the API. Key motivation for this study as well as critical methodological considerations are outlined here to provide a greater level of context for the subsequent study.

6.1.1. Context and motivation

HMNs offer a promising platform for ID drug delivery for treatments including, but not limited to, vaccines and localised therapies, owing to their minimally invasive profile, reduced pain induction, and dermal cell targeting (288). However, clinical adoption of this novel technology requires not only the demonstration of biological efficacy equivalency comparable to the current accepted gold standard, but also consistently reliable delivery performance. Variation and inconsistency in delivery and diffusion patterns may compromise therapeutic outcomes, particularly for biologics and treatments with narrow therapeutic windows. Regulatory agencies worldwide are aligned in stressing the importance of delivery repeatability and reliability in injectable systems; a requirement that becomes especially critical for platforms proposed for self-administration devices (289).

Fluid drug delivery *via* HMN and hypodermic needle injections are governed by complex structural and material interactions, with factors such as insertion angle and skin heterogeneity having notable effects on delivery efficiency and drug efficacy (290). These variables become even more significant when viewed in a clinical context, where consistency and repeatability is critical for not just effective, but safe, drug administration.

Previous chapters of this thesis have examined in detail the mechanics of insertion, specifically mapping strain and rupture characteristics of HMNs in comparison to 25-G hypodermic devices. However, to obtain a more comprehensive view of device performance, the fluid injection phase must be examined – an underexplored but significant factor that directly influences dosing reliability and, by extension, device performance.

6.1.2. Injection Repeatability

Injection repeatability refers to the platform's ability to consistently deliver a defined fluid volume with reproducible dispersion characteristics and spatial distribution (291). Despite such significant clinical importance, this aspect remains under-investigated within the research sphere, which primarily prioritises fabrication, insertion dynamics, and penetration success. Most injection studies employ skin models (*in vivo* or *ex vivo*), followed by analysis techniques such as OCT. However, the use of biological tissue introduces inherent inter-sample variability in parameters such as elasticity, hydration, and thickness. These are influenced by donor age, sex, lifestyle, and the time elapsed between sample collection and testing (292). As a result, assessment of injection-to-injection consistency is confounded by biological noise which, while relevant in real-world deployment, is suboptimal for controlled, laboratory-based investigations (279). Furthermore, the models currently deployed within the field fail to enable any real-time visualisation and investigation of the delivery during and immediately post injection.

Despite a recent expansion in the MN research sphere, there is a relatively small body of literature concerned with device delivery performance, with repeatability remaining poorly characterised, with therapeutic efficacy of API delivered measured in its place. The ambiguity introduced by these biological models is reflected across the literature, with research reporting pronounced differences in dye diffusion and penetration depth using porcine skin (293, 294). However, the underlying cause of this variation could not clearly be attributed to either device repeatability and performance, or local tissue heterogeneity (295). Similarly, Shrestha *et al.,* observed inconsistent delivery volumes across replicate injections, attributing this variability to local differences in tissue hydration and anatomical site, which complicates distinguishing true device performance from biological variability (296). Furthermore, the influence of post-mortem tissue alterations and donor-specific variability in cadaveric samples complicates the generalisation of injection repeatability findings, as evidenced by Ranamukhaarachi *et al.*, (297). Additionally, they also demonstrated that skin properties, including stiffness and permeability, degrade progressively after excision and preservation, introducing further uncontrollable variability prior to any injection procedure (297). Although recent studies have begun to use more generic models to investigate HMN-mediated fluidic delivery, these remain largely limited to simple mediums such as air and water (190). In instances whereby injections were performed into relevant mediums, such as *ex vivo* porcine skin, only leakage during and post injection was measured, limiting the utilising of the research in evidencing repeatability

(298). Most recently, Oyarte *et al.*, (2019) investigated insertion into an agarose skin mimic to image, at high speed, the impact and deposition of ink *via* a tattoo gun (299). However, although similar in size to microneedles, the focus of this study lay in highlighting the micro-scale damage occurring upon impact, failing to provide any detail over the repeatability and reliability of deposition. To provide meaningful insight into physiological performance, future studies should employ more physiologically relevant media and phantoms to better approximate the dermal environment. Collectively, these studies highlight a recurrent theme in the literature: variability in fluid delivery is routinely observed but is either rarely isolated from biological noise or it is investigated in oversimplified models, severely limiting the ability to draw definitive conclusions on device repeatability. More often reported as ancillary observations while investigating other phenomena, these findings suggest that factors such as back-pressure, partial clogging, or subtle mechanical shifts during insertion may further contribute to inter-injection variability (300, 301). However, such device-related inconsistencies remain largely unexplored in a systematic, real-time context. Without a stable and well-characterised injection medium, the true reliability of MN-based fluid delivery platforms continues to be obscured.

6.1.3. Dermal Simulants

In recent years, synthetic skin simulants have gained traction as invaluable tools for medical training, particularly in the context of surgical models that rely heavily on silicone-based materials (302-305). In contrast to *in vivo* and *ex vivo* models, which are inherently variable and constrained by donor availability and ethical considerations, phantoms offer a standardised platform for a more robust investigation into repeatability of device behaviour; a domain which such simulants remain underutilised (306).

In addition to silicone-based phantoms, a range of hydrogel-based skin simulants are also available, with a range of materials employed, including polyvinyl alcohol (PVA), sodium alginate (SA), gelatine, and HA (307). More commonly used hydrogels, like gelatine, although are accessible in cost and production, are deployed more to investigate frictional or mechanical interactions (308, 309). However, once set, are not conducive to diffusion-based investigations. Further, despite good optical clarity and common deployment within a research environment, PVA/SA hydrogels have low mechanical strength, which in some instances can provide practical limitations to its utility, in addition to the polymer networks imposing diffusion limitations for drug delivery based studies (310).

HA hydrogels have gained particular prominence due to their physiological relevance. HA is found in its greatest concentration within the dermal ECM, where it plays a crucial role in maintain hydration, regulating viscoelastic properties, and the modulation of interstitial transport (311-313). Given its dermal ubiquity, HA-based gels offer excellent biological resonance for modelling dermal drug delivery in a translational manner in comparison to rigid silicone models or synthetic hydrogels such as PVA/SA which are both incompatible with biological tissue constituents (314).

HA-based gels boast the advantages of offering tuneable mechanical properties whilst being free of donor/site-specific variation (315). Their optical clarity allows the investigation of injection repeatability, enabling imaging and frame by frame analysis of injection plume and diffusion (316). Currently, other hydrogels are used for tissue mimics, however unlike HA they are often not a pH or ionic environment match, often introducing artificial chemicals and components which may have a considerable impact on diffusion repeatability (317). Buffered saline solutions, such as PBS, are often used to produce gels, allowing a closer approximation of both ionic and pH conditions in the interstitium; a critical consideration when investigating solute behaviour during injection (318).

Looking further afield than laboratory applications, HA-based gels and formulations are currently being deployed in clinical and aesthetic based settings, including sustained release formulations and dermal fillers (319). This widespread adoption and use further reinforces its translational relevance as a model substance for evaluating injection and dermal delivery applications.

6.1.4. Study aim and scope

Whilst drug delivery using MNs is currently being investigated heavily, there is a distinct gap in the research sphere in the shape of injection repeatability evaluation. The geometry of the injection plays an essential role in determining the spatial distribution of the therapeutic, which then influences the diffusion dynamics and tissue-level bioavailability (128, 320, 321). Further to this, there is limited reporting of the characterisation of injections in controlled mediums, with groups such as Ripolin *et al.,* calling for more reproducible testing environments to better characterise injection performance (288, 322). Despite current literature reporting investigation of the efficacy of therapeutic payloads delivered by HMN devices, a methodology has not yet been established for assessing consistency and repeatability across injections and device types (323). This chapter reports the development of a methodology which enables the assessment of injection repeatability using a dermal simulant and fixed insertion and injection parameters. Additionally, this methodology allows a direct comparison of the repeatability of different device types, facilitating the determination of which device type exhibits the most reproducible fluid delivery, when all environmental and procedural variables are controlled and standardised. The findings from this chapter address a critical translational barrier highlighted by regulatory guidance, whereby delivery consistency is crucial to clinical validation and adoption.

6.2. Materials and methodology

This section will present the experimental methodology and required materials used to investigate the intradermal delivery pattern following injection by hypodermic and HMN devices. The apparatus, including the dermal phantom preparation, syringe-driver, controlled insertion and imaging setup will be reported, in addition to the protocol for image acquisition and frame processing.

6.2.1. Experimental instrumentation

The following subsection outlines the key experimental instrumentation employed during the intradermal delivery study. It will encompass the devices investigated, phantoms used, and injection system, in addition to the insertion apparatus and the image acquisition setup. The use of this setup supported in producing a controlled environment for the assessment of injection repeatability.

Device types

Devices investigated in this chapter, as with Chapter 4, were silicon HMNs in a 1x5 array format and stainless steel 25-G hypodermic needles (Figure 34). The HMNs (600 μm height, 100 μm bore diameter) were fabricated *via* the process detailed in Chapter 3. The 25-G hypodermic needle was selected as a clinically relevant benchmark and served as the gold standard comparator. This same device was also used in Chapter 4 to facilitate methodological continuity and consistency across the thesis. A new device was used for each repeat, with three independent repeats conducted *per* device type. Devices were visually inspected prior to use to identify any potential defects which may impact performance. All devices within each group were nominally identical to ensure consistency across the repeats.

Dermis phantom

A 1 % HA gel (9067-32-7) was prepared using a PBS solution (7647-14-5). Each sample required 1 g of HA powder to be weighed and added gradually to 100 ml PBS, whilst being continuously mixed (increased to 600 rpm slowly to prevent bubble formation) using a magnetic stirring rod until homogenous. The solution was gently heated (below 40 °C) to aid dissolution. The pH of the solution was confirmed to be approximately 7.4 using indicator strips prior to decanting the solution into a clear acrylic box (5 x 5 x 5 cm), sealed, and left to set at room temperature for 7 weeks. The prolonged setting period was trialled and determined to be most appropriate to ensure complete gelation and stabilisation prior to testing.

Injection dye and delivery system

Methylene blue (61-73-4) dye was used at a concentration of 0.1 mg/ml to produce a drug mimic with good contrast for better imaging quality. With its known biocompatibility and wide clinical use, methylene blue offers a good mimic of many drugs traditionally delivered through 25-G hypodermic devices, such as lidocaine. Often delivered intradermally (0.1 ml) through 25-G devices for local anaesthesia during procedures such as skin biopsies, dermatological surgeries, and allergy testing, lidocaine is similar to methylene blue with respect to their size (270 g/mol and 319 g/mol respectively) and water solubility, allowing for similar diffusion behaviour through hydrated gel networks (324, 325).

A 50 ml syringe was filled with the aforementioned prepared methylene blue dye. This was loaded into a Cole Palmer 78-8100C syringe pump, which was used to control the injection speed (flow rate 0.6 ml/min) and volume (0.1 ml).

Controlled insertion system

An Instron Universal Testing System (68SC-2, 2kN load cell, BlueHill® software Version 4.42) was used to control insertion dynamics, controlling the insertion speed to 1 mm/s, as reported in Chapter 4. The top platen was replaced by an adaptor designed to be mounted to the Universal Testing System, with a side inlet for the injection fluid, and a bottom adaptor for sample mounting (Figure 59). The bottom platen was replaced with a previously designed and machined mount which allowed it to be adjusted to fix the sample boxes into place (Figure 59). Devices were inserted (0.1 mm/s) to full length, following which, injection was initiated. When the full 0.1 ml had been dispensed, devices were removed.

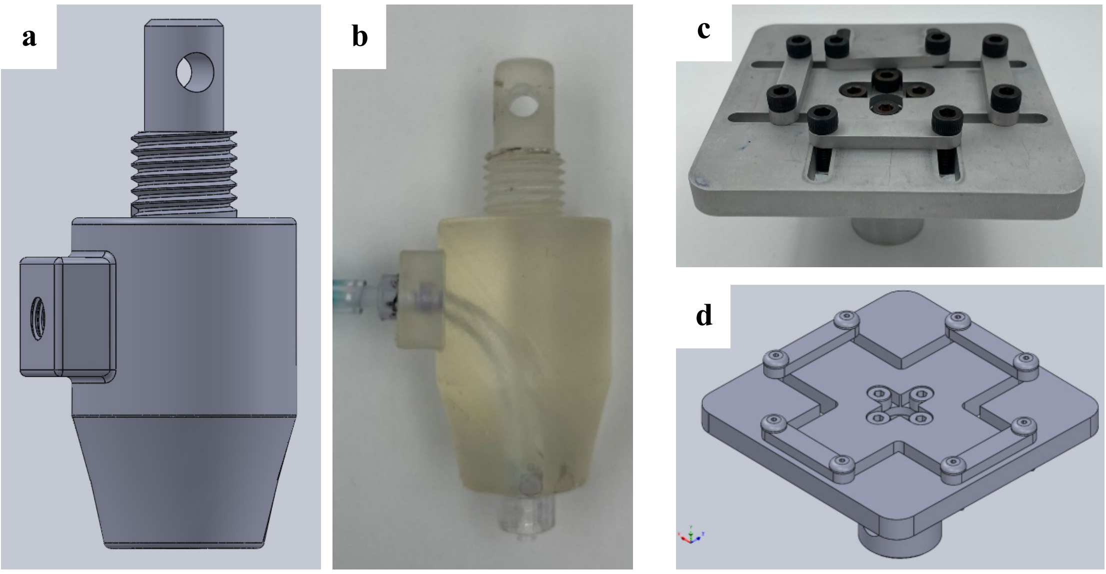

Figure 59. Mounts for force station (a-b) to hold needle and dye inlet (c-d) to hold the box containing the dermal mimic

Visual acquisition setup

A Nikon D7200 camera and Laowa 100 mm lens was used to record the injection period (60 fps, 1280x720, 10 s), the immediate post-injection period (60 fps, 1280x720, 2 mins), and the extended dye diffusion phase (1 frame *per* 30 seconds programmed into the camera, 1280x720, 60 mins). The camera was mounted on a tripod and positioned perpendicular to the injection site to ensure optimal imaging of the area of interest. A GSVITEC MultiLED QX-Mini (GS00284) light emitting diode (LED) light source was positioned to provide uniform illumination across the injection zone (Figure 60).

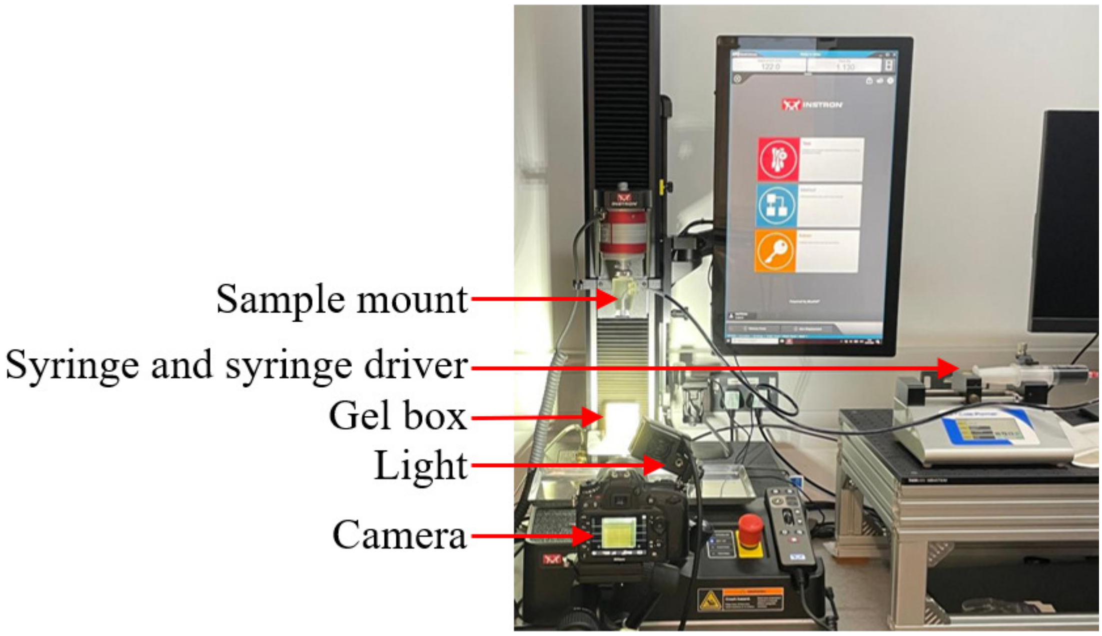

Figure 60. Picture of setup with camera, light, syringe drive, and needle mounted onto force station visible

6.2.2. Analytical methodology

From the recorded videos, frames were extracted at key timepoints corresponding to 0 %, 25 %, 50 %, 75 %, and 100 % progression through both the 2-min recording and the 60-min timelapse sequences. A consistent crop size, defined by fixed pixel dimensions, was established and uniformly applied to all extracted frames to ensure comparability. Each image was aligned by centring the injection site within the crop, using this as the spatial reference point. Following cropping, all images were normalised on a per-frame basis. Each RGB channel was normalised relative to the maximum intensity of the blue channel in that frame, corresponding to the drug mimic dye colour, ensuring the pixels were scaled proportionally. *Per*-frame normalisation was the selected processing approach, allowing emphasis on the spatial consistency and reproducibility of the drug mimic plume. This enabled direct comparison of dispersion patterns across both repeats and device groups. The same processing route was applied to both the MN and hypodermic datasets to ensure internal consistency was maintained within each device group. To facilitate assessment of repeatability, images from multiple repeats were overlaid with an opacity set to 33.3 %, such that stacking three images achieved full opacity (100 %), enabling clear visualisation of consistent versus variable plume regions. This methodology allowed for detailed, time-resolved comparison of fluid dispersion patterns across replicates while preserving spatial fidelity.

6.3. Experimental results

Figures in this section comprise frames extracted at set timepoints across the injection and dye-dispersion period, followed by overlaid and thresholded images to allow assessment of repeatability. The colour scale on all figures indicated the dye intensity of the frames and overlaid images as a percentage between replicates, as a measure of repeatability. In all images, higher colour intensity corresponded to greater dye concentration within the gel. Darker blue regions indicated areas of higher localised dye accumulation, whereas paler blue regions indicated lower dye presence or greater dilution.

6.3.1. 2 minutes post injection

This subsection presents the experimental results based on the frames captured within the first 2 minutes post injection. Three repeats (*n* = 3) for each device type has been displayed below.

<u>Microneedle array</u>

Post-MN devices injection, (time point = 0 s), gel samples presented a consistent dome-shaped dye zone, with the dye artifacts from each individual needle tip visible across all samples, demonstrating good array performance. Immediate dispersion was highly lateral, with shallow dispersion and diffusion of dye at t=0 (Figure 61). All MN samples exhibited consistent and repeatable morphology at the first extracted timepoint. Despite some variation (MN1 exhibited the most localised deposition and MN3 showed the more diffuse pattern) there was minimal variation between injection consistency diffusion patterns immediately post injection (Figure 61).

A further 25 % into the 2 mins recording sees limited immediate diffusion, with dye remaining fairly localised and largely static in both shape and intensity, especially in seen in MN1. MN2 and MN3 exhibited a modest lateral expansion of the bolus, identifiable through the diffusion of the MN tip point artefacts (Figure 61). At the halfway point (1 min) through recording, expansion spread beyond the immediate needle regions, with merging occurring.

As approaching the final frame, although the extent of change remained relatively low, all three samples demonstrated further lateral diffusion as identifiable by the softening of the dye boundaries. MN1 maintained the most compact bolus throughout, with MN2 and MN3 showing greater bolus expansion over time through less defined edges and a slight gradient surrounding the gel/bolus interface (Figure 61).

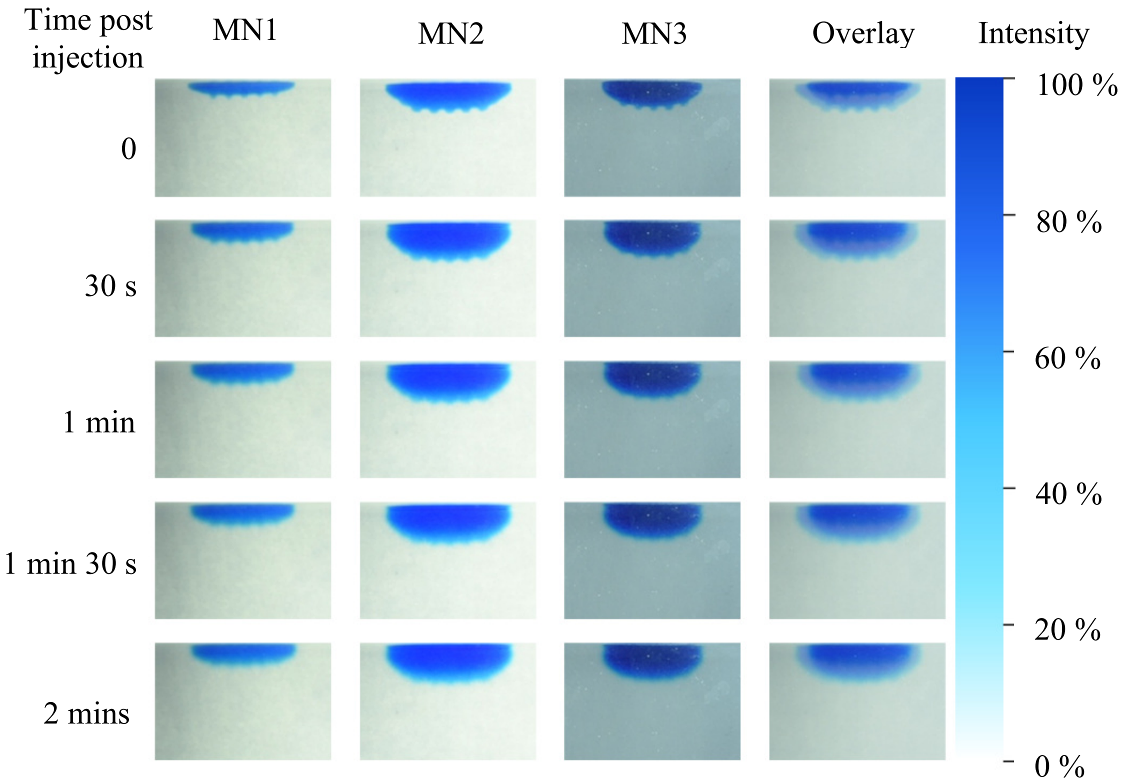

Figure 61. A matrix of frames extracted at various times post injection (0 – 2 mins) for each microneedle repeat (n = 3). Frames taken at each time point have been overlaid for visualisation of repeatability

To further support the investigation of injection repeatability, a fixed-size overlay was applied across the samples at each timepoint to provide a more standard visualised comparison of the bolus morphology and diffusion. By using a constant frame of reference, the interpretability of injection consistency improved, enabling the visual assessment of localisation and spread. All MN samples demonstrated a consistently localised zone of bolus delivery, with minimal lateral or vertical deviation. The overlay highlighted that the shape and degree of dye diffusion through the gel remained aligned, specifically at timepoints of 1 min and 1 min 30 s (Figure 61). Furthermore, the overlay made it evident that all three array samples achieved similar dispersion, reinforcing the injection volume, location, and diffusion reliability. Whilst there was subtle variation in boundary sharpness (MN3) and degree of lateral spread (MN1), all MN samples remained relatively confined within the same spatial limits, strengthening the evidence for controlled and repeatable delivery facilitated by MN devices.

Although there was lighting variations observed between recordings, most notably in brightness (MN3), there was limited effect on data interpretation (Figure 61). The high contrast afforded by the dye prevented any comprised data collection, with clear delineation of the injection zone across all timepoints, which allows for robust cross-sample comparison and reliability assessment.

Hypodermic needle

Immediately after the injection volume was dispensed, significant variation in morphology was observed between replicates, ranging from narrow and elongated channels (sample 1) to a narrow shaft with a bulbous head (sample 2), and a broader bulbous dye volume (sample 3) (Figure 62). All samples, as expected, displayed a more elongated dye shape compared to all MN samples. Additionally, some immediate leakage and backflow were noted at the surface in all three hypodermic repeats.

At 30 s post-injection, modest lateral expansion was observed, with dye boundaries beginning to soften visibly (Figure 62). Samples 2 and 3 exhibited slightly asymmetrical diffusion patterns compared to the more columnar shape of sample 1 (Figure 62). This asymmetry may be due to delivery bias associated with the bevel length of the hypodermic needle.

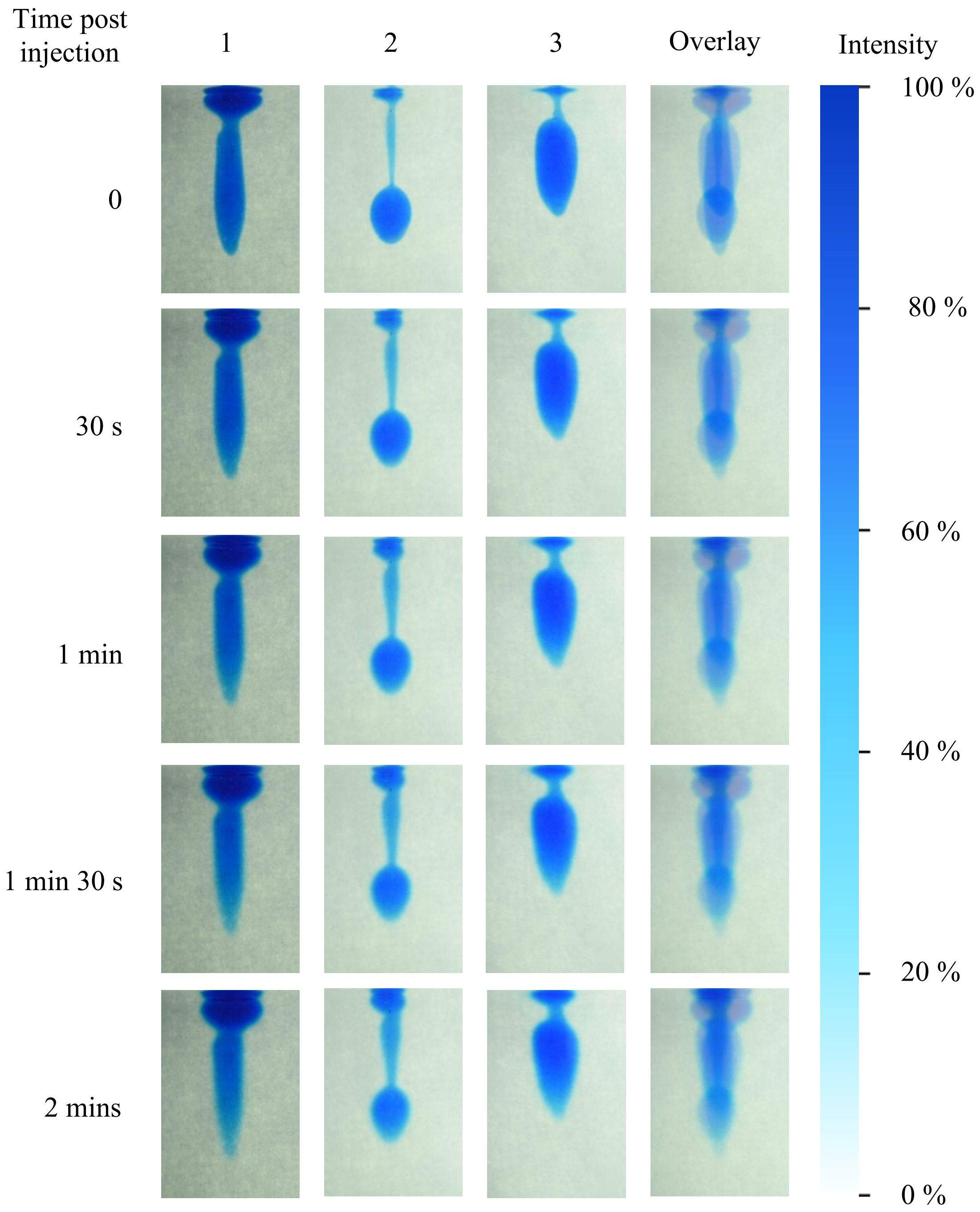

Figure 62. A matrix of frames extracted at various times post injection (0 – 2 mins) for each hypodermic needle repeat (n = 3). Frames taken at each time point have been overlaid for visualisation of repeatability

Approaching the halfway point of data collection (1 min), dye intensity increased at the central point on the sample surface, suggesting upward progression along the needle tract and pooling. Vertical elongation of the dye region continued at this time point, with diffusion extending beyond the initial bolus zone (Figure 62). Sample 1 retained the most compact shape, while samples 2 and 3 showed greater lateral expansion

(Figure 62). Sample 3 demonstrated evidence of merging between the shallower leakage zone and the deeper bolus area.

By 1 min 30 s, all replicates exhibited more pronounced elongation, with localized areas of higher density within the core and lighter density within the plume, indicating uneven dye distribution (Figure 62). At 2 mins post-delivery, significant vertical migration of dye through the needle tract and pooling at the surface was evident, accompanied by softening of dye boundaries vertically, contrasting with the preferential lateral diffusion observed in MN samples (Figure 62). Across all three samples, lateral spread remained secondary. Notable variation persisted among hypodermic samples, with deeper penetration apparent in samples 1 and 2, and more irregular diffusion morphology in sample 3 (Figure 62). Repeatability up to the 2-min mark appeared poor, with variability in plume shape, diffusion patterns, and dye intensity clearly apparent.

Overlaying the hypodermic samples highlighted a high degree of variability, with misalignment of deep dye fronts between repeats leading to inconsistent delivery depths and diffusion paths. Consequently, the lack of comparability in delivery and diffusion up to 2 mins post-injection indicated less predictable morphology, suggesting reduced repeatability in targeted localisation.

Device comparison

Thresholded images enabled identification of areas of high repeatability in dye delivery. The larger areas of high colour intensity observed in the MN samples, particularly at the 0 s and 30 s time points, demonstrated strong intra-group repeatability in deposition morphology (Figure 63). In contrast, the small core of intense colour surrounded by a more diffuse region in the hypodermic samples indicated greater inter-sample variability, with significant inconsistency in dye diffusion between replicates.

Across all five time points, MN delivery exhibited more localised and lateral diffusion compared to the broader vertical dispersion associated with the deeper penetration enabled by the longer hypodermic needles (Figure 63). The MN replicates produced tighter alignment and more defined edges in the overlayed images, whereas the hypodermic overlays appeared misaligned, suggesting greater variability and reduced predictability in injection delivery and diffusion profiles.

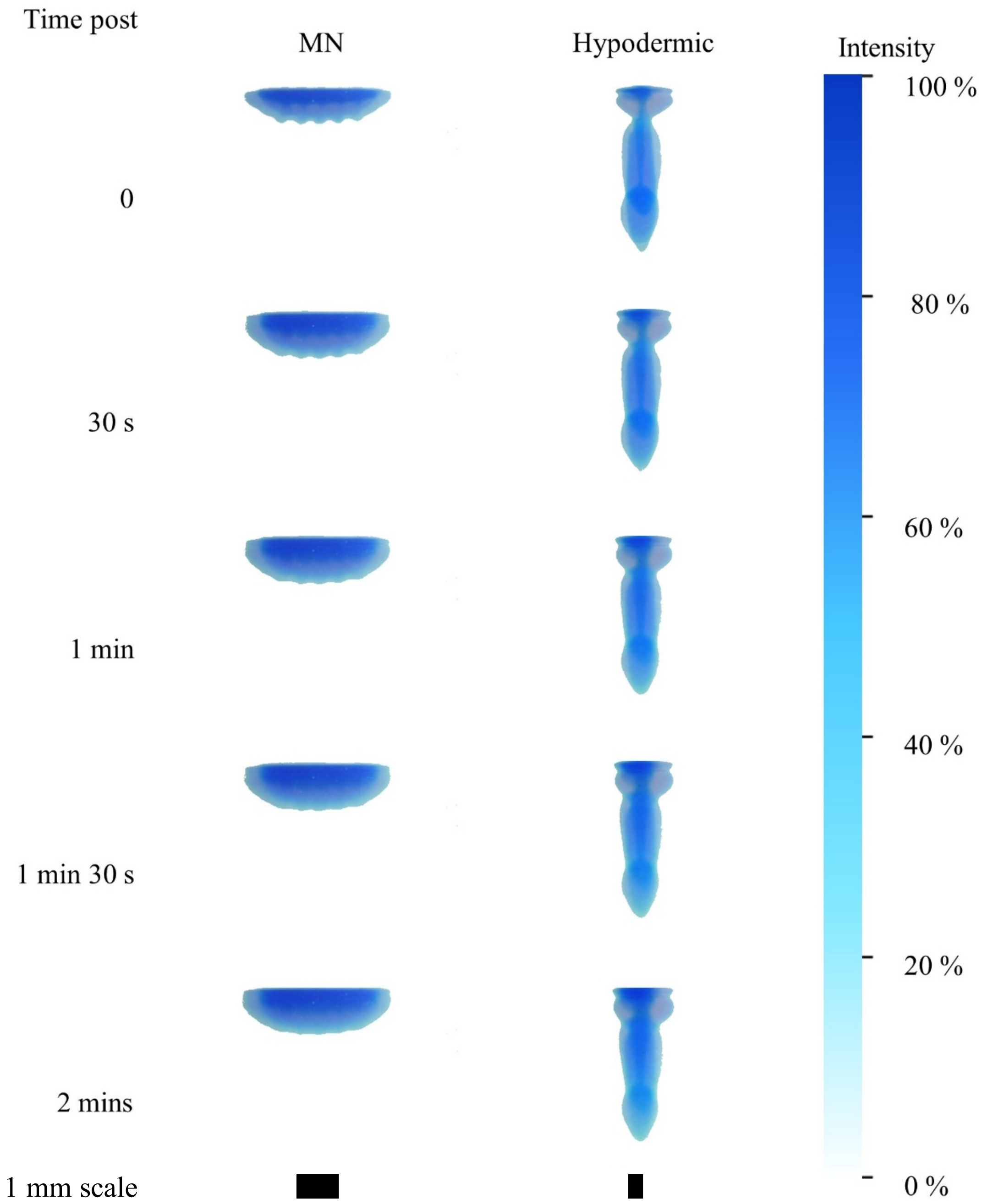

Figure 63. A comparison of the overlays of microneedle sample frames and hypodermic sample frames from 0 – 2 min. Scale bar represents 1 mm

6.3.2. 60 minutes post injection

This subsection presents the experimental results based on the frames captured within the 60 minute post injection timelapse recording. Three repeats (n = 3) for each device type has been displayed below.

Microneedle array

Figure 64 presents regular time points spanning from injection completion (0 mins) across the timelapse video up to 60 mins post-injection. Across the entire data collection period, all MN replicates presented a compact, shallow, lateral dispersion, with distinct deposition sites from individual MN tips clearly visible at t=0 for all samples. High repeatability was demonstrated in the consistent size, shape, and intensity observed across replicates.

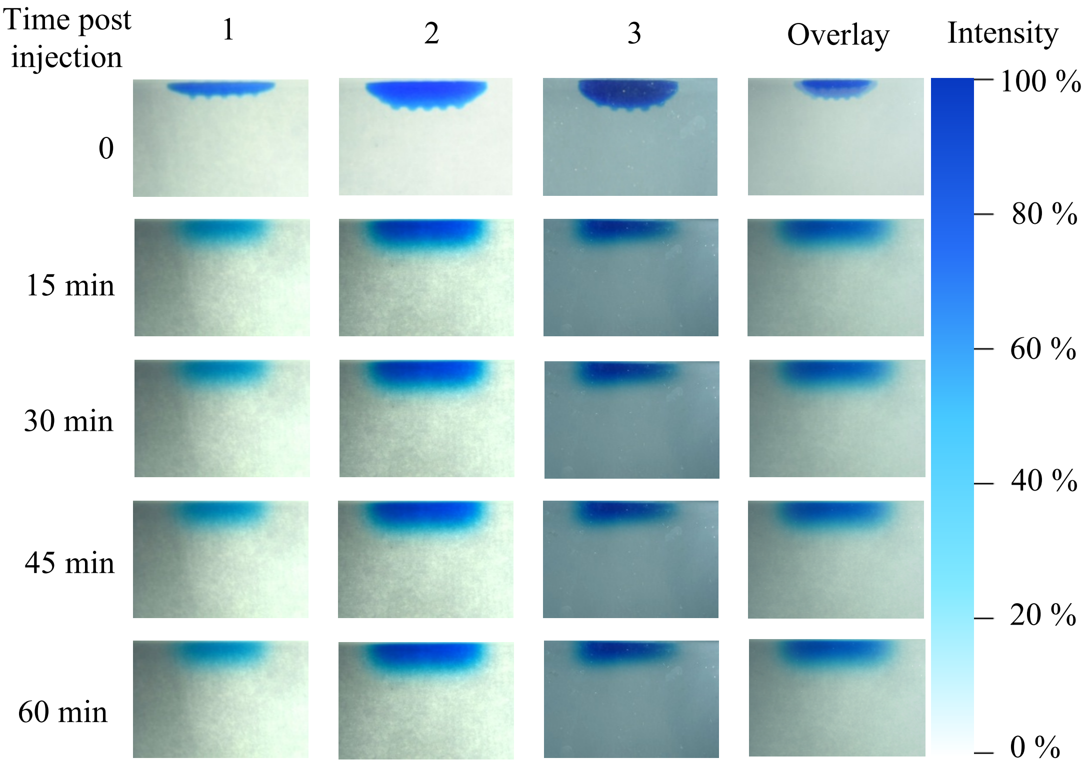

Figure 64. A matrix of frames extracted at various times post injection (0 – 60 min) for each microneedle repeat (n = 3). Frames taken at each time point have been overlaid for visualisation of repeatability

At the 15 min time point, minimal expansion was observed, with the dye front remaining relatively well defined (Figure 64). Although MN2 and MN3 showed slight lateral diffusion, MN1 remained highly compact. Tip-site artefacts visible at t=0 were no longer present at 15 mins, indicating that lateral movement and diffusion had resulted in merging relatively early in the observed time period.

By the 30 min mark, there was significant merging between adjacent deposition zones due to lateral spread (Figure 64). There was no evidence of directional bias, with uniform diffusion occurring in all directions from the original site in each sample. The dye intensity at the core remained relatively centralised, indicating more passive diffusion rather than active fluid movement. Boundaries between diffuse edges and the core continued to soften beyond the 45 min time point, with increased coalescence of previously distinct diffusion zones (Figure 64). Diffusion appeared to progress symmetrically across individual replicates, with MN3 presenting the greatest lateral spread.

At the end of the observation period (60 mins), dye zones in MN1 and MN3 had largely merged into a horizontal band, while MN2 retained a centralised core intensity despite significant softening (Figure 64). By this time point, there was no clear evidence of substantial depth penetration, with controlled lateral diffusion remaining the predominant direction of dye spread. There was limited evidence of leakage or preferential pooling at the gel surface. Across the full 60 mins, all three MN samples exhibited minimal asymmetry, with small differences arising only from variations in the degree of merging and edge softness.

Hypodermic needle

Immediately post-injection, there was significant variation in morphology, with injections exhibiting narrow vertical channels (sample 1) and more bulbous heads (sample 3), as previously discussed. In addition to the elongated profiles, the entry points were less defined in all hypodermic samples than in the MN injections, suggesting greater gel disturbance.

By the 15 min time point, diffusion had clearly progressed in a vertical manner in all replicates, with only modest lateral spread (Figure 65). The combination of vertical diffusion bias and limited lateral movement resulted in greater asymmetry developing by approximately 25% of the imaged time period. Dye intensity increased in a band near the entry site in hypodermic samples 2 and 3, while in sample 1 the vertical column showed a marked reduction in intensity in favour of pooling near the surface (Figure 65).

At the 30 min time point, vertical diffusion remained the dominant pattern, with dye intensity again increasing in the core band at the surface and boundary softening along the vertical column deeper into the gel, as seen in the overlayed image (Figure 65). Sample 2 exhibited uneven lateral widening at the mid-depth area, producing an irregular morphology.

By 45 mins, lateral diffusion and symmetry across all replicates remained inconsistent, with samples 1 and 3 showing significant broadening, while sample 2 maintained a narrower profile (Figure 65). The overlayed image showed further softening of diffusion zone boundaries, with greater intensity in the secondary zone surrounding the core, suggesting that deeper penetration continued.

By the final frame (60 mins), all dye zones across the three replicates were broad and diffuse, despite varying morphologies, intensities, and diffusion depths (Figure 65). Across the entire 60 min observation period, dye diffusion was predominantly vertical, with irregularity in lateral spread and boundaries. As time progressed, a core zone at the top of the gel increased in intensity, despite generally high variability in morphology and depth between replicates. The larger bore and deeper penetration appeared to result in greater structural disturbance within the gel, contributing to inconsistency in diffusion.

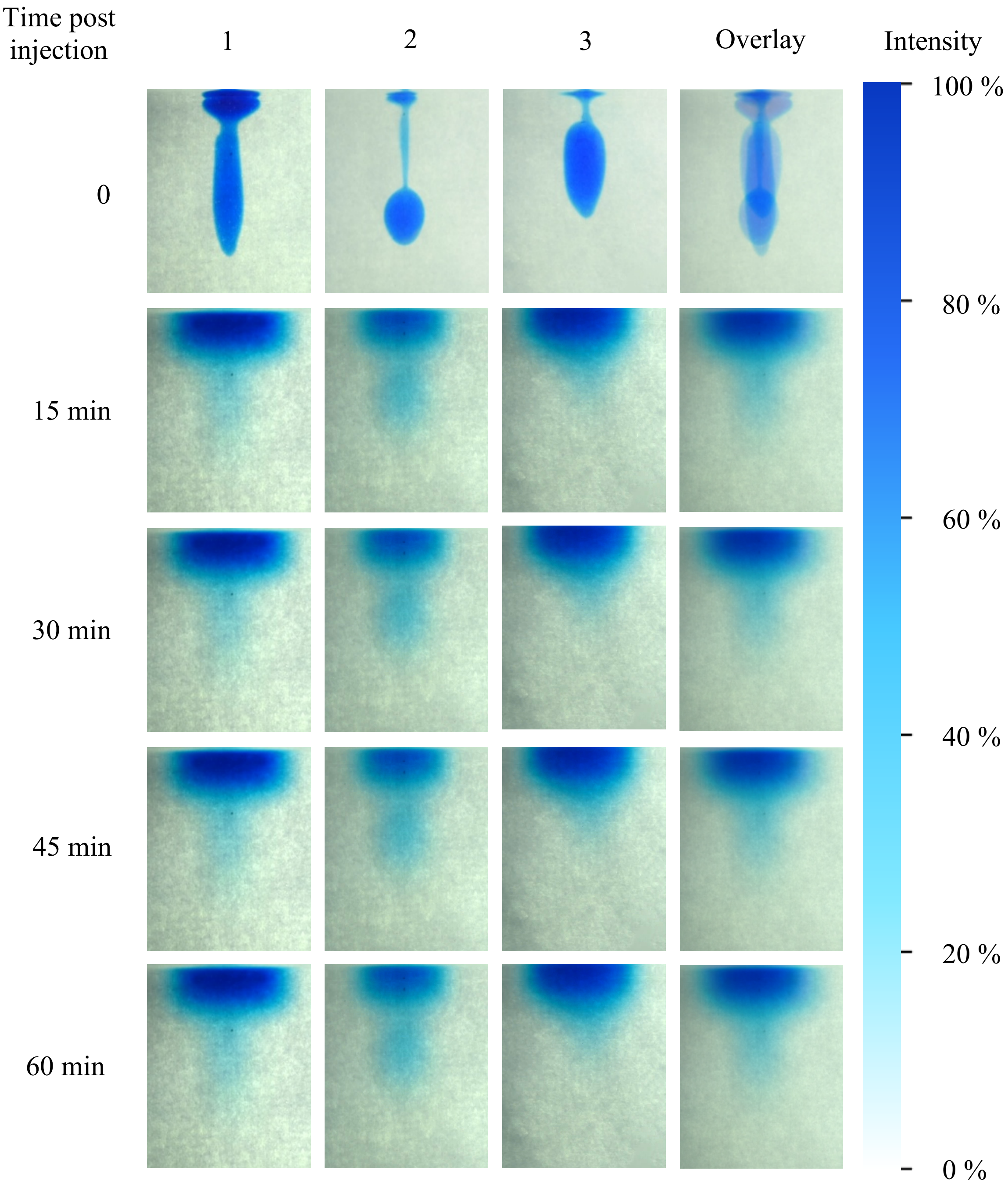

Figure 65. A matrix of frames extracted at various times post injection (0 – 60 min) for each hypodermic needle repeat (n = 3). Frames taken at each time point have been overlaid for visualisation of repeatability

<u>Device comparison</u>

Figure 66 presents overlayed, thresholded images of dye dispersion over the 60-min timelapse following MN and hypodermic insertion. As with Figure 63, the colour scale represents the dye intensity of the overlap between replicates, expressed as a percentage, providing a measure of repeatability. The thresholded images reveal a high overlap of MN-delivered dye immediately after injection (t=0), with a consistent, high-intensity zone visible at the centre of the overlays. Over time, lateral spread appears to dominate, progressing with minimal morphological change to the bolus shape (Figure 66). The intensity of the core decreases as time advances, indicating limited dye movement back into the primary injection area. Misalignment was minimal, with both the central high-intensity zone and the surrounding lower-intensity zone remaining well defined (Figure 66). Overall, MN samples demonstrate high repeatability across the full 60-min period, with good temporal consistency and spatial delivery evident through well-aligned overlap regions of constant intensity (Figure 66).

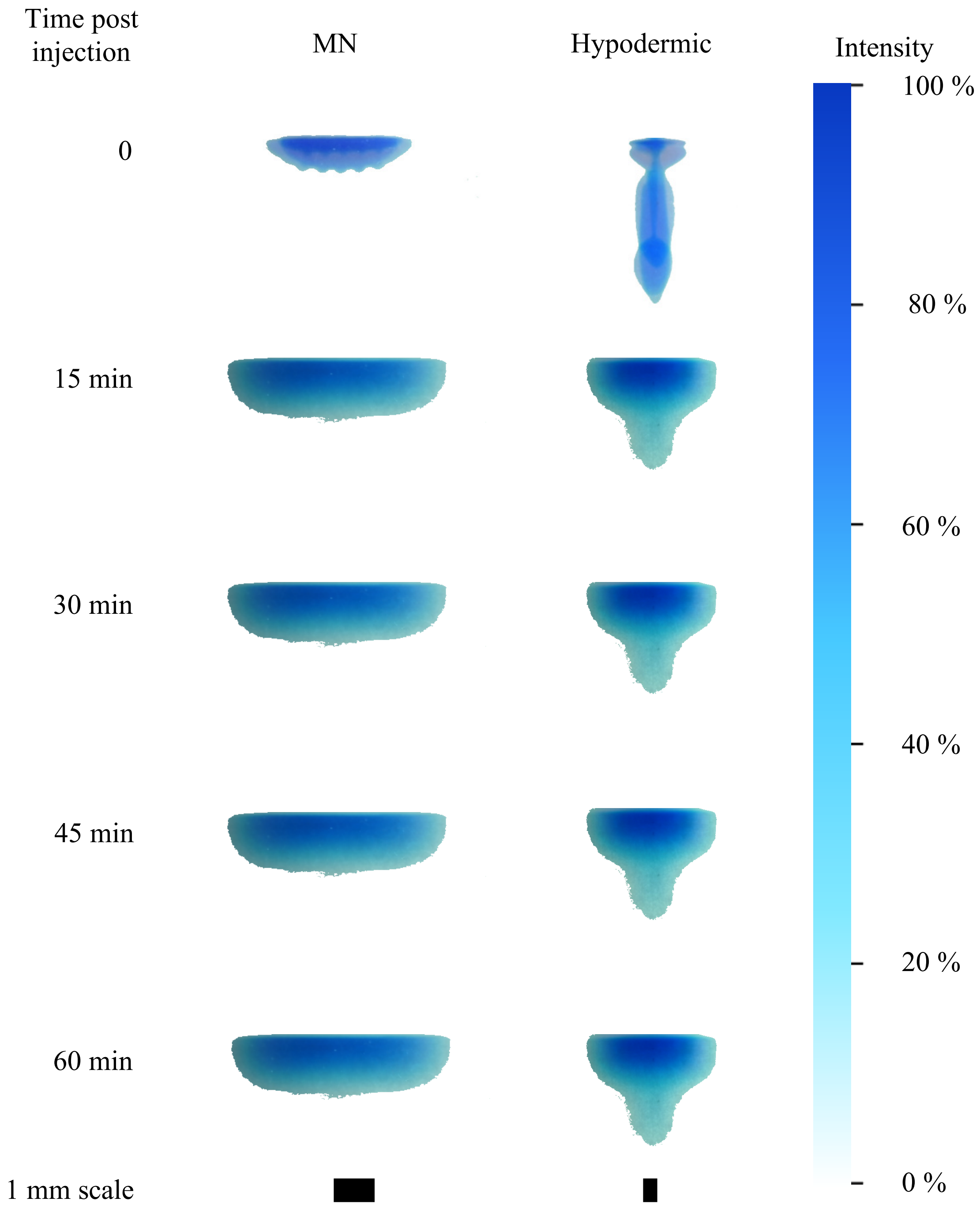

Figure 66. A comparison of the overlays of microneedle sample frames and hypodermic sample frames from 0 – 60 min. Scale bar represents 1 mm

In contrast, the thresholded overlay images of hypodermic repeats show a smaller and more irregular intense core from t=0. The overlays display a thin common area of higher intensity, surrounded by a diffuse lower-intensity zone. At the initial timepoint, significant variation was observed not only in morphology but also in bolus deposition depth, with misalignment of the deeper dye front further reducing overlap intensity. As time progresses, boundaries soften rapidly, and diffusion adopts a less regular pattern, producing an uneven, cone-like morphology (Figure 66). Temporally, hypodermic injections exhibit progressive divergence between replicates compared to the MN repeats, likely due to the deeper initial penetration. Over time, the overall cone shape persists through the dye depth, but localisation decreases (Figure 66). A clearer distinction emerges between the high-intensity core near the penetration site and the surrounding diffusion zone, suggesting dye was flowing back into the larger void created by the hypodermic shaft.

Comparatively, MN devices produce a more lateral and regular dispersion pattern, whereas hypodermic devices show vertical elongation and irregular lateral diffusion (Figure 66). Spatial control appears greater in MN samples, resulting in more uniform dispersion than observed with hypodermic injections. In terms of repeatability, hypodermic devices exhibit greater variation, particularly in initial delivery, contrasting with the consistent size, shape, and location of MN primary delivery and subsequent dispersion. By the end of the 60-min period, MN injection replicates demonstrate greater localisation and morphological consistency than hypodermic alternatives, as evidenced by the more uniform and intense overlap regions visible in the thresholded images (Figure 66).

6.4. Discussion

This chapter investigated the repeatability of MN array-mediated injections compared with the hypodermic gold standard (25-G) in a dermal gel phantom. Reliable spatial and temporal control is essential for both regulatory approval and clinical effectiveness, particularly for novel medical devices intended for precise ID delivery (326). Although the repeatability of device-mediated skin puncture is well documented, and device-induced strain was examined in Chapter 4, the repeatability of the injection process itself, independent of biological treatment response, remains poorly characterised (288, 322, 323). This study therefore aimed to fill this gap, providing insight into the consistency and precision of MN and hypodermic injection patterns under controlled conditions. Repeatability of spatial control is particularly critical, as the precise localisation of the delivered drug payload can substantially affect the efficacy of therapies targeting the dermal layer (326). ID treatments, which require highly localised delivery, demand a high degree of repeatability with respect to bolus and diffusion profiles, making it essential to investigate this independently of therapeutic effect in order to fairly compare MN device performance with currently used injection-based devices (99).

6.4.1. Early observations

In the first 2 mins post-injection, the MN-injected samples displayed a consistent lateral distribution, with a well-aligned bolus across replicates, indicating that the devices can achieve precise, dermis-specific delivery (Figure 61). This early repeatability establishes a foundation for a more consistent diffusion pattern over time and further supports the use of MNs in applications requiring high localisation, such as ID vaccines, where controlled dosing is critical for efficacy (327). The repeatability may also result from the minimal mechanical disruption induced by MN devices, which appears to promote a more predictable local diffusion pattern compared with the greater disruption observed with 25-G hypodermic needles. In contrast, the depth variability noted during early hypodermic insertion may establish an inconsistent starting point for subsequent diffusion, introducing variability that could limit the effectiveness of dermal-specific drug delivery (Figure 62). These early observations provide insight into the mechanisms underlying divergence in longer-term diffusion patterns and potential therapeutic outcomes, particularly in applications where reliability and precision are essential.

6.4.2. Long-term observations

Over the full 60-min observation period, the MN-injected samples retained a surface-constrained distribution, with both overlay and thresholded images demonstrating the stability and reproducibility of this approach for ID delivery (Figure 64, Figure 66). In contrast, the hypodermic-injected samples, though showing the greater penetration depth expected from their longer shaft length, developed variable diffusion patterns that by 60 mins reflected markedly lower predictability (Figure 65, Figure 66). Clinically, such inconsistency may produce uneven treatment outcomes. Taken together, these patterns indicate that MN arrays achieve a more controlled and localised delivery, whereas hypodermic devices create a broader bolus that disperses in a less consistent, and therefore less dependable, manner over time. This initial characterisation established the baseline performance of both devices, enabling subsequent comparison of their capacity to deliver dye into the simulant matrix.

In terms of repeatability, MN injections showed minimal variation between replicates, maintaining consistent localisation across samples (Figure 66). By contrast, hypodermic injections produced a poorly defined, cone-like morphology with reduced spatial precision (Figure 66). Such variability may arise from the greater mechanical disruption and void formation caused by the hypodermic insertion, effects that can alter subsequent diffusion behaviour. These differences suggest that MNs are better suited to applications demanding precise localisation and uniform dosing, while hypodermics may compromise delivery accuracy in scenarios where diffusion control is critical (328, 329). These early post-injection differences provided a foundation for assessing how dispersion evolved over the following hour.

Furthermore, the controlled and gradual spread of dye across the full observation period reinforces the potential of MN arrays for sustained retention in dose-sensitive therapies. Such stability suggests that MN devices could serve effectively as an adjunct to, rather than a replacement for, hypodermic delivery, and be reserved for cases where precise ID targeting is required. In contrast, the reduced spatial precision of the 25-G hypodermic makes it more suited to applications where broader distribution and systemic uptake are advantageous.

6.4.3. Mechanical considerations

The repeatable lateral distribution following MN delivery may be attributed to the minimal mechanical disruption exerted during penetration. With only local compression and generally negligible voids, the MN devices displace a reduced volume of gel, limiting alterations in the initial injection deposition. In contrast, the hypodermic devices, with their greater penetration depth, result in greater gel displacement, creating voids and morphological inconsistencies. It is important to acknowledge, however, that in real skin, the highly complex tissue architecture would provide additional mechanical resistance that may moderate these effects (330). The minimal depth and low variability of MN insertion support high repeatability and consistent bolus alignment, whereas the increased void depth from hypodermic insertion produced greater tissue displacement, a non-predictable variable (331, 332). This establishes a non-uniform baseline that can propagate into less reproducible diffusion and dispersion patterns.

6.4.4. Methodological limitations and future work recommendations

It is important to acknowledge the limitations within the experimental setup, which may have impacted the results and observations, the most significant being the constraints of the model. The HA gel was selected for its hydrophilic nature, physiological relevance to dermal composition, and optical clarity. Nonetheless, it lacks the structural complexity of native skin, including collagen fibres and elastin networks, which are absent in most phantoms. The gel cannot reproduce the microstructural constraints of real tissue, and the absence of vasculature and live cells prevents the capture of dynamics such as recoil and IF movement. Therefore, although the HA gel provides a reproducible and optically ideal platform for assessing and comparing injection reproducibility, extrapolation to clinical outcomes in physiological conditions must be approached with caution.

The imaging setup used in this study was designed to provide a qualitative visualisation of injection, enabling direct comparison between MN and hypodermic delivery in a controlled setting. The image resolution was sufficient to capture the overall dye spread, with analysis focused on relative, global differences rather than specific quantitative measurements. However, modifications such as opacity adjustments and thresholding to improve feature visibility may have introduced minor variations in perceived intensity that do not directly reflect actual concentration changes. Accordingly, dye intensity was interpreted as a comparative indicator rather than an absolute, calibrated metric.

Whilst the present study provided valuable insights into the reproducibility of MN and hypodermic needle injections, further work is needed to assess these delivery methodologies in phantoms that more closely replicate tissue architecture, including a defined dermis–epidermis interface. Building on the current findings, future studies could employ multi-layer, optically clear gels to better mimic the mechanical characteristics of native skin whilst enabling optical-based investigation. Incorporating multiple cameras positioned at varying angles would allow three-dimensional reconstruction of the injection bolus and its subsequent dispersion, providing a more comprehensive spatial analysis. In addition, systematic variation in MN array geometry and hypodermic gauge could be explored to establish a stronger relationship between device design and resultant diffusion behaviour, which may also inform considerations for scaled-up manufacture where array pitch and layout are modified.

7. Chapter 7: Scaled Up Manufacture

This chapter describes the activities undertaken to facilitate the scale-up of silicon MN fabrication from 100 mm to 150 mm silicon wafer scale. Process modifications and quality considerations implemented during these scale-up activities are presented. The quality and critical dimensions of devices produced using scaled-up methodologies will be discussed. Throughout, the challenges associated with scaling the fabrication of silicon MNs will be highlighted, with specific regard to optimising a more commercially ready manufacturing process.

7.1. Introduction

Scaling from small-scale, laboratory-based fabrication to more industrially relevant wafer sizes represents a critical transition in advancing silicon MN technologies through higher TRLs. This step is essential for enabling robust assessments of process scalability and economic viability. Foundries and MEMS fabrication facilities predominantly operate with 300 mm wafer formats, with a gradual transition towards larger wafers also underway (333). To improve the TRL of silicon MN platforms, upscaling is necessary to ensure compatibility with these industry standards prior to engagement with regulatory or translational activities. Larger wafer formats, such as 300 mm, offer a balance between high-throughput manufacture and cost-effectiveness, and as such, industrial infrastructure and tooling are typically configured for this sizing (334). Therefore, to facilitate integration into industrial-scale manufacturing and to reduce the cost-*per*-device, scale-up trials are required to optimise etch parameters for consistent CDs across the wafer. Furthermore, the scale-up process enables investigation of array reproducibility, device yield, and process robustness under more demanding and potentially fully automated conditions than those encountered in Chapter 3's small-batch prototyping.

The 100 mm, 10-wafer batch fabrication process reported in Chapter 3 provided a validated proof-of-concept for the fabrication of silicon MNs using the reported DRIE-based methodology. Building on this, scale-up activities were undertaken on a step-by-step basis, with challenges extending beyond handling size. These included new lithographic constraints, increased open area of silicon, and etch uniformity considerations, all of which required optimisation to ensure process continuity and future commercial feasibility. The same experimental instrumentation and manufacturing technologies reported in Chapter 3 were employed in this scale-up study; however, 150 mm silicon wafers were used as the starting material, and carrier wafer mounting was no longer required. The increase from 100 mm to 150 mm wafers represented a 125 % increase in surface area, providing an additional 9818 mm^2 of usable wafer real estate for device production. As a result, this enabled a greater number of devices to be produced *per* batch, thereby lowering per-unit production cost.

A secondary opportunity afforded by the scale-up of the wafer size was the inclusion of novel sub-regions for experimental trials, such as modified array pitches and altered bore positions, which could later be characterised and compared with the original array design. Design modifications were implemented in the 150 mm photolithography masks to reflect learnings from the 100 mm study, including the removal of coffin wall structures surrounding each array and the addition of an exclusion zone around the wafer's perimeter to facilitate vacuum clamping and wafer handling during processing. These changes, in combination with the larger open silicon area, necessitated re-optimisation of each DRIE etch step to account for altered gas conductance and flow distribution.

7.2. Materials and methodology

The following section will describe the materials and fabrication methodologies used for the scale-up activities required for the manufacture of silicon MNs at 150 mm wafer scale. This section reports the optimisation work performed on this process thus far, and encompasses photolithography, thin film deposition, and DRIE processing.

7.2.1. Materials

This subsection details the materials used for the scale-up proof of concept for silicon MN production. It will detail the chemicals used, photolithography masks designed, and any alterations to photolithography and etch recipes designed to maintain processing steps and ensure device fidelity.

Chemicals

Chemicals used for photolithography were listed in Chapter 3. Additional chemicals required include the positive PR AZ 12XT, and developing agent AZ MIF 726.

Photolithography masks

A new photolithography mask set was designed using KLayout (version 0.27.11) based on the initial design reported in Chapter 3 and manufactured by Photronics. The general design of the masks can be seen in Figure 67, with the new test die and alignment marks pictured in Figure 68 and Figure 69 respectively.

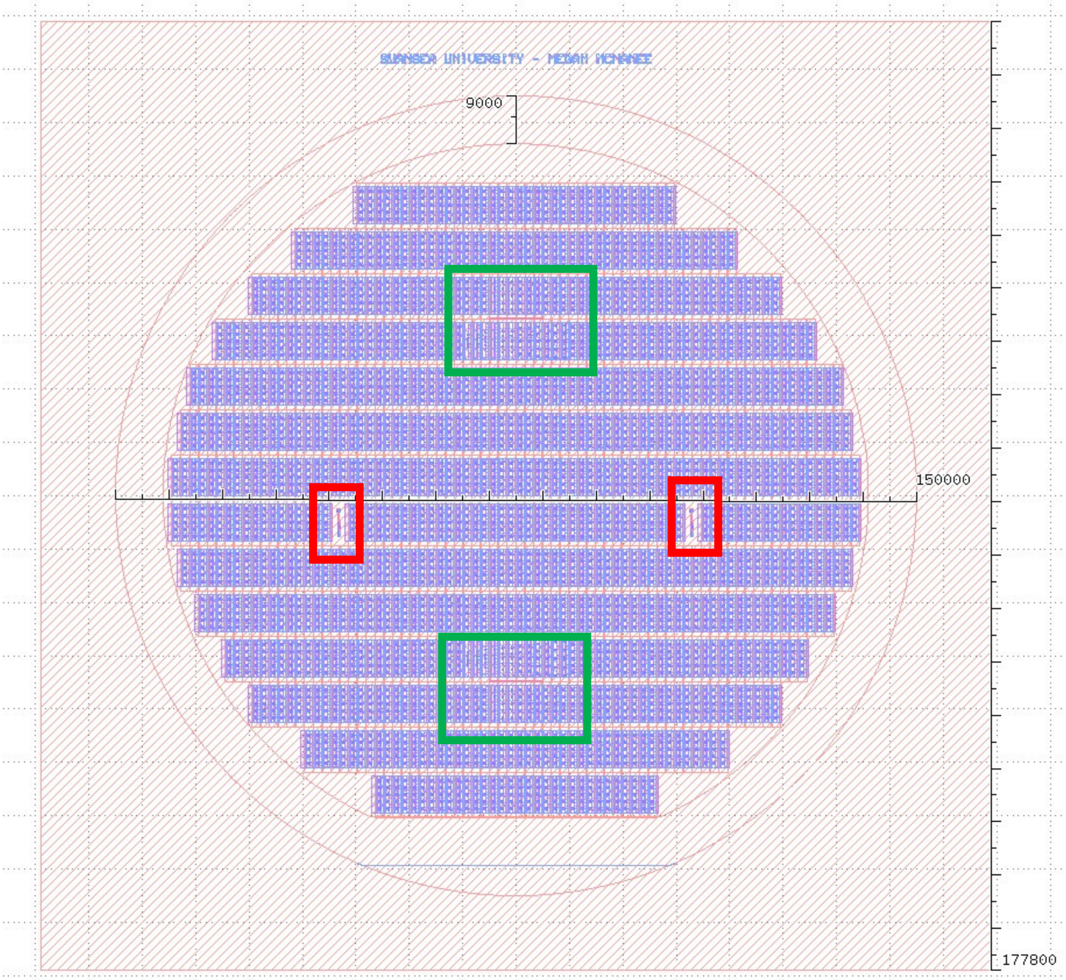

Figure 67. The 150 mm photolithography mask design with following key features: red circle (wafer stencil), 9 mm exclusion zone, blue rectangles (device arrays), red box (alignment marks) and green box (test die region)

The test die had arrays with an alteration in bore position (from 100 to 75 µm) was altered from, and pitches were varied from the standard pitch (1300 µm) to cover the pitch range of 600 – 1600 µm (Figure 68). The new mask design produced 884 dies (844 5x1 arrays, 4 dies for alignment marks, 36 test arrays); a 140% increase in die number from the original mask set (351 arrays) (Table 26). The wafer surface area was increased by 125 % when scaling from 100 mm to 150 mm wafers, with the die number *per* wafer increasing by approximately 140 %. This was attributable to more efficient die arrangement, reduced exclusion zone, and removal of coffin-like architecture surround the die, allowing a greater proportion of the wafer's real estate to be utilised. The glass mask set was ordered in 6 layers, including outlines, marker, bevel, bore, shaft, and dice masks. Alignment marks were rearranged into a vertical orientation to reduce the wafer real estate requirement and improve visibility (Figure 69).

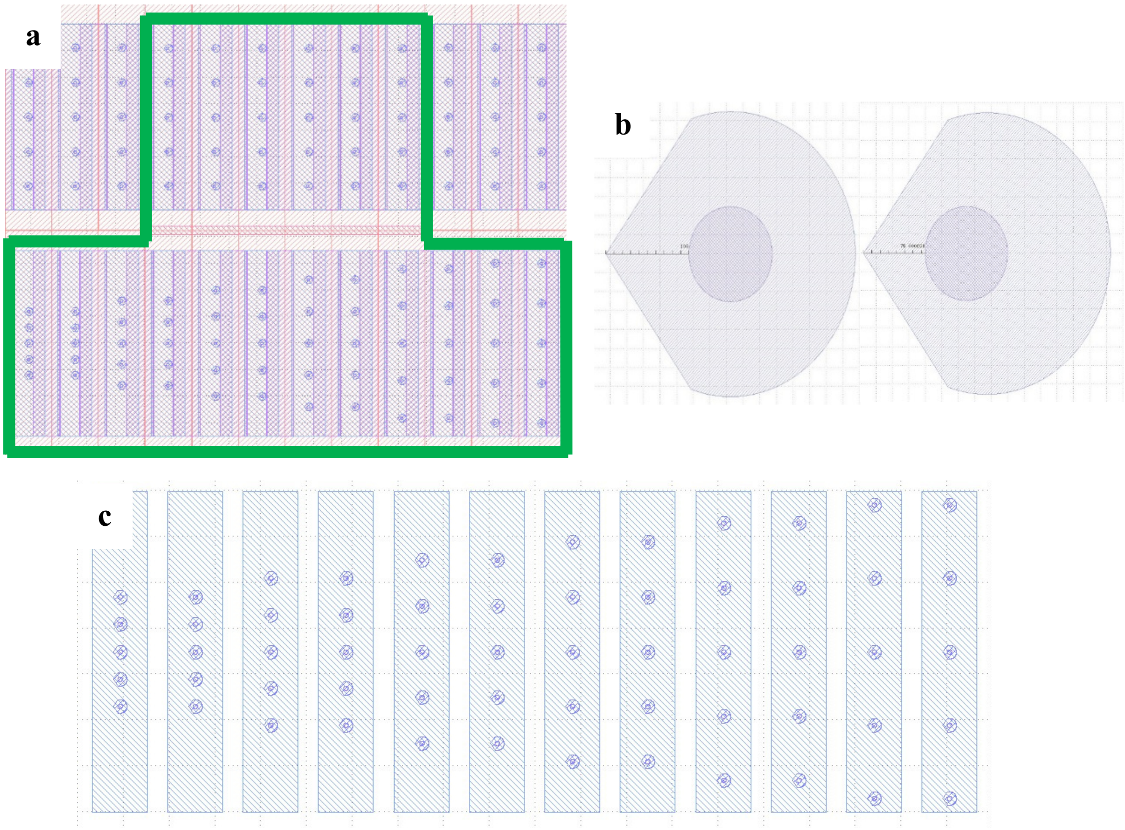

Figure 68. Test die region (a) green box representing the test die region. Upper section with altered bore position, lower section with altered device pitches (b) altered bore position (c) altered pitch

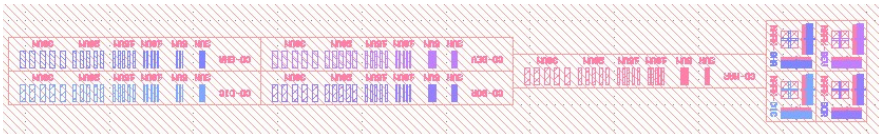

Figure 69. New alignment marks format, presented here horizontally, however are in the vertical orientation on the mask

Table 26. A comparison of the number of various die sizes on 100 and 150 mm silicon wafers, and the die increase (%) on the increased wafer size

Wafer size	*Die number*					*Total die*	*Die % increase*
	5x1	*4x1*	*3x1*	*Replaced by alignment marks*	*Test die*		
100	333	16	6	4	0	351	140 %
150	884	0	0	4	36	844	

7.2.2. Experimental instrumentation and manufacture methodology

The fabrication of silicon MN arrays on 150 mm silicon wafers was carried out using the same experimental instrumentation and manufacturing processes as reported in Chapter 3, including the spin coater, hot plate, mask aligner, and DSi-v™ DRIE system. No additional or modified equipment was introduced during this scale-up study. All equipment was calibrated as previously described, and no deviations in operational parameters were introduced unless otherwise stated in the subsequent process-specific subsections. The primary difference from the 100 mm fabrication process was the use of 150 mm, single-side polished silicon wafers as starting substrates. These were processed directly without mounting to carrier wafers, due to the improved handling compatibility of full-size wafers with the DSi-v™ system.

In Chapter 3, spray coating was required for shaft patterning to accommodate the topography of 3D-etched features. During scale-up, all wafers remained flat at the point of each patterning step due to process segmentation and independent optimisation of each etch stage. Consequently, spray coating was not required. A spin coater was therefore used for PR deposition during shaft patterning, both for consistency and due to limitations in spray coater availability at the time of processing. The spin coating procedure for shaft patterning using AZ 12XT resist is summarised as recipe 4 in Table 27. This process yielded approximately 15 µm-thick PR layers.

Table 27. Spin coating recipe for AZ 12XT

Spin Coater Recipe #	*Chemical*		*Recipe*					
			Step 1			*Step 2*		
	name	*class*	rpm	accr	time (s)	rpm	accr	time (s)
4	AZ 12XT	positive photoresist	300	1000	10	1000	1000	30

Optimisation of etch steps required consideration of potential alterations in etch depth, duty cycle, platen power, etch length, and time ramps. The effects of varying these control parameters are detailed in Table 28. The switched etching, as described in Chapter 3, can also be controlled by the time allocated for E1 and E2, with E1 and E2 time determining the length of time allotted for removal of process deposition and for chemical etch respectively.

Table 28. The main controlling parameters of the etch recipe, their role, what they can control, and the resultant effect of altering them

Parameter	*Role*	*Control*	*Effect*
Duty cycle	Notch suppression	Sets % of etch cycle with RF power	Lower values reduce notching
Platen power	Etch anisotropy	Increases ion energy	Higher power improves verticality
Time ramp	Etch depth and aspect-ratio control	Adjusts etch/passivation time ratio	Maintains depth control and sidewall profile

7.2.3. Analytical methodology and characterisation

Analytical methodology and characterisation techniques used for scale-up activities were consistent with those previously reported in Chapter 3. Namely, optical microscopy and SEM was used to assess photolithography alignment and development, and PR thickness respectively. No additional analytical methodologies were introduced during the scale-up optimisation.

7.2.4. Bevel 150 mm fabrication

A batch of 10, 150 mm silicon wafers were photolithographically patterned as reported in Chapter 3 and repeated in brevity here. Wafers were solvent and plasma cleaned, and spin coated with AZ 125nXT-10A. Following which they were left to homogenise (5 mins), softbaked (130 ºC, 13 mins), and rehydrated (5 mins). Newly designed masks (Figure 67) were utilised during soft contact exposure (MA8 Mask Aligner, 1500 mJ/cm^2) and aligned to the wafer flat, following which they were developed in AZ 726

(4 mins). Wafers were washed (DI water), dried, and all necessary quality checks (CD, development, and alignment) were performed on the patterned wafers using an optical microscope.

Wafers were etched using the DSi-v™ previously described in Chapter 3 initially at half-depth using the original bevel etch recipe developed for the 100 mm wafer size to investigate etch quality, before being run at full-depth (recipe found in Appendix A). Post etch, wafers were cleaved and samples from the centre and edge were sputtered in gold and imaged using a SEM.

7.2.5. Bore 150 mm fabrication

Bore patterning was performed on a batch of 10, 150 mm silicon wafers as described in Chapter 3. Following spin coating (AZ 125nXT-10A), resist coated wafers were homogenised (5 mins) softbaked (130 ^{o}C, 13 mins), and rehydrated (5 mins). Exposure was performed using the MA8 mask aligner, performing manual alignment of the new mask (Figure 67) to the wafer flat, exposing the resist using soft contact (1500 mJ/cm^2). Wafers were developed in AZ 726 (2 mins). Wafers were rinsed (DI water), dried, and all necessary quality checks were performed on the patterned wafers using an optical microscope.

Wafers were etched using the DSi-v™ previously described in Chapter 3 initially at half-depth using the original bore etch recipe developed for the 100 mm wafer size to investigate etch quality, before being run at full-depth (recipe found in Appendix A). Post etch, wafers were cleaved and samples from the centre and edge were sputtered in gold and imaged using a SEM.

7.2.6. Shaft 150 mm fabrication

A batch (10) of blank 150 mm silicon wafers were spin coated using recipe 4 (Table 27, subsection 7.2.2) and baked (110 °C, 4 mins). Exposure was performed using the MA8 mask aligner (200 mJ) using the new mask set (Figure 67), which was manually aligned to the wafer flat. Following a post exposure bake (90 °C, 60 s), wafers were developed in 2x 60 s baths of AZ MIF 726 and rinsed in DI water. Quality checks were performed on the patterned wafers using the optical microscope.

The DSi-v™ was used to etch wafers, as previously described (Chapter 3, subsection 3.2.4), initially using the original recipe at half-depth (recipe found in Appendix A). The recipe alterations made during optimisation are detailed below (Table 29, Figure 70). Iterations were run in the order listed.

Table 29. A register of the recipe number, its original base recipe, the depth it etched to, and any additional modifications to the base recipe for shaft recipe iterations

Recipe no.	*Base recipe*	*Depth*	*Modifications*	
R01	-	½		
R04	R01	½	½ duty cycle	2x platen power
R05	R01	½	Reduction in E2	
R02	R01	Full		
R03	R01	½	Aggressive time ramp	
R06	R01	½	Reduced E1	
R07	R04	Full		
R08	R01	Full	Aggressive time ramp	½ duty cycle

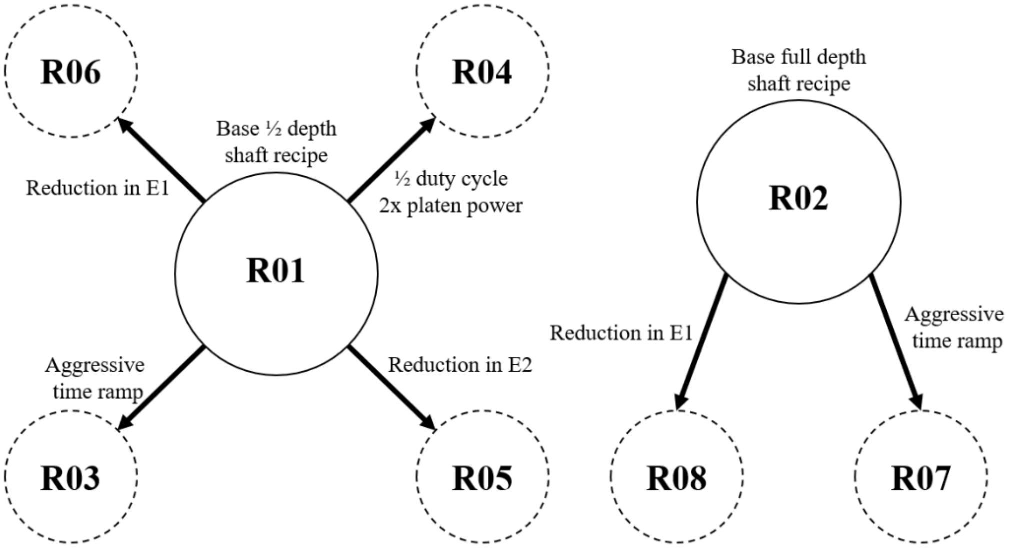

Figure 70. A schematic of shaft recipe alterations during optimisation

7.3. Experimental results

The results in this section are organised by MN feature, with separate subsections for the bevel, bore, and shaft. Each includes quantitative data on shared etch parameters such as depth, feature widths, calculated shaft profile, etch rate, and etch selectivity. All calculated profiles are measured as the profile of the remaining silicon. Etch selectivity was calculated as the etch rate of the target material relative to the etch rate of etch rate of masking material, with higher values more desirable and reported as a ratio. Feature-specific metrics are also reported where applicable. Cross-sectional SEM images from the wafer centre and south edge are provided to qualitatively support profile assessment.

7.3.1. Bevel recipe development

The critical dimensions and device fidelity of the bevel feature produced are detailed here. The evaluation of the features produced *via* a half etch depth (R01) in addition to full etch depth (R02) are presented.

Bevel R01

Bevel R01 achieved an average etch depth of 555.4 µm, with minimal variation observed across the wafer (± 2.2 %) (Table 30) (Figure 71).The centre sample presented with a slower etch rate (552.4 µm) than the south sample (577.1 µm), with 23.39 µm unetched PR remaining on the south sample (Table 30). A tight uniformity with respect to the calculated profile was observed, with a non-uniformity (NU) of ± 1.2 % on the average of 103.2 µm (Figure 71). There was significant variation in the mask etch rate observed between the centre and south (3.8 µm/min and 28.1 µm/min respectively) resulting in an inflated non-uniformity of ± 76 %. This discrepancy contributed to driving a larger selectivity variation (144.5 µm *versus* 20.5 µm). SEMs show that the etched samples were free of debris or grass formation (Figure 71). The mask etch rate was calculated form the centre sample to be 9.2 µm/min, this was expected to be consistent across the wafer. Etch selectivity was calculated as 144.5:1 and 20.6:1 for the centre and south respectively, presenting with a large non-uniformity (75.1 %), due to the lift off of residual PR on the south sample.

Table 30. Measured post-etch features and calculated etch rate for bevel sample post R01 etch recipe at the centre and south of the sample

Parameter	*Unit*	*Bevel: R01*			
		Centre	*South*	*Average*	*NU (±%)*
Depth	µm	543.2	567.5	555.4	2.2
Etch Rate	µm/min	9.2	9.6	9.4	2.2
Etch selectivity	Si:PR	144.5:1	20.6:1	82.5:1	75.1

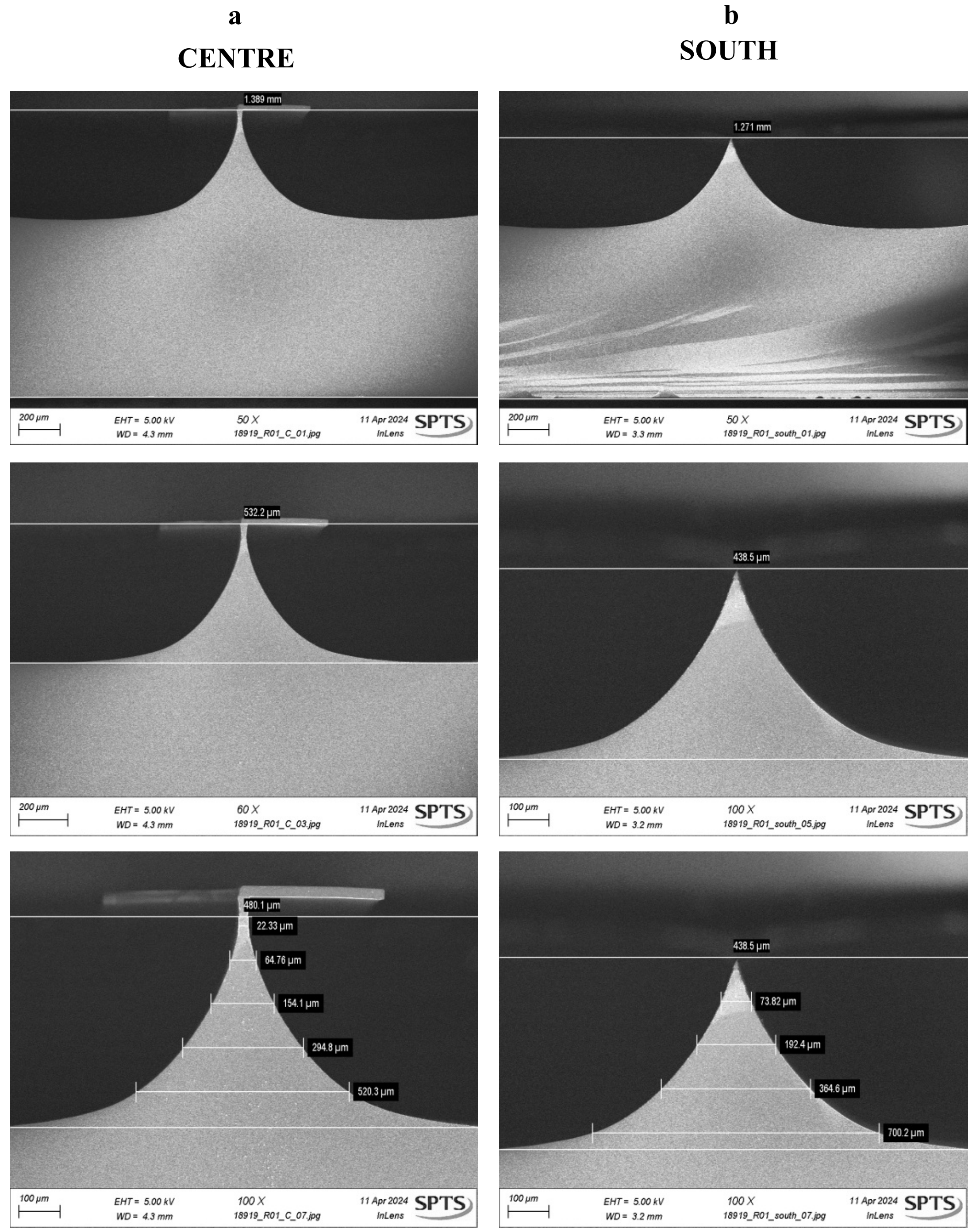

Figure 71. Scanning electron microscope images of bevel features following recipe Bevel R01. Images from (a) a centre sample and (b) a south sample

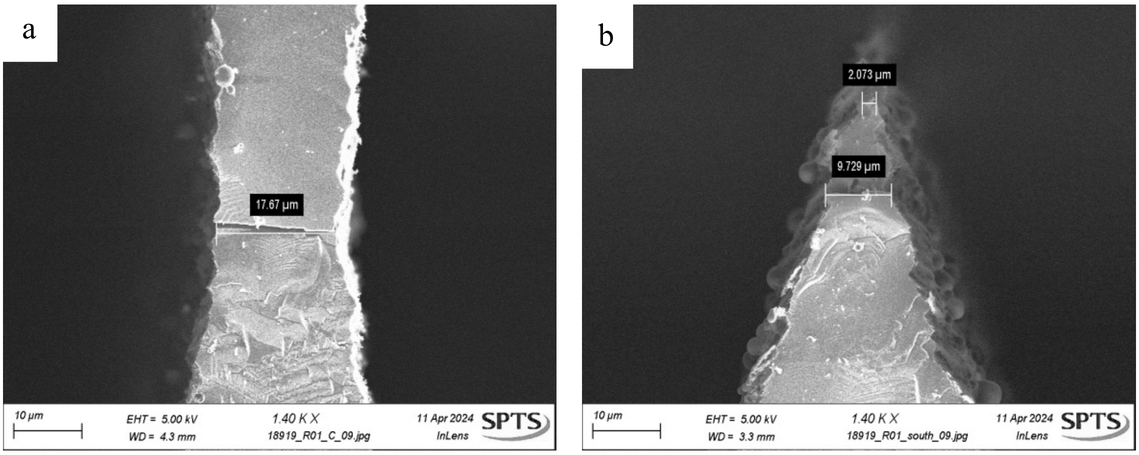

Figure 72. Tip of bevel on a Bevel R01 from (a) centre with remaining photoresist and (b) south

<u>Bevel R02</u>

Bevel R02 achieved a greater average etch depth of 640.1 µm with excellent uniformity (NU ± 1.0 %) (Table 31) (Figure 73). Unlike Bevel R01, no PR mask remained on either the centre or south sample following the etch. Selectivity was consistent across the wafer, with a NU of ± 1.8 %. Some debris was visible in the SEM images of the Bevel R02 etch, although this was attributed to cleaving and sample preparation artefacts rather than to the etch process itself (Figure 73). Etch selectivity was consistent across the wafer, calculated as 23.8:1 and 23.0:1 for the centre and south respectively (NU ± 1.8 %).

Table 31. Measured post-etch features and calculated etch rate for bevel sample post R02 etch recipe at the centre and south of the sample

Parameter	*Unit*	*Bevel: R02*			
		Centre	*South*	*Average*	*NU (±%)*
Depth	µm	646.5	633.6	640.1	1.0
Etch Rate	µm/min	9.7	9.5	9.6	1.0
Etch selectivity	Si:PR	23.8:1	23.0:1	23.4:1	1.8

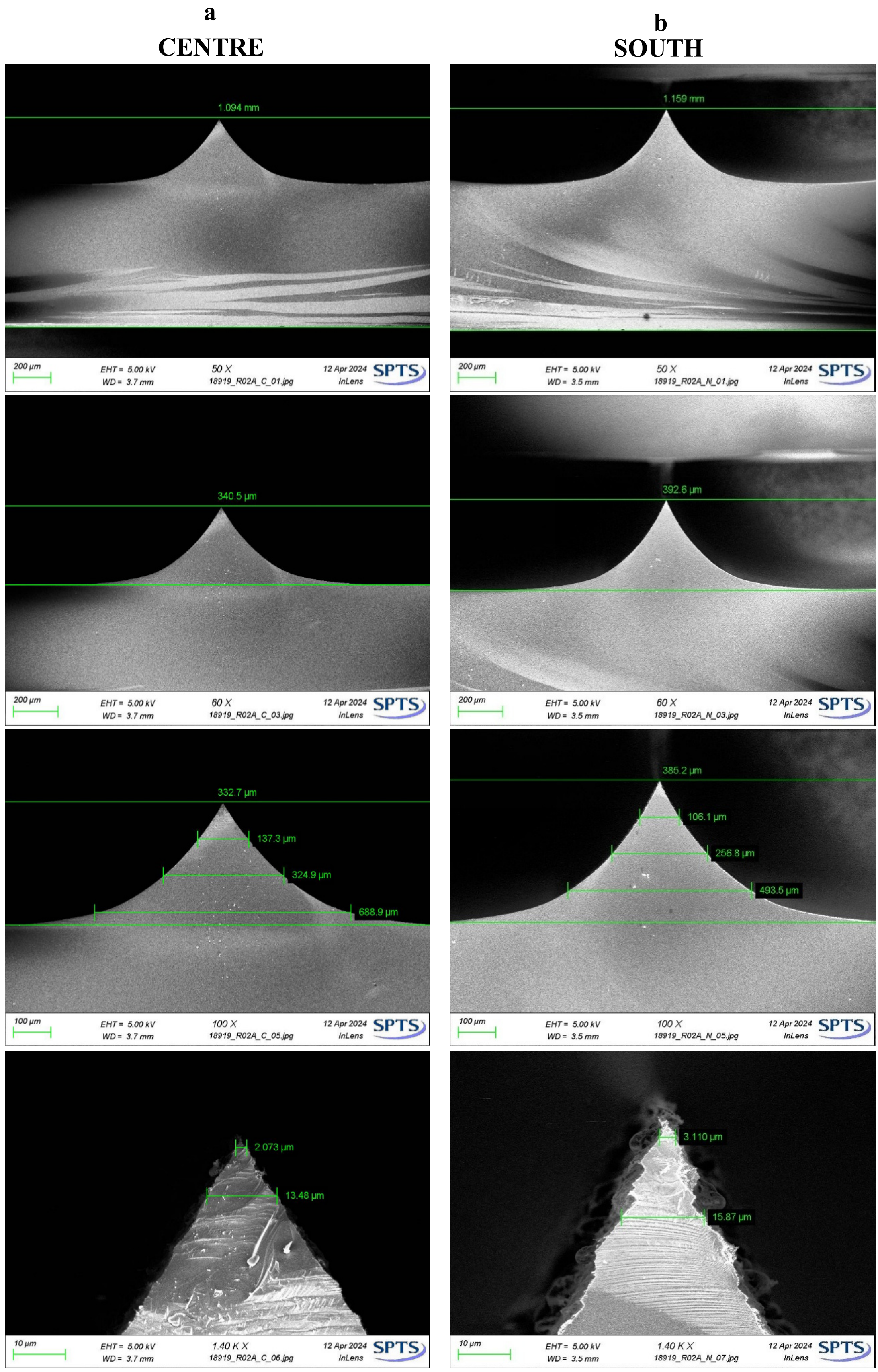

Figure 73. Scanning electron microscope images of bevel features following recipe Bevel R02. Left and right column presents images from a centre and south sample respectively

7.3.2. Bore recipe development

This subsection presents an evaluation of the bore feature produced at 150 mm wafer scale. Bore features produced at half-depth (R01) and full-depth (R02) are presented.

Bore R01

Bore R01 achieved an average etch depth of 798 µm, with very minimal NU (± 0.8 %) (Table 32). The south samples were measured as slightly narrower than the centre (NU ± 2.6 %) at the top of the feature, although the bottom width (average 90.0 µm) exhibited greater variation, with a NU of ± 10.4 % (Table 32). The south samples presented with a greater degree of bow, with a middle with of 104.2 µm, which was too excessive to be as a result of an off-centre cleave, identifiable *via* the striations visible in Figure 74. The south sample bottom width, however, was measured to be substantially lower (80.64 µm) than that of the centre, however, was as a result of the cleave line (Figure 74). The feature profile angle averaged 89.8° (NU ± 0.3 %), indicative of well-controlled etch sidewalls nearing the ideal value of 90°. The selectivity was calculated 50.8:1 and 54.6:1 for the centre and south samples respectively (NU ± 3.6 %).

Table 32. Measured post-etch features and calculated etch rate for bore sample post R01 etch recipe at the centre and south of the sample

Parameter	*Unit*	*Bore: R01*			
		Centre	*South*	*Average*	*NU (±%)*
Depth	µm	804	792	798.0	0.8
Top width	µm	98.08	93.04	95.6	2.6
Middle width	µm	100.6	104.2	102.4	1.8
Bottom width	µm	99.32	80.64	90.0	10.4
Scallop width	nm	< 600	< 570		
Calculated Profile	°	90.0	89.5	89.8	0.3
Etch Rate	µm/min	11.3	11.3	11.3	0.1
Etch selectivity	Si:PR	50.8:1	54.6:1	52.7:1	3.6

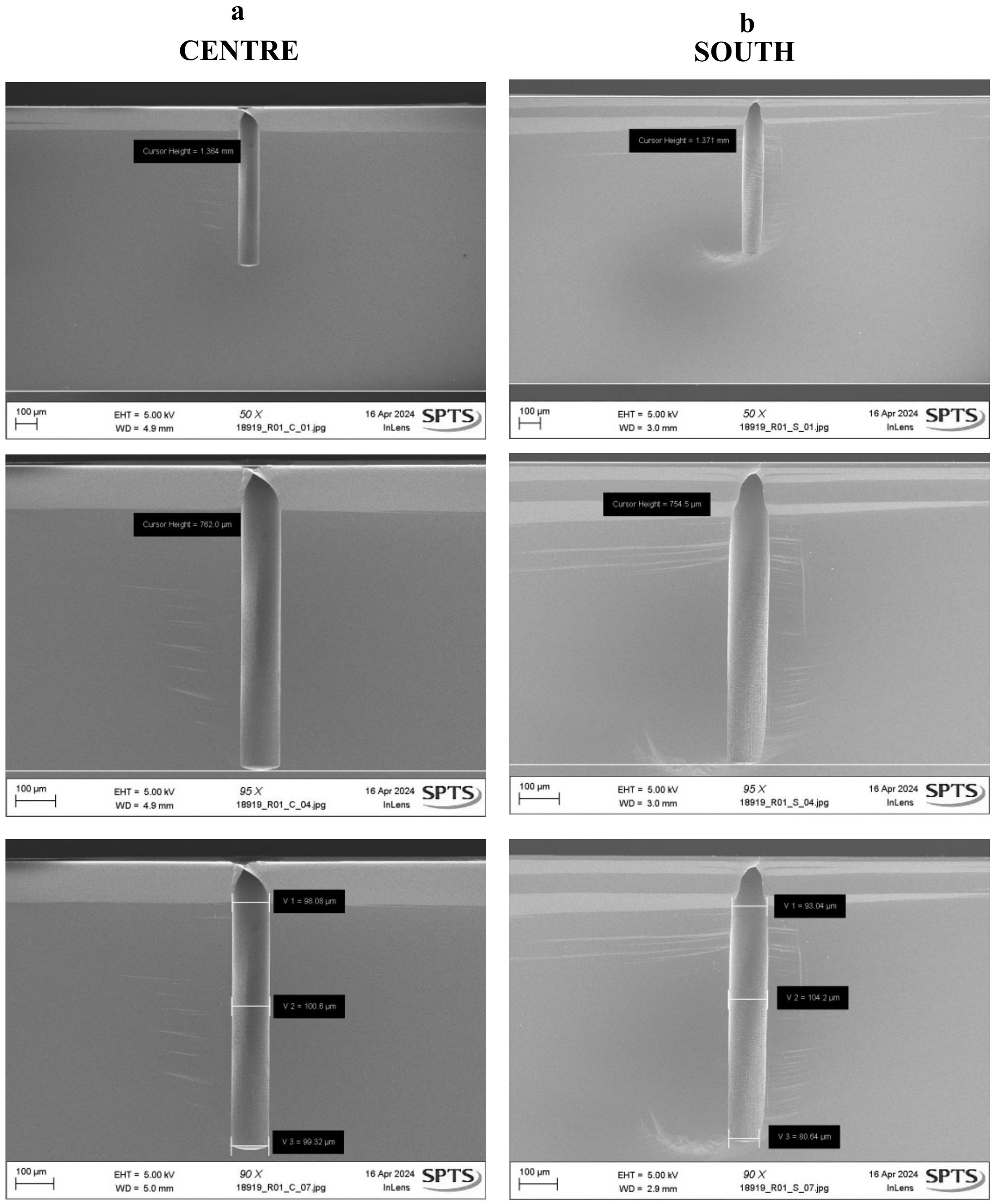

Figure 74. Scanning electron microscope images of bore features following recipe Bore R01. Left and right column presents images from a centre and south sample respectively

Bore R02

The full-depth Bore R02 etch achieved an excellent average etch depth (1335.5 µm depth etch on a 1400 µm thick wafer) with excellent wafer uniformity (± 0.3 %) and highly consistent top and middle widths across the centre and south samples (NU ≤ 0.8 %) (Table 33) (Figure 75). However, bottom widths were measured to have the largest variation, with an increased NU of ± 22.2 %. The bore profile angle averaged 89.0°

(NU ± 0.3 %), comparable to that of Bore R01. The etch rate was consistent across centre and south samples (9.9 µm/min). The etch selectivity was calculated to be a reduction from that in R01, at 23.8:1 and 23.0:1 (NU ± 1.8 %) for the centre and south respectively.

Table 33. Measured post-etch features and calculated etch rate for bore sample post R02 etch recipe at the centre and south of the sample

Parameter	*Unit*	*Bore: R02*			
		Centre	*South*	*Average*	*NU (±%)*
Depth	µm	1331	1340	1335.5	0.3
Top width	µm	105.6	104	104.8	0.8
Middle width	µm	103.5	102	102.8	0.7
Bottom width	µm	46.69	73.41	60.1	22.2
Scallop width	nm	< 1.2	< 2.7		
Calculated Profile	°	88.7	89.3	89.0	0.3
Etch rate	µm/min	9.9	9.9	9.9	0.3
Etch selectivity	Si:PR	23.8:1	23.0:1	23.4:1	1.8

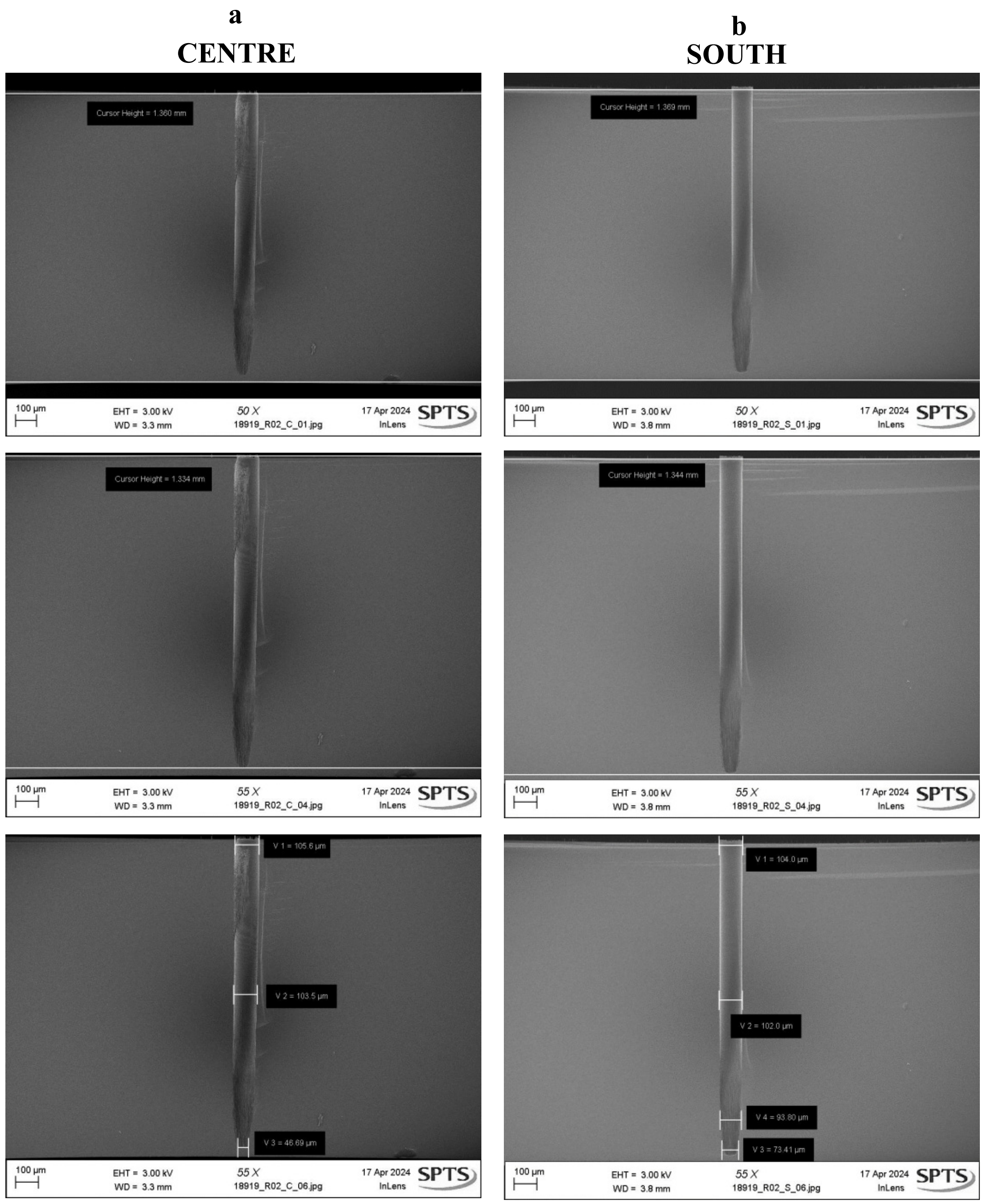

Figure 75. Scanning electron microscope images of bore features following recipe Bore R02. Left and right column presents images from a centre and south sample respectively

7.3.3. Shaft recipe development

The evaluation of the shaft feature produced at 150 mm wafer scale is presented in this subsection. The features produced at half etch depth (R01, 3, 4, and 5) and full etch depth (R02, 7, and 9) are presented separately. The analysis to be reported focused on critical dimensions for this feature, such as etch depth, rate, and profile, to provide insight into the effects of recipe parameters on etch uniformity and feature geometries.

Half-depth recipes

The evaluation of device and etch quality following the shaft etch at half-depth and at 150 mm will be presented here. Four half-depth shaft etches (R01, 3, 4, and 5) will be presented and evaluated to provide insight into how etch recipe alterations in can impact device geometry and etch uniformity across the wafer.

Shaft R01 (Base Recipe)

The half-depth etch recipe, Shaft R01, produced an average etch depth of 349.0 µm, with minimal NU across the centre and south samples (NU ± 2.6 %) (Table 34). Shaft feature width across centre and south samples remained consistent relative to their heights, with top, middle, and bottom widths measured to be 295.3 µm (NU ± 0 %), 267.7 µm (NU ± 0.9 %), and 230.9 µm (NU ± 1.6 %) respectively (Figure 76). Despite centre/south symmetry, the gradual decrease in feature width with increasing etch depth resulted in a calculated average profile angle of 84.7° (NU ± 0.5°), indicating steep but slightly tapered sidewalls. There was no grass formation or debris identified on the SEMs post etch (Figure 76). The average etch rate was 5.5 µm/min (NU ± 2.6 %). The etch selectivity for Shaft R01 was calculated as 72.2:1 and 68.7:1 (NU ± 2.5 %) for centre and south respectively.

Table 34. Measured post-etch features and calculated etch rate for shaft sample post R01 etch recipe at the centre and south of the sample

Parameter	*Unit*	*Shaft: R01*			
		Centre	*South*	*Average*	*NU (± %)*
Depth	µm	340	358	349.0	2.6
Top width	µm	295.3	295.3	295.3	0.0
Middle width	µm	265.2	270.2	267.7	0.9
Bottom width	µm	227.2	234.5	230.9	1.6
Calculated profile	°	84.3	85.1	84.7	0.5
Etch rate	µm/min	5.3	5.6	5.5	2.6
Etch selectivity	Si:PR	72.2:1	68.7:1	70.5:1	2.5

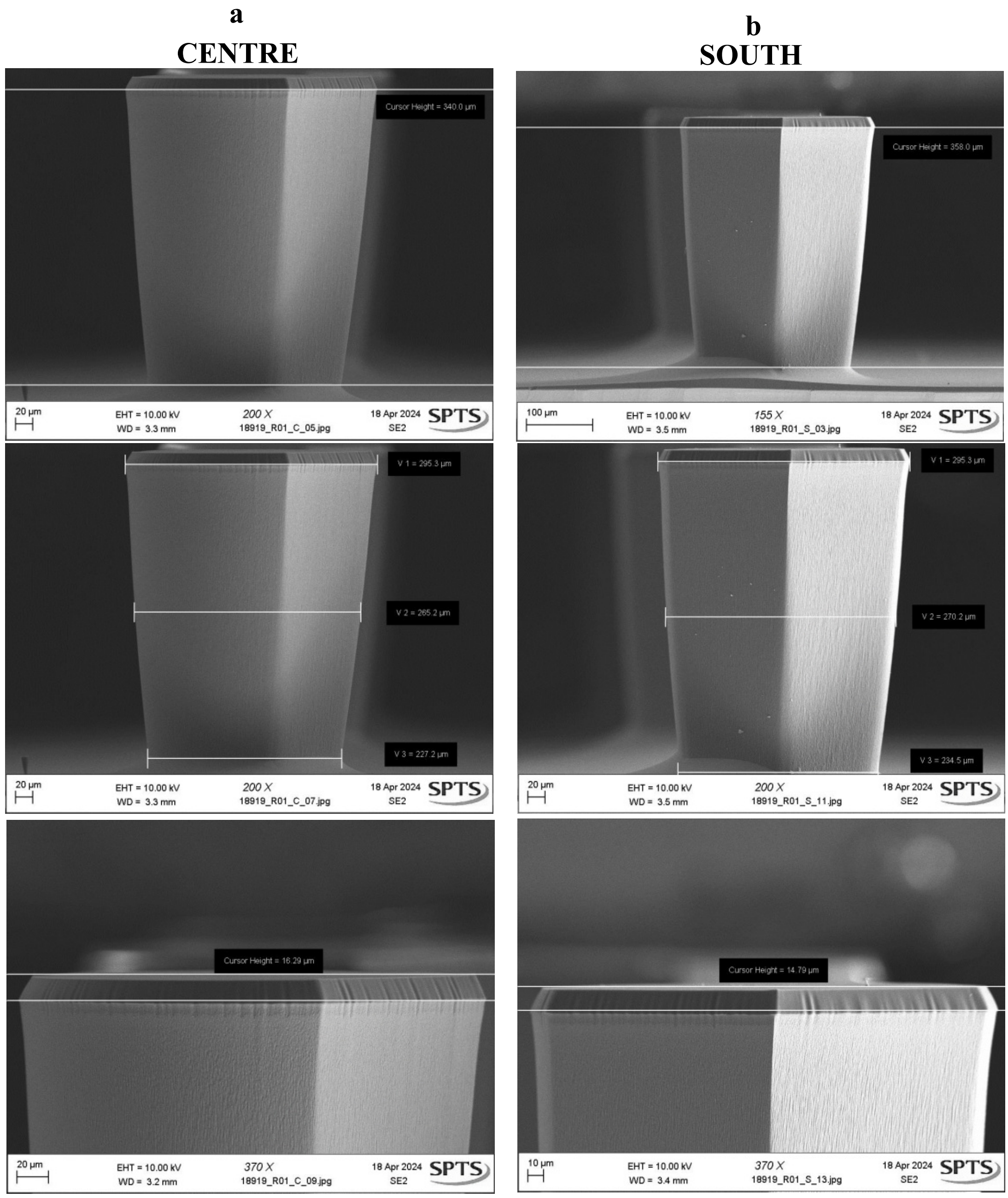

Figure 76. Scanning electron microscope images of shaft features following recipe Shaft R01. Left and right column presents images from a centre and south sample respectively

Shaft R04 (Base Recipe, ½ duty cycle, 2x platen power)

The Shaft R04 recipe produced a slightly shallower average etch depth (337.9 µm) than R01, with a significant reduction in wafer non-uniformity (NU ± 0.6 %) (Table 35, Figure 77). Top, middle, and bottom widths showed slight increases relative to R01, measuring 297.0 µm, 276.9 µm, and 247.9 µm respectively, with improved uniformity at the bottom of the features (NU ± 0.5 %). The calculated profile angle averaged 85.8° with negligible variation (NU ± 0.0°), indicating steep sidewalls with a slight reduction in taper compared to Shaft R01 (84.7°, NU ± 0.5°). The etch rate across the wafers was calculated to be 5.3 µm/min (NU ± 0.6 %). The etch selectivity for the centre and south samples were calculated to be 47.2:1 and 42.5:1 respectively, with a NU of ± 5.3 %.

Table 35. Measured post-etch features and calculated etch rate for shaft sample post R04 etch recipe at the centre and south of the sample

Parameter	*Unit*	*Shaft: R04*			
		Centre	*South*	*Average*	*NU (± %)*
Depth	µm	340	335.7	337.9	0.6
Top width	µm	298.1	295.9	297.0	0.4
Middle width	µm	278	275.8	276.9	0.4
Bottom width	µm	249	246.7	247.9	0.5
Calculated profile	°	85.9	85.8	85.8	0.0
Etch rate	µm/min	5.3	5.3	5.3	0.6
Etch selectivity	Si:PR	47.2:1	42.5:1	44.9:1	5.3

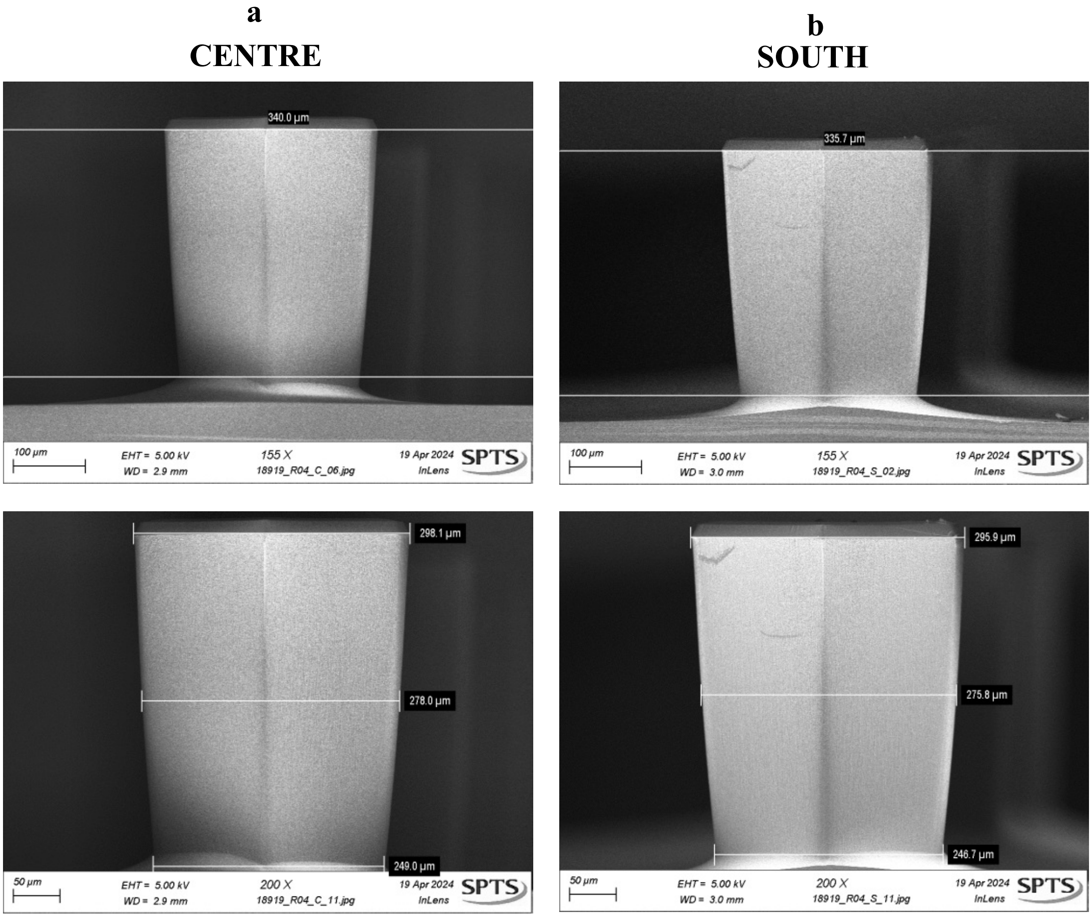

Figure 77. Scanning electron microscope images of shaft features following recipe Shaft R04. Left and right column presents images from a centre and south sample respectively

Shaft R05 (Base recipe, 0.5s reduction in E2)

Shaft R05 produced features with a reduced average etch depth of 290.0 µm and moderate wafer non-uniformity (NU ± 2.4 %) across the centre and south samples (Table 36, Figure 78). Alongside the decrease in etch depth, middle and bottom widths exhibited increased non-uniformity compared to R04 (NU ± 1.3 % and 2.5 %, respectively). Despite this, the calculated profile angle averaged 86.8° (NU ± 0.5°), reflecting slightly steeper sidewalls, which may partly result from the shallower etch depth. The average etch rate calculated was 5.0 µm/min (NU ± 2.4 %). SEM images showed no evidence of grass or debris formation (Figure 78). The etch selectivity for the centre (38.8:1) and south (43.6:1) samples had a NU calculated to be ± 5.9 %.

Table 36. Measured post-etch features and calculated etch rate for shaft sample post R05 etch recipe at the centre and south of the sample

Parameter	*Unit*	*Shaft: R05*			
		Centre	*South*	*Average*	*NU (±%)*
Depth	µm	283.1	296.8	290.0	2.4
Top width	µm	299.2	296.4	297.8	0.5
Middle width	µm	288.6	281.4	285.0	1.3
Bottom width	µm	272.4	259	265.7	2.5
Calculated Profile	°	87.3	86.4	86.8	0.5
Etch rate	µm/min	4.9	5.2	5.0	2.4
Etch selectivity	Si:PR	38.8:1	43.6:1	41.2:1	5.9

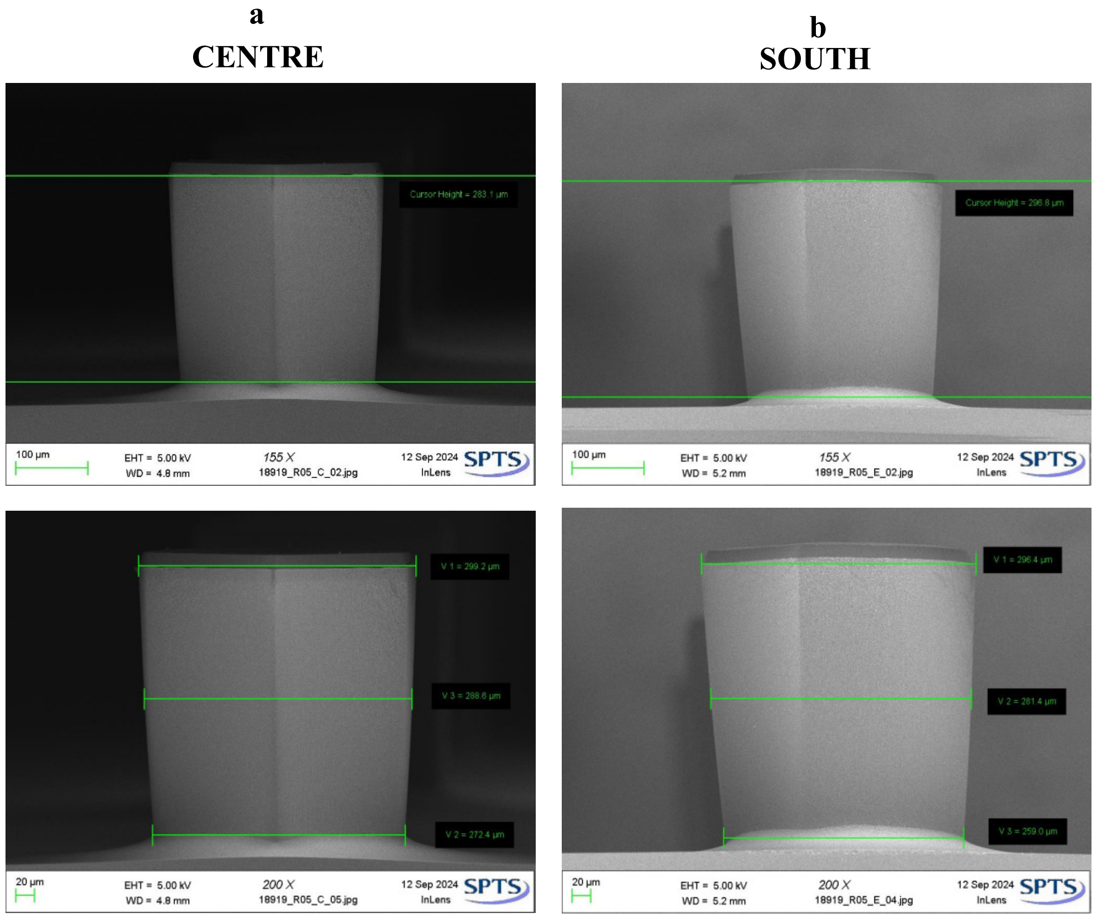

Figure 78. Scanning electron microscope images of shaft features following recipe Shaft R05. Left and right column presents images from a centre and south sample respectively

Shaft R03 (Base recipe, aggressive time ramp)

The half-depth Shaft R03 etch produced an average depth of 305.1 µm with moderate non-uniformity across the wafer (NU ± 1.8 %) (Table 37). Top, middle, and bottom widths were measured at 300.4 µm, 289.8 µm, and 274.4 µm, respectively, exhibiting tight uniformity (NU ≤ ± 0.3 %). These dimensions yielded a calculated profile angle of 87.6°, indicating well-controlled sidewalls with slightly increased steepness relative to previous half-depth etches (Figure 79). The etch rate was calculated to be 3.3 µm/min and was consistent across the wafer. Centre and south etch selectivity values were calculated to be 60.9:1 and 68.1:1 (NU ± 5.6 %).

Table 37. Measured post-etch features and calculated etch rate for shaft sample post R03 etch recipe at the centre and south of the sample

Parameter	*Unit*	*Shaft: R03*			
		Centre	*South*	*Average*	*NU (±%)*
Depth	µm	310.5	299.7	305.1	1.8
Top width	µm	299.8	300.9	300.4	0.2
Middle width	µm	289.2	290.3	289.8	0.2
Bottom width	µm	273.5	275.2	274.4	0.3
Calculated Profile	°	87.6	87.5	87.6	0.0
Etch rate	µm/min	3.3	3.2	3.3	1.8
Etch selectivity	Si:PR	60.9:1	68.1:1	64.5:1	5.6

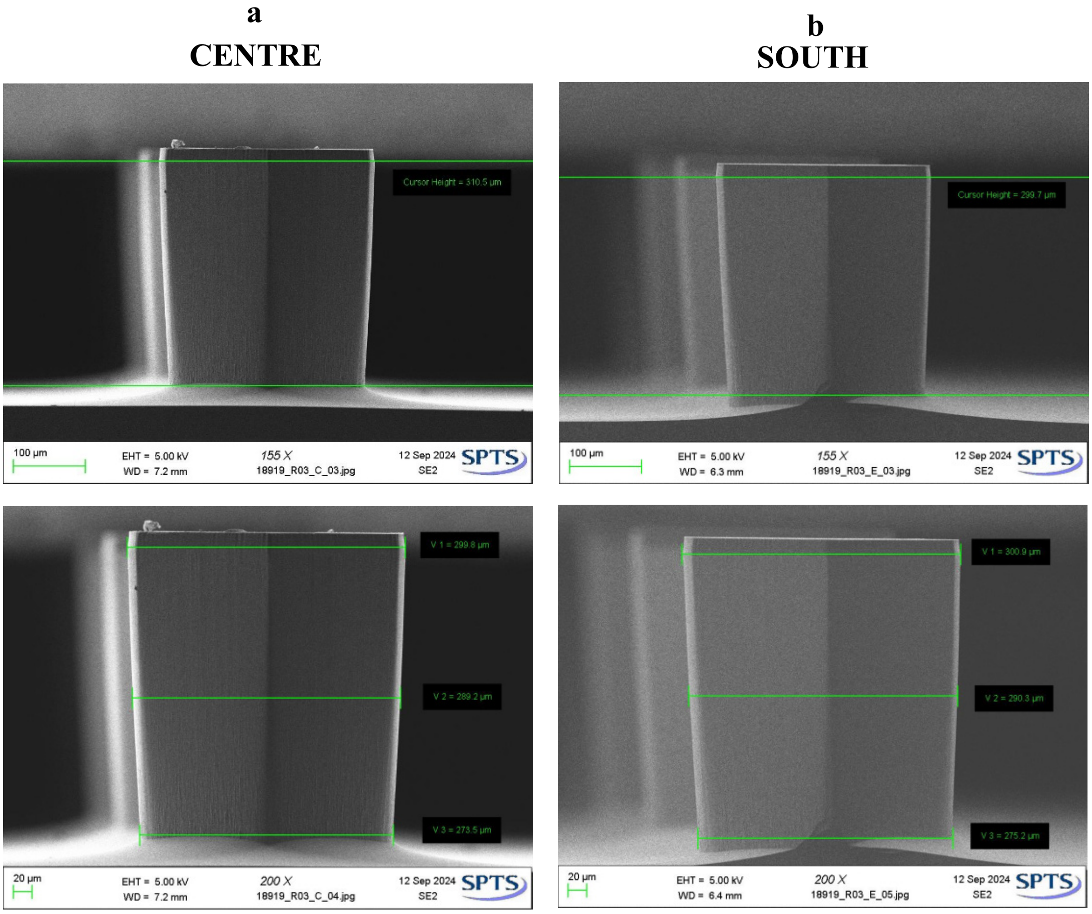

Figure 79. Scanning electron microscope images of shaft features following recipe Shaft R03. Left and right column presents images from a centre and south sample respectively

Shaft R06 (0.2s reduction in E1)

With an average etch depth of 308.7 µm, Shaft R06 produced features of widths consistent with that previously reported by R03, generating a profile angle average of 87.6° but with greater non-uniformity (± 0.3 %) (Table 38) (Figure 80). Feature widths at the top, middle, and bottom points were measured to be 300.1 µm, 288.4 µm, and 273.9 µm respectively. Notably, this etch recipe failed at 490 out of 750 loops, at 198.0 µm etch depth, due to a cooling failure, requiring the etch to be restarted. This caused in a build-up of polymer on the shaft, and resultantly, striations appear in a 19 µm band immediately after the point of failure, prior to the last 82.76 µm etch depth (Figure 80). Additionally, undesirable architecture was visible in the SEMs, which may have been present due to the polymer build up preventing uniform etching (Figure 80). The etch rate remained consistent across the wafer at 5.0 µm/min, regardless of the pause in etching. Etch selectivity for Shaft R06 was calculated as 77.3:1 at the centre, and 75.2:1 at the south, with a NU of ± 1.3 %.

Table 38. Measured post-etch features and calculated etch rate for shaft sample post R06 etch recipe at the centre and south of the sample

Parameter	*Unit*	*Shaft: R06*			
		Centre	*South*	*Average*	*NU (± %)*
Depth	µm	309	308.3	308.7	0.1
Top width	µm	299.2	300.9	300.1	0.3
Middle width	µm	286.4	290.3	288.4	0.7
Bottom width	µm	270.2	277.5	273.9	1.3
Calculated profile	°	87.3	87.8	87.6	0.3
Etch rate	µm/min	5.0	5.0	5.0	0.1
Etch selectivity	Si:PR	77.3:1	75.2:1	76.3:1	1.3

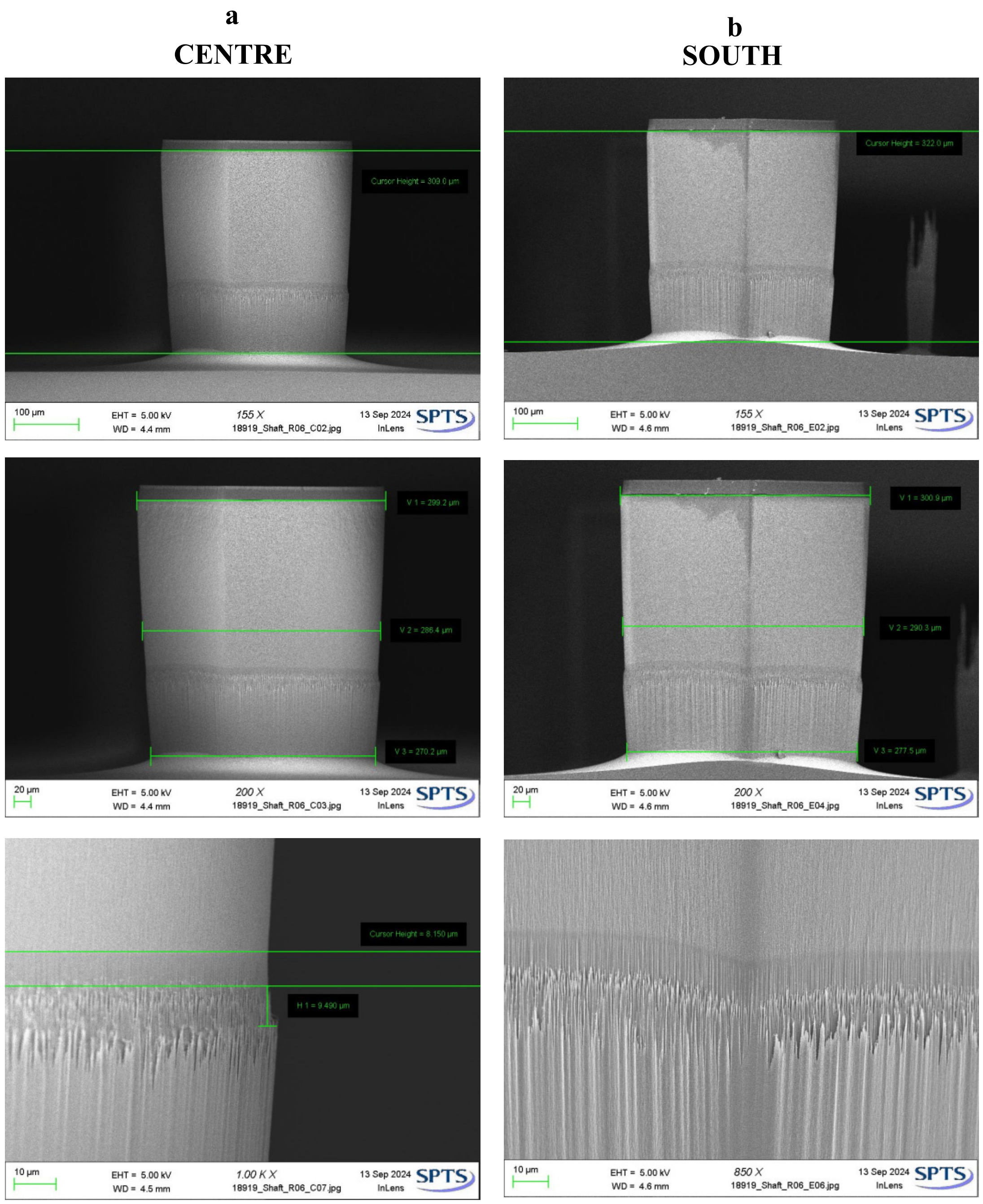

Figure 80. Scanning electron microscope images of shaft features following recipe Shaft R06. Left and right column presents images from a centre and south sample respectively

<u>Full-depth recipes</u>

The evaluation of shaft feature and etch quality following the full-depth etches at 150 mm wafer scale are presented here. Three full-depth shaft etches were run (R02, 7, and 8) and will be examined with respect to the impact their variations has on device critical dimensions, etch quality, and etch uniformity.

Shaft R02 (Base recipe)

The full-depth Shaft R02 recipe produced an average etch depth of 664.7 µm with excellent uniformity across the wafer (NU ± 0.4 %) (Table 39). Top widths were highly consistent (293.5 µm, NU ± 0.3 %), whereas greater variation was observed in the middle (242.0 µm, NU ± 2.4 %) and bottom widths (142.3 µm, NU ± 2.8 %) (Figure 81). The calculated profile angle averaged 86.8° (NU ± 0.5°), slightly exceeding that of the half-depth R01 etch (84.7°, NU ± 0.5°), indicating well-controlled, steep sidewalls. The etch rate was calculated to be 5.2 µm/min, and selectivity for both the centre and south samples was calculated to be 58.6:1 and 62.4:1 respectively (NU ± 3.2 %).

Table 39. Measured post-etch features and calculated etch rate for shaft sample post R02 etch recipe at the centre and south of the sample.

Parameter	*Unit*	*Shaft: R02*			
		Centre	*South*	*Average*	*NU (±%)*
Depth	µm	667.5	661.9	664.7	0.4
Top width	µm	294.5	292.5	293.5	0.3
Middle width	µm	236.1	247.9	242.0	2.4
Bottom width	µm	138.2	146.3	142.3	2.8
Calculated profile	°	87.3	86.4	86.8	0.5
Etch rate	µm/min	5.2	5.2	5.2	0.4
Etch selectivity	Si:PR	58.6:1	62.4:1	60.5:1	3.2

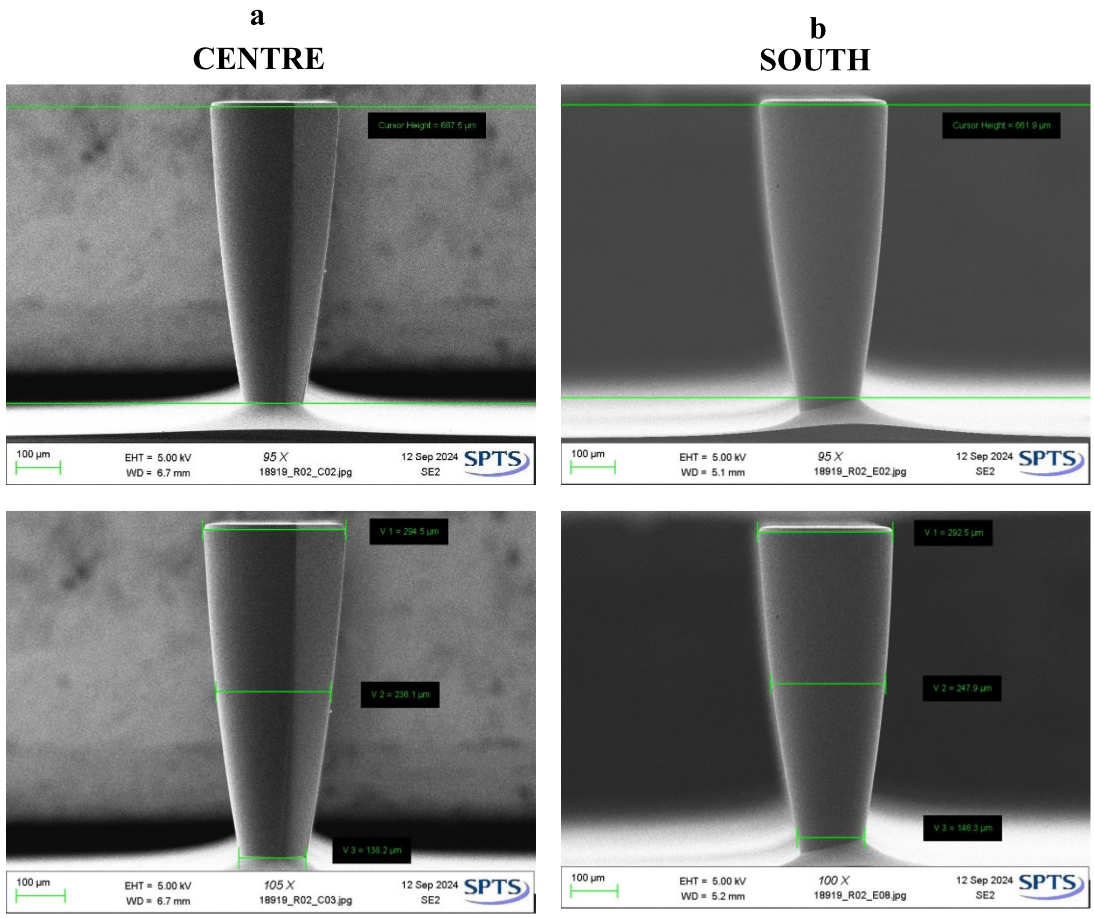

Figure 81. Scanning electron microscope images of shaft features following recipe Shaft R02. Left and right column presents images from a centre and south sample respectively

Shaft R07 (Base recipe, aggressive time ramp)

Shaft R07, a full-depth etch recipe, produced an average etch depth of 657.0 µm, representing a slight reduction compared with the previous full-depth recipe, Shaft R02 (664.7 µm, NU ± 0.4 %) (Table 40, Figure 82). Non-uniformity between the centre and south samples was greater than for R02, with NU ± 2.1 %. Feature widths measured at the top, middle, and bottom of the shaft showed minimal variation, with calculated widths averaging 294.5 µm, 254.7 µm, and 177.1 µm, respectively (NU < ± 1 %). The calculated sidewall profile angle averaged 84.9°, representing the most tapered profile among the full-depth shaft etches to date. SEMs of the etched samples showed no grass or debris formation, and qualitative inspection revealed a visually more tapered sidewall profile compared with features produced by Shaft R02 (Figure 82). The etch rate average was calculated to be 5.2 µm/min. The etch selectivity of Shaft R07 was calculated to be 61.2:1 at the centre and 69.2:1 at the south (NU ± 6.1 %).

Table 40. Measured post-etch features and calculated etch rate for shaft sample post R07 etch recipe at the centre and south of the sample

Parameter	*Unit*	*Shaft: R07*			
		Centre	*South*	*Average*	*NU (±%)*
Depth	µm	642.9	671.1	657.0	2.1
Top width	µm	294.5	294.5	294.5	0.0
Middle width	µm	254.1	255.2	254.7	0.2
Bottom width	µm	175.5	178.6	177.1	0.9
Calculated Profile	°	84.7	85.1	84.9	0.2
Etch rate	µm/min	5.0	5.3	5.2	2.1
Etch selectivity	Si:PR	61.2:1	69.2:1	65.2:1	6.1

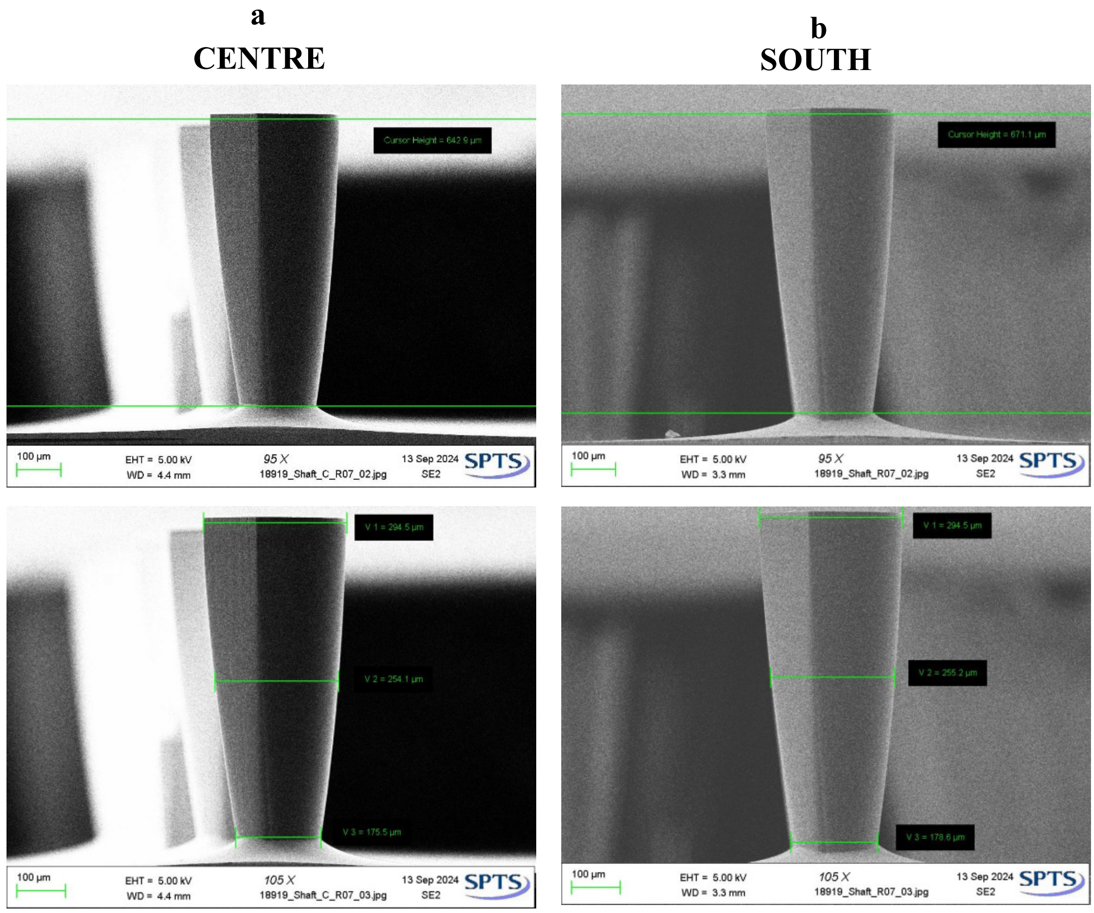

Figure 82. Scanning electron microscope images of shaft features following recipe Shaft R07. Left and right column presents images from a centre and south sample respectively

Shaft R08 (Base recipe, 0.2s reduction in E1)

Shaft R08 full-depth etch recipe produced the lowest average etch depth of all full-depth recipes (633.5 µm) with moderate non-uniformity (± 1.6 %) (Table 41, Figure

83). The three point measurement of feature width enabled the calculation of profile angle (85.2°) with a minimal non-uniformity value (± 0.1 %). This profile angle average indicates that, although closer to the ideal 90° than R07 (84.9°), it was still inferior to the profile angle average produced by R02 (86.8°). The etch rate was also reduced in comparison to R07, with an average of 5.0 µm/min. The etch selectivity of Shaft R08 was 70.7:1 and 78.9:1 for the centre and south samples respectively (NU ± 5.5 %).

Table 41. Measured post-etch features and calculated etch rate for shaft sample post R08 etch recipe at the centre and south of the sample

Parameter	*Unit*	*Shaft: R08*			
		Centre	*South*	*Average*	*NU (± %)*
Depth	µm	643.7	623.3	633.5	1.6
Top width	µm	295.6	297.7	296.7	0.4
Middle width	µm	253.1	260.5	256.8	1.4
Bottom width	µm	189.3	189.3	189.3	0.0
Calculated profile	°	85.3	85.0	85.2	0.1
Etch rate	µm/min	5.0	4.9	5.0	1.6
Etch selectivity	Si:PR	70.7:1	78.9:1	74.8:1	5.5

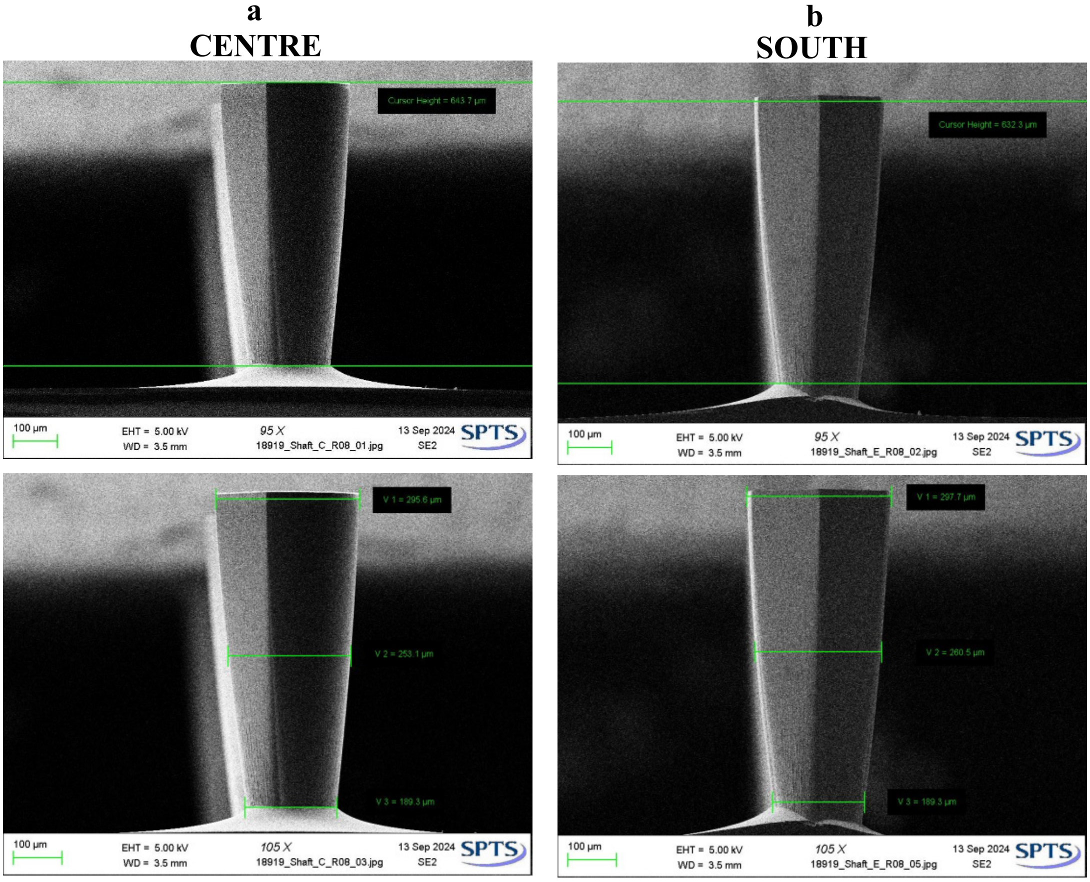

Figure 83. Scanning electron microscope images of shaft features following recipe Shaft R08. Left and right column presents images from a centre and south sample respectively

7.4. Discussion

This chapter presents an initial proof of concept for the scale-up of silicon MN fabrication. The primary aim was to scale up the process from 100 mm to 150 mm, which was performed by optimising each etch step individually, establishing a robust foundation for integration into a continuous manufacturing process. Evaluation of the bevel, bore, and shaft etch recipes enabled the characterisation of baseline process uniformity and feature fidelity. A key constraint in this study was that the shaft photolithography was performed *via* spin coating, rather than the spray coating required for consecutive processing, limiting the direct transferability to a scaled-up continuous workflow.

7.4.1. Bevel etch observations

The bevel etch demonstrated that target depths and sidewall control could be achieved reliably, providing confidence in the reproducibility of this initial process step and its suitability for integration into subsequent etch stages. The reduced depth etch (Bevel R01, average depth 555.4 µm) presented with notable variation in bottom widths and pronounced left/right side asymmetry (Table 30). Upon performing the Bevel R02 (average depth 640.1 µm), wafer uniformity improved (NU ± 1.0 %), demonstrating that this etch step could reliably produce deep, high-aspect-ratio bevel features, with only minor variations in feature widths across the wafer (Table 31). Average etch rates for Bevel R01 and R02 were 9.4 µm/min and 9.6 µm/min respectively, demonstrating that the bevel etch was well-suited for the production of these shallow features, where uniformity and profile control can be readily maintained (Table 30, Table 31). These etch rates are sufficiently high enough to enable efficient throughput yet remain controlled enough to ensure feature fidelity was preserved throughout the process.

Residual PR observed on the centre of Bevel R01 did not indicate incomplete etching, but rather partial detachment of the resist due to thinning at the point of attachment (Figure 71). In some regions, the resist had effectively detached, while in others small remnants remained adhered, explaining why the calculated selectivity values for R01 wafer south, and R02 wafer centre and south appear artificially low; the post-etch resist thickness could not be reliably measured in these areas. Consequently, the most representative measure of the bevel etch selectivity was the 144.5:1 value calculated at the Bevel R01 centre, which confirmed that the bevel etch provides sufficient selectivity to maintain mask integrity. This consistency is advantageous for reproducibility, particularly as the bevel etch represents the first step in a more complex and sequential fabrication process. Despite some minor debris, attributed to cleaving during sample SEM preparation, the bevel features produced by both etches were observed to be clean, indicating a well-controlled process that requires minimal post-fabrication cleaning.

Importantly, the production of uniform, sharp bevels at the needle tip has direct implications for downstream performance: it ensures the MN tip is well-defined, facilitating its penetration of skin with minimal insertion force and tissue strain, supporting both mechanical robustness and minimal tissue trauma. Consequently, these results suggest a low risk of device defect introduction when integrated into the full process flow and indicate that subsequent etches will be built upon a reliable, well-formed foundation.

7.4.2. Bore etch observations

The bore etch step was evaluated to determine the process’ ability to produce deep, high-aspect-ratio features with controlled sidewalls and reproducible dimensions on a wafer with an increased open silicon area (150 mm wafer). The half-depth etch, Bore

R01, produced an average feature depth of 798 µm; however, the measured feature widths exhibited notable variation (*e.g.,* bottom width NU ± 10.4 %) (Table 32, Figure 74). From the perspective of integration into a consecutive process flow, this indicated potential challenges in maintaining feature fidelity when etched at full-depth.

Upon investigation of the full-depth etch, Bore R02 (average feature depth 1335.5 µm, NU ± 0.3 %), achieved highly consistent top and middle widths with a low non-uniformity rate (± 0.3 %). This demonstrating an increased level of reproducibility in deeper, high-aspect-ratio features compared with Bore R01 (Table 33). Despite this improvement, bottom widths retained higher levels of variation (NU ± 22.2 %), reinforcing the intrinsic challenges of achieving dimensional fidelity in extremely high-aspect-ratio structures. The profile of both etches remained consistent (average calculated profile 89.8° ± 0.3 and 89.0° ± 0.3° respectively), which was promising for integration into a full process flow, as it demonstrated that the bore sidewall control was maintained despite increasing etch depth (Table 32, Table 33). This is critical for device function, as variations in bore geometry may substantially influence downstream fluid delivery by altering flow resistance and compromising dosing reliability.

Bore etches had moderately high etch rates (R01 11.3 µm/min, R02 9.9 µm/min), achieving a favourable balance between efficient process time and precise sidewall control, while maintaining minimal tapering of these high-aspect-ratio features (Table 32, Table 33). Selectivity of the half-depth bore etches exceeded 50:1, decreasing to approximately 23:1 for the full-depth etches. This reduction reflects the increased challenge of preserving mask integrity as etch depth increases, highlighting the greater demand on selectivity to prevent mask erosion or feature broadening during prolonged etching.

Minimal etch artefacts, such as striations in the silicon, were visible in the bore sample SEMs, however no other debris was identifiable, indicating a well-controlled process (Figure 74, Figure 75). Overall, the bore etch at both half-depth and full-depth scales successfully demonstrated readiness for transfer to continuous wafer-scale processing through its excellent depth and uniformity. Potential issues may arise from tapering at the bottom width of the bore feature. However, when this step is performed following the bevel etch, rather than independently, the effective starting depth of the bore will be reduced. Resultantly, the impact of base tapering and enhancing reproducibility will be mitigated in the full process flow.

7.4.3. Shaft etch observations

Half-depth recipes

The optimisation of the shaft etch at 150 mm scale required substantially greater recipe development, due to both the modified photolithography protocol employed and to the large volume of silicon that requires removal. Given the significant time required for these etches, shaft recipes were first run at half-depth, allowing the assessment of CDs such as sidewall and profile control, uniformity, and etch depth, before committing tooling time and samples to full-depth etches. All half-depth SEMs showed clean etches with no grass or artefacts observed, despite the 19 µm band produced due to polymer build up in the failed R06 etch, which highlighted the process' sensitivity to interruptions (Figure 76-Figure 80). Average etch depth measured across the half-depth etches varied by 59 µm, which is not insignificant. The shallowest etch depth was observed in the sample produced using a recipe with a reduction in E2 time (Shaft R05). Interestingly, this same etch produced the median profile angle (86.8°) (Figure 78). The profile angles closest to 90° were produced by shaft etches R03 and R06 (87.6°), however these again yielded shallower etches (305 µm and 307 µm respectively) with lower etch rates (3.3 µm/min and 5.0 µm/min respectively) (Table 37, Table 38). Despite the aggressive time ramp (R03) and reduced E1 time (R06) recipes producing slightly improved calculated profiles (> 42 µm reduction in etch depth from R01), it suggests the profile may have progressively tapered as etch depth increased (Figure 80). Resultantly, the modifications made in R03 and R06 may not be beneficial to the structural integrity of the resultant MN device structure. Conversely, Shaft R01 and R04 produced the greatest depth features with the corresponding highest etch rates (349 µm and 5.5 µm/min, and 337 µm and 5.3 µm/min respectively) (Table 34, Table 35). R04 also presented with all NU values below 1 %, in comparison with R01 producing feature with NU values < 2.7 % (Table 35).

The etch rates calculated for the half-depth etches ranged from 3.3 µm/min – 5.6 µm/min. These rates are slower than those calculated for the bevel and bore etches, contributing to enhanced sidewall precision and dimensional fidelity, which are critical for the tall, high-aspect-ratio shaft features. Reduced etch rates minimise the risk of structural defects, such as tapering, and ensure reproducibility of the resultant MN geometry. Variations in etch rate between recipes highlight the sensitivity of the shaft geometry to process parameters, demonstrating that even minor modifications can substantially affect key process parameters and resultantly, final feature quality. With respect to etch selectivity, half-depth shaft recipes R01 and R06 exhibited high selectivity exceeding 70:1, indicating robust mask preservation under these conditions, while R03 also maintained strong selectivity above > 60:1. In contrast, R04 and R05 showed notably lower selectivity values, below < 50:1, illustrating the influence of parameters such as duty cycle and platen power on mask integrity, even at half-depth. These observations confirmed that mask performance was highly sensitive to recipe adjustment, emphasising the importance of a delicate balance of process parameters to achieve high fidelity features. In subsequent full-depth trials, longer etch durations would further challenge mask integrity and resultantly sidewall fidelity, allowing a better assessment of process robustness under conditions more representative of final device fabrication.

The evaluation of the half-depth shaft etches collectively reveal the balance between etch depth and sidewall profile angle, with Shaft R01 and R04 identified as offering the most favourable compromise for progression to full-depth and scale-up. These findings contributed towards informing the design of full-depth etch recipes; R02 as a direct extension of R01; R07 a full-depth version of R04 (half duty cycle and doubled platen power of the base recipe); and lastly R08, merging the aggressive time ramp of R03 and half duty cycle of R04. This strategy ensured the full-depth trials were guided by the most favourable half-depth outcomes, whilst also evaluating additional parameter modifications to improve feature fidelity.

Full-depth recipes

Based on the half-depth etch observations, R02, R07, and R08 full-depth etch recipes were developed and trialled. Full-depth etches present substantial fabrication challenges due to the increased etch time and progressive silicon removal, which leaves minimal surrounding material to act as a heat sink. This can result in drift in uniformity and sidewall profile, most notably manifesting as tapering of the shaft feature. Accordingly, the evaluation of the full-depth trial etches was focused on maintaining the balance between depth and sidewall profile, in order to produce tall MN shafts with minimal tapering and sufficient structural integrity for medical device use.

Measured full etch depth varied by 31.2 µm between R02 and R08, with R02 achieving the greatest depth of 664.7 µm (Table 39). Although R07 reaches a comparable depth, falling short only by 7.7 µm, the measured profile angle produced *via* this recipe resulted in the most tapered of the full-depth etches, averaging 84.9° (Table 40). Despite sharing an etch rate (5.2 µm/min) and similar etch depth, R02 and R07 produce significantly different feature profiles (86.8° and 84.9° respectively), highlighting the sensitivity of sidewall angle to process parameters (Table 39, Table 40). The calculated profile is critical, as increased taper is associated with a higher risk of device damage during skin penetration. Shaft R08, which combined an aggressive time ramp and half duty cycle, produced the shallowest etch (633.5 µm) with the lowest etch rate (5.0 µm/min), while maintaining a moderate profile angle (85.2°) (Table 41).

Full-depth trials for shaft etches, including R02, R07, and R08, exhibited average etch rates of between 5.0 µm/min - 5.2 µm/min. These rates are slower than those observed for the bevel and bore etches, reflecting the necessity of reduced etch speed to maintain precise sidewall control and dimensional fidelity in high-aspect-ratio shaft structures. Notably, these etch rates were consistent with the half-depth shaft recipes, indicating that the fundamental process dynamics are preserved during scale-up and that parameter control was maintained even at extended etch durations. The observed consistency between half-depth and full-depth trials demonstrates that the shaft etch can be reliably scaled without compromising control over key process parameters or final feature geometry.

With respect to etch selectivity, full-depth etches presented values > 50:1, with R08 notably exceeding 70:1. These selectivity values remain sufficient to protect the PR mask and maintain sidewall fidelity over the extended etch period, which is critical given the increased aspect-ratios and associated risks of mask erosion, aperture broadening, and shaft tapering. While the selectivity of full-depth etches does not present an immediate concern, the effect of sequential etch step integration on feature critical dimensions will require careful monitoring. This is to ensure that the reproducible production of high-quality, high-aspect-ratio shaft features is maintained, and that the cumulative effects of extended etch durations does not compromise device structural integrity or dimensional accuracy.

Collectively, these full-depth etches have demonstrated that, whilst target depths exceeding 600 μm are achievable, the sidewall profile angle remains highly sensitive to recipe parameter modifications. In this regard, the most structurally favourable shaft features were produced by R02. These findings offer essential guidance for the integration of the shaft etch into the full, scaled up MN fabrication process in a manner that preserves needle integrity and process consistency.

7.4.4. Implications for full process integration

The findings in this chapter demonstrate that each etch step can be tuned to produce clean and reproducible etch features, providing a solid foundation prior to their sequential integration into a full process flow. The shaft etch step has been optimised here to the limits permitted by the employed photolithography method (spin coating, rather than the spray coating). Sequential execution of the optimised 150 mm scale bevel, bore, and shaft etch steps represents the next critical step to evaluate the cumulative process flow and resulting device characteristics, thereby establishing the overall fidelity of the complete fabrication flow. Importantly, the etch trials revealed notable sensitivities, indicating that consecutive processing may introduce risk, such as defects in PR or polymer residue accumulation from etch errors, which could compromise feature quality if not carefully managed. Nevertheless, the observed consistency of feature profiles and minimal non-uniformity provide confidence that sequential integration is feasible within a scaled-up manufacturing workflow.

7.4.5. Methodological limitations and future work recommendations

Whilst individual etch steps have been trialled and optimised, several methodological limitations remain to be addressed to enable successful scale-up to 150 mm silicon wafers. Observed issues such as polymer build from etch failure appear largely unavoidable at the equipment level. However, at batch scale, the likelihood of these effects could be mitigated through the use of test wafers, standard process pauses, and routine equipment maintenance, thereby reducing the impact of hardware-related errors on overall device yield. Specific to the shaft etch, although spin coating proved sufficient for proof-of-concept etches, this coating technique is incompatible with sequential processing on bevelled wafers due to topography constraints. Therefore, further trials of the shaft etch on bevelled wafers, spray coated with PR, will be required to finalise an optimised etch recipe. Furthermore, the sequential execution of the bevel, bore, and shaft steps may introduce additional variability, the effects of which on final device characteristics are currently unknown. This is less a limitation, and more the next challenge to address as the fabrication process is progressed to full 150 mm wafer manufacturing scale.

8. Chapter 8: Discussion & Conclusions

This final chapter consolidates the key findings of the research performed, reflecting on how novel insights from the data have built upon each other and provided a greater support for the advancement of the silicon MN platform for parenteral drug delivery. By drawing together the findings from each stage of research, this chapter outlines the progress made towards validating silicon MNs as a drug delivery platform, summarises limitations within the research performed, and concludes with the identification of areas for continued investigation to support and guide future device development.

8.1. General discussion

This overarching aim of this research was to establish a foundation of evidence to support the progression of silicon MNs through the regulatory pathway. To achieve this, a systematic approach to the project was designed to encompass device manufacture, mechanical testing, biological assessment, assessments of device performance and reliability, and finally to consider manufacturing scale-up.

To initiate the research pathway, Chapter 3 (small-scale manufacture) marked the first step in translating this aim into actionable progress, focusing on the production of both solid and hollow silicon MNs. This phase built upon previously reported methodologies, improving historical yields in small batch processes by incorporating additional fabrication steps to protect device fidelity, including oxide layers and subsequent wet etches. The manufacturing effort centred on hollow devices, which demonstrated good yield (up to 82 %) and structural quality, with minimal defects and high-aspect ratio features. Instances of suboptimal etch quality were recorded, investigated, and the root cause identified, enabling continuous learning for further wafer processing. The devices fabricated in this chapter provided the physical basis for subsequent investigations, providing MN arrays for mechanical testing, insertion mechanics assessment, cytotoxicity evaluation, and delivery repeatability (Chapters 3-6). The conclusions from these chapters informed die structure modifications, which influenced the later design decisions within Chapter 7 when providing a proof-of-concept for the fabrication of devices at a more industrially relevant scale.

Following the production of devices *via* a small-scale batch process, Chapter 4 focused on insertion mechanics by investigating the effect of HMN insertion on a skin-mimicking membrane. This study provided novel insights into device performance in a repeatable and controllable fashion, utilising DIC to capture surface strain patterns throughout the insertion period. The results demonstrated a consistent and substantial fourfold reduction in the strain profile and stress concentration factor of the membrane following MN insertion in comparison to hypodermics. The more predicable peak forces and dispersed strain patterns induced by MNs validated a more repeatable insertion event, favourable for patient experience, with minimal strain and potentially reduced tissue trauma. Despite the limitations associated with the utilisation of a membrane in place of *ex vivo* skin and imaging 30 % of the hypodermic needle insertion depth, in-depth insights were derived from this study, including the identification of local strain patterns, with positions 2 and 4 resulting in less local strain. Consequently, this finding informed the later scale-up chapter (Chapter 7), with pitch position varied in multiple test arrays to later investigate the effect of this on induced strain uniformity.

Building on the production and mechanics investigation of Chapters 3 and 4, Chapter 5 shifted focus to assessing biocompatibility and potential cytotoxicity. This study aimed to assess the effect of the device starting material, and devices post-fabrication on human keratinocytes, which dominate the epidermal layer of the skin. By complying with ISO 10993-5 in experimental design, a standardised assay and exposure protocol was employed to quantify and assess the impact of devices on cell viability. Results confirmed that the starting materials and processed devices, both hollow and solid, have no significant cytotoxicity on the viability of HaCaT keratinocytes, confirming their compatibility with their intended cellular environment. Prior to translating this work to an *in vivo* environment, this work should be repeated on other relevant cell types such as dermal fibroblasts to ensure a robust assessment of *in vitro* cytotoxicity. Notwithstanding this, the determination of keratinocyte compatibility provides essential preliminary evidence for regulatory evaluation and addresses a key knowledge gap identified in the literature review and research objectives for this project.

With prior validation of insertion repeatability and biological safety, the research progressed to functional testing, concentrating on investigating the repeatability and consistency of device-facilitated ID delivery. Chapter 6 detailed the assessment of the reliability of delivery through hollow silicon MNs into a gel-based mimic of the dermal compartment. A dye-based injection system was used to visualise and assess the penetration depths, bulbous delivery, and lateral dispersion. Results demonstrated consistent delivery performance of the MN devices with respect to initial dye-load localisation and the following dispersion footprint. In contrast, hypodermic needles exhibited far greater variability in both initial delivery localisation and the resultant dye dispersion. It is acknowledged that the HA gel model utilised was a simplification of the native dermal environment, and that increasing this complexity to a multi-layer model could have provided a more accurate representation. Despite this limitation, these findings not only demonstrate the functional reliability of silicon MNs but also provide critical validation prior to *in vivo* testing, strengthening the evidence base for their use as a consistent and controllable parenteral drug delivery platform.

Having demonstrated reduced strain profiles, confirmed biocompatibility, and reliable ID delivery at small-scale, research progressed to optimising scaled-up manufacturing processes. Chapter 7 focused on optimising the photolithography and etch processes at a 150 mm wafer format; a size more appropriate for integration into the existing industrial infrastructure. This transition led to an increase in wafer surface area and usable device die number by 125 % and 140 % respectively. Design modifications were introduced based on insights established in chapters 3-6, including the removal of unnecessary artefacts such as the dicing lanes and the inclusion of test die with variations in pitch to enhance the uniformity of insertion performance. The research performed on the devices produced *via* small-scale fabrication enabled a feedback-driven approach to scale-up optimisation. Therefore, despite the optimised etch steps not being performed cumulatively to produce devices, this satisfied the overarching aims of optimising individual processes required industrial scale fabrication, improving cost-effectiveness whilst maintaining device fidelity and functional reliability.

8.2. Conclusions

This thesis aimed to create a body of evidence to support the progression of silicon MNs down the regulatory pathway. This aim was addressed through five clearly defined objectives encompassing manufacture, mechanical evaluation, biological safety assessment, delivery performance, and scalability. The conclusions associated with each objective are summarised below.

8.2.1. Objective (i): Small-scale manufacture of silicon microneedles

This objective was met by the production of both solid and hollow silicon MNs on 100 mm wafers. HMNs achieved yields of up to 82 % under optimised conditions, surprising previous small scale fabrication benchmarks. Structural fidelity was enhanced through the inclusion of key process modifications including protective oxide layers and wet etching, which supported the production of high aspect ratio features. Fabrication challengers were investigated and root causes identified, to inform later process decisions. The resulting devices manufactured formed the basis for all downstream evaluations.

8.2.2. Objective (ii): Investigation of microneedles insertion mechanics

This objective was fulfilled through the use of a membrane-based model and full-field DIC to observe and analyse strain evolution during insertion. This technique captured dynamic strain patterns, demonstrating that MNs induce lower and more evenly distributed strains than hypodermic needles. Although the model differs from native skin, these results demonstrate controlled and repeatable mechanical interactions on a reproducible platform. This supports the potential for reduced tissue trauma using MN devices.

8.2.3. Objective (iii): Cytotoxicity assessment of silicon microneedles

The achievement of this objective was demonstrated by an ISO standard compliant cytotoxicity assessment of silicon MNs and their constituent materials using HaCaT keratinocytes. No significant reduction in cell viability was observed, confirming that, post-sterilisation, there was no cytotoxicity induced by the starting materials or devices over the 24hr exposure period. These findings establish a preliminary safety profile for translational progression. Further testing in other dermal cell types is advisable, however the objective of establishing a baseline *in vitro* biocompatibility was satisfied.

8.2.4. Objective (iv): Evaluation of intradermal delivery repeatability

This objective was fulfilled through the evaluation of HMNs using a gel-based dermal model. Repeated injections demonstrated consistent bolus localisation, depth, and dispersion patterns. Silicon HMNs exhibited superior delivery repeatability compared with hypodermic alternatives, which showed great variability. Despite the model's simplification of native skin, these findings provide strong evidence for the reproducibility of the MN-mediated intradermal delivery, thereby satisfying the objective.

8.2.5. Objective (v): Initiation of fabrication scale-up

The successful attainment of this objective was achieved through the initiation and optimisation of silicon MN fabrication at 150 mm scale, aligning development with industrial standards. This scale-up increased usable wafer area and device numbers and enabled the incorporation of design modifications including layout alterations and pitch variations. Although a complete batch fabrication was not performed, the optimisation of individual lithography and etch steps provides proof-of-concept for scalability, thereby satisfying the objective.

8.3. Future work recommendations

When reflecting on the outcomes of this research, there are several areas that would benefit from further work and investigation to advance the development and translational readiness of silicon MNs.

First, whilst Chapter 7 details the optimisation of individual etch steps, further work should focus on the integration of these into one continuous process flow to produce devices at 150 mm wafer size. In addition to providing a more accurate representation of the industrial feasibility of these devices, it would also provide test die with altered geometries for further characterisation and investigation.

Secondly, when test die are produced *via* the upscaled fabrication process, the DIC study should be repeated. This would provide valuable evidence as to whether the mechanical performance or device insertion efficiency and strain alters with pitch and bore variants. Such reassessment would enable the identification of whether the current design offers peak performance, or whether a mask redesign to align with the better performing die is more appropriate. The establishment of this is essential before committing to advancing to large-scale fabrication.

Finally, as with any medical device, thorough *in vivo* studies should follow the *in vitro* validation performed in Chapter 5. This would involve the pursuit of an in depth evaluation of the biological response elicited to active pharmaceutical agents delivered through the silicon MNs. This would include, but not be limited to, the assessment of PKs, therapeutic efficacy and dose sparing potential, and local tissue response to contact with the device.

This work has made meaningful progress and aided in laying a more robust foundation for silicon MN evaluation. Nevertheless, as with any medical device, future progress will rely on the convergence of co-ordinated efforts of engineering innovation, pharmaceutical development, and regulatory engagement, to enable these devices to realise their full clinical potential.

9. References

1. Henry S, McAllister DV, Allen MG, Prausnitz MR. Microfabricated microneedles: a novel approach to transdermal drug delivery. J Pharm Sci. 1998;87(8):922-5.
2. Bell GA. A new approach to the sharpening of hypodermic needles. Lancet (London, England). 08/15/1959;2(7094).
3. UNeedle. Silicon Microneedle | Innovation in Precision 2025 [Available from: https://www.uneedle.com/silicon-microneedles.
4. Ando T, Fu X-A. Materials: Silicon and beyond. Sensors and Actuators A: Physical. 2019;296:340-51.
5. Yi T, Li L, Kim C-J. Microscale material testing of single crystalline silicon: process effects on surface morphology and tensile strength. Sensors and Actuators A: Physical. 2000;83(1):172-8.
6. Tilli M, Haapalinna A. Handbook of Silicon Based MEMS Materials and Technologies. In: Tilli M, Paulasto-Krockel M, Petzold M, Theuss H, Motooka T, Lindroos V, editors. Handbook of Silicon Based MEMS Materials and Technologies (Third Edition). 3 ed: Elsevier; 2020. p. 3-17.
7. Lei W-S, Kumar A. Delamination and Reliability Issues in Packaged Devices. Adhesion in Microelectronics2014. p. 267-312.
8. Yunoki S, Ikoma T, Monkawa A, Ohta K, Tanaka J, Sotome S, et al. Influence of γ Irradiation on the Mechanical Strength and In Vitro Biodegradation of Porous Hydroxyapatite/Collagen Composite. Journal of the American Ceramic Society. 2006;89(9):2977-9.
9. Cottam E, Hukins DWL, Lee K, Hewitt C, Jenkins MJ. Effect of sterilisation by gamma irradiation on the ability of polycaprolactone (PCL) to act as a scaffold material. Medical Engineering & Physics. 2009;31(2):221-6.
10. Sanjanwala D, Shinde A, Patravale V. Formulation, sterilization, and clinical evaluation of microneedles for vaccine and biologic delivery: A review. International Journal of Pharmaceutics. 2025;682:125874.
11. PWC. State of the semiconductor industry 2024 [updated 28/11/24. Available from: https://www.pwc.com/gx/en/industries/technology/state-of-the-semicon-industry.html.
12. Cha S-H. The history of vaccination and current vaccination policies in Korea. Clin Exp Vaccine Res. 2012;1(1):3-8.
13. Gill HS, Prausnitz MR. Does Needle Size Matter? Journal of Diabetes Science and Technology. 2007;1(5):725-9.
14. Usach I, Martinez R, Festini T, Peris J-E. Subcutaneous Injection of Drugs: Literature Review of Factors Influencing Pain Sensation at the Injection Site. Advances in Therapy. 2019;36(11):2986-96.
15. Kulchar RJ, Singh R, Ding S, Alexander E, Leong KW, Daniell H. Delivery of biologics: Topical administration. Biomaterials. 2023;302:122312.
16. Hmingthansanga V, Singh N, Banerjee S, Manickam S, Velayutham R, Natesan S. Improved Topical Drug Delivery: Role of Permeation Enhancers and Advanced Approaches. Pharmaceutics. 2022;14(12).
17. Guy RH. Drug delivery to and through the skin. Drug Delivery and Translational Research. 2024;14(8):2032-40.
18. Gulati N, Gupta H. Parenteral drug delivery: a review. Recent Pat Drug Deliv Formul. 2011;5(2):133-45.
19. Homayun B, Lin X, Choi HJ. Challenges and Recent Progress in Oral Drug Delivery Systems for Biopharmaceuticals. Pharmaceutics. 2019;11(3).
20. Kumari N, Siddhanta K, Panja S, Joshi V, Jogdeo C, Kapoor E, et al. Oral Delivery of Nucleic Acid Therapies for Local and Systemic Action. Pharmaceutical Research. 2023;40(1):107-22.

21. NHS. Launch of resources on preventing needlestick injuries 2023 [Available from: https://resolution.nhs.uk/2023/03/30/launch-of-resources-on-preventing-needle-stick-injuries/.

22. Werther RL, Choo S, Lee KJ, Poole D, Allen KJ, Tang ML. Variability in skin prick test results performed by multiple operators depends on the device used. World Allergy Organ J. 2012;5(12):200-4.

23. Iwata H, Kakita K, Imafuku K, Takashima S, Haga N, Yamaguchi Y, et al. Safety and dose-sparing effect of Japanese encephalitis vaccine administered by microneedle patch in uninfected, healthy adults (MNA-J): a randomised, partly blinded, active-controlled, phase 1 trial. The Lancet Microbe. 2022;3(2):e96-e104.

24. Boopathy AV, Mandal A, Kulp DW, Menis S, Bennett NR, Watkins HC, et al. Enhancing humoral immunity via sustained-release implantable microneedle patch vaccination. 2019.

25. Salmon JK, Armstrong CA, Ansel JC. The skin as an immune organ. West J Med. 1994;160(2):146-52.

26. Bai H, Graham C. Introduction: Skin. Yale J Biol Med. 2020;93(1):1-2.

27. Bjerke JR. [The skin as an immunological organ]. Tidsskr Nor Laegeforen. 2002;122(8):793-6.

28. Nguyen AV, Soulika AM. The Dynamics of the Skin's Immune System. International Journal of Molecular Sciences. 2019;20(8):1811.

29. Egawa G, Kabashima K. A new player in the dermis. eLife. 2021;10.

30. Romani N, Flacher V, Tripp CH, Sparber F, Ebner S, Stoitzner P. Targeting Skin Dendritic Cells to Improve Intradermal Vaccination. Current Topics in Microbiology and Immunology: Springer Berlin Heidelberg; 2011. p. 113-38.

31. Levin C, Perrin H, Combadiere B. Tailored immunity by skin antigen-presenting cells. Human Vaccines & Immunotherapeutics. 2015;11(1):27-36.

32. Sandby-Møller J, Poulsen T, Wulf HC. Epidermal thickness at different body sites: relationship to age, gender, pigmentation, blood content, skin type and smoking habits. Acta Derm Venereol. 2003;83(6):410-3.

33. Pan Y, Ma X, Zhao J, Yan S, Liu Q, Zhao H. The Interaction of Age and Anatomical Region Influenced Skin Biophysical Characteristics of Chinese Women. Clin Cosmet Investig Dermatol. 2020;13:911-26.

34. Luebberding S, Krueger N, Kerscher M. Mechanical properties of human skin in vivo: A comparative evaluation in 300 men and women. Skin research and technology : official journal of International Society for Bioengineering and the Skin (ISBS) [and] International Society for Digital Imaging of Skin (ISDIS) [and] International Society for Skin Imaging (ISSI). 2013;20.

35. Krueger N, Luebberding S. Age-Related Changes in Skin Mechanical Properties. 2015. p. 1-9.

36. Firooz A, Sadr B, Babakoohi S, Sarraf-Yazdy M, Fanian F, Kazerouni-Timsar A, et al. Variation of biophysical parameters of the skin with age, gender, and body region. ScientificWorldJournal. 2012;2012:386936.

37. Roberts N, Horsley V. Developing stratified epithelia: lessons from the epidermis and thymus. Wiley Interdiscip Rev Dev Biol. 2014;3(6):389-402.

38. Waghule T, Singhvi G, Dubey SK, Pandey MM, Gupta G, Singh M, et al. Microneedles: A smart approach and increasing potential for transdermal drug delivery system. Biomedicine & Pharmacotherapy. 2019;109:1249-58.

39. Tapfumaneyi P, Imran M, Mohammed Y, Roberts MS. Recent advances and future prospective of topical and transdermal delivery systems. Frontiers in Drug Delivery. 2022;Volume 2 - 2022.

40. Chien AL, Mu EW, Kang S. Chapter 30 - Skin in Osteogenesis Imperfecta. In: Shapiro JR, Byers PH, Glorieux FH, Sponseller PD, editors. Osteogenesis Imperfecta. San Diego: Academic Press; 2014. p. 283-8.

41. Nishifuji K, Yoon JS. The stratum corneum: the rampart of the mammalian body. Vet Dermatol. 2013;24(1):60-72.e15-6.

42. Brito S, Baek M, Bin B-H. Skin Structure, Physiology, and Pathology in Topical and Transdermal Drug Delivery. Pharmaceutics. 2024;16(11):1403.
43. Maeda K. Skin-Moisturizing Effect of Collagen Peptides Taking Orally. Journal of Nutrition & Food Sciences. 2018;08.
44. Brandner JM, Zorn-Kruppa M, Yoshida T, Moll I, Beck LA, De Benedetto A. Epidermal tight junctions in health and disease. Tissue Barriers. 2015;3(1-2):e974451.
45. Deckers J, Hammad H, Hoste E. Langerhans Cells: Sensing the Environment in Health and Disease. Front Immunol. 2018;9:93.
46. Scott DW, Miller WH. Chapter 1 - Structure and Function of the Skin. In: Scott DW, Miller WH, editors. Equine Dermatology. Saint Louis: W.B. Saunders; 2003. p. 1-58.
47. Bento-Lopes L, Cabaço LC, Charneca J, Neto MV, Seabra MC, Barral DC. Melanin's Journey from Melanocytes to Keratinocytes: Uncovering the Molecular Mechanisms of Melanin Transfer and Processing. Int J Mol Sci. 2023;24(14).
48. Bataille A, Le Gall C, Misery L, Talagas M. Merkel Cells Are Multimodal Sensory Cells: A Review of Study Methods. Cells. 2022;11(23).
49. McGrath JA. Structure and function of skin, hair and nails. Medicine. 2025;53(7):417-22.
50. McGrath JA, Uitto J. Structure and Function of the Skin. Rook's Textbook of Dermatology2024. p. 1-50.
51. Fede C, Clair C, Pirri C, Petrelli L, Zhao X, Sun Y, et al. The Human Superficial Fascia: A Narrative Review. International Journal of Molecular Sciences. 2025;26(3):1289.
52. Rivera-Gonzalez G, Shook B, Horsley V. Adipocytes in skin health and disease. Cold Spring Harb Perspect Med. 2014;4(3).
53. Lee SH, Sacks DL. Resilience of dermis resident macrophages to inflammatory challenges. Experimental & Molecular Medicine. 2024;56(10):2105-12.
54. Menon GK, Cleary GW, Lane ME. The structure and function of the stratum corneum. International Journal of Pharmaceutics. 2012;435(1):3-9.
55. Bosko CA. Skin Barrier Insights: From Bricks and Mortar to Molecules and Microbes. J Drugs Dermatol. 2019;18(1s):s63-7.
56. CDC. Vaccine Administration: Needle Gauge and Length 2020 [Available from: https://www.cdc.gov/vaccines/hcp/admin/downloads/vaccine-administration-needle-length.pdf.
57. McNamee M, Wong S, Guy O, Sharma S. Microneedle technology for potential SARS-CoV-2 vaccine delivery. https://doiorg/101080/1742524720232209718. 2023.
58. Zhang C, Merana GR, Harris-Tryon T, Scharschmidt TC. Skin immunity: dissecting the complex biology of our body's outer barrier. Mucosal Immunology. 2022;15(4):551-61.
59. Guttman-Yassky E, Zhou L, Krueger JG. The skin as an immune organ: Tolerance versus effector responses and applications to food allergy and hypersensitivity reactions. Journal of Allergy and Clinical Immunology. 2019;144(2):362-74.
60. Yanez DA, Lacher RK, Vidyarthi A, Colegio OR. The role of macrophages in skin homeostasis. Pflugers Arch. 2017;469(3-4):455-63.
61. Lacy P, Stow JL. Cytokine release from innate immune cells: association with diverse membrane trafficking pathways. Blood. 2011;118(1):9-18.
62. Abrbekoh FN, Salimi L, Saghati S, Amini H, Karkan SF, Moharamzadeh K, et al. Application of microneedle patches for drug delivery; doorstep to novel therapies. https://doiorg/101177/20417314221085390. 2022.
63. Quan FS, Kim YC, Compans RW, Prausnitz MR, Kang SM. Dose sparing enabled by skin immunization with influenza virus-like particle vaccine using microneedles. J Control Release. 2010;147(3):326-32.
64. Moon S, Wang Y, Edens C, Gentsch JR, Prausnitz MR, Jiang B. Dose sparing and enhanced immunogenicity of inactivated rotavirus vaccine administered by skin vaccination using a microneedle patch. Vaccine. 2013;31(34):3396-402.
65. Lunny C, Antony J, Rios P, Williams C, Ramkissoon N, Straus SE, et al. Safety and effectiveness of dose-sparing strategies for intramuscular seasonal influenza vaccine: a rapid scoping review. BMJ Open. 2021;11(9):e050596.

66. Dimitrov D, Adamson B, Matrajt L. Evaluating the use of dose-sparing vaccination strategies for Monkeypox. medRxiv. 2022:2022.11.04.22281966.

67. Schnyder JL, de Jong HK, Grobusch MP. Intradermal immunization-a dose-sparing strategy to combat global shortages of severe acute respiratory syndrome coronavirus 2 vaccines? Clin Microbiol Infect. 2022;28(1):6-8.

68. Tanaka R, Hiramitsu M, Shimizu S, Kawashima S, Sato A, Iwase Y. Efficient drug delivery to lymph nodes by intradermal administration and enhancement of anti-tumor effects of immune checkpoint inhibitors. Cancer Treatment and Research Communications. 2023;36:100740.

69. Hamabe-Horiike T, Harada SI, Yoshida K, Kinoshita J, Yamaguchi T, Fushida S. Adipocytes contribute to tumor progression and invasion of peritoneal metastasis by interacting with gastric cancer cells as cancer associated fibroblasts. Cancer Rep (Hoboken). 2022:e1647.

70. Chen Y, Xu S, Huang C, Ling Y, Liang C, Miao Y, et al. Cancer cells invasion to the gastric bare area adipose tissue: a poor prognostic predictor for gastric cancer. World Journal of Surgical Oncology. 2020;18(1):300.

71. Bellanger D, Dziagwa C, Guimaraes C, Pinault M, Dumas JF, Brisson L. Adipocytes Promote Breast Cancer Cell Survival and Migration through Autophagy Activation. Cancers (Basel). 2021;13(15).

72. Wu Q, Li B, Li Z, Li J, Sun S, Sun S. Cancer-associated adipocytes: key players in breast cancer progression. Journal of Hematology & Oncology. 2019;12(1):95.

73. Nieman KM, Kenny HA, Penicka CV, Ladanyi A, Buell-Gutbrod R, Zillhardt MR, et al. Adipocytes promote ovarian cancer metastasis and provide energy for rapid tumor growth. Nat Med. 2011;17(11):1498-503.

74. Lengyel E, Makowski L, DiGiovanni J, Kolonin MG. Cancer as a Matter of Fat: The Crosstalk between Adipose Tissue and Tumors. Trends Cancer. 2018;4(5):374-84.

75. Calabrese C, Miserocchi G, De Vita A, Spadazzi C, Cocchi C, Vanni S, et al. Lipids and adipocytes involvement in tumor progression with a focus on obesity and diet. Obesity Reviews. 2024;25(12):e13833.

76. Takeuchi A, Nomoto Y, Watanabe M, Kimura S, Morimoto Y, Ueda H. Application of Microneedles to Skin Induces Activation of Epidermal Langerhans Cells and Dermal Dendritic Cells in Mice. Biol Pharm Bull. 2016;39(8):1309-18.

77. Duong HTT, Yin Y, Thambi T, Kim BS, Jeong JH, Lee DS. Highly potent intradermal vaccination by an array of dissolving microneedle polypeptide cocktails for cancer immunotherapy. Journal of Materials Chemistry B. 2020;8(6):1171-81.

78. Iliopoulos F, Sil BC, Evans CL. The role of excipients in promoting topical and transdermal delivery: Current limitations and future perspectives. Frontiers in Drug Delivery. 2022;Volume 2 - 2022.

79. Davis DA, Martins PP, Zamloot MS, Kucera SA, Williams RO, 3rd, Smyth HDC, et al. Complex Drug Delivery Systems: Controlling Transdermal Permeation Rates with Multiple Active Pharmaceutical Ingredients. AAPS PharmSciTech. 2020;21(5):165.

80. Ramadon D, McCrudden MTC, Courtenay AJ, Donnelly RF. Enhancement strategies for transdermal drug delivery systems: current trends and applications. Drug Deliv Transl Res. 2022;12(4):758-91.

81. Jin X, Imran M, Mohammed Y. Topical Semisolid Products-Understanding the Impact of Metamorphosis on Skin Penetration and Physicochemical Properties. Pharmaceutics. 2022;14(11).

82. Yu YQ, Yang X, Wu XF, Fan YB. Enhancing Permeation of Drug Molecules Across the Skin via Delivery in Nanocarriers: Novel Strategies for Effective Transdermal Applications. Front Bioeng Biotechnol. 2021;9:646554.

83. Alkilani AZ, McCrudden MT, Donnelly RF. Transdermal Drug Delivery: Innovative Pharmaceutical Developments Based on Disruption of the Barrier Properties of the stratum corneum. Pharmaceutics. 2015;7(4):438-70.

84. Drosopoulou K, Kosheleva RI, Ofrydopoulou A, Tsoupras A, Mitropoulos A. Topical and Transdermal Delivery of Nonsteroidal Anti-Inflammatory Drugs (NSAIDs) for

Inflammation and Pain: Current Trends and Future Directions in Delivery Systems. Processes. 2025;13(3):907.
85. Zhao L, Chen J, Bai B, Song G, Zhang J, Yu H, et al. Topical drug delivery strategies for enhancing drug effectiveness by skin barriers, drug delivery systems and individualized dosing. Front Pharmacol. 2023;14:1333986.
86. Stott PW, Williams AC, Barry BW. Transdermal delivery from eutectic systems: enhanced permeation of a model drug, ibuprofen. Journal of Controlled Release. 1998;50(1):297-308.
87. Wong WF, Ang KP, Sethi G, Looi CY. Recent Advancement of Medical Patch for Transdermal Drug Delivery. Medicina (Kaunas). 2023;59(4).
88. Nicolas JF, Guy B. Intradermal, epidermal and transcutaneous vaccination: from immunology to clinical practice. Expert Rev Vaccines. 2008;7(8):1201-14.
89. Ebrahim HM, Albalate W. Efficacy of microneedling combined with tacrolimus versus either one alone for vitiligo treatment. J Cosmet Dermatol. 2020;19(4):855-62.
90. Du H, Liu P, Zhu J, Lan J, Li Y, Zhang L, et al. Hyaluronic Acid-Based Dissolving Microneedle Patch Loaded with Methotrexate for Improved Treatment of Psoriasis. ACS Appl Mater Interfaces. 2019;11(46):43588-98.
91. Tekko IA, Permana AD, Vora L, Hatahet T, McCarthy HO, Donnelly RF. Localised and sustained intradermal delivery of methotrexate using nanocrystal-loaded microneedle arrays: Potential for enhanced treatment of psoriasis. Eur J Pharm Sci. 2020;152:105469.
92. Taberner A, Hogan NC, Hunter IW. Needle-free jet injection using real-time controlled linear Lorentz-force actuators. Med Eng Phys. 2012;34(9):1228-35.
93. Engwerda EE, Tack CJ, de Galan BE. Needle-free jet injection of rapid-acting insulin improves early postprandial glucose control in patients with diabetes. Diabetes Care. 2013;36(11):3436-41.
94. Millar JD, Roberto RR, Wulff H, Wenner HA, Henderson DA. Smallpox vaccination by intradermal jet injection. I. Introduction, background and results of pilot studies. Bull World Health Organ. 1969;41(6):749-60.
95. Barolet D, Benohanian A. Current trends in needle-free jet injection: an update. Clin Cosmet Investig Dermatol. 2018;11:231-8.
96. CDC. Flu Vaccination by Jet Injector 2024 [Available from: https://www.cdc.gov/flu/vaccine-types/jet-injector.html.
97. Mitragotri S. Current status and future prospects of needle-free liquid jet injectors. Nat Rev Drug Discov. 2006;5(7):543-8.
98. El-Laboudi A, Oliver NS, Cass A, Johnston D. Use of microneedle array devices for continuous glucose monitoring: a review. Diabetes Technol Ther. 2013;15(1):101-15.
99. Kim Y-C, Park J-H, Prausnitz MR. Microneedles for drug and vaccine delivery. Advanced drug delivery reviews. 2012;64(14):1547-68.
100. Abbasi M, Heath B. Iontophoresis and electroporation-assisted microneedles: advancements and therapeutic potentials in transdermal drug delivery. Drug Deliv Transl Res. 2025;15(6):1962-84.
101. Marathe D, Bhuvanashree VS, Mehta CH, T A, Nayak UY. Low-Frequency Sonophoresis: A Promising Strategy for Enhanced Transdermal Delivery. Adv Pharmacol Pharm Sci. 2024;2024:1247450.
102. Oberli MA, Schoellhammer CM, Langer R, Blankschtein D. Ultrasound-enhanced transdermal delivery: recent advances and future challenges. Ther Deliv. 2014;5(7):843-57.
103. Liu B, Sood R, Wang F, Zhang F, Sun L, Qiu X, et al. Principles and clinical applications of transcutaneous laser-assisted drug delivery: A narrative review. Scars Burn Heal. 2024;10:20595131241234715.
104. Kinnunen HM, Mrsny RJ. Improving the outcomes of biopharmaceutical delivery via the subcutaneous route by understanding the chemical, physical and physiological properties of the subcutaneous injection site. J Control Release. 2014;182:22-32.
105. Kim H, Park H, Lee SJ. Effective method for drug injection into subcutaneous tissue. Sci Rep. 2017;7(1):9613.

106. Zou P, Wang F, Wang J, Lu Y, Tran D, Seo SK. Impact of injection sites on clinical pharmacokinetics of subcutaneously administered peptides and proteins. J Control Release. 2021;336:310-21.
107. Sindelka G, Heinemann L, Berger M, Frenck W, Chantelau E. Effect of insulin concentration, subcutaneous fat thickness and skin temperature on subcutaneous insulin absorption in healthy subjects. Diabetologia. 1994;37(4):377-80.
108. Polania Gutierrez JJ, Munakomi S. Intramuscular Injection. StatPearls. Treasure Island (FL): StatPearls Publishing

Copyright © 2025, StatPearls Publishing LLC.; 2025.
109. Kataoka M, Fukahori M, Ikemura A, Kubota A, Higashino H, Sakuma S, et al. Effects of gastric pH on oral drug absorption: In vitro assessment using a dissolution/permeation system reflecting the gastric dissolution process. Eur J Pharm Biopharm. 2016;101:103-11.
110. Nicoll LH, Hesby A. Intramuscular injection: an integrative research review and guideline for evidence-based practice. Appl Nurs Res. 2002;15(3):149-62.
111. Freeman D, Loe BS, Chadwick A, Vaccari C, Waite F, Rosebrock L, et al. COVID-19 vaccine hesitancy in the UK: the Oxford coronavirus explanations, attitudes, and narratives survey (Oceans) II. Psychol Med. 2022;52(14):3127-41.
112. Zuckerman JN. The importance of injecting vaccines into muscle. Different patients need different needle sizes. Bmj. 2000;321(7271):1237-8.
113. Schnyder JL, De Pijper CA, Garcia Garrido HM, Daams JG, Goorhuis A, Stijnis C, et al. Fractional dose of intradermal compared to intramuscular and subcutaneous vaccination - A systematic review and meta-analysis. Travel Med Infect Dis. 2020;37:101868.
114. Hashmi S, Ling P, Hashmi G, Reed M, Gaugler R, Trimmer W. Genetic transformation of nematodes using arrays of micromechanical piercing structures. BioTechniques. 1995;19:766-70.
115. Makvandi P, Kirkby M, Hutton ARJ, Shabani M, Yiu CKY, Baghbantaraghdari Z, et al. Engineering Microneedle Patches for Improved Penetration: Analysis, Skin Models and Factors Affecting Needle Insertion. Nano-Micro Letters. 2021;13(1):93.
116. Prabhu A, Baliga V, Shenoy R, Dessai AD, Nayak UY. 3D printed microneedles: revamping transdermal drug delivery systems. Drug Deliv Transl Res. 2025;15(2):436-54.
117. Gupta J, Gill HS, Andrews SN, Prausnitz MR. Kinetics of skin resealing after insertion of microneedles in human subjects. J Control Release. 2011;154(2):148-55.
118. Iliescu F, Dumitrescu-Ionescu D, Petrescu M, Iliescu C. A Review on Transdermal Drug Delivery Using Microneedles: Current Research and Perspective. Annals of Academy of Romanian Scientists Series on Science and Technology of Information. 2014;7:7-34.
119. Kalluri H, Banga AK. Formation and closure of microchannels in skin following microporation. Pharm Res. 2011;28(1):82-94.
120. Donnelly RF, Singh TR, Alkilani AZ, McCrudden MT, O'Neill S, O'Mahony C, et al. Hydrogel-forming microneedle arrays exhibit antimicrobial properties: potential for enhanced patient safety. Int J Pharm. 2013;451(1-2):76-91.
121. Gill HS, Prausnitz MR. Coated microneedles for transdermal delivery. Journal of Controlled Release: Official Journal of the Controlled Release Society. 2007;117(2):227-37.
122. Bariya SH, Gohel MC, Mehta TA, Sharma OP. Microneedles: an emerging transdermal drug delivery system. Journal of Pharmacy and Pharmacology. 2011;64(1):11-29.
123. Haj-Ahmad R, Khan H, Arshad MS, Rasekh M, Hussain A, Walsh S, et al. Microneedle Coating Techniques for Transdermal Drug Delivery. Pharmaceutics. 2015;7(4):486-502.
124. Liang L, Chen Y, Zhang BL, Zhang XP, Liu JL, Shen CB, et al. Optimization of dip-coating methods for the fabrication of coated microneedles for drug delivery. Journal of Drug Delivery Science and Technology. 2020;55:101464.
125. Hiraishi Y, Nandakumar S, Choi SO, Lee JW, Kim YC, Posey JE, et al. Bacillus Calmette-Guérin vaccination using a microneedle patch. Vaccine. 2011;29(14):2626-36.

126. Nguyen HX, Bozorg BD, Kim Y, Wieber A, Birk G, Lubda D, et al. Poly (vinyl alcohol) microneedles: Fabrication, characterization, and application for transdermal drug delivery of doxorubicin. Eur J Pharm Biopharm. 2018;129:88-103.
127. Ingrole RSJ, Gill HS. Microneedle Coating Methods: A Review with a Perspective. J Pharmacol Exp Ther. 2019;370(3):555-69.
128. Kim YC, Park JH, Prausnitz MR. Microneedles for drug and vaccine delivery. Adv Drug Deliv Rev. 2012;64(14):1547-68.
129. Moawad F, Pouliot R, Brambilla D. Dissolving microneedles in transdermal drug delivery: A critical analysis of limitations and translation challenges. Journal of Controlled Release. 2025;383:113794.
130. Moawad F, Ruel Y, Rezaei N, Alsarraf J, Pichette A, Legault J, et al. Microneedles with Implantable Tip-Accumulated Therapeutics for the Long-Term Management of Psoriasis. Small. 2024;20(51):e2405927.
131. Park Y-H, Ha SK, Choi I, Kim KS, Park J, Choi N, et al. Fabrication of degradable carboxymethyl cellulose (CMC) microneedle with laser writing and replica molding process for enhancement of transdermal drug delivery. Biotechnology and Bioprocess Engineering. 2016;21(1):110-8.
132. Moga KA, Bickford LR, Geil RD, Dunn SS, Pandya AA, Wang Y, et al. Rapidly–Dissolvable Microneedle Patches Via a Highly Scalable and Reproducible Soft Lithography Approach. Advanced Materials. 2013;25(36):5060-6.
133. Zhu Z, Luo H, Lu W, Luan H, Wu Y, Luo J, et al. Rapidly Dissolvable Microneedle Patches for Transdermal Delivery of Exenatide. Pharmaceutical Research. 2014;31(12):3348-60.
134. Song JE, Jun SH, Park SG, Kang NG. A Semi-Dissolving Microneedle Patch Incorporating TEMPO-Oxidized Bacterial Cellulose Nanofibers for Enhanced Transdermal Delivery. Polymers (Basel). 2020;12(9).
135. Lee JW, Park JH, Prausnitz MR. Dissolving microneedles for transdermal drug delivery. Biomaterials. 2008;29(13):2113-24.
136. Li Y, Zhang H, Yang R, Laffitte Y, Schmill U, Hu W, et al. Fabrication of sharp silicon hollow microneedles by deep-reactive ion etching towards minimally invasive diagnostics. Microsystems & Nanoengineering. 2019;5(1):41.
137. Bolton CJW, Howells O, Blayney GJ, Eng PF, Birchall JC, Gualeni B, et al. Hollow silicon microneedle fabrication using advanced plasma etch technologies for applications in transdermal drug delivery. Lab on a Chip. 2020;20(15):2788-95.
138. Li W-Z, Huo M-R, Zhou J-P, Zhou Y-Q, Hao B-H, Liu T, et al. Super-short solid silicon microneedles for transdermal drug delivery applications. International Journal of Pharmaceutics. 2010;389(1-2):122-9.
139. Pradeep Narayanan S, Raghavan S. Solid silicon microneedles for drug delivery applications. The International Journal of Advanced Manufacturing Technology. 2017;93(1):407-22.
140. Lim H, Ha S, Bae M-G, Yoon SH. A highly robust approach to fabricate the mass-customizable mold of sharp-tipped biodegradable polymer microneedles for drug delivery. International journal of pharmaceutics. 2021:120475.
141. Ali Z, Türeyen EB, Karpat Y, Çakmakcı M. Fabrication of Polymer Micro Needles for Transdermal Drug Delivery System Using DLP Based Projection Stereo-lithography. Procedia CIRP. 2016;42:87-90.
142. Sirbubalo M, Tucak A, Muhamedagic K, Hindija L, Rahić O, Hadžiabdić J, et al. 3D Printing-A "Touch-Button" Approach to Manufacture Microneedles for Transdermal Drug Delivery. Pharmaceutics. 2021;13(7).
143. Evens T, Castagne S, Seveno D, Van Bael A. Comparing the Replication Fidelity of Solid Microneedles Using Injection Compression Moulding and Conventional Injection Moulding. Micromachines (Basel). 2022;13(8).
144. Oh JH, Park HH, Do KY, Han M, Hyun DH, Kim CG, et al. Influence of the delivery systems using a microneedle array on the permeation of a hydrophilic molecule, calcein. Eur J Pharm Biopharm. 2008;69(3):1040-5.

145. Kathuria H, Kochhar JS, Fong MH, Hashimoto M, Iliescu C, Yu H, et al. Polymeric Microneedle Array Fabrication by Photolithography. J Vis Exp. 2015(105).
146. Hartmann XH, van der Linde P, Homburg EF, van Breemen LC, de Jong AM, Luttge R. Insertion Process of Ceramic Nanoporous Microneedles by Means of a Novel Mechanical Applicator Design. Pharmaceutics. 2015;7(4):503-22.
147. McAlister DV, Wang PM, Davis SP, Park J-H, Canatella PJ, Allen MG, et al. Microfabricated needles for transdermal delivery of macromolecules and nanoparticles: Fabrication methods and transport studies. PNAS. 2003;100(24):13755-60.
148. Omatsu T, Chujo K, Miyamoto K, Okida M, Nakamura K, Aoki N, et al. Metal microneedle fabrication using twisted light with spin. Optics Express. 2010;18(17):17967-73.
149. Hu Z, Meduri CS, Ingrole RSJ, Gill S. H, Kumar G. Solid and hollow metallic glass microneedles for transdermal drug-delivery. 2020.
150. Zhang L, Guo R, Wang S, Yang X, Ling G, Zhang P. Fabrication, evaluation and applications of dissolving microneedles. International Journal of Pharmaceutics. 2021;604:120749.
151. Champeau M, Jary D, Mortier L, Mordon S, Vignoud S. A facile fabrication of dissolving microneedles containing 5-aminolevulinic acid. Int J Pharm. 2020;586:119554.
152. Lee K, Lee HC, Lee D-S, Jung H. Drawing Lithography: Three-Dimensional Fabrication of an Ultrahigh-Aspect-Ratio Microneedle. Advanced Materials. 2010;22(4):483-6.
153. Kochhar JS, Zou S, Chan SY, Kang L. Protein encapsulation in polymeric microneedles by photolithography. Int J Nanomedicine. 2012;7:3143-54.
154. O'Mahony C. Structural characterization and in-vivo reliability evaluation of silicon microneedles. Biomedical Microdevices. 2014;16(3):333-43.
155. Yi Y, Shinomiya K, Kobayashi R, Komine H, Yoshihara S, Furushima T. A novel superplastic dieless drawing using fracture phenomenon for fabrication of metal tubular microneedles. CIRP Annals. 2022;71(1):237-40.
156. Evens T, Malek O, Castagne S, Seveno D, Van Bael A. A novel method for producing solid polymer microneedles using laser ablated moulds in an injection moulding process. Manufacturing Letters. 2020;24:29-32.
157. Guimarães TMT, Moniz T, Nunes C, Zaharieva MM, Kaleva M, Yoncheva K, et al. Polymeric Microneedles for Transdermal Delivery of Rivastigmine: Design and Application in Skin Mimetic Model. Pharmaceutics. 2022;14(4):752.
158. Johnson AR, Procopio AT. Low cost additive manufacturing of microneedle masters. 3D Printing in Medicine. 2019;5(1):2.
159. Lee K, Lee CY, Jung H. Dissolving microneedles for transdermal drug administration prepared by stepwise controlled drawing of maltose. Biomaterials. 2011;32(11):3134-40.
160. McGrath MG, Vucen S, Vrdoljak A, Kelly A, O'Mahony C, Crean AM, et al. Production of dissolvable microneedles using an atomised spray process: Effect of microneedle composition on skin penetration. European Journal of Pharmaceutics and Biopharmaceutics. 2014;86(2):200-11.
161. Wang R, Jiang G, Aharodnikau UE, Yunusov K, Sun Y, Liu T, et al. Recent Advances in Polymer Microneedles for Drug Transdermal Delivery: Design Strategies and Applications. Macromolecular Rapid Communications. 2022;43(8):2200037.
162. Chen J, Huang W, Huang Z, Liu S, Ye Y, Li Q, et al. Fabrication of Tip-Dissolving Microneedles for Transdermal Drug Delivery of Meloxicam. AAPS PharmSciTech. 2017;19.
163. Ortega-Rivera OA, Matthew DS, Angela C, Veronique B, Miguel AM-G, Miguel AL-R, et al. Trivalent Subunit Vaccine Candidates for COVID-19 and Their Delivery Devices. 2021.
164. Zhang N, Zhou X, Liu L, Zhao L, Xie H, Yang Z. Dissolving Polymer Microneedles for Transdermal Delivery of Insulin. Front Pharmacol. 2021;12:719905.
165. He M, Yang G, Zhao X, Zhang S, Gao Y. Intradermal Implantable PLGA Microneedles for Etonogestrel Sustained Release. J Pharm Sci. 2020;109(6):1958-66.

166. Hiraishi Y, Nakagawa T, Quan YS, Kamiyama F, Hirobe S, Okada N, et al. Performance and characteristics evaluation of a sodium hyaluronate-based microneedle patch for a transcutaneous drug delivery system. Int J Pharm. 2013;441(1-2):570-9.
167. Marin A, Andrianov AK. Carboxymethylcellulose–Chitosan-coated microneedles with modulated hydration properties. Journal of Applied Polymer Science. 2011;121(1):395-401.
168. Oh NG, Hwang SY, Na YH. Fabrication of a PVA-Based Hydrogel Microneedle Patch. ACS Omega. 2022;7(29):25179-85.
169. Sun W, Araci Z, Inayathullah M, Manickam S, Zhang X, Bruce MA, et al. Polyvinylpyrrolidone microneedles enable delivery of intact proteins for diagnostic and therapeutic applications. Acta Biomater. 2013;9(8):7767-74.
170. Ito Y, Yoshimitsu J, Shiroyama K, Sugioka N, Takada K. Self-dissolving microneedles for the percutaneous absorption of EPO in mice. J Drug Target. 2006;14(5):255-61.
171. Ito Y, Kashiwara S, Fukushima K, Takada K. Two-layered dissolving microneedles for percutaneous delivery of sumatriptan in rats. Drug Dev Ind Pharm. 2011;37(12):1387-93.
172. Huang S, Liu H, Huang S, Fu T, Xue W, Guo R. Dextran methacrylate hydrogel microneedles loaded with doxorubicin and trametinib for continuous transdermal administration of melanoma. Carbohydrate Polymers. 2020;246:116650.
173. He M, Yang G, Zhang S, Zhao X, Gao Y. Dissolving Microneedles Loaded With Etonogestrel Microcrystal Particles for Intradermal Sustained Delivery. J Pharm Sci. 2018;107(4):1037-45.
174. Kim S, Lee J, Shayan FL, Kim S, Huh I, Ma Y, et al. Physicochemical study of ascorbic acid 2-glucoside loaded hyaluronic acid dissolving microneedles irradiated by electron beam and gamma ray. Carbohydr Polym. 2018;180:297-303.
175. Matsuo K, Yokota Y, Zhai Y, Quan YS, Kamiyama F, Mukai Y, et al. A low-invasive and effective transcutaneous immunization system using a novel dissolving microneedle array for soluble and particulate antigens. J Control Release. 2012;161(1):10-7.
176. Zhang Y, Jiang G, Yu W, Liu D, Xu B. Microneedles fabricated from alginate and maltose for transdermal delivery of insulin on diabetic rats. Mater Sci Eng C Mater Biol Appl. 2018;85:18-26.
177. Khosraviboroujeni A, Mirdamadian SZ, Minaiyan M, Taheri A. Preparation and characterization of 3D printed PLA microneedle arrays for prolonged transdermal drug delivery of estradiol valerate. Drug Deliv Transl Res. 2022;12(5):1195-208.
178. Camcı Y, Türk S, Gepek E, İyibilgin O, Özsoy Mİ. Fabrication and characterization of innovative chitosan/doxorubicin coated 3D printed microneedle patch for prolonged drug delivery. Journal of Applied Polymer Science. 2022;139(32):e52759.
179. Yu J, Zhang Y, Ye Y, DiSanto R, Sun W, Ranson D, et al. Microneedle-array patches loaded with hypoxia-sensitive vesicles provide fast glucose-responsive insulin delivery. Proc Natl Acad Sci U S A. 2015;112(27):8260-5.
180. Kim J, Jeong J, Jo JK, So H. Hollow microneedles as a flexible dosing control solution for transdermal drug delivery. Materials Today Bio. 2025;32:101754.
181. Ghate V, Renjith A, Badnikar K, Pahal S, Jayadevi SN, Nayak MM, et al. Single step fabrication of hollow microneedles and an experimental package for controlled drug delivery. Int J Pharm. 2023;632:122546.
182. Martanto W, Moore JS, Kashlan O, Kamath R, Wang PM, O'Neal JM, et al. Microinfusion using hollow microneedles. Pharm Res. 2006;23(1):104-13.
183. Gade S, Glover K, Mishra D, Sharma S, Guy O, Donnelly RF, et al. Hollow microneedles for ocular drug delivery. J Control Release. 2024;371:43-66.
184. Benbrook N, Zhan W. Mathematical modelling of hollow microneedle-mediated transdermal drug delivery. Drug Delivery and Translational Research. 2025;15(9):3226-51.
185. Novinject. HIGHLY CUSTOMISABLE HOLLOW POLYMER MICRONEEDLE SOLUTIONS 2018 [Available from: https://www.ondrugdelivery.com/wp-content/uploads/2018/02/Novinject-HR.pdf.

186. Wang PC, Paik SJ, Kim SH, Allen MG. Hypodermic-Needle-Like Hollow Polymer Microneedle Array: Fabrication and Characterization. Journal of Microelectromechanical Systems. 2014;23(4):991-8.

187. Khanna P, Luongo K, Strom J, Bhansali S. Sharpening of hollow silicon microneedles to reduce skin penetration force. J Micromech Microeng J Micromech Microeng. 2010;20247112.

188. Vicente-Pérez EM, Quinn HL, McAlister E, O'Neill S, Hanna LA, Barry JG, et al. The Use of a Pressure-Indicating Sensor Film to Provide Feedback upon Hydrogel-Forming Microneedle Array Self-Application In Vivo. Pharm Res. 2016;33(12):3072-80.

189. Wonglertnirant N, Todo H, Opanasopit P, Ngawhirunpat T, Sugibayashi K. Macromolecular delivery into skin using a hollow microneedle. Biological & Pharmaceutical Bulletin. 2010;33(12):1988-93.

190. Wang P-C, Wester B, Rajaraman S, Paik S-J, Kim S-H, Allen M. Hollow Polymer Microneedle Array Fabricated by Photolithography Process Combined with Micromolding Technique. Conference proceedings : Annual International Conference of the IEEE Engineering in Medicine and Biology Society IEEE Engineering in Medicine and Biology Society Conference. 2009;2009:7026-9.

191. Ji J, Tay F, Miao J. Microfabricated Hollow Microneedle Array Using ICP Etcher. Journal of Physics: Conference Series. 2006;34:1132.

192. Yang J, Liu X, Fu Y, Song Y. Recent advances of microneedles for biomedical applications: drug delivery and beyond. Acta Pharmaceutica Sinica B. 2019;9(3):469-83.

193. Suzuku M, Takahashi T, Aoyagi S. 3D laser lithographic fabrication of hollow microneedle mimicking mosquitos and its characterisation. International Journal of nanotechnology. 2018.

194. Ashraf MW, Tayyaba S, Nisar A, Afzulpurkar N, Bodhale DW, Lomas T, et al. Design, fabrication and analysis of silicon hollow microneedles for transdermal drug delivery system for treatment of hemodynamic dysfunctions. Cardiovasc Eng. 2010;10(3):91-108.

195. Miller PR, Moorman M, Boehm RD, Wolfley S, Chavez V, Baca JT, et al. Fabrication of Hollow Metal Microneedle Arrays Using a Molding and Electroplating Method. MRS Advances. 2019;4(24):1417-26.

196. Ovsianikov A, Chichkov B, Mente P, Monteiro-Riviere N, Doraiswamy A, Narayan J. Two Photon Polymerization of Polymer–Ceramic Hybrid Materials for Transdermal Drug Delivery. International Journal of Applied Ceramic Technology. 2007;4:22-9.

197. Hara Y, Yamada M, Tatsukawa C, Takahashi T, Suzuki M, Aoyagi S. Fabrication of Stainless Steel Microneedle with Laser-Cut Sharp Tip and its Penetration and Blood Sampling Performance. Int J Autom Technol. 2016;10:950-7.

198. Donnelly RF, Majithiya R, Singh TRR, Morrow DIJ, Garland MJ, Demir YK, et al. Design, Optimization and Characterisation of Polymeric Microneedle Arrays Prepared by a Novel Laser-Based Micromoulding Technique. Pharmaceutical Research. 2011;28(1):41-57.

199. Evens T, Van Hileghem L, Dal Dosso F, Lammertyn J, Malek O, Castagne S, et al. Producing Hollow Polymer Microneedles Using Laser Ablated Molds in an Injection Molding Process. Journal of Micro and Nano-Manufacturing. 2021;9(3).

200. Shikida M, Hasegawa Y, Al Farisi MS, Matsushima M, Kawabe T. Advancements in MEMS technology for medical applications: microneedles and miniaturized sensors. Japanese Journal of Applied Physics. 2021;61.

201. Staples M, Daniel K, Cima M, Langer R. Application of Micro- and Nano-Electromechanical Devices to Drug Delivery. Pharmaceutical research. 2006;23:847-63.

202. Renlund M, Kopp Fernandes L, Rangsten P, Hillmering M, Mosel S, Issa Z, et al. Use of a Silicon Microneedle Chip-Based Device for the Extraction and Subsequent Analysis of Dermal Interstitial Fluid in Heart Failure Patients. Diagnostics. 2025;15(8):989.

203. Ma B, Liu S, Gan Z, Guojun L, Cai X, Zhang H, et al. A PZT Insulin Pump Integrated with a Silicon Micro Needle Array for Transdermal Drug Delivery. Microfluidics and Nanofluidics. 2006;2:417-23.

204. Van Damme P, Oosterhuis-Kafeja F, Van der Wielen M, Almagor Y, Sharon O, Levin Y. Safety and efficacy of a novel microneedle device for dose sparing intradermal influenza vaccination in healthy adults. Vaccine. 2009;27(3):454-9.
205. Carey JB, Pearson FE, Vrdoljak A, McGrath MG, Crean AM, Walsh PT, et al. Microneedle Array Design Determines the Induction of Protective Memory CD8+ T Cell Responses Induced by a Recombinant Live Malaria Vaccine in Mice. PLOS ONE. 2011;6(7):e22442.
206. Chiappini C, De Rosa E, Martinez JO, Liu X, Steele J, Stevens MM, et al. Biodegradable silicon nanoneedles delivering nucleic acids intracellularly induce localized in vivo neovascularization. Nat Mater. 2015;14(5):532-9.
207. Deng Y, Chen J, Zhao Y, Yan X, Zhang L, Choy K, et al. Transdermal Delivery of siRNA through Microneedle Array. Sci Rep. 2016;6:21422.
208. Dervisevic M, Alba M, Yan L, Senel M, Gengenbach TR, Prieto-Simon B, et al. Transdermal Electrochemical Monitoring of Glucose via High-Density Silicon Microneedle Array Patch. Advanced Functional Materials. 2022;32(3):2009850.
209. Huang X, Liang B, Huang S, Liu Z, Yao C, Yang J, et al. Integrated electronic/fluidic microneedle system for glucose sensing and insulin delivery. Theranostics. 2024;14(4):1662-82.
210. Gilman JJ. Why silicon is hard. Science. 1993;261(5127):1436-9.
211. Zahn JD, Talbot NH, Liepmann D, Pisano AP. Microfabricated Polysilicon Microneedles for Minimally Invasive Biomedical Devices. Biomedical Microdevices. 2000;2(4):295-303.
212. Kanďárová H, Pôbiš P. The "Big Three" in biocompatibility testing of medical devices: implementation of alternatives to animal experimentation-are we there yet? Front Toxicol. 2023;5:1337468.
213. Kim D, Bang J, Jeong J, Koo DL, Ko SH. Intelligent soft wearable bioelectronics for neurological disorders. Materials Horizons. 2025;12(14):4970-97.
214. Aldawood FK, Andar A, Desai S. A Comprehensive Review of Microneedles: Types, Materials, Processes, Characterizations and Applications. Polymers. 2021;13(16):2815.
215. Standardization IOf. Biological evaluation of medical devices - Part 1: Evaluation and testing within a risk management process [ISO 10993-1:2018]. 2018.
216. Intel. Ocotillo Campus 2021 [Available from: https://www.exploreintel.com/ocotillo.
217. Administration USFaD. Sterile Drug Products Produced by Aseptic Processing — Current Good Manufacturing Practice. 2004.
218. Agency EM. Good manufacturing practice 2025 [cited 2025 10/11/25]. Available from: https://www.ema.europa.eu/en/human-regulatory-overview/research-development/compliance-research-development/good-manufacturing-practice?
219. Levin Y, inventor; NANOPASS TECHNOLOGIES LTD, assignee. Systems and methods for intradermal delivery of therapeutics using microneedles. US2014 2014-11-27.
220. Liu J, Huang G, Wang RN, He J, Raja AS, Liu T, et al. High-yield, wafer-scale fabrication of ultralow-loss, dispersion-engineered silicon nitride photonic circuits. Nat Commun. 2021;12(1):2236.
221. Crawford L, Wyatt M, Bryers J, Ratner B. Biocompatibility Evolves: Phenomenology to Toxicology to Regeneration. Adv Healthc Mater. 2021;10(11):e2002153.
222. Sen O, Poddar P, Sarkar P, Das S, Manna S. Current advancements in microneedle technology for therapeutic and biomedical applications. Sensors International. 2025;6:100325.
223. Dul M, Alali M, Ameri M, Burke MD, Creelman BP, Dick L, et al. White paper: Understanding, informing and defining the regulatory science of microneedle-based dosage forms that are applied to the skin. Journal of Controlled Release. 2025;378:402-15.
224. Choi J, Lieff SA, Meltzer GY, Grivel MM, Chang VW, Yang LH, et al. Anti-Vaccine Attitudes among Adults in the U.S. during the COVID-19 Pandemic after Vaccine Rollout. Vaccines (Basel). 2022;10(6).

225. Administration F, Drug. Use of International Standard ISO 10993-1, "Biological evaluation of medical devices - Part 1: Evaluation and testing within a risk management process". 2020.
226. Administration USFaD. Premarket Notification (510(k)) Database: K092746 2025 [Available from: https://www.accessdata.fda.gov/scripts/cdrh/cfdocs/cfpmn/pmn.cfm?ID=k092746.
227. Gera AK, Burra RK. The Rise of Polymeric Microneedles: Recent Developments, Advances, Challenges, and Applications with Regard to Transdermal Drug Delivery. Journal of Functional Biomaterials. 2022;13(2):81.
228. Leone M, Van Oorschot BH, Nejadnik MR, Bocchino A, Rosato M, Kersten G, et al. Universal Applicator for Digitally-Controlled Pressing Force and Impact Velocity Insertion of Microneedles into Skin. Pharmaceutics [Internet]. 2018; 10(4).
229. Oliveira C, Teixeira JA, Oliveira N, Ferreira S, Botelho CM. Microneedles' Device: Design, Fabrication, and Applications. Macromol [Internet]. 2024; 4(2):[320-55 pp.].
230. Ahmed Saeed Al-Japairai K, Mahmood S, Hamed Almurisi S, Reddy Venugopal J, Rebhi Hilles A, Azmana M, et al. Current trends in polymer microneedle for transdermal drug delivery. Int J Pharm. 2020;587:119673.
231. Shi Z, Jefimovs K, Romano L, Stampanoni M. Towards the Fabrication of High-Aspect-Ratio Silicon Gratings by Deep Reactive Ion Etching. Micromachines [Internet]. 2020; 11(9).
232. Jansen HV, Gardeniers H, Boer MD, Elwenspoek M, Fluitman JHJ. A survey on the reactive ion etching of silicon in microtechnology. Journal of Micromechanics and Microengineering. 1996;6:14-28.
233. Mumford R, Bolton C, inventors; SPTS Technologies Ltd, assignee. Method of reducing surface roughness. US patent US12417910B2. 2025.
234. Singh OP, Bocchino A, Guillerm T, Hu Y, Stam F, O'Mahony C. Flexible, Conductive Fabric-Backed, Microneedle Electrodes for Electrophysiological Monitoring. Advanced Materials Technologies. 2023;9.
235. Satti AT, Park J, Park J, Kim H, Cho S. Fabrication of Parylene-Coated Microneedle Array Electrode for Wearable ECG Device. Sensors [Internet]. 2020; 20(18).
236. Zhang Y, Hou Z, Si C, Han G, Zhao Y, Lu X, et al. Effects of Mask Material on Lateral Undercut of Silicon Dry Etching. Micromachines [Internet]. 2023; 14(2).
237. Harieth Alrimawi B, Lee JY, Ng KW, Goh CF. In vitro evaluation of microneedle strength: a comparison of test configurations and experimental insights. RSC Pharmaceutics. 2024;1(2):227-33.
238. Gittard SD, Chen B, Xu H, Ovsianikov A, Chichkov BN, Monteiro-Riviere NA, et al. The Effects of Geometry on Skin Penetration and Failure of Polymer Microneedles. Journal of adhesion science and technology. 2013;27(3).
239. Mamun AA, Zhao F. In-Plane Si Microneedles: Fabrication, Characterization, Modeling and Applications. Micromachines [Internet]. 2022; 13(5).
240. Khanna P, Luongo K, Strom J, Bhansali S. Axial and shear fracture strength evaluation of silicon microneedles. Microsystem Technologies. 2010;16:973-8.
241. Makatsori M, Pfaar O, Calderon MA. Allergen Immunotherapy: Clinical Outcomes Assessment. The Journal of Allergy and Clinical Immunology: In Practice. 2014;2(2):123-9.
242. Åström M, Thet Lwin ZM, Teni FS, Burström K, Berg J. Use of the visual analogue scale for health state valuation: a scoping review. Qual Life Res. 2023;32(10):2719-29.
243. Chang EM, Gillespie EF, Shaverdian N. Truthfulness in patient-reported outcomes: factors affecting patients' responses and impact on data quality. Patient Relat Outcome Meas. 2019;10:171-86.
244. Begum MR, Hossain M. VALIDITY AND RELIABILITY OF VISUAL ANALOGUE SCALE (VAS) FOR PAIN MEASUREMENT. 2019;2:394-402.
245. Madden VJ, Kamerman P, Leake HB, Catley MJ, Heathcote LC, Moseley GL. The Sensation and Pain Rating Scale: easy to use, clear to interpret, and responsive to clinical change. medRxiv. 2024.

246. Jansen N, Snijders M-LAHC, Buitenweg JR. Interpretation of subjective ratings within pain research: What about context effects? an induced secondary hyperalgesia example. Medical Hypotheses. 2025;195:111571.
247. McNamee M, Pritchard T, Mitchell J, Bolton C, Roberts K, Guy O, et al. Novel stereo DIC characterisation of microneedle and hypodermic needle insertion. Frontiers in Bioengineering and Biotechnology. 2025;Volume 13 - 2025.
248. Kao AR, Loghmani TM, Gerling GJ. Strain-based biomarkers at the skin surface differentiate asymmetries in soft tissue mobility associated with myofascial pain. J Mech Behav Biomed Mater. 2025;172:107175.
249. Edin BB. Quantitative analyses of dynamic strain sensitivity in human skin mechanoreceptors. J Neurophysiol. 2004;92(6):3233-43.
250. Lewin GR, Moshourab R. Mechanosensation and pain. J Neurobiol. 2004;61(1):30-44.
251. Hao J, Bonnet C, Amsalem M, Ruel J, Delmas P. Transduction and encoding sensory information by skin mechanoreceptors. Pflugers Arch. 2015;467(1):109-19.
252. Chu DH, Loomis CA. 48 - Structure and Development of the Skin and Cutaneous Appendages. In: Polin RA, Abman SH, Rowitch DH, Benitz WE, Fox WW, editors. Fetal and Neonatal Physiology (Fifth Edition): Elsevier; 2017. p. 490-8.e1.
253. Halata Z, Grim M, Baumann KI. Current understanding of Merkel cells, touch reception and the skin. Expert Review of Dermatology. 2010;5(1):109-16.
254. Fleming MS, Luo W. The anatomy, function, and development of mammalian Aβ low-threshold mechanoreceptors. Front Biol (Beijing). 2013;8(4).
255. Yagmur C, Akaishi S, Ogawa R, Guneren E. Mechanical Receptor-Related Mechanisms in Scar Management: A Review and Hypothesis. Plastic and reconstructive surgery. 2010;126:426-34.
256. Sperry MM, Ita ME, Kartha S, Zhang S, Yu YH, Winkelstein B. The Interface of Mechanics and Nociception in Joint Pathophysiology: Insights From the Facet and Temporomandibular Joints. J Biomech Eng. 2017;139(2):0210031-02100313.
257. Yam MF, Loh YC, Tan CS, Khadijah Adam S, Abdul Manan N, Basir R. General Pathways of Pain Sensation and the Major Neurotransmitters Involved in Pain Regulation. Int J Mol Sci. 2018;19(8).
258. Abraira VE, Ginty DD. The sensory neurons of touch. Neuron. 2013;79(4):618-39.
259. Donnelly RF, Garland MJ, Morrow DI, Migalska K, Singh TR, Majithiya R, et al. Optical coherence tomography is a valuable tool in the study of the effects of microneedle geometry on skin penetration characteristics and in-skin dissolution. J Control Release. 2010;147(3):333-41.
260. Potts MR, Evans SL, Pullin R, Coulman SA, Birchall JC, Wyatt H. An analysis of the relationship between microneedle spacing, needle force and skin strain during the indentation phase prior to skin penetration. Computer Methods in Biomechanics and Biomedical Engineering. 2023;26(14):1719-31.
261. Shu W, Heimark H, Bertollo N, Tobin D, O'Cearbhaill E, Annaidh A. Insights into the mechanics of solid conical microneedle array insertion into skin using the finite element method. Acta Biomaterialia. 2021;135:403-13.
262. Shu W, Kilroy S, Ní Annaidh A, O'Cearbhaill ED. Multiphysics modelling of the impact of skin deformation and strain on microneedle-based transdermal therapeutic delivery. Acta Biomaterialia. 2025;194:233-45.
263. Bogusz P, Krasoń W, Pazur K. Application of Digital Image Correlation for Strain Mapping of Structural Elements and Materials. Materials [Internet]. 2024; 17(11).
264. Pan B, Qian K, Xie H, Asundi A. TOPICAL REVIEW: Two-dimensional digital image correlation for in-plane displacement and strain measurement: a review. Measurement Science & Technology - MEAS SCI TECHNOL. 2009;20.
265. Su Y, Gao Z, Zhang Q, Wu S. Spatial uncertainty of measurement errors in digital image correlation. Optics and Lasers in Engineering. 2018;110:113-21.
266. Rothermel TM, Mirmohammad H, Weaver JD, Porter DA, Nguyen M, He Z, et al. Full-field strain measurements on medical devices using digital image correlation:

Considerations and practical examples. Journal of the Mechanical Behavior of Biomedical Materials. 2025;170:107020.
267. Shintake J, Sonar H, Piskarev E, Paik J, Floreano D, editors. Soft pneumatic gelatin actuator for edible robotics. IEEE/RSJ International Conference on Intelligent Robots and Systems (IROS); 2017 2017; Vancouver, BC, Canada: IEEE.
268. Kalra AM, Lowe A, Al-Jumaily AM. Mechanical Behaviour of Skin: A Review. Journal of Material Sciences & Engineering. 2016;5:1-7.
269. Huang NF, Lee RJ, Li S. Engineering of aligned skeletal muscle by micropatterning. American journal of translational research. 2010;2(1):43.
270. Miranda I, Souza A, Sousa P, Ribeiro J, Castanheira EMS, Lima R, et al. Properties and Applications of PDMS for Biomedical Engineering: A Review. Journal of Functional Biomaterials. 2021;13(1).
271. Reidy TM, Luo D, Rana P, Huegel B, Cheng X, Reidy TM, et al. Transparency of PDMS based microfluidic devices under temperature gradients. Journal of Micromechanics and Microengineering. 2018;29(1).
272. Leonardi L, Viganò M, Nicolucci A. Penetration force and cannula sliding profiles of different pen needles: the PICASSO study. Medical Devices (Auckland, NZ). 2019;12.
273. Asadian A, Patel R, R. Kermani M. Dynamics of Translational Friction in Needle–Tissue Interaction During Needle Insertion. Annals of biomedical engineering. 2013;42.
274. Gonçalves AC, Cavassana S, Chavarette FR, Outa R, Casarin SJ, Corazza AV. Variation of the Penetration Effort in an Artificial Tissue by Hypodermic Needles. J Healthc Eng. 2020;2020:8822686.
275. Meyer CH, Kaymak H, Liu Z, Saxena S, Rodrigues EB. Geometry, penetration force, and cutting profile of different 23-gauge trocars systems for pars plana vitrectomy. Retina. 2014;34(11):2290-9.
276. Visscher M, Frijlink HW, Hinrichs WLJ. What Is the Optimal Geometry of Dissolving Microneedle Arrays? A Literature Review. Pharmaceutics [Internet]. 2025; 17(1).
277. Mahvash M, Dupont PE. Fast Needle Insertion to Minimize Tissue Deformation and Damage. IEEE Int Conf Robot Autom. 2009;2009:3097-102.
278. Sahlabadi M, Khodaei S, Jezler K, Hutapea P. Insertion mechanics of bioinspired needles into soft tissues. Minim Invasive Ther Allied Technol. 2018;27(5):284-91.
279. Larrañeta E, Moore J, Vicente-Pérez EM, González-Vázquez P, Lutton R, Woolfson AD, et al. A proposed model membrane and test method for microneedle insertion studies. International Journal of Pharmaceutics. 2014;472(1):65-73.
280. Salthouse D, Novakovic K, Hilkens CMU, Ferreira AM. Interplay between biomaterials and the immune system: Challenges and opportunities in regenerative medicine. Acta Biomaterialia. 2023;155:1-18.
281. Ramakrishna S, Huang ZM. 9.06 - Biocomposites. In: Milne I, Ritchie RO, Karihaloo B, editors. Comprehensive Structural Integrity. Oxford: Pergamon; 2003. p. 215-96.
282. Jain MR, Bandyopadhyay D, Sundar R. Chapter 9 - Scientific and Regulatory Considerations in the Development of in Vitro Techniques for Toxicology. In: Dhawan A, Kwon S, editors. In Vitro Toxicology: Academic Press; 2018. p. 165-85.
283. Jeon B, Kim MO, Kim Y-s, Han H-y, Yun J-H, Kim J, et al. Optimization and validation of a method to identify skin sensitization hazards using IL-1 α and IL-6 secretion from HaCaT. Toxicology in Vitro. 2019;61:104589.
284. Seo MD, Kang TJ, Lee CH, Lee AY, Noh M. HaCaT Keratinocytes and Primary Epidermal Keratinocytes Have Different Transcriptional Profiles of Cornified Envelope-Associated Genes to T Helper Cell Cytokines. Biomol Ther (Seoul). 2012;20(2):171-6.
285. Miclăuş T, Valla V, Koukoura A, Nielsen AA, Dahlerup B, Tsianos GI, et al. Impact of Design on Medical Device Safety. Ther Innov Regul Sci. 2020;54(4):839-49.
286. Colombo I, Sangiovanni E, Maggio R, Mattozzi C, Zava S, Corbett Y, et al. HaCaT Cells as a Reliable In Vitro Differentiation Model to Dissect the Inflammatory/Repair Response of Human Keratinocytes. Mediators Inflamm. 2017;2017:7435621.
287. Carreño EA, Alberto AV, de Souza CA, de Mello HL, Henriques-Pons A, Anastacio Alves L. Considerations and Technical Pitfalls in the Employment of the MTT Assay to

Evaluate Photosensitizers for Photodynamic Therapy. Applied Sciences [Internet]. 2021; 11(6).
288. Larrañeta E, McCrudden MT, Courtenay AJ, Donnelly RF. Microneedles: A New Frontier in Nanomedicine Delivery. Pharm Res. 2016;33(5):1055-73.
289. van den Bemt BJF, Gettings L, Domańska B, Bruggraber R, Mountian I, Kristensen LE. A portfolio of biologic self-injection devices in rheumatology: how patient involvement in device design can improve treatment experience. Drug Deliv. 2019;26(1):384-92.
290. Murty R, Sankaranarayanan A, Bowland, II, Mena-Lapaix J, Prausnitz MR. Angled Insertion of Microneedles for Targeted Antigen Delivery to the Epidermis. Pharmaceutics. 2022;14(2).
291. Hirsch LJ, Strauss KW. The Injection Technique Factor: What You Don't Know or Teach Can Make a Difference. Clin Diabetes. 2019;37(3):227-33.
292. Jacquet E, Chambert J, Pauchot J, Sandoz P. Intra- and inter-individual variability in the mechanical properties of the human skin from in vivo measurements on 20 volunteers. Skin Res Technol. 2017;23(4):491-9.
293. Gomaa YA, Garland MJ, McInnes FJ, Donnelly RF, El-Khordagui LK, Wilson CG. Flux of ionic dyes across microneedle-treated skin: Effect of molecular characteristics. International Journal of Pharmaceutics. 2012;438(1):140-9.
294. Garland MJ, Migalska K, Tuan-Mahmood TM, Raghu Raj Singh T, Majithija R, Caffarel-Salvador E, et al. Influence of skin model on in vitro performance of drug-loaded soluble microneedle arrays. Int J Pharm. 2012;434(1-2):80-9.
295. Enfield J, O'Connell ML, Lawlor K, Jonathan E, O'Mahony C, Leahy M. In-vivo dynamic characterization of microneedle skin penetration using optical coherence tomography. J Biomed Opt. 2010;15(4):046001.
296. Shrestha P, Stoeber B. Fluid absorption by skin tissue during intradermal injections through hollow microneedles. Scientific Reports. 2018;8(1):13749.
297. Ranamukhaarachchi SA, Lehnert S, Ranamukhaarachchi SL, Sprenger L, Schneider T, Mansoor I, et al. A micromechanical comparison of human and porcine skin before and after preservation by freezing for medical device development. Sci Rep. 2016;6:32074.
298. Norman JJ, Choi S-O, Tong NT, Aiyar AR, Patel SR, Prausnitz MR, et al. Hollow microneedles for intradermal injection fabricated by sacrificial micromolding and selective electrodeposition. Biomedical Microdevices. 2013;15(2):203-10.
299. Oyarte Gálvez L, Brió Pérez M, Fernández Rivas D. High speed imaging of solid needle and liquid micro-jet injections. Journal of Applied Physics. 2019;125(14).
300. Vosseler M, Jugl M, Zengerle R. A Smart Interface for Reliable Intradermal Injection and Infusion of High and Low Viscosity Solutions. Pharmaceutical research. 2011;28:647-61.
301. Allmendinger A, Mueller R, Schwarb E, Chipperfield M, Huwyler J, Mahler H-C, et al. Measuring Tissue Back-Pressure - In Vivo Injection Forces During Subcutaneous Injection. Pharmaceutical research. 2014;32.
302. Warnung L, Sattler S, Haiden E, Schober S, Pahr D, Reisinger A. A mechanically validated open-source silicone model for the training of gastric perforation sewing. BMC Medical Education. 2023;23(1):261.
303. Zare M, Ghomi ER, Venkatraman PD, Ramakrishna S. Silicone-based biomaterials for biomedical applications: Antimicrobial strategies and 3D printing technologies. Journal of Applied Polymer Science. 2021;138(38):50969.
304. Monda SM, Weese JR, Anderson BG, Vetter JM, Venkatesh R, Du K, et al. Development and Validity of a Silicone Renal Tumor Model for Robotic Partial Nephrectomy Training. Urology. 2018;114:114-20.
305. Chang DR, Lin RP, Bowe S, Bunegin L, Weitzel EK, McMains KC, et al. Fabrication and validation of a low-cost, medium-fidelity silicone injection molded endoscopic sinus surgery simulation model. The Laryngoscope. 2017;127(4):781-6.
306. Stupic KF, Ainslie M, Boss MA, Charles C, Dienstfrey AM, Evelhoch JL, et al. A standard system phantom for magnetic resonance imaging. Magn Reson Med. 2021;86(3):1194-211.

307. Wang P, Qian L, Liang H, Huang J, Jin J, Xie C, et al. A Polyvinyl Alcohol/Acrylamide Hydrogel with Enhanced Mechanical Properties Promotes Full-Thickness Skin Defect Healing by Regulating Immunomodulation and Angiogenesis Through Paracrine Secretion. Engineering. 2024;37:138-51.
308. Cao H, Wang J, Hao Z, Zhao D. Gelatin-based biomaterials and gelatin as an additive for chronic wound repair. Front Pharmacol. 2024;15:1398939.
309. Dąbrowska A, Rotaru GM, Spano F, Affolter C, Fortunato G, Lehmann S, et al. A water-responsive, gelatine-based human skin model. Tribology International. 2017;113:316-22.
310. Candry P, Godfrey BJ, Wang Z, Sabba F, Dieppa E, Fudge J, et al. Tailoring polyvinyl alcohol-sodium alginate (PVA-SA) hydrogel beads by controlling crosslinking pH and time. Scientific Reports. 2022;12(1):20822.
311. Sakai S, Yasuda R, Sayo T, Inoue S, Ishikawa O. Hyaluronan Exists in the Normal Stratum Corneum. Journal of Investigative Dermatology. 2000;114(6):1184-7.
312. Fakhari A, Berkland C. Applications and emerging trends of hyaluronic acid in tissue engineering, as a dermal filler and in osteoarthritis treatment. Acta Biomaterialia. 2013;9(7):7081-92.
313. Everett JS, Sommers MS. Skin Viscoelasticity: Physiologic Mechanisms, Measurement Issues, and Application to Nursing Science. Biological Research For Nursing. 2012;15(3):338-46.
314. Lamouche G, Kennedy BF, Kennedy KM, Bisaillon CE, Curatolo A, Campbell G, et al. Review of tissue simulating phantoms with controllable optical, mechanical and structural properties for use in optical coherence tomography. Biomed Opt Express. 2012;3(6):1381-98.
315. Klimovič Š, Beckerová D, Věžník J, Kabanov D, Lacina K, Jelinkova S, et al. Hyaluronic acid-based hydrogels with tunable mechanics improved structural and contractile properties of cells. Biomaterials Advances. 2024;159:213819.
316. Cheng J, Chen Z, Lin D, Yang Y, Bai Y, Wang L, et al. A high clinically translatable strategy to anti-aging using hyaluronic acid and silk fibroin co-crosslinked hydrogels as dermal regenerative fillers. Acta Pharmaceutica Sinica B. 2025;15(7):3767-87.
317. Horkay F, Basser PJ, Londono DJ, Hecht A-M, Geissler E. Ions in hyaluronic acid solutions. The Journal of Chemical Physics. 2009;131(18).
318. Ström A, Larsson A, Okay O. Preparation and physical properties of hyaluronic acid-based cryogels. Journal of Applied Polymer Science. 2015;132(29).
319. Bayer IS. Hyaluronic Acid and Controlled Release: A Review. Molecules. 2020;25(11).
320. Cormier M, Johnson B, Ameri M, Nyam K, Libiran L, Zhang DD, et al. Transdermal delivery of desmopressin using a coated microneedle array patch system. Journal of Controlled Release: Official Journal of the Controlled Release Society. 2004;97(3):503-11.
321. Romanyuk AV, Zvezdin VN, Samant P, Grenader MI, Zemlyanova M, Prausnitz MR. Collection of analytes from microneedle patches. Anal Chem. 2014;86(21):10520-3.
322. Ripolin A, Quinn J, Larrañeta E, Vicente-Perez EM, Barry J, Donnelly RF. Successful application of large microneedle patches by human volunteers. Int J Pharm. 2017;521(1-2):92-101.
323. Ita K. Transdermal Delivery of Drugs with Microneedles-Potential and Challenges. Pharmaceutics. 2015;7(3):90-105.
324. Kitahara LBW, Silva VPD, Peres G, Miot HA, Schmitt JV. Efficacy of different concentrations of lidocaine and association of vasoconstrictor in local infiltration anesthesia in adults. An Bras Dermatol. 2021;96(5):623-5.
325. Bahar E, Yoon H. Lidocaine: A Local Anesthetic, Its Adverse Effects and Management. Medicina (Kaunas). 2021;57(8).
326. Prausnitz MR, Langer R. Transdermal drug delivery. Nature Biotechnology. 2008;26(11):1261-8.
327. Meiser SL, Pielenhofer J, Hartmann AK, Stein L, Dettweiler J, Grabbe S, et al. Microneedle-enhanced drug delivery: fabrication, characterization, and insights into release and permeation of nanocrystalline imiquimod. Front Drug Deliv. 2024;4:1425144.

328. Norman JJ, Gupta J, Patel SR, Park S, Jarrahian C, Zehrung D, et al. Reliability and accuracy of intradermal injection by Mantoux technique, hypodermic needle adapter, and hollow microneedle in pigs. Drug Deliv Transl Res. 2014;4(2):126-30.
329. Mansoor I, Eassa HA, Mohammed KHA, Abd El-Fattah MA, Abdo MH, Rashad E, et al. Microneedle-Based Vaccine Delivery: Review of an Emerging Technology. AAPS PharmSciTech. 2022;23(4):103.
330. Pailler-Mattei C, Bec S, Zahouani H. In vivo measurements of the elastic mechanical properties of human skin by indentation tests. Med Eng Phys. 2008;30(5):599-606.
331. Gupta J, Park SS, Bondy B, Felner EI, Prausnitz MR. Infusion pressure and pain during microneedle injection into skin of human subjects. Biomaterials. 2011;32(28):6823-31.
332. Pereira BP, Lucas PW, Swee-Hin T. Ranking the fracture toughness of thin mammalian soft tissues using the scissors cutting test. J Biomech. 1997;30(1):91-4.
333. Quack N, Takabayashi A, Sattari H, Edinger P, Jo G, Bleiker S, et al. Integrated silicon photonic MEMS. Microsystems & Nanoengineering. 2023;9.
334. Hahn PO. The 300 mm silicon wafer — a cost and technology challenge. Microelectronic Engineering. 2001;56(1):3-13.

10. Appendix A – Scaled Up Manufacture Recipes

REDACTED